Novel photoactive materials based on carbogenic nanoparticles

by

Diogo Fernandes

A thesis submitted in partial fulfilment for the requirements for the degree of Doctor of Philosophy at the University of Central Lancashire

April 2018

STUDENT DECLARATION FORM

University of Central Lancashire

Type of Award   Doctor of Philosophy

School   School of Physical Sciences and Computing

1.   Concurrent registration for two or more academic awards

*I declare that while registered as a candidate for the research degree, I have not been a registered candidate or enrolled student for another award of the University or other academic or professional institution

2.   Material submitted for another award

*I declare that no material contained in the thesis has been used in any other submission for an award and is solely my own work.

3.   Collaboration

Where a candidate's research programme is part of a collaborative project, the thesis must indicate in addition clearly the candidate's individual contribution and the extent of the collaboration. Please state below:

N.A.

4.   Use of a Proof-reader

*No proof-reading service was used in the compilation of this thesis.

Signature of Candidate

_____

Print name:

_____

Abstract

By virtue of their non-toxic nature and their attractive photoluminescence (PL) properties, Carbon-dots (or C-dots) represent an emerging class of environmentally benign multifunctional materials. They exhibit excitation-dependent emission and demonstrate colloidal and structural stability. As a result, C-dots are promising candidates for a wide spectrum of applications.

In this work, C-dots were produced from thermal treatment of citric acid in the presence of ethanolamine, and, in another approach, from crude biomass pyrolysis based on previously published methods. The former produced self-passivated C-dots, with high quantum yield and colloidal stability, whilst the latter produced considerably lower quantum yield, although both materials displayed self-quenching effects in the solid-state. In contrast, hybrid nanopowders based SiO_2, TiO_2 and Laponite, in a weight ratio of 1:150, were able to suppress these self-quenching effects. The powders were tested under a fluorescence microscope and it was found that not only the entire material became illuminated, but also displayed colour-tuneability, or excitation dependent emission, as the powders assumed distinct colours when exposed to different wavelength excitation sources.

The hybrid powders were tested as fingerprint developers. To this end, fingerprints were deposited on a variety surfaces - glass slide, large metal spatula and a plastic foil from a soda bottle. The drink foil was selected due its strongly coloured background and to simulate a more casual scenario. It was concluded that the as-prepared powders had the necessary flowability to be used as fingerprint recovery powders, and their ability to produce well-resolved fingerprints was confirmed by Automated Fingerprint Identification System (AFIS, identifies fingerprints minutiae) results when compared to a commercial forensic powder.

Carbogenically coated silica nanohybrids (C-SiO_2), prepared by pyrolysis of polymer coated SiO_2, were also shown to exhibit advantages in recovering latent fingerprints. Owing to their core/shell nature, they were able to inhibit C-dots quenching predisposition, while maintaining their colour-tuneability.

The use of these nanohybrid systems would assist with contrast, for instance, when surfaces are multi-coloured. Their colour-tuneabiity would allow forensic experts to apply one type of powder, and then adjust it to achieve optimum contrast between the fingerprint and the surface, regardless of how strongly coloured or even fluorescent it is. This would allow forensic experts not to have to carry several powders to crime scenes and even minimize the amount of fingerprint evidence lost due to an inefficient development procedure.

An alternative application suggested for the C-SiO$_2$ nanohybrids is as anti-counterfeit tools. Colour-tuneable nano-assemblies, were obtained when suspensions with pH lower than 7 were precipitated (tagged) in different surfaces. The way these nanotags assemble has been demonstrated to happen randomly, and their patterns can be highly influenceable by changing the pH, concentration of the initial solution and even the surface used for the deposition. These colour-tuneable nanotags are cost-efficient, easy to prepare and less toxic alternatives to the quantum dots and rare-earth nanocrystals which have been suggested thus far.

In addition, it has been demonstrated that C-dots can be prepared *in situ* in polymers matrices. Fluorescent polymers are of particular interest for a variety of fields like sensing, biomedical applications and optoelectronics. However, methodology to produce these materials are still in general complex, expensive and frequently involve the use of toxic materials. The *in situ* preparation here established shows that C-dots can be synthesized inside polymers matrix by melt-mixing with a carbon-rich precursor, without producing any significant effect on polymers' crystallinity. Moreover, by using a N-rich carbon precursor, the C-dots' prepared showed high fluorescence intensity in the solid-state. Due to the distinct characteristics of the polymers used (polyethylene – highly water insoluble, and high MW, and polyethylene glycol – high water solubility, and low MW), the method here presented suggests that this protocol can be followed to obtain different types fluorescent polymers.

Briefly, new applications for C-dots nanoparticles are demonstrated. By following various bottom-up approaches and using various carbon-rich precursors, C-dots-based materials with distinct properties have been prepared and their applications have been evidenced in fingerprint recovery, anticounterfeit purposes, and as fluorescence sources to be formed *in situ* in polymeric matrices.

Table of Contents

Acknowledgments

I would like to express my sincere gratitude to everyone who has contributed towards making this an unforgettable journey.

Firstly, I would like to show my full appreciation for all the patience and support my supervisory team has shown during my PhD. To Dr. Marta Krysmann, I deeply appreciate all the hours you spent, training me, for the kindness showed and for being always available. To Dr. Antonios Kelarakis, not enough appreciation can be given to the contribution you have had to my professional and personal development. I am certain that our never-ending meetings have made me a better chemist, but also a more mature person. For that, an honest thank you.

During my time at UCLan I have met some memorable people. I would like to thank all the people I have met in the labs, in the office, or even outside the university, that have made this a more enjoyable experience. By no means in order of importance, a special thanks to Anthony, Damian, Fiona, Pippa, Reece and Tien, for all the support and cheerful times they have provided me with. A word of gratitude to all the technicians at UCLan as well, for all the technical support throughout my project, with a special mention to Tamar and Pete, without whom this would have a been a lot bumpier road.

I would also like to express how thankful I am to my family, in particular my parents, not only for all the financial contribution that made it possible for me to pursue this PhD, but also for all the encouraging words from beginning to end. Without you I definitely wouldn't be here. To my sister as well, which still today pretends to have a grasp of what I do, and is always happy to share her opinions. On a more serious note, you do know you are one of the pillars. Thank you.

And finally, but not the least in any way, I would like to thank you Ana, for it was your unconditional love and support that allowed me to see this project through. A final word to you Balto as well, as you could always find a way to cheer me up. Thanks buddy!

List of Figures

13

List of Abbreviations

aC-dots…………………………………… Citric acid/ethanolamine derived C-dots

AFIS…………………………………… Automated Fingerprint Identification System

AFM…………………………………… Atomic Force Microscopy

AuNPs…………………………………… Gold nanoparticles

bC-dots………………………………….. Crude biomass derived C-dots

C_{60}……………………………………….. Fullerenes

CA………………………………………….. Citric acid

C-dots…………………………………… Carbon dots

CNTs………………………………….. Carbon nanotubes

$C-SiO_2$…………………………………… Carbonised silica

EA…………………………………… Ethanolamine

ECL…………………………………… Electrochemiluminescence

FTIR…………………………………… Fourier Transform Infrared

GO………………………………………... Graphite oxide

GQDs………………………………….. Graphene Quantum Dots

HOMO…………………………………… Highest occupied molecular orbital

HRTEM……………………… High-resolution Transmission Electron microscopy

I_{max}………………………………… Wavelength at which the intensity is the highest

IR…………………………………….. Infrared

Lap…………………………………… Laponite clay

LED………………………………….. Light-emitting diodes

LUMO………………………………….. Lowest unoccupied molecular orbital

NIR………………………………….. Near-Infrared

PBS…………………………………… Phosphate buffer solution

PE…………………………………… Poly(ethylene)

PEG…………………………………... Poly(ethylene glycol)

PEG$_{1500N}$…………………………………... Amine terminated PEG (MW = 1500)

PL…………………………………… Photoluminescence

PPE…………………………………… Poly(p-phenylene ethynylene)

PPEI-EI………………………… Poly(propionylethylene imine-co-ethyleneimine)

QCE…………………………………… Quantum confinement effects

QDs…………………………………... Quantum Dots

QLEDs………………………………… Quantum Dots-based Light-Emitting Diodes

QY…………………………………… Quantum yield

SWCNTs……………………………… Single-walled carbon nanotubes

TEM…………………………………... Transmission Electron Microscopy

UV…………………………………… Ultraviolet

Vis…………………………………… Visible

WFP………………………………… White fingerprint commercial powder

X$_2$…………………………………… Diatomic halogens

XPS…………………………………... X-Ray Photoelectron Spectroscopy

XRD…………………………………... X-Ray Diffraction

1 Introduction

1.1 Aims and objectives

- To synthesize different types of carbogenic nanoparticles with unique fluorescent properties, by following distinct experimental procedures;
- To apply the prepared fluorescent nanopowders to the recovery of latent fingerprints;
- To develop Silica/C-dots core-shell systems for the development of fluorescent nanotags for anti-counterfeit purposes;
- To develop a simple protocol for inducing fluorescent properties to readily available polymers.

1.2 Fluorescent materials overview

Fluorescent materials are nowadays considered vital for optoelectronics, sensoring, bioimaging, among many other fields[1]. Fluorescence occurs when an electron is excited, and upon its return to the ground state, a photon is emitted, most typically, within the UV and NIR wavelength region. Materials' fluorescence properties are thus defined by a range of parameters that are intrinsic to them, such as: emission intensity, excitation and emission wavelengths, emission anisotropy (where light is emitted by a fluorophore with varying intensities over different axes of polarization), and photoluminescence lifetime (a measure of the averaged time excited electrons take to return to the ground state). The different values these parameters may assume are what affords them such a versatility within science and society.[1]

The list of available fluorescent materials is immense, but the most typically investigated can be classified as: organic fluorophores (or dyes)[2], lanthanide chelates[3], fluorescent nanoparticles[1] and fluorescent macromolecular systems (*e.g.* fluorescent polymers[4] and proteins[2]). Through organic synthesis, a number of organic dyes have been synthesized, and they benefit from high quantum yields (fraction of the excited electrons that return to the ground state and emit light, QY) [5] in the UV-Vis range, highly tuneable chemical design, and thus have found use in several fields (pictures on the right of Figure 1-1)[6].
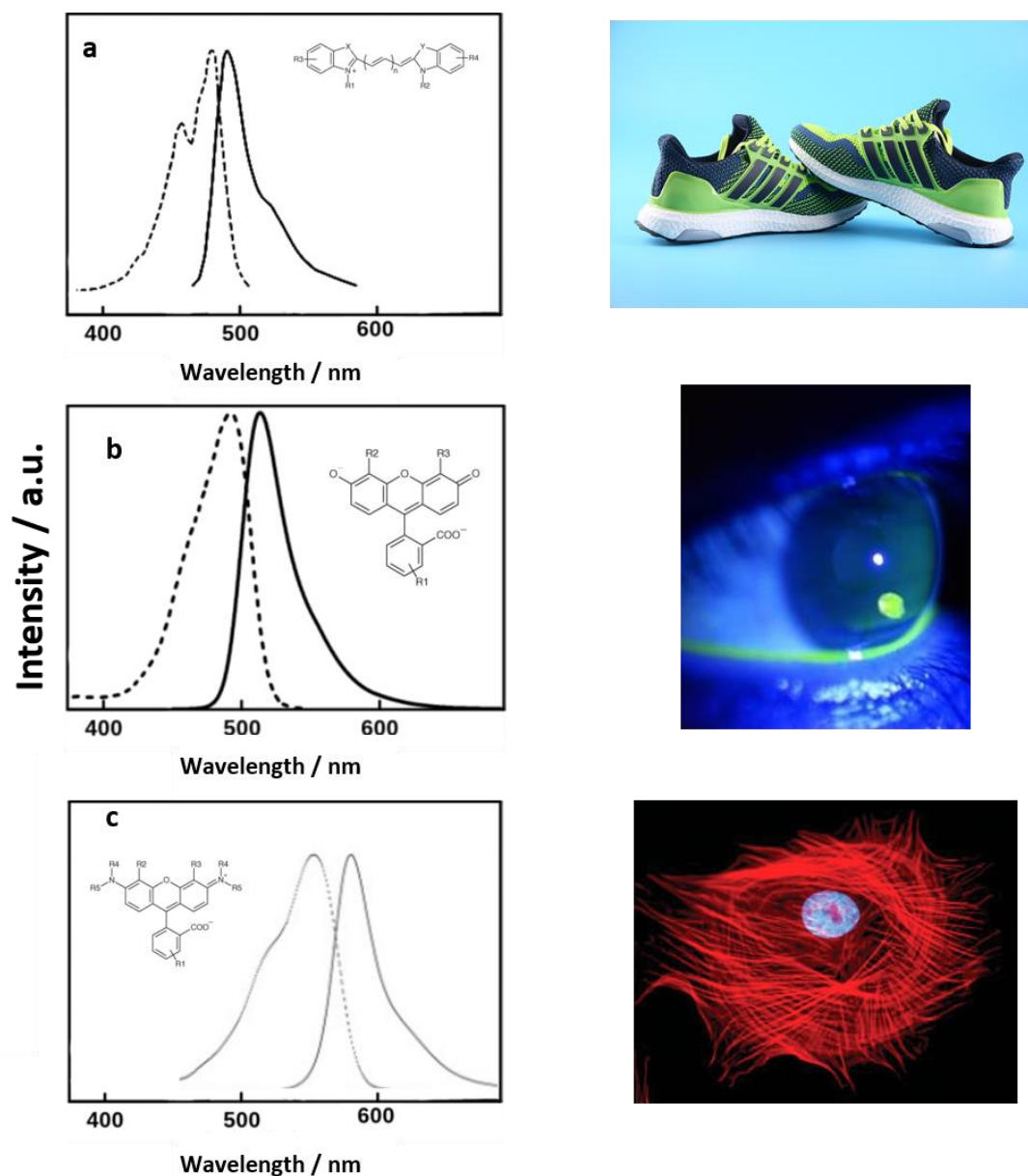
Figure 1-1 – Examples of some of the most common organic dyes, their emission spectra and representative applications: a) cyanine, used by some brands to make fluorescent shoes, b) fluorescein, employed by opticians for better illumination during eye tests, and c) Rhodamine 6G, for cell imaging. Adapted from Ref. 7–9.

Fluorescein, for instance, is currently one of the most used organic dyes (Figure 1-1 b). Its fluorescence properties are highly pH-dependent - it occurs as a cation, anion and neutral forms in aqueous solution. As demonstrated in Figure 1-2 a, fluorescein shows two main absorption peaks in acidic (pH = 2) and basic solutions (pH = 10), at 437 nm and 490 nm, respectively. As the pH decreases, the absorption is

progressively shifted from one to the other, and the emission intensity is reduced (Figure 1-2 b). Fluorescein's highest QY recorded, measured against a standard glycogen solution, has been calculated to be 93%[8,10] for its anionic species (in basic solution). The reason for this higher QY has been attributed to the more rigid form of the anionic species (Figure 1-2 c), which reduces the amount of relaxation through bonding vibrations (lower energy and typically non-emissive transitions)[8].
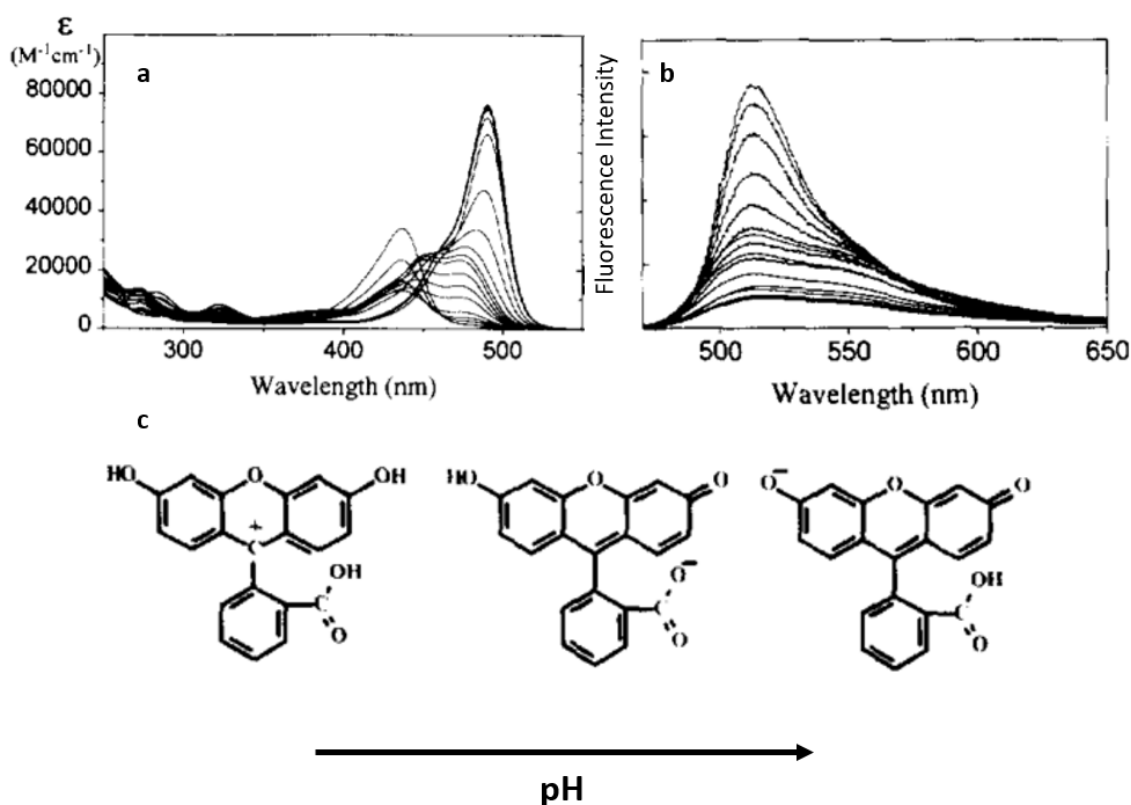
Figure 1-2 – a) UV-Vis absorption spectra and b) emission spectra of fluorescein in aqueous solutions at different pH, and c) evolution of fluorescein from the cationic form (left) to anionic (middle) and dianionic (right) form, with increasing pH. Adapted from Ref. 8.

There are, however, certain limitations that organic dyes tend to display, most significantly: low photostability – making them susceptible to hostile environments, narrow excitation bands, small Stokes shifts (plots on the left of Figure 1-1), and short fluorescence lifetimes[5]. Furthermore, they have very low QYs in the Infra-red region, which is a particularly disadvantage for *in vivo* studies, since the human body is invisible to this type of radiation.[1]

22

Quantum-dots (QDs), semiconductor nanocrystals (typically ranging from ~ 2 – 10 nm) composed of elements from groups II/VI and III/V, are a class of fluorescent nanomaterials that has gained momentum in the field. QDs display heavily size-dependent optical properties - smaller particles emit at lower wavelengths, with higher energy levels, and larger particles emit at higher wavelengths with lower energies associated (Figure 1-3 a). This effect is known as Quantum Confinement, and only takes place in the nanoscale [1,11,12]. As the crystal radius of the QDs (or in other words, the size of the nanoparticles) decreases and the Bohr-exciton radius remains constant (*e.g.* 5.6 nm for CdSe nanoparticles[13]), the band gap increases. This results on more energetic transitions and thus, a shift in visible emission, from near-IR to near UV [14], Figure 1-3 b. Furthermore, these nanoparticles display high photostability in a range of solvents, broad excitation bands, high molar extinction coefficients (ε), and have been prepared with a variety of surface chemistry designs[1]. Some examples of QDs include cadmium selenide (CdSe), cadmium telluride (CdTe), lead selenide (PbSe), zinc sulphide (ZnS), gallium nitride (GaN), indium arsenide (InAs), among many others, and each has a specific size-dependent range of emission wavelengths, as demonstrated in Figure 1-3 c.
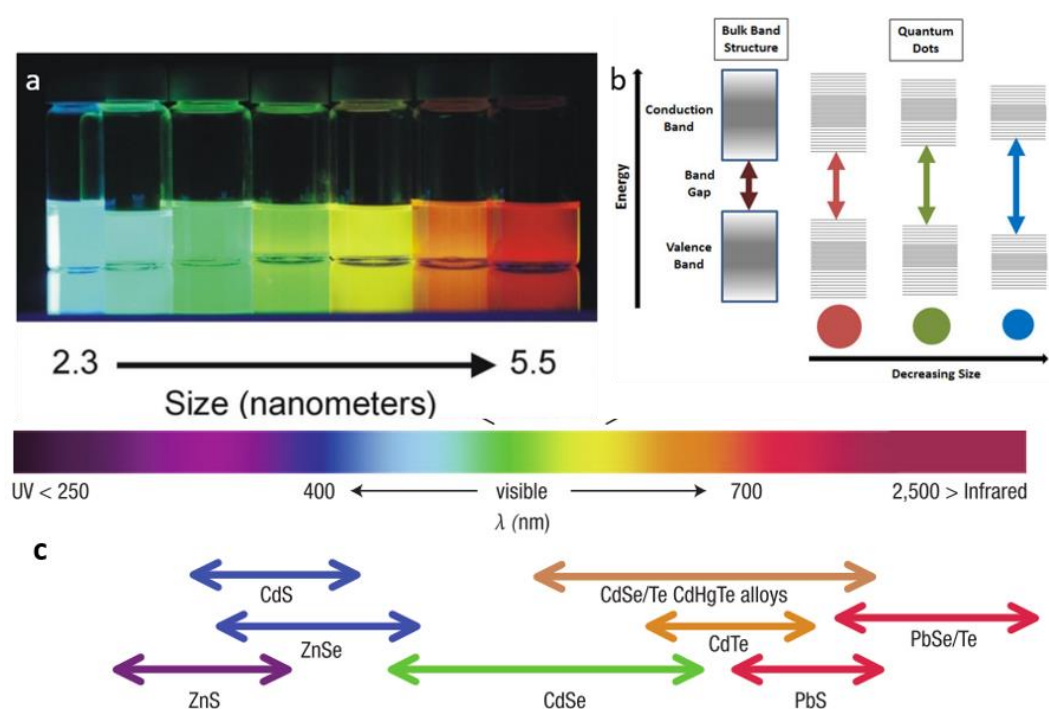
Figure 1-3 – a) Solutions of Cadmium-based quantum dots exposed to UV radiation, showing different emission colours depending on the nanoparticles size, b) schematic illustration of the Quantum

More recently, quantum dots experienced a rise in their popularity owing to a series of international brands using them for improved display technologies. The greatest asset they bring to Light-Emitting Diodes displays (LED) are their tuneable band gap which affords more vibrant and wider range of colours. In these systems, a charge injection occurs, an electron and a hole are formed and migrate along a charge transport layer creating an exciton on the QDs layer. The exciton is then recombined and releases the photon which emits light in the form of the desired colour[13].

Due to QDs fluorescence properties, it is possible to better study their cytotoxicity. Considering the wider range of emission wavelengths of the Cadmium-based quantum dots, it comes as no surprise that these have become of primary importance to researchers all over the world[1]. In Figure 1-4 a, the effect in the metabolic activity (which directly relates to cell survival rate), of Cd-based QDs with various surface chemistry, is demonstrated. In this experiment, a negative control (CTRL), where cell's metabolic activity was studied with no interferents, and two positive controls, consisting of cells injected with different amounts of Cd^{2+} (0.5 μM and 1 μM), were used. This allowed, initially, a correlation between the decrease in the metabolic activity and the presence of certain types of quantum dots (Figure 1-4 a), which was then attributed to an increase in the cellular uptake (both intra- and extracellularly) of Cd^{2+} (Figure 1-4 b).
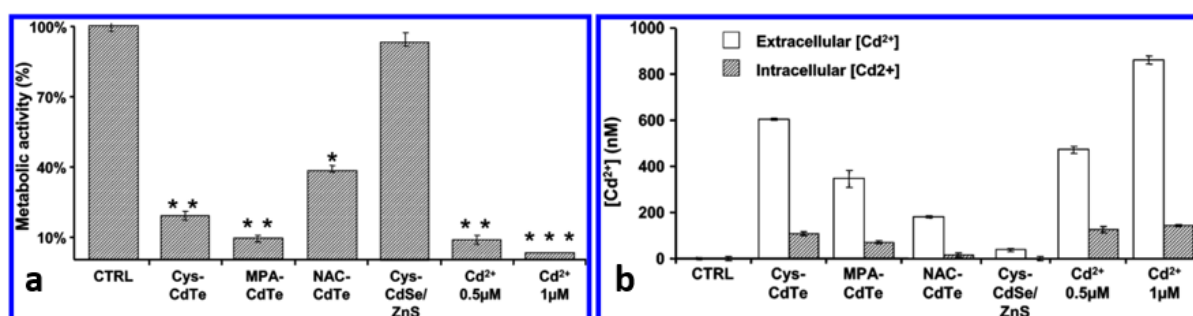
Figure 1-4 – a) Impact of different QDs in the metabolic activity of human cells, and b) the extracellular and intracellular concentration of Cd2+ after exposure to the different types of QDs and functional groups (Ctrl – control; Functional groups: Cys- cysteine; MPA – 3-mercaptopropionic acid; NAC – *N*-acetyl-*L*-cysteine). Adapted from Ref. 19.

This effect is attributed to the fact that QDs are known to be susceptible to photooxidation in cells, under aerobic conditions. Potentially, this may lead to the formation of superoxides (O^{2-}), through electron transfer from the free Cd^{2+} (in the case of Cd-based QDs) or excited quantum dots, to the O_2 molecules, and other reactive oxygen species (ROS), since the excited QDs can form the higher energy and reactive form of singlet oxygen[19]. Furthermore, the unpaired hole can induce cleavage decomposition of the nanoparticles' outer surface[19], which may result in the intracellular release of heavy metals. Strategies to overcome this have mostly focused on the attachment of biocompatible functional groups or polymer chains to the quantum dots surface. By analysing Figure 1-4, it is clear that the unprotected CdTe QDs, independently of the functional groups attached, tend generate higher quantities of Cd^{2+} and have greater impact in the cells' metabolic activity. However, the ZnS-covered CdSe QDs, potentially due to the protection of the outer shell, seem to generate minor amounts of Cd^{2+} and have therefore, negligible impact on the metabolic activity[19]. Similarly, Acuña et al.[20], demonstrated that by Ni-surface-passivating ZnSe/ZnS core/shell QDs, the cell viability could be maintained at 100% up to concentrations as high as 500 µg/mL, whilst undoped QDs showed a loss in cell viability of ~ 20% at concentrations of 200 µg/mL (Figure 1-5).
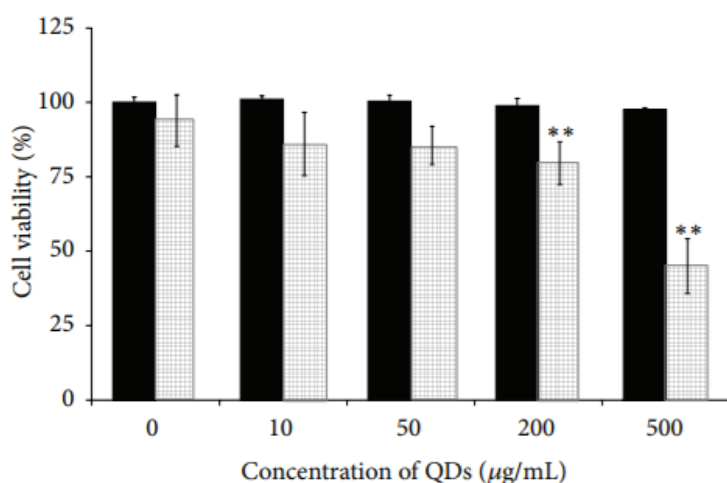
Figure 1-5 – Cell viability (%) after exposure of undoped (grey bars) and Ni-doped (black bars) ZnSe/ZnS core/shell QDs at different concentrations. Adapted from 20.

Dubertret et al.[21], suggested the use of incapsulated ZnS-over-coated CdSe quantum dots in poly(ethylene glycol) (PEG)-based micelles, with the nanohybrids sizes ranging from 10-15 nm (Figure 1-6 a), and the quantum yield was measured at 24%. These nanoparticles were found to be able to penetrate the nuclei of frogs' embryos and it was possible to monitor their growth, as seen in Figure 1-6 b, c and d.

Other types of QDs have been suggested which display significantly less toxicity, for instance, Si-based QDs. Even though bulk Si displays optimum electron conductivity it shows no photoluminescence (PL) properties. However due to quantum confinement effects, Si can be used for QDs preparation and display similar PL properties[22]. Of particular interest is the fact that, even when they decompose, they form silicic acid which is a molecule of biological importance and shows inherent biodegrability[23,24].

Nevertheless, it is still not clear the full extent of toxicity effects of quantum dots and more conclusive studies in the field are needed[25]. For that reason, nanomaterial scientists have focused on bringing new alternatives with potentially less harmful effects.
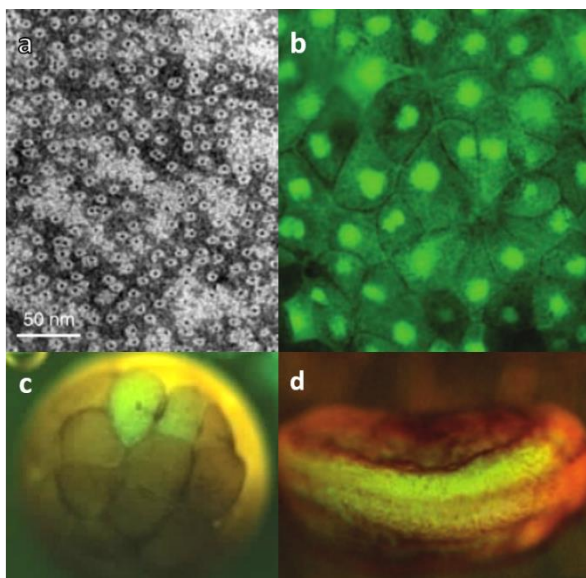
Figure 1-6 – a) TEM image of CdSe QDs incapsulated in PEG-based micelles (size ranges from 10-15 nm), b) intra- and c)/d) extracellular imaging of frogs' embryos in different stages of development. Adapted from Ref. 21.

1.3 Carbon Dots

The rapid emergence of carbon-based nanoparticles (typically referred to as carbon-dots or C-dots) is in no small part due to their low toxicity and PL properties that rival those of QDs. Depending on their structure, they can be classified as graphene quantum dots (hereafter referred to as GQDs) or amorphous carbon nanodots. They brought new possibilities to the nanomaterials science, as they pose as biocompatible, cost-efficient and easily processed alternatives to the mainly heavy metal-based quantum dots.

1.3.1 Graphene Quantum Dots

GQDs are fragments of graphene sheets small enough to display quantum confinement effects – typically with sizes below 20 nm[26]. Rather than quasi-spherical particles, like C-dots, they can be formed by 1 to 10 fractioned graphene layers and have a predominant zigzag edge structure[27,28]. Bulk graphene displays zero band gap and charge carriers have at the band edges effective masses of 0, consequently having infinite exciton Bohr radius. Due to their reduced sized, GQDs display quantum confinement effects which, contrarily to graphene sheets, result on photoluminescent materials.[29]

GQDs can be synthesized using top-down methods, which consist of cleavage of graphene-based structures. On the other hand, bottom-up approaches focus on the synthesis of the GQDs from molecules with aromatic structures. Even though these tend to be more complex procedures, they allow for better size and morphology control [26,30].

In the following section, some of the most common/significant methods for the synthesis of GQD will be reviewed.

1.3.1.1 Top-down routes

Top-down synthetic approaches for the preparation of GQDs benefit from cheap procedures for the cleavage of readily available bulk materials, like graphite. Most

methods rely initially on the oxidation of the graphite sheets to graphite oxide (GO) sheets, typically through a modified Hummers method[31], while differing on the strategy followed to produce the GQDs from the GO sheets[32]. Briefly, the Hummers method consists of oxidation of the graphene layers by mixing with sulfuric acid, sodium nitrate and potassium permanganate, which then creates epoxy, hydroxyl and carbonyl groups. These result on defects sites on the GO sheets, susceptible to being successively attacked and cleaved into forming smaller fragments (Figure 1-7), until dimensions smaller than the Bohr radius are achieved and GQDs are obtained. Hence, theoretically, any carbogenic materials with aromatic sp^2 carbons can be used as starting materials, such as carbon nanotubes[33], carbon black[34] and carbon fibres[35].
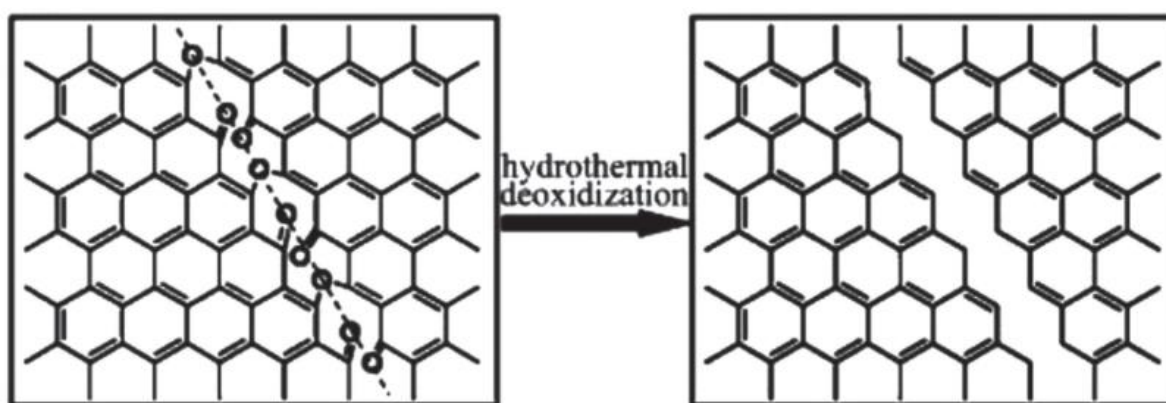
Figure 1-7 – Schematic illustration of the cleavage of oxidized graphene sheets on the susceptible carbonyl groups resulting on fragmented graphene sheets, after hydrothermal treatment. Adapted from 36.

One of the most common methods followed is the electrochemical peeling of GQDs from graphite rods, CNTs or coal, as starting materials [33,37–40]. In a typical procedure[37], a graphite rod is used as the working electrode, a Pt mesh used as the counter electrode, Ag/AgCl as a reference electrode and a PBS buffer (pH = 7) as the electrolyte (Figure 1-8 a). A potential is applied at 0.1 V/s cycled between the range of -3.0 to 3.0 V. A schematic representation of the extraction of GQDs through this method is illustrated in Figure 1-8 b.

Electrochemical exfoliation of graphite rods, as Lu et. al.[40] described, affords highly stable water dispersions of GQDs and with high reaction yields. The authors reduced GQDs with hydrazide, resulting in particles with a size distribution between 4 and 10 nm. Raman spectroscopy (Figure 1-9 a) of these nanoparticles showed a relatively

small index of disordered carbon: a ratio of the characteristic D band (1337 cm^{-1}, attributed to amorphous carbon defects) over the G band (1595 cm^{-1}, associated with sp^2 bonded carbon) of I_D/I_G = 0.91. This suggests graphitic interplanar vibrations on the GQDs with some other defects arising from smaller fractions of disordered carbon. X-ray diffraction (XRD) patterns (Figure 1-9 b) show a broad peak at 25°, with a Miller index of (002), and it is ascribed to the thinness and the presence of disordered carbon in some of GQDs layers.
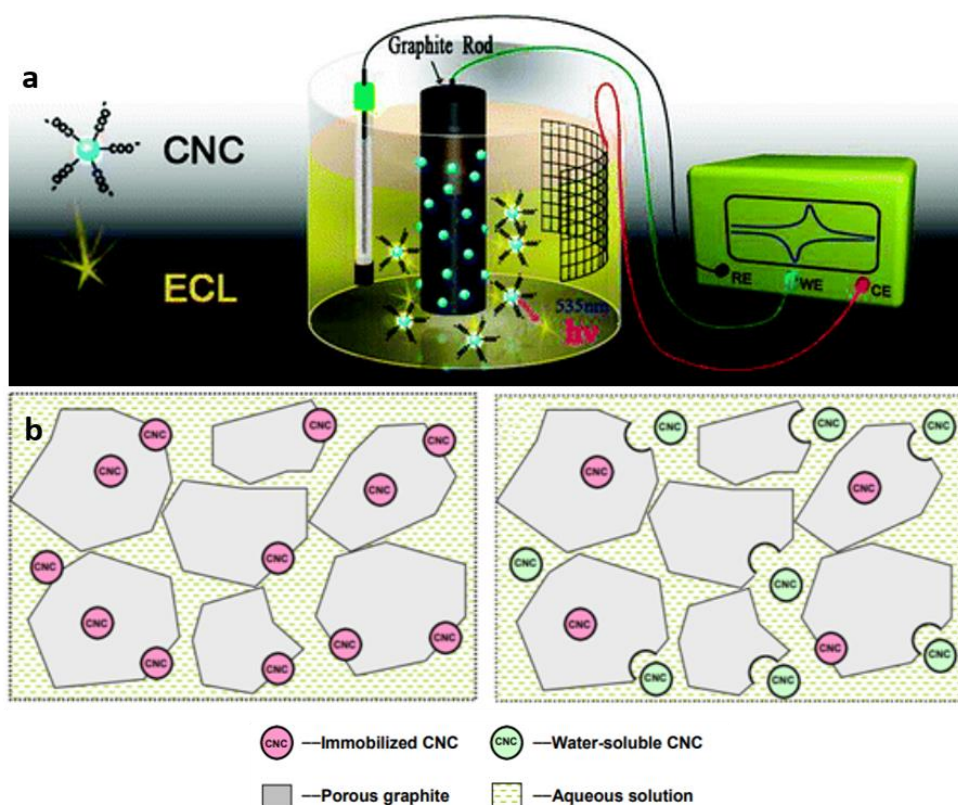
Figure 1-8 – Schematic representation of a) the electrochemical apparatus for the exfoliation of the b) immobilized GQDs (or CNCs as referred to by the authors) on graphite oxide. Adapted from Ref. 37.
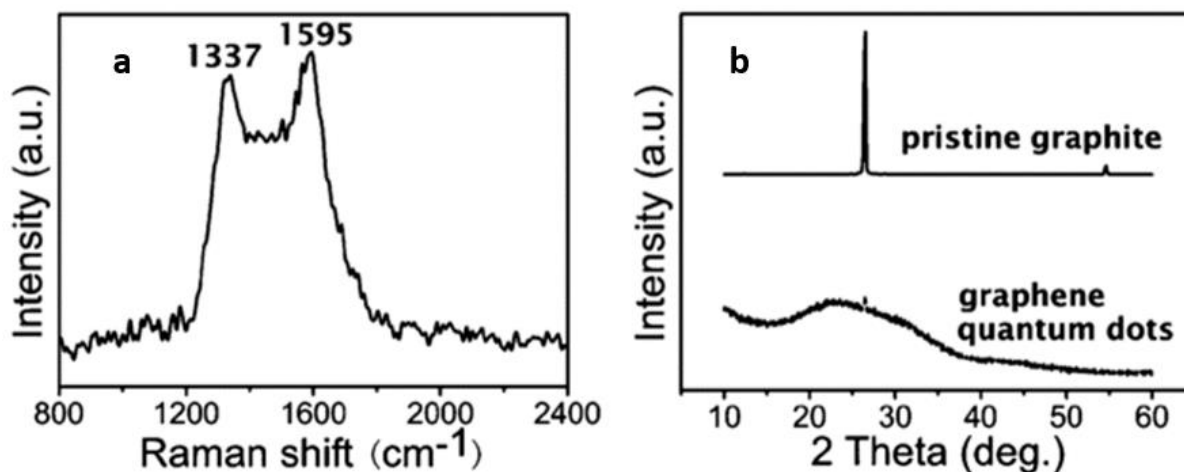
Figure 1-9 – a) Raman spectrum of the GQDs showing D and G bands, b) XRD patterns of pristine graphite and GQDs. Adapted from Ref. 40.

Another strategy frequently pursued, due to its simplicity and cost-efficiency, is the hydrothermal cutting of graphitic structures. Pan et al.[36] were one of the first research groups to report the hydrothermal treatment of graphene sheets, for the preparation of GQDs with sizes under 10 nm. Albeit simple, the method involved too many steps, as it required graphite oxide to be thermally reduced to graphene sheets, followed by oxidation of the graphene sheets with concentrated H_2SO_4/HNO_3, and then, finally the hydrothermal treatment (200°C) that affords the GQDs. The suggested mechanism for the formation of the GQDs, was based on the known break down of CNTs into tubes of smaller dimensions, or "unzipping" and fractioning into nanoribbons at low pH[41]. Briefly, in acidic media, epoxy groups are formed linearly along carbon lattices which causes the breaking of C-C bonds. Given the unstable nature of the epoxy groups, they are further oxidized into epoxy pairs and finally into the more stable carbonyl functional groups. These remain after GQDs formation and are what impart them with remarkable water stability.

A later report by the same research group[42], demonstrated the importance of temperature in the size of the as-synthesized GQDs. Higher temperatures (600°C), produced nanoparticles with smaller sizes and narrower size distribution: 1.5 nm to 5 nm compared to the previously obtained 2 to 16 nm (Figure 1-10 a and c). However, this was achieved at the expenses of the graphitic structure of the GQDs as demonstrated by Raman spectroscopy, showing a higher index of disordered carbon, $I_D/I_G = 1.47$ against the previous 1.26 (Figure 1-10 b and d).

30
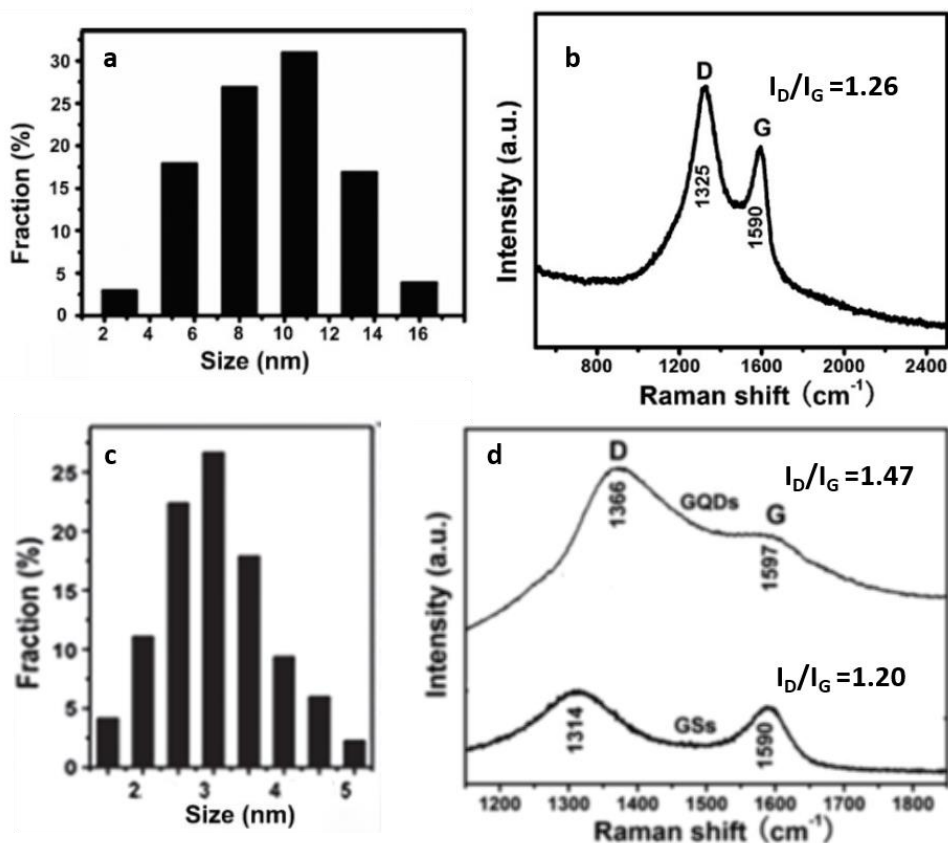
Figure 1-10 – GQDs particle size distribution for hydrothermal treatment of graphite oxide at – a) 200°C and c) at 600°C, during the thermal reduction process, b) and d) Raman spectroscopy for respective temperatures showing the effect on the graphitic structure of the GQDs (GS: graphene sheets). Adapted from Ref. 36,42.

Shen et al.[43] developed a system where they initially undertook the oxidation of GO sheets with HNO_3, followed by treatment of the GQDs precursor with PEG_{1500N} and then a final reduction by hydrazine hydrate to obtain the GQDs. Furthermore, the same research group presented an improved version of this method[44] where GO sheets are reduced to GQDs in an aqueous HNO_3 solution, and the carboxylic groups generated on their surface serve as active sites for esterification with the hydroxyl groups on PEG. These systems were tested as photoelectrodes and showed promising photon-to-electron conversion capability, particularly when compared to bare GQDs.

Dong et al.[34], on the other hand, developed a method for the production of GQDs from carbon black CX-72. This was a particularly attractive method due to the abundance of the starting material. These materials consist of 30 nm sized spherical graphite aggregates which can be broken down, by oxidation with HNO_3, to produce GQDs1

31

with a considerably high reaction yield (48%). After centrifugation, a fraction of the material sedimented, which required further treatment with HCl, and resulted in a second material GQDs2 (reaction yield = 9%). The two types of GQDs afforded by this method: GQDs1, with average size of 15 nm and an average topographic height of 0.5 nm, suggesting a single layer of graphene; and GQDs2, with an average particle size of 18 nm and topographic height of 1-3 nm, which indicates nanoparticles consisting of 2 – 6 layers of graphene fragments (Figure 1-11 a and b, respectively). The deconvolution of the C1s peak of the GQDs, obtained by X-ray photoelectron spectroscopy (XPS), show presence of the sp^2 C=C bonds, C-O bonds and carboxylic groups (O=C-OH), at binding energies of 284 eV, 286 eV and 288 eV, respectively for both systems (Figure 1-11 c). It is noteworthy, that the counts for the oxygen-containing groups and results from elemental analysis indicate a higher content of oxygen for GQDs1, ($GQDs1_{Oxy}$ = 54.3% > $GQDs2_{Oxy}$ = 44.8%). The authors suggest this may be the reason behind the greater interlayer spacing of GQDs1 found by XRD (Figure 1-11 d).
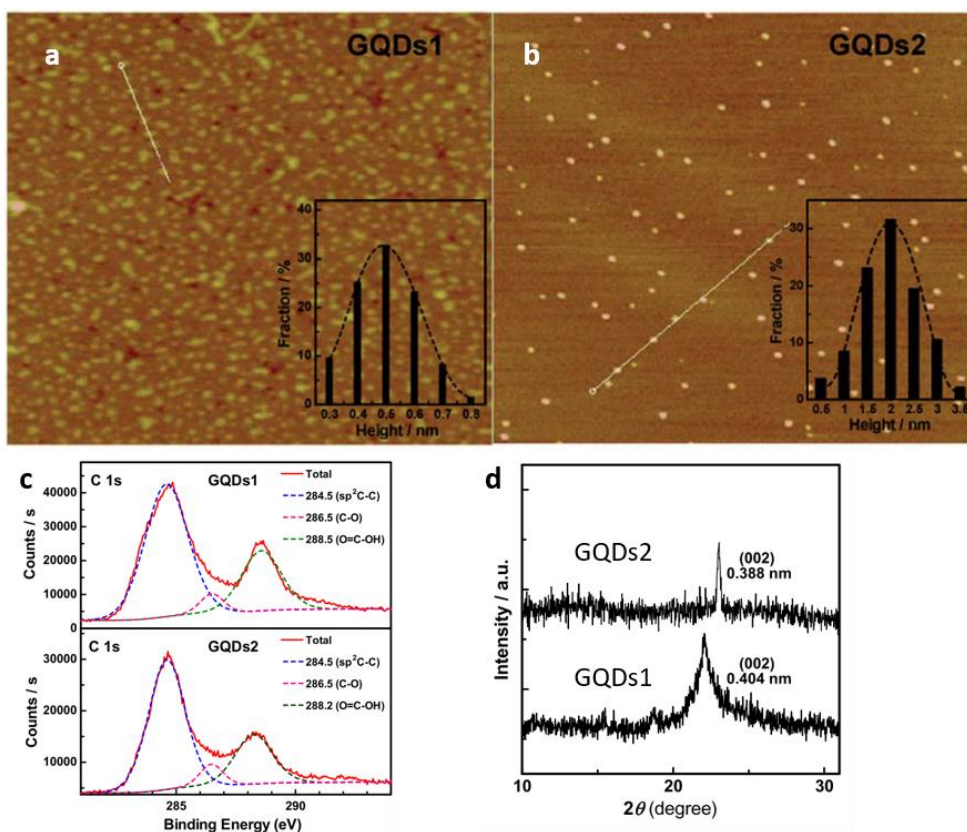
Figure 1-11 – a) and b) atomic force microscopy images of GQDs1 and GQDs2, respectively (insets showing height distribution), c) XPS C1s peak deconvolution and d) XRD patterns comparing the two systems. Adapted from Ref. 34.

In one particularly distinct method, GQDs are formed from the cage opening of fullerenes (C_{60}) mediated by a Ru-catalysed reaction. The underlying mechanism takes advantages of the attractive forces between the Ru crystals and the C_{60}, leading the opening of the C_{60} cages, followed by a temperature step, resulting on the GQDs with different shapes - triangular and hexagonal shaped GQDs, when exposed to ~ 450°C and 550°C, respectively (Figure 1-12).
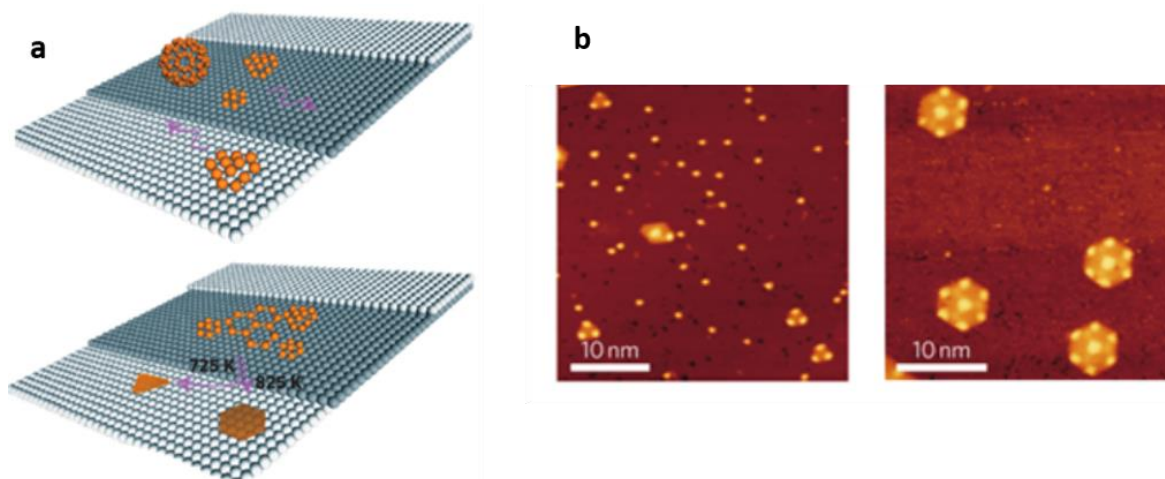
Figure 1-12 – a) Schematic representation of the C60 cage opening catalysed by Ru crystals, resulting on the temperature-dependent differently shaped GQDs, and b) scanning tunnel microscopy images of the triangular and hexagonal shaped GQDs. Adapted from Ref. 45.

Fullerenes have been known to display PL properties for some time (Catalan, 1993). There was initially some debate on whether the reported fluorescence of fullerenes arises from the presence of impurities, since the excitation and absorption spectra reported in the literature frequently did not mimic each other (Cite a few of the previous papers cited on Catalan, 1993). Catalan et al. demonstrated that fullerenes C60 and C70 dispersed in cyclohexane at room temperature display excitation spectra correlating to their corresponding absorption spectra. More recently, fluoroalkyl-doped fullerenes, were suggested as alternatives to graphene quantum dots. Their main advantage is that they are less prone to multi-layer stacking, which allows for better defined dimensions and morphology of this nanoparticles (Castro, 2013). However, their quantum yields are considerably low compared to C-dots, as well as displaying significantly small Stokes-shifts. Nonetheless, as the fullerenes cage opening study suggested they can, thus be of substantial importance not only as precursors for C-dots, but also to understand C-dots photoluminescent properties.

1.3.1.2 _Bottom-up routes_

The synthetic strategy behind bottom-up routes rely on the use of polycyclic aromatic compounds in their structure to synthesize GQDs[26].

In one procedure, GQDs with the larger number of conjugated carbons reported (130-170) were prepared through oxidative condensation reactions of polyphenylene dendritic precursors[46]. The GQDs were then stabilized by attaching bulky 2,4,6-trialkyl phenyl groups on their edges, which prevented self-aggregation due to an energy-minimized conformation assumed.

Liu et al.[47] suggested an alternative approach where they used unsubstituted hexa-peri-hexabenzocoronene (HBC) as the carbon precursor for the synthesis of GQDS. The preparation of the GQDs involved the carbonization of the HBC precursor, followed by oxidation, surface passivation with PEG_{1500N} and a final reduction with hydrazine. A schematic representation of the overall synthetic procedure can be seen in Figure 1-13 a. TEM images (Figure 1-13 b) indicated that this method afforded well-defined large nanoparticles (diameters of ~ 60 nm) and AFM topography images showed 2-3 nm thick layers GQDs with disk-like shape (Figure 1-13 c).
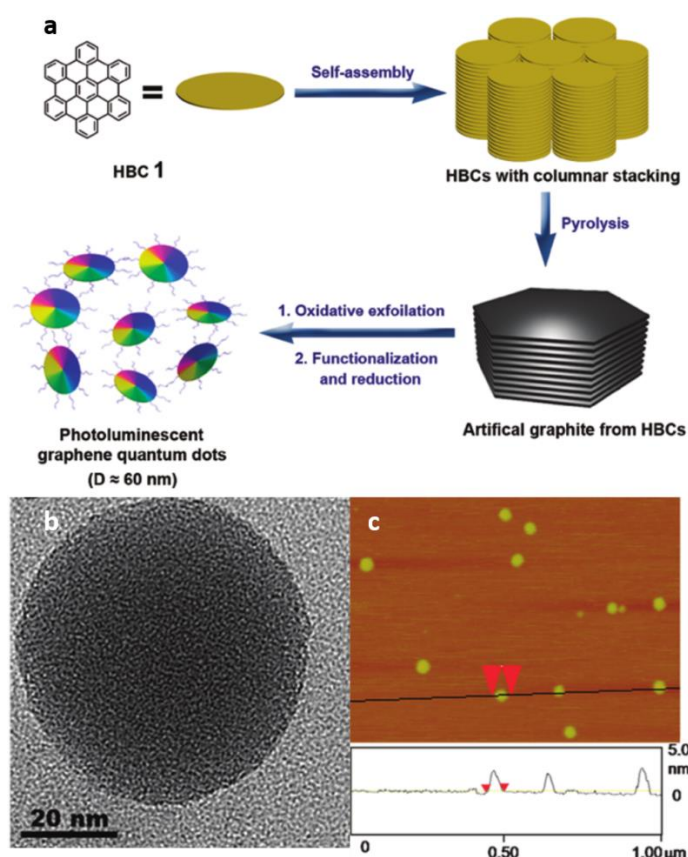
Figure 1-13 – a) Schematic illustration of the preparation strategy of GQDs from HBC precursor, b) TEM image of the as-prepared GQDs and c) AFM images and topographic heights. Adapted from Ref. 47.

1.3.2   Amorphous Carbon Dots

Amorphous C-dots are typically formed by bottom-up approaches (*e.g.* by hydrothermal treatment[48–50], microwave pyrolysis[51–53], etc) of carbon-rich precursors, and are the most attractive due to their typical facile and fast methodology[54]. Some of the approaches involved the use of renewable materials like grass[55], candle soot[56], soy milk[57], orange juice[50], among many others. Further steps frequently consist of surface passivation with strong acids, to make them more water-soluble or functionalization with amine groups, which was found to enhance their PL properties[58].

Zhu et al.[52] developed a fast and facile method of synthesizing C-dots, by microwave pyrolysis of PEG and a saccharide (Figure 1-14 a). The authors suggested that longer pyrolysis times would generate larger C-dots, resulting on a red-shift of the fluorescence emission. The method afforded C-dots with narrow size distribution (2.75 +/- 0.45 nm), and FTIR spectrum showed mainly C-OH, C-H and C=O stretching vibrations (Figure 1-14 b). Jaiswal and coworkers[51] further explored this and prepared C-dots by microwave caramelization of PEG, which afforded nanoparticles with 3.5 – 5.5 nm. HRTEM and XRD analysis of the as-prepared C-dots suggest highly disordered carbon, as no lattice fringes were discernible, and the XRD peak at 4.1 Å is attributed to non-graphitic and highly disordered carbon structures (Figure 1-15 a and b, respectively).
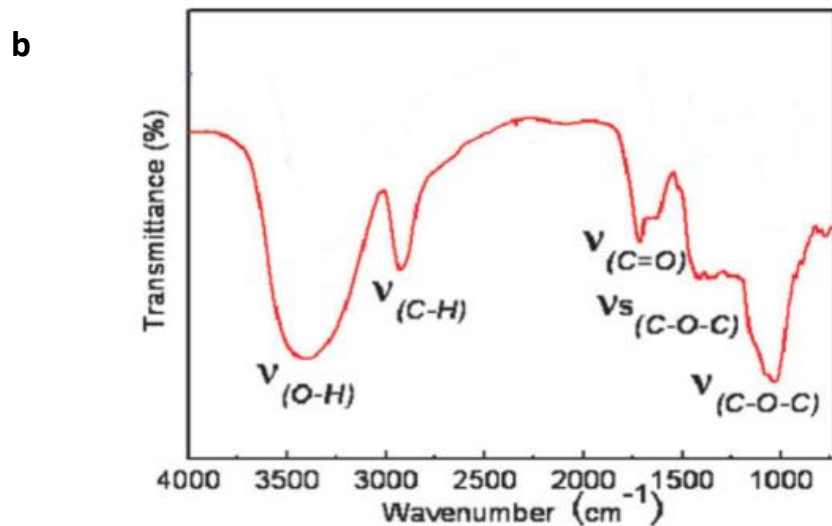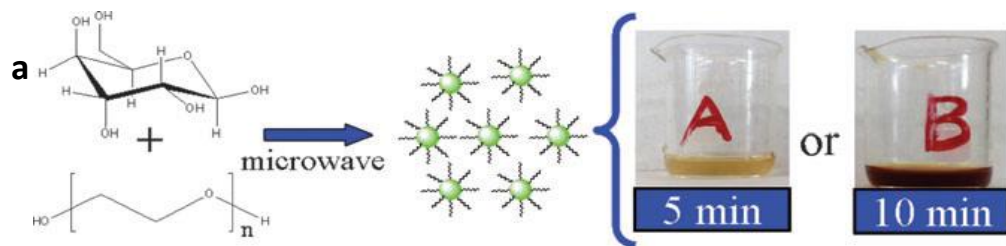
Figure 1-14 – a) Synthetic route to produce C-dots from microwave pyrolysis of PEG and a saccharide, and b) FTIR spectrum of the as-prepared C-dots. Adapted from Ref. 52.
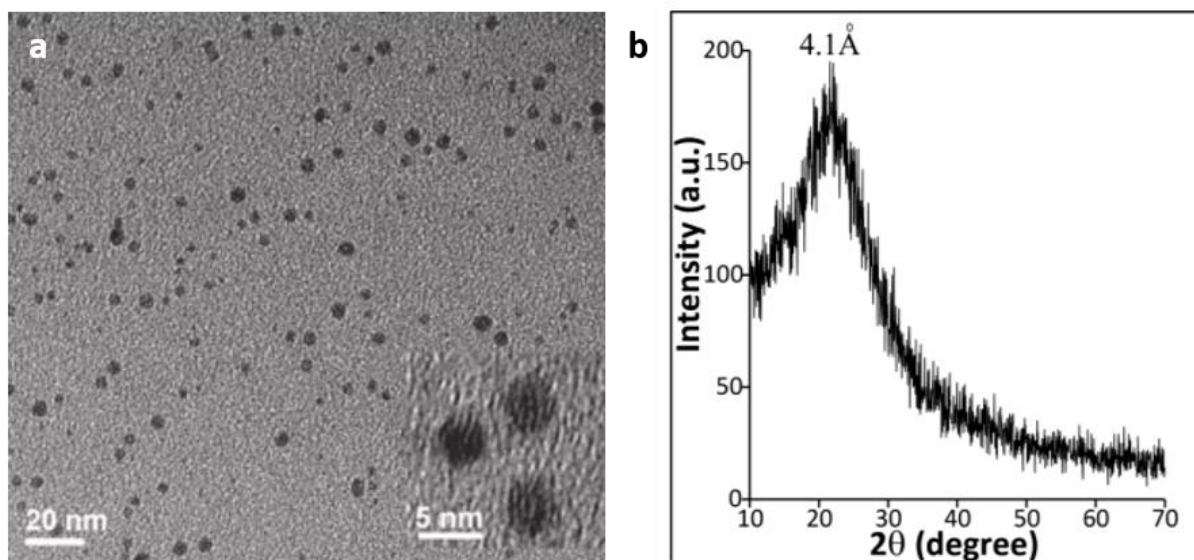
Figure 1-15 – C-dots derived from microwave pyrolysis of PEG: a) TEM image (inset HRTEM image), b) XRD pattern. Adapted from Ref. 51.

In another report, Liu et al.[59] demonstrated an alternative route for the mediated synthesis of C-dots. The authors used surfactant-modified silica nanoparticles as carriers for the localized growth of C-dots (Figure 1-16). After a pyrolysis step (2h at 900°C in argon atmosphere), the C-dots SiO$_2$ composites were then removed by etching in basic solution (2 M NaOH aqueous solution), the C-dots were oxidized in 3 M HNO$_3$, and finally PEG was added as passivation agent through ultrasonication.
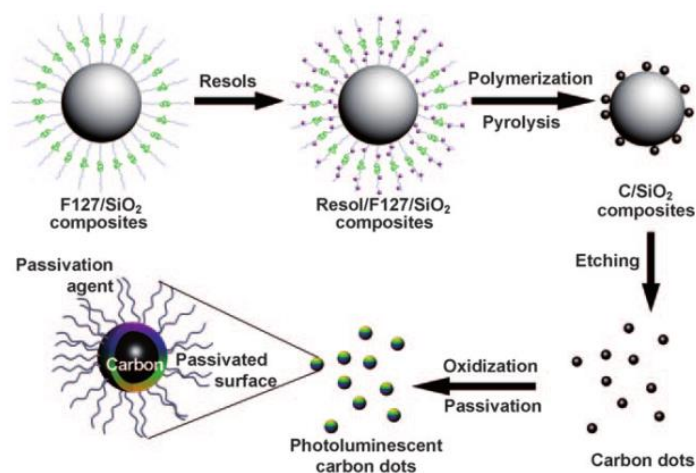
Figure 1-16 – Schematic illustration for the silica-mediated C-dots preparation. Adapted from Ref. 59.

1.3.2.1 _Heteroatoms_

One of the most attractive features of amorphous C-dots, when compared to GQDs, is the possibility of adding several heteroatoms to C-dots surface, either during their synthesis or by functionalization, resulting on different defect sites and the possibility for enhanced PL properties.

In a representative example, Zhu et al.[57] synthesized N-rich C-dots (13 – 40 nm) by hydrothermal treatment of soy milk. The authors described that by following this green route, C-dots synthesis, surface passivation and N-doping occurs simultaneously. The high N content, was evidenced by XPS, which showed mainly carbon, oxygen, nitrogen and minor amounts of P (Figure 1-17 a). Deconvolution of the C1s peak (Figure 1-17 b) showed four extra peaks 284.5, 285.6, 286.6, and 287.9 eV, ascribed to C–C, C–N, C–O, and C=N/C=O, respectively.
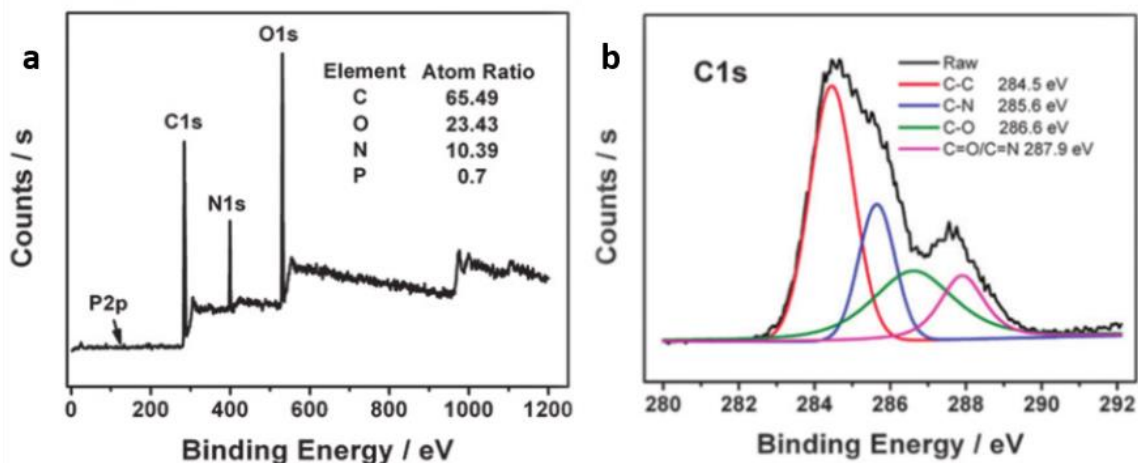
Figure 1-17 – a) XPS peaks of C-dots obtained by hydrothermal treatment of soy milk and b) deconvolution of the C1s peaks. Adapted from Ref. 57.

P- and N-rich C-dots (~ 9 nm) were synthesized through a one-step microwave pyrolysis of phytic acid (high phosphorous content) and ethylenediamine[60] (Figure 1-18). These C-dots showed a red-shift in their fluorescence and were successfully used as bio labels for C6 cells.
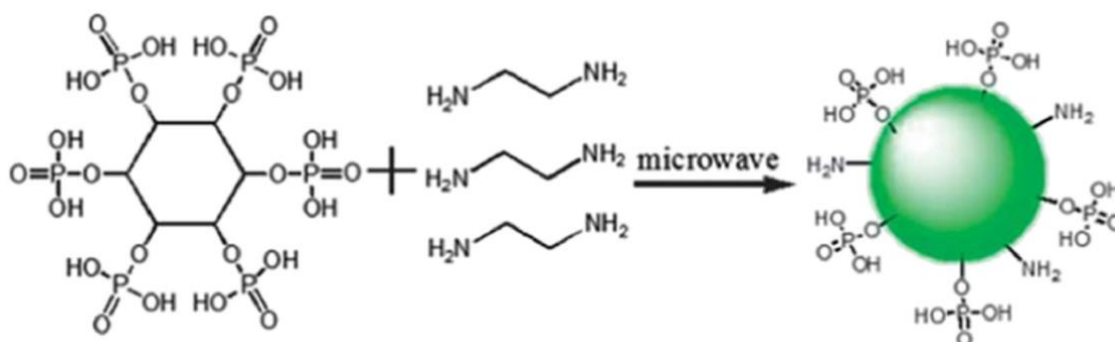
Figure 1-18 – Illustration of strategy for the preparation of P,N-rich C-dots through microwave pyrolysis. Adapted from Ref. 60.

In one particularly interesting report, Sun and coworkers[61] used hair fibres for the synthesis of S- and N-doped C-dots (2-10 nm). In a typical procedure, human hair fibres were mixed with concentrated H_2SO_4 and were ultrasonicated for 30 minutes. The authors reported that increasing temperatures would generate higher percentage of heteroatoms, while ensuing smaller C-dots' sizes. XPS spectra (Figure 1-19 a) showed mainly C and O, but also smaller peaks for S and N, whereas C1s peak deconvolution exhibited the typical peaks for undoped C-dots and C-S and C-N peaks

at 285.3 and 286 eV, respectively (Figure 1-19b). Furthermore, deconvolution of the N1s peaks, indicated the presence of pyridinic and pyrrole N ($\equiv$N-, and -NH-, respectively), whilst S2p peak deconvolution suggest the presence of thiopene (C-S) and Sulphates or sulphonates (C-SO$_x$).
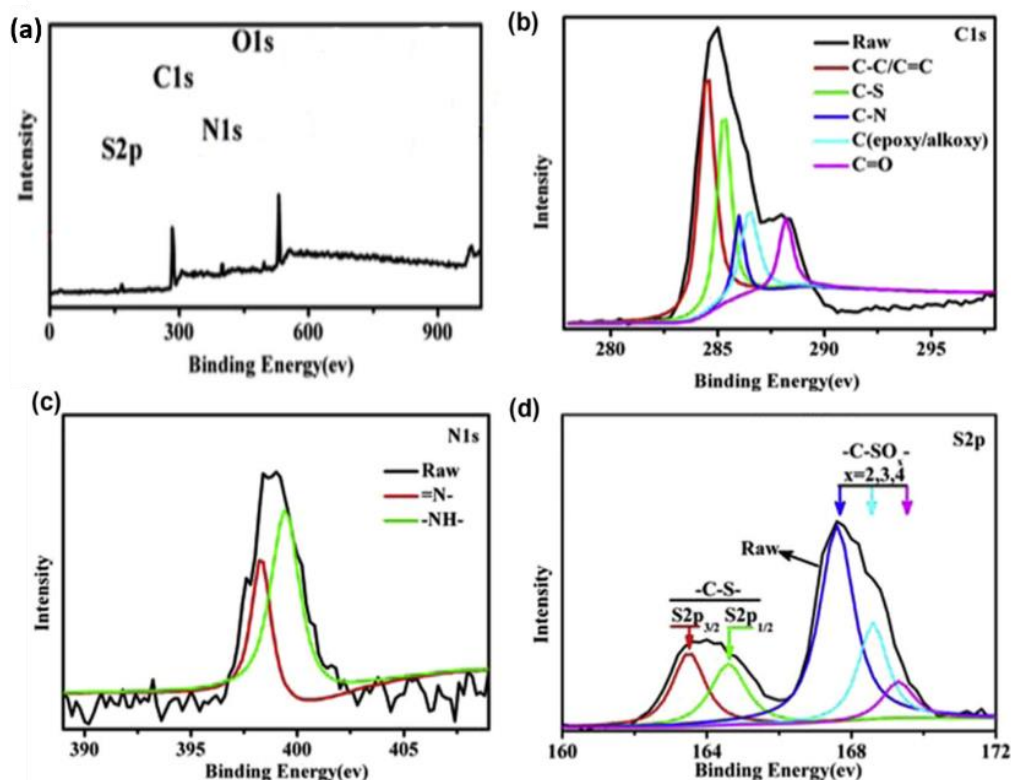
Figure 1-19 – a) XPS spectra of C-dots obtained from pyrolysis of hair fibres and b), c) and d) deconvolution of the C1s, N1s and S2p peaks, respectively. Adapted from Ref. 61.

Zhou et al.[62] demonstrated the preparation of Cl-doped C-dots (3 – 5 nm) which could be then functionalized with other halogens and that this affected their PL properties. The synthetic procedure (Figure 1-20) relied on the solvo-thermal reaction of carbon tetrachloride and quinol, and further treatment with BR$_2$ and I$_2$ to obtain the Br-C-dots and I-C-dots respectively. Furthermore, the authors suggested this could be an alternative method for N-doped C-dots stabilization/modification, as the halogens could be easily substituted when thermally treated with ethylenediamine.
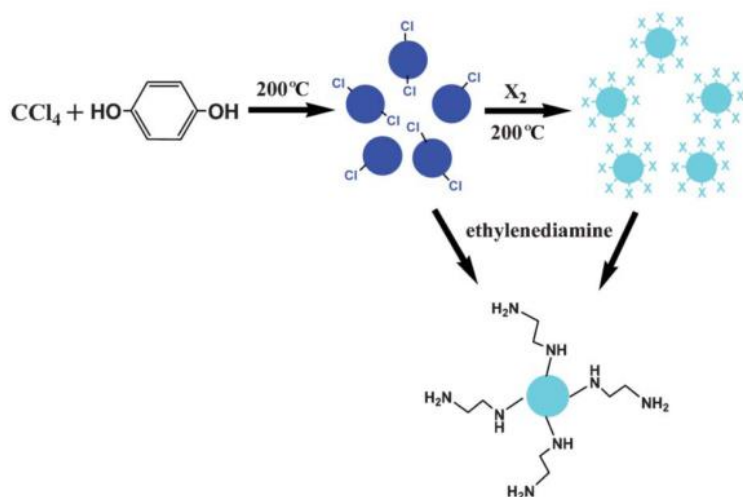
Figure 1-20 – Schematic illustration of the synthetic procedure for the preparation of halogenated-doped C-dots, and N-substitution of the halogens to form N-doped C-dots (X_2: Br_2 or I_2). Adapted from Ref. 62.

1.3.3 Photoluminescence properties

Regardless of their structural differences, C-dots in general display some similarities in terms of photoluminescence behaviour. C-dots show a strong and broad absorption band in the UV region, that extends to the visible region. The two most typical peaks appear at ~ 270 nm and ~ 350 nm (Figure 1-21 a), which are usually ascribed to the aromatic C-C bonds' π- π* transitions and C=O bonds' *n*- π* transitions, respectively [63,64].

Arguably, the most important C-dots' asset is their PL properties, and is the main reason why they have attracted so much interest of late. It is then of great importance to have a solid understanding of C-dots PL mechanism in order to take full advantage of their extensive range of potential applications. C-dots display wide emission peaks and large stoke shifts, which when compared to organic dyes present as a clear advantage over background fluorescence suppressing[65]. One particularly unique property C-dots show, independent of the synthetic route used, is the emission peaks shifting as a consequence of varying excitation wavelengths (excitation-dependent emission Figure 1-21 b). Even though a consensus is still to be reached regarding the exact reason behind this phenomenon, most authors agree that it arises from a variety of effects, namely excitons, oxygen-containing functional groups, emissive traps,

quantum confinement effects, edge and zigzag effects (the latter being more associated with GQDs)[30,32,65].
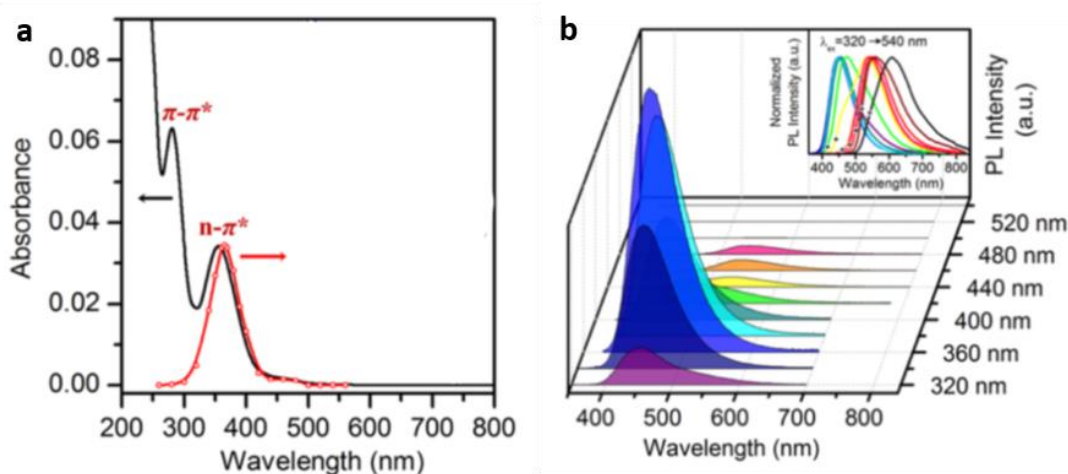
Figure 1-21 – a) Typical absorption (black) and excitation (red) spectra of C-dots showing the π- π* (C-C) and n- π* (C=O) transitions, and b) emission spectra of C-dots showing the excitation-dependent emission (inset shows normalized emission spectra). Adapted from Ref. 64.

1.3.3.1   *Quantum confinement effects*

Even though C-dots PL properties cannot be entirely explained by QCE there are already a few reports demonstrating that certain types of C-dots may display size tuneable fluorescence. QCE in QDs occurs when their dimensions are smaller than those of their exciton Bohr radius[66]. Theoretical calculations showed that the band gap is at a maximum on benzene-like GQDs (C_6) at 7 eV, where as it decreases to 2 eV for GQDs containing around 20 aromatic rings[67]. Due to their typical smaller sizes, this tend to mean that C-dots show blue PL emission, however this can be tuned by adjusting the number of π-conjugated domains[65].

In an early report, Liu et al.[56] demonstrated that C-dots (< 2 nm) derived from candle soot oxidation (HNO_3) followed by neutralization, could be separated into different fractions of fluorescent material by polyacrylamide gel electrophoresis (PAGE), as seen in Figure 1-22 a. The fact that the fastest fraction of the material (and potentially with smaller dimensions) showed the shortest wavelength emission maximum and, consequently, the higher energetic transition, and vice-versa (Figure 1-22 b), suggests that these C-dots display size-dependent PL properties.
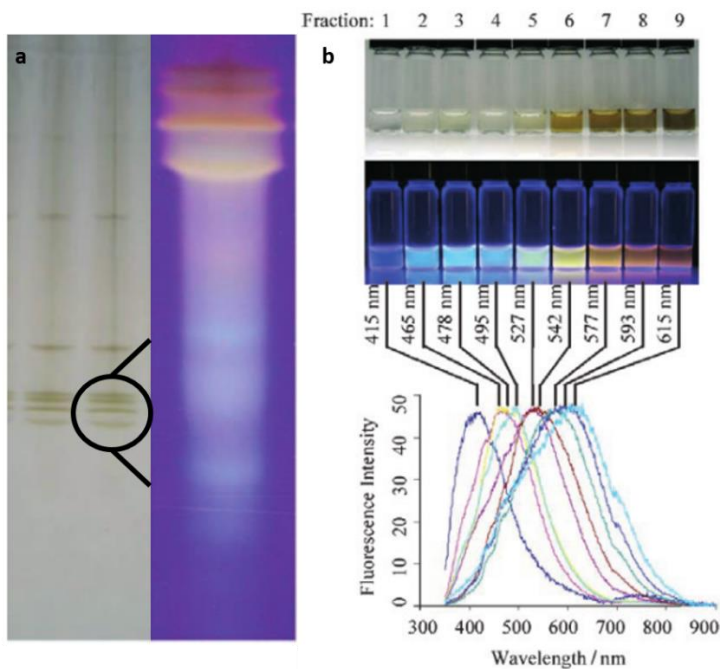
Figure 1-22 – a) Separation of the candle soot derived C-dots by electrophoresis, under white light (left) and UV light (right, fastest fraction magnified) and b) emission spectra for each of the separated fractions. Adapted from Ref. 56.

Li et al[68] investigated this effect and demonstrated that GQDs (1.2 – 3.8 nm) prepared by a one-step alkali-assisted electrochemical exfoliation of graphite rods displayed size-dependent effects on the PL properties (Figure 1-23 a and b). Particles with greater dimensions showed a red-shift in their emission spectra (Figure 1-23 c). Theoretical calculations suggested a relationship between the luminescence and band gap on the GQDs. From Figure 1-23 d, it is clear the dependence of the number of graphene fragments (and thus size of the clusters) on the HOMO-LUMO band gap, as with the increase of the fragments' number, a decrease occurs on the band gap resulting on lower energetic electronic transitions.
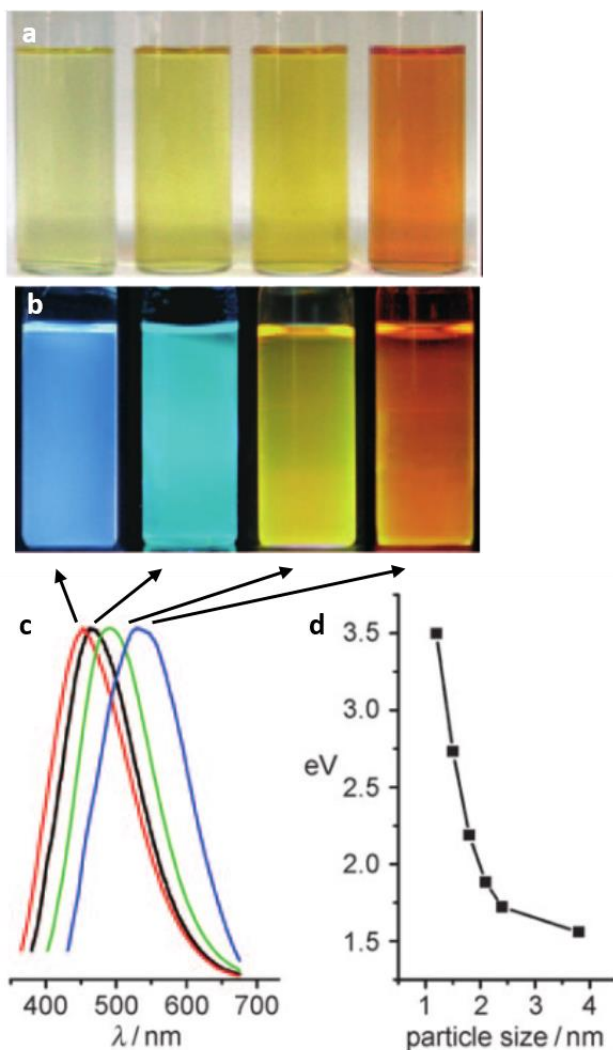
Figure 1-23 – GQDs derived from alkali-assisted electrochemical oxidation of graphite rods after size separation by column chromatography, under a) white light and b) UV light, c) emission spectra of the separated GQDs at maximum excitation wavelength (arrows indicate to which sample belongs each emission spectrum) and d) the pronounced effect of particle size on the PL properties of GQDs. Adapted from Ref. 68.

Notably, graphene oxide sheets display PL properties which when deconvoluted show two main contributions (I_{p1} and I_{p2} in Figure 1-24 a). By reducing GO, rather than expanding the existing sp^2 domains, the authors suggest that the removal of the oxygen atoms displaced from the π-conjugated domains occurs preferentially. This leads to the formation of smaller sp^2 islands (Figure 1-24 d), which emit at lower wavelengths, and could therefore be explained by QCE, as the gradual reduction of the GO induces an increase in the number of smaller islands and in I_{p2} intensity (Figure 1-24 a, b and c).
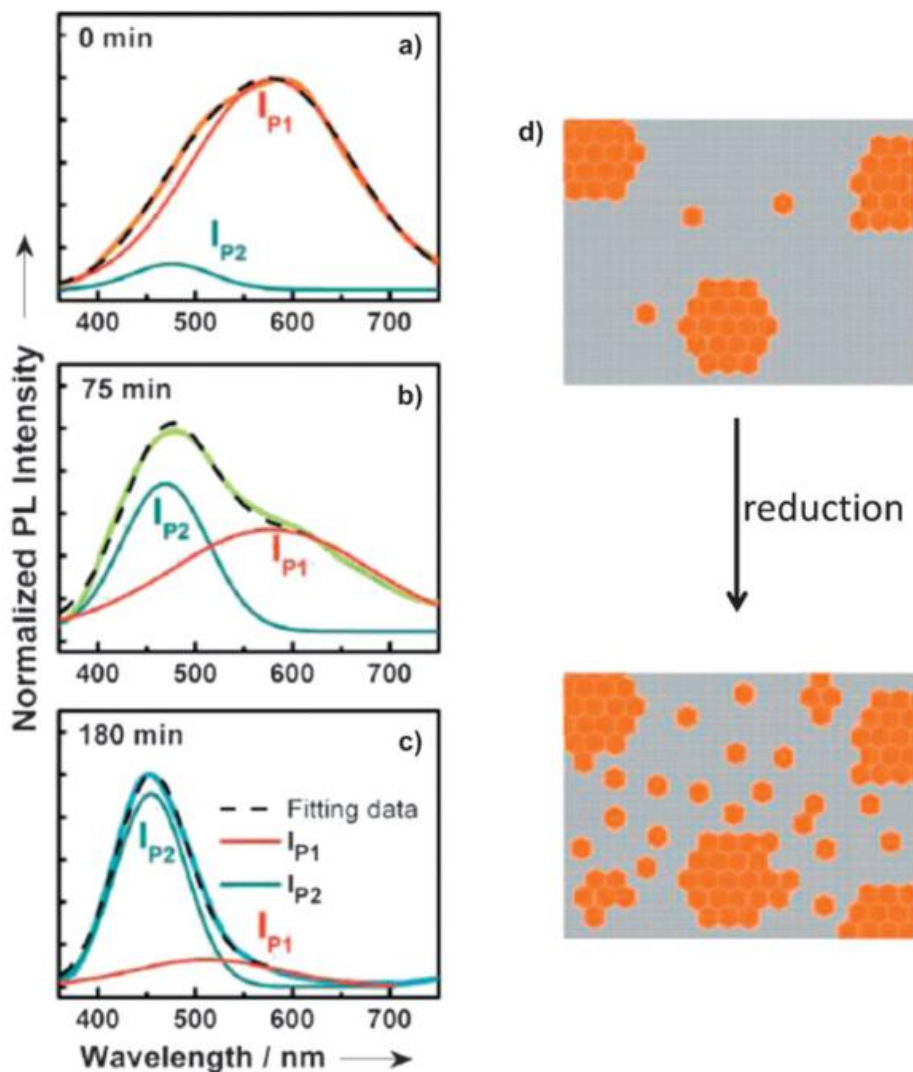
Figure 1-24 – Emission spectra of the GO with different reduction times: a) 0 min, b) 75 min, c) 180 min, showing the gradual change between the two fluorescence contributions, and d) schematic representation of the gradual formation of the sp² islands depending on reduction. Adapted from Ref. 69,70.

1.3.3.2 *Surface/edge state in C-dots*

When graphene sheets are cut into smaller fragments, edges are created. Theses edges can be classified as either zigzag edges or arm-chair edges (Figure 1-25). The format of theses edges is what impart remarkable electronic and PL properties to GQDs. Predominantly, GQDs contain zigzag edges, due to the presence of non-bonding π-electron states (edge states), which is absent in the armchair edges, and plays an important role in the GQDs properties[65,71]. Furthermore, zigzag edges display predominantly carbene site in the triplet ground state form, which typically show higher

HOMO-LUMO gaps, than the most predominantly singlet ground state on the armchair edges[27].
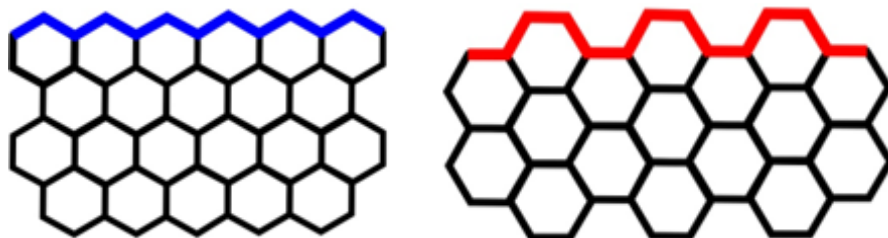
Figure 1-25 – Schematic representation of the zigzag edge (left) and armchair edge (right) structures.

Pan et al.[36] investigated the importance of the carbene groups with the triplet ground states on their edge sites. GQDs (9.6 nm), formed by hydrothermal cutting of graphene, were significantly quenched in acidic solution (pH = 1), due to the protonation of the edge sites (Figure 1-26 b). The authors verified that this was a reversible effect, as when returning alkali conditions (pH = 13) the fluorescence was "unquenched" (Figure 1-26 d). The presence of the triplet carbenes was proved by PL excitation spectra (Figure 1-26 c) where two peaks are visible at 257 nm and 320 nm. If it was a singlet ground state carbene, then the only peak visible would be at 257 nm, since it is attributed to transitions from σ-orbitals on the HOMO to the LUMO and singlet carbenes have the π-orbitals unoccupied. Hence, the carbene has an electron in the σ-orbitals and on the π-orbitals on the HOMO which are responsible for the transitions seen on Figure 1-26 a, and the two peaks on the absorption spectra. Furthermore, Lin et al[72] developed GQDs from CNTs and graphite flakes with different sizes (9.6 nm and 20 nm, respectively) with identical optical properties. The zigzag structure was evident from AFM and bright-field HRTEM, which, in addition to the changing dimensions of the nanoparticles and constant optical properties, suggests that predominant parameter for this GQDs are the zigzag edges and triplet ground states, over QCE.
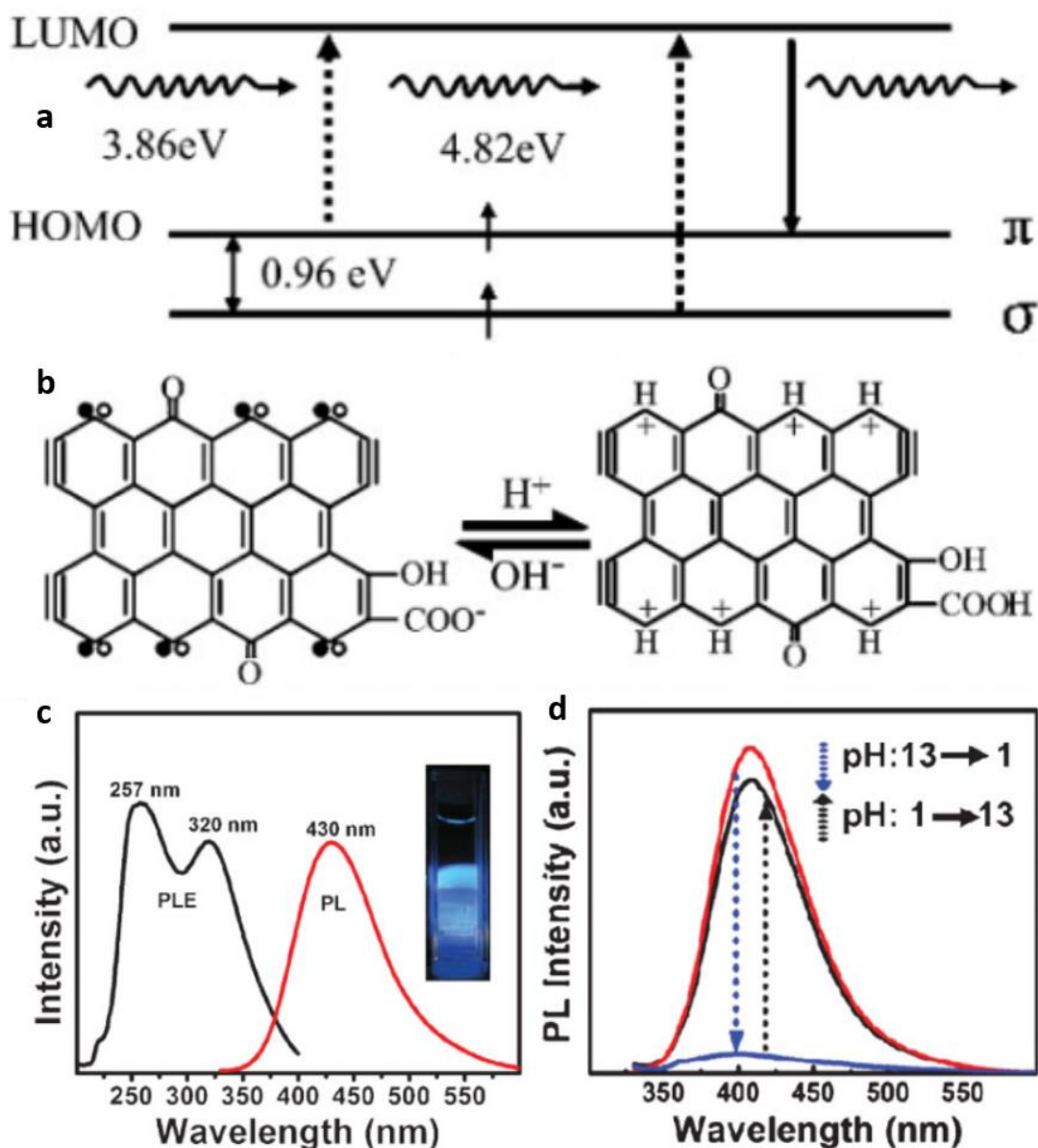
Figure 1-26 – a) Typical electronic transitions of carbene with triplet ground states on zigzag edges, showing the σ-orbitals and π-orbitals on the HOMO to the LUMO, b) schematic representation of the reversibility of the protonation of the triplet carbenes (full and empty circles represent σ-electrons and π-electrons, respectively) on the GQDs obtained by hydrothermally cut graphene sheets, c) PL excitation (black) and emission spectra of the as-prepared GQDs (inset shows solution fluorescence under UV radiation) and d) quenching effects of the protonation of the as-prepared GQDs. Adapted from Ref. 36.

Even though amorphous C-dots do not display the same edge site effects as GQDs, they tend to display several functional groups on their surface with various energy levels, which result in different emissive traps. A denser surface modification on C-dots results on a red-shift of the emission, as emissive traps tend to dominate amorphous C-dots core's PL[65]. The need for surface modification can be explained by the susceptibility of the confined photon-generated electron and hole pairs. Hence,

passivation agents protect these sites and maintain/improve the PL properties of C-dots[30].

The most typical surface state in C-dots is oxidation-based surface modification, as it has been demonstrated throughout literature that, on a first instance, researchers focused on the functionalization with heavily oxygen-containing molecules[51,65,73,74]. For example, C-dots (~5 nm) produced from laser ablation of a carbon target, functionalized with PEG$_{1500N}$, afforded stable particles and prevented the aggregation of the initially unfunctionalized C-dots which displayed no fluorescence (Figure 1-27). Furthermore, they established that other organic molecules could be used as passivation agents, such as poly(propionylethylene imine - co -ethyleneimine) (PPEI-EI), and similar results were obtained, proving that the PL mechanism mainly stems surface emissive traps[74].
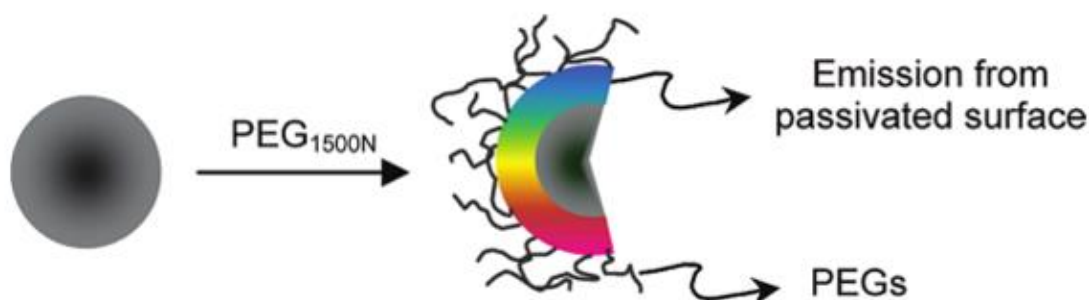
Figure 1-27 – Schematic representation of C-dots functionalization with PEG-based molecules, and resulting fluorescence from surface energy traps. Adapted from Ref. 74.

Liu et al.[56] argued that C-dots (< 2 nm) obtained from candle soot oxidation showed fraction separation by electrophoresis, due to the different sizes the particles displayed. However, another possibility to explain this separation, would be the different degree of surface state oxidation[65]. Interestingly, a series of studies on the oxidation of C-dots surface seem to suggest that higher degree of oxidation induces a red shift on the PL emission, whereas a reduction of these oxidized surface states induce a blue shift. For instance, Bao et al.[75] demonstrated that electrochemically produced C-dots (2.2 – 3 nm) could have their PL tuned from blue to green, depending on the degree of surface oxidation (Figure 1-28), induced by a change in the applied potential. It is noteworthy that, even though the size of the nanoparticles changed, the

resultant PL occurred in an opposite way to that of expected for QCE (smaller particles emitted at longer wavelengths, and vice versa), proving that the change in PL was resultant from change in the surface oxidation state.
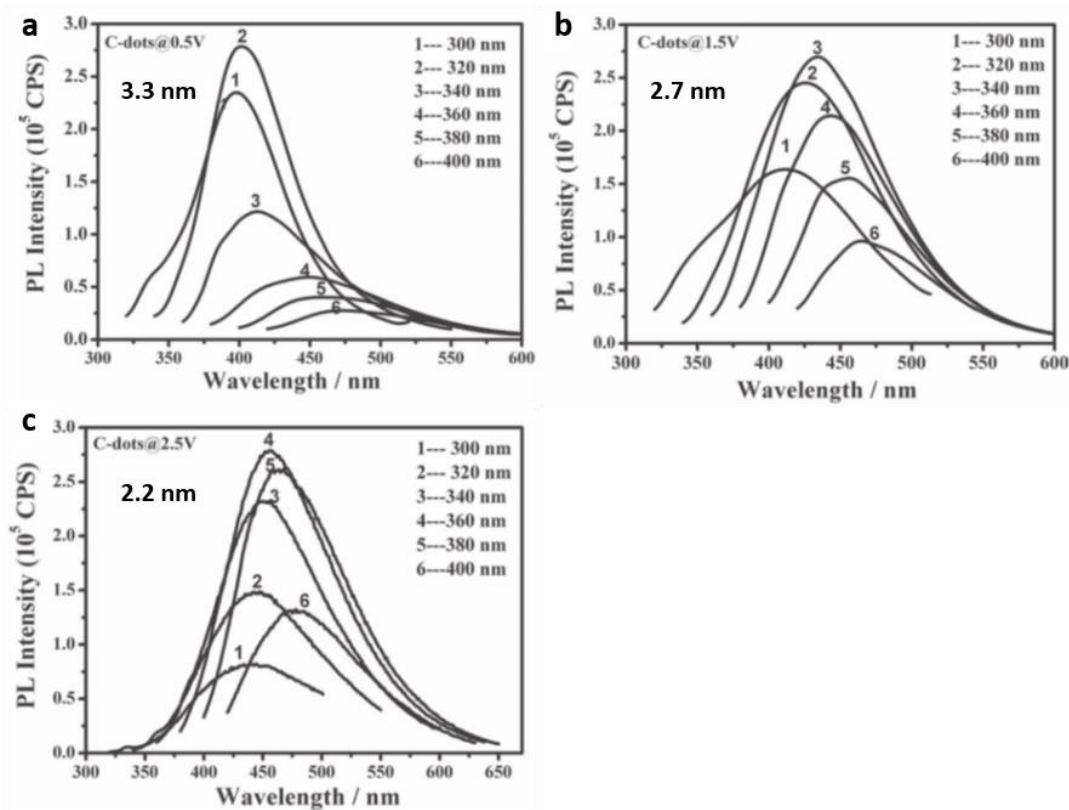
Figure 1-28 – Red-shift in the PL I$_{max}$ from blue gradually to green, induced by a change of applied potential of a) 0.5V, b) 1.5V and c) 2.5V. Adapted from Ref. 75.

On the other hand, Zheng and coworkers[76] demonstrated that the reverse could also be achieved. C-dots (~3 nm) prepared by oxidation (HNO_3) of a carbon precursor, thus with a high degree of oxidation, showed green luminescence, but when reduced with sodium borohydride displayed a blue-shift in their PL emission (Figure 1-29). In an attempt to explain this phenomenon, Richards et al.[77] suggested that C-dots display multiple fluorophore units attached to their cores and oxygen-based defect sites where emissive traps are located. They demonstrated that in highly oxidized surface states the emissive traps are predominant, showing a single emission level, whereas in the reduced surface state most C-dots display various levels of excited states. Furthermore, the authors suggested that PL emission occurs between these two levels in the oxidized state, as the highly-absorbing oxidised sites transfer the photons to the lower emissive energy levels. Contrarily, in the reduced state the multiple, but lower,

energy levels are often bare and get easily removed or blocked. This would explain the need for surface passivation – to prevent the removal/blocking of these more susceptible lower emissive levels.
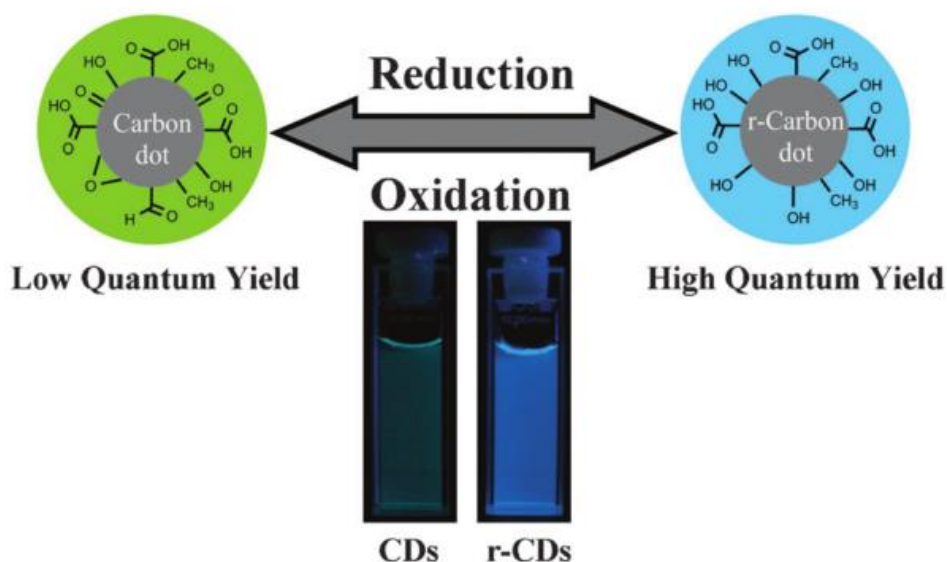
Figure 1-29 – Illustration of the reversible change in the PL emission from green to blue due to the reduction of the C-dots surface. Adapted from Ref. 76.

1.3.3.3 *Quantum yield*

The quantum yield of C-dots has been quite variable, depending on the synthetic route used. The first reports in the field with unfunctionalized C-dots, displayed considerably low quantum yields (1.6%[73] and 1.9%[56]). Surface passivation has been reported to afford C-dots with considerably higher QY. For example, GQDs (13 nm) prepared by hydrothermal treatment of GO sheets displayed QY of 13.1%, while their PEG functionalized counterparts afforded QY as high as 28%[44]. In a comparison between passivation agents, Sun et al.[74] confirmed that PEG produced higher QY than PPEI-EI (by 6%) when attached to C-dots (~5 nm) produced by laser ablation. Remarkably, the PPEI-EI could be removed from C-dots' surface, and if PEG was attached an increase in the QY would still be observed.

It has been demonstrated that the introduction of amine-rich functional groups to C-dots surface also produces a positive effect on C-dots QY [78,79]. Tetsuka et al.[78]

established that the fluorescence of GQDs could be tuned from violet to yellow (Figure 1-30 a and b), depending on the concentration of the amine and hydrothermal process temperature (QY = 19 – 40 %). The higher QY here was attributed to the reduced number of non-radiative relaxation electron-hole centres, such as epoxide groups.
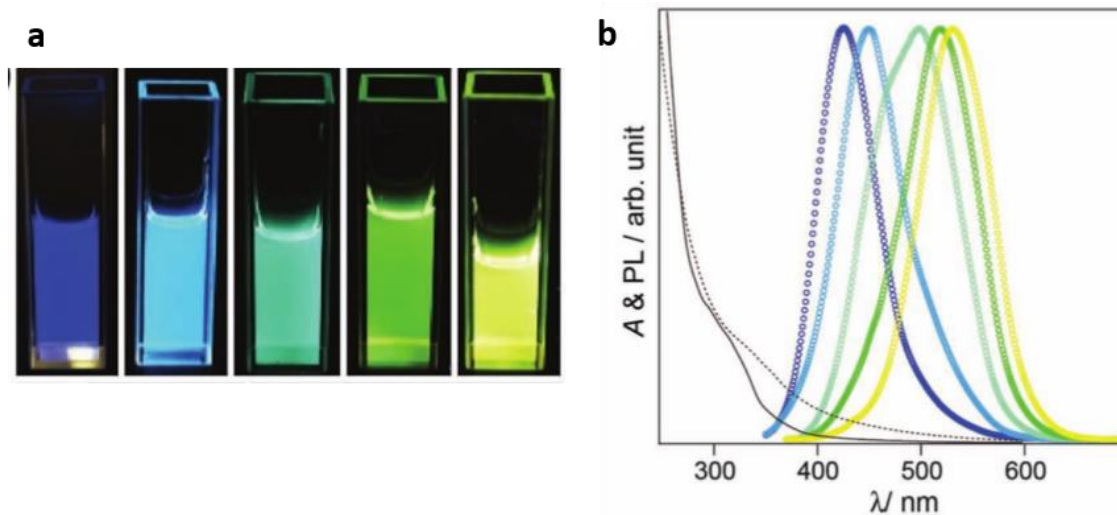
Figure 1-30 – a) Pictures of UV-irradiated C-dots solutions functionalized with different initial concentrations of an amine-rich precursor, b) showing a progressive red-shift in their PL emission spectra. Adapted from Ref. 78.

Krysmann et al.[58] suggested that by adding amine-containing surface passivation agents to the hydrothermal treatment of a carbogenic precursors, it would result in the simultaneous surface passivation and enhancement of QY. The authors argued that this was a direct consequence of the presence of two fluorescent species – C-dots and a temperature-susceptible organic fluorophore. Increasing temperatures during the hydrothermal treatment would result on an increase of C-dots/fluorophore ratio (Figure 1-31 a and b), and a quantum yield reduction would be observed (from QY = 50% at 180°C, to QY = 15% at 230°C), until a point where the fluorophore would be degraded and the fluorescence would arise mainly from C-dots contribution (Figure 1-31 c).
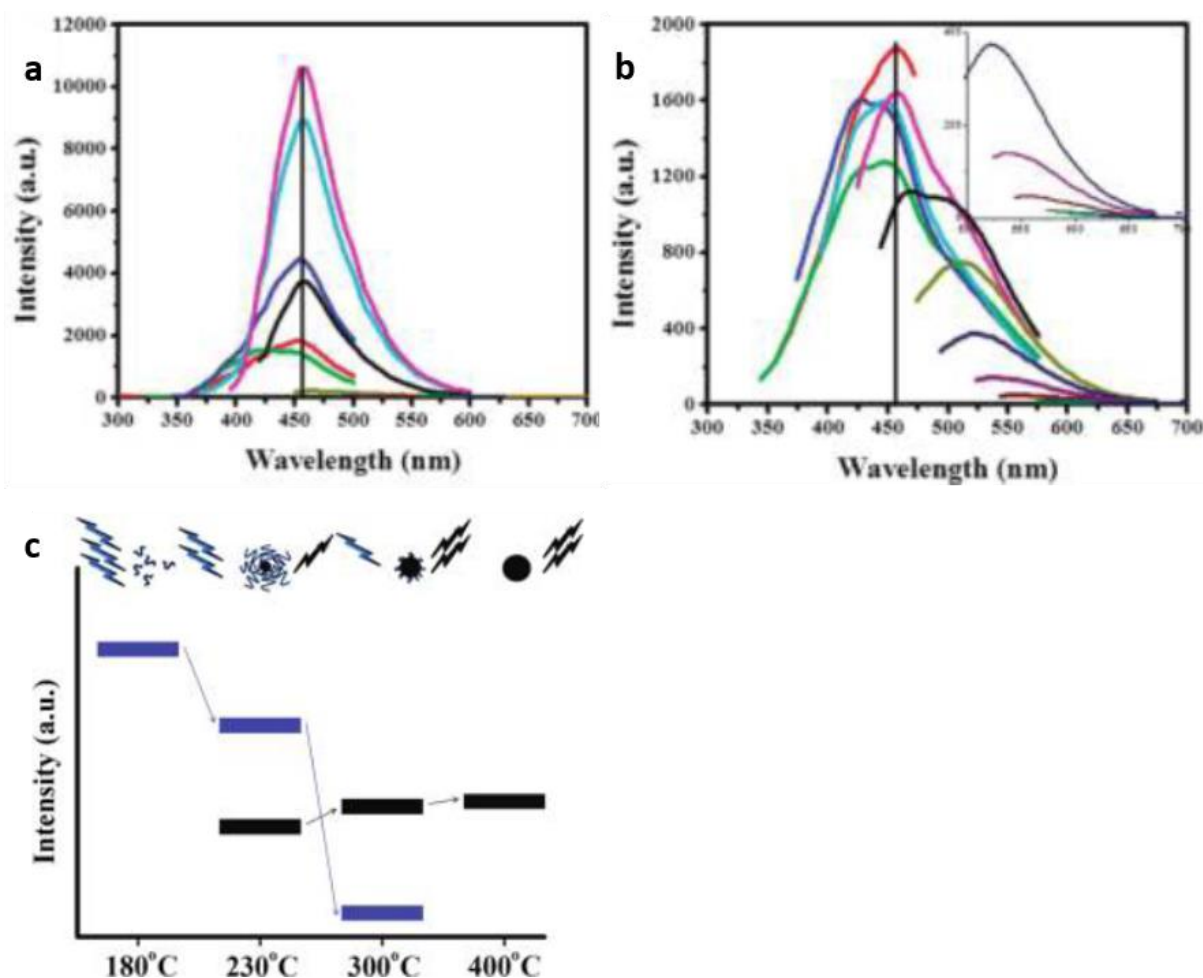
Figure 1-31 – a) PL emission spectra of the fluorophore produced at 180°C and b) PL emission spectra of the C-dots produced at 300°C, showing the excitation independent and excitation dependent emission, respectively, and c) schematic illustration of the progressive degradation of the fluorophore and consequent formation of C-dots, and contrast between their fluorescence intensities. Adapted from Ref. 58.

1.3.3.4   *Upconversion photoluminescence*

More recently, it has been reported that anti-Stokes electronic transitions may occur in some types of C-dots. This happens when energy released during PL emission is higher that the energy absorbed initially by an electron. Shen et al.[43] reported that surface passivated GQDs (13.3 nm) prepared by hydrazine hydrate reduction of GO sheets, would emit PL at lower wavelengths (Vis) when excited at the NIR region of the spectrum (Figure 1-32 a). The authors argue that this is only possible on GQDs with zigzag edge structures, since it requires the excitation of π-electrons and their return to a σ-orbital in the HOMO. Thus, the energy involved in the excitation (π_{HOMO}-

π_{LUMO}) would be lower than the involved in the emission (π_{LUMO}-σ_{HOMO}), as seen in Figure 1-32 b.
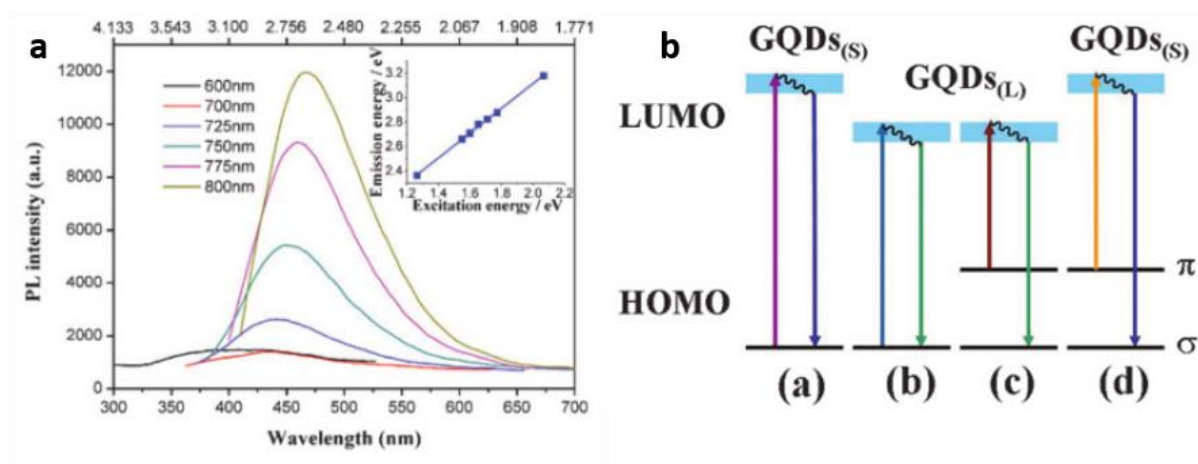
Figure 1-32 – a) Upconversion PL emission of GQDs showing the emission of light in the visible range while excited in the NIR region, (inset shows the energy (in eV) involved in PL emission as a function of the energy in the excitation) and b) proposed mechanism for the Stokes PL emission (a) and (b) and for anti-Stokes PL emission (c) and (d). Adapted from Ref. 43.

Another mechanism where upconversion may take place is when two low-energy photons are absorbed, and an electro transitions to an excited state, and upon returning to the ground state emits more energetic radiation. The general mechanism for two-photon absorption is depicted in Figure 1-33.

Pan et al.[80] reported that C-dots (2.9 nm) prepared from microwave pyrolysis of glutathione in formamide displayed two-photon absorption and upconversion emission when irradiated with a 850 nm wavelength source. When excited with an 850-nm laser, even with different laser powers, a fixed emission in the visible range occurs (~ 680 nm), proving the upconversion nature of these nanoparticles.
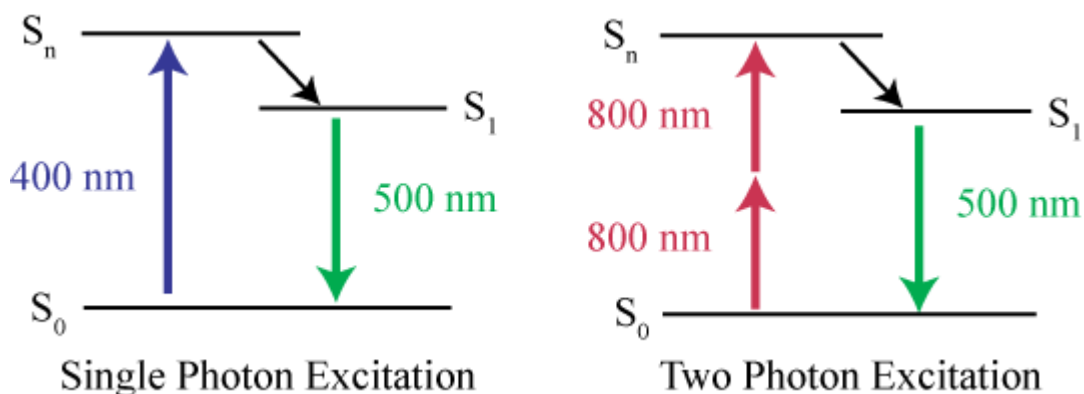
Figure 1-33 – Schematic illustrations comparing the mechanisms for single photon absorption (or excitation) and two-photon absorption, and respective emissions. Adapted from Ref. 79.

There are, however, some claims that second-order diffraction of light ($\lambda/2$), from monochromators in spectrophotometres, could also produce similar effects, making it necessary for new and better characterization methods to be developed before this effect can be fully explored and understood [65].

1.3.3.5 *Electrochemiluminescence*

Electrochemiluminescence (ECL) involves the generation of excited-states by applying a current, and the consequent the emission of light by relaxation to the ground state. These are well known to occur in lanthanide metal complexes, polycyclic aromatic compounds and QDs semiconductors [81]. Zheng et al.[37] were one of the first research groups to report that GQDs possessed ECL. GQDs (~ 2 nm) produced from electrochemical exfoliation of a graphite rod showed ECL emission when applied a potential within the range of -1.5 V and 1.8 V. The authors suggested that ECL emission arises from electron transfer annihilation of positively and negatively charged species (R$^{\bullet+}$ and R$^{\bullet-}$, respectively) forming an excited-state on C-dots (R*), as depicted in Figure 1-34 a. The greater intensity of the cathodic ECL (Figure 1-34 b), when compared to the anodic ECL, suggest that the R$^{\bullet+}$ species are more stable than their counterparts. Furthermore, the authors evidenced the potential of this method as a sensing technique, since, when $S_2O_8^{2-}$ was added to the solution, a dramatic change in the ECL occurred, as demonstrated in Figure 1-34 c.
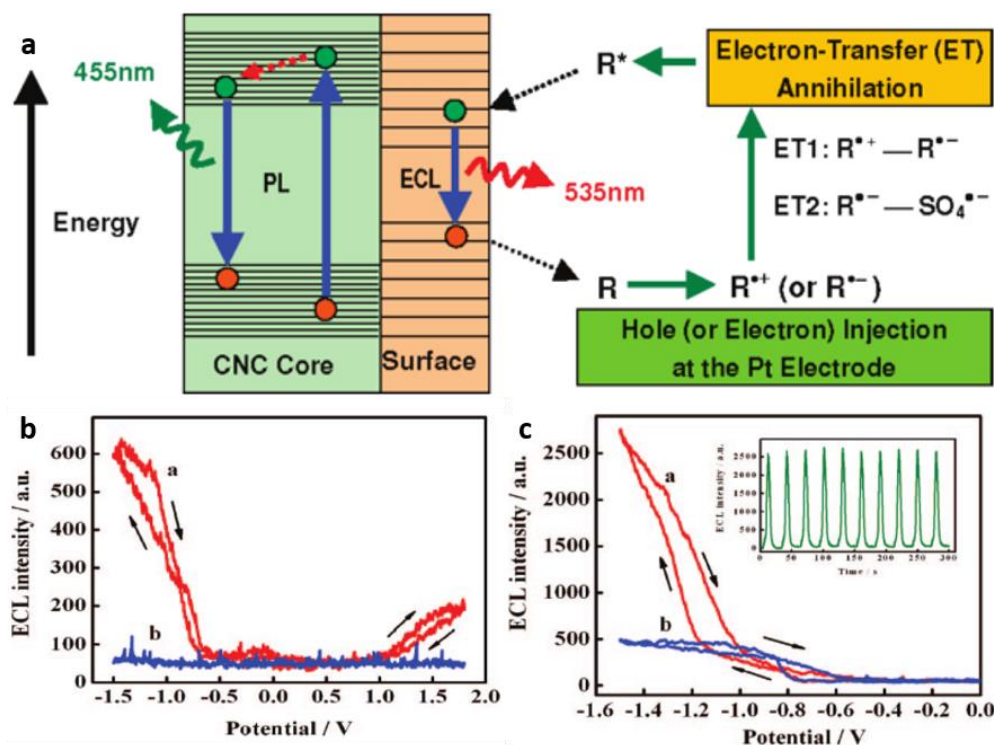
Figure 1-34 – a) Schematic representation of the ECL mechanism compared with the PL mechanism for the same C-dots, b) ECL emission of C-dots showing the emission of light at a cathodic (R•+) and anodic (R•⁻) ECL (ν = 0.1V/s), and c) ECL response of C-dots in the presence (red) and absence (blue) of 1mM $S_2O_8^{2-}$. Adapted from Ref. 37.

1.3.4 Toxicity

There is an increasing concern about certain harms nanomaterials might pose to human health. Due to their important potential in the biomedical sciences, C-dots toxicity has been extensively studied and a brief overview will be discussed in the following section.

Ray et al.[82] demonstrated that C-dots (12.5 nm) obtained from nitric acid oxidation of candle soot could readily pass through cell's membrane without any need for further functionalization. Cytotoxicity was assessed using MTT (a colorimetric test for metabolic activity) and Trypan Blue (cell viability test by exclusion) assays, HepG2 cells were exposed to 0.1-1 mg/mL of C-dots solutions for 24 hours, then absorbance was measured at 550 nm. Results obtained showed minimal cell death at concentrations needed - reports suggest that 50 – 500 µg/mL[83–85] are sufficient for bioimaging studies (Figure 1-35 a).

GQDs (~7 nm) prepared from electrolysis of a graphite rod, against a Pt wire counter electrode, were also tested for biocompability[40]. It was concluded that GQDs had no significant effect on cell viability even when exposed during prolonged periods of time and at greater concentrations than those needed (Figure 1-35 b).
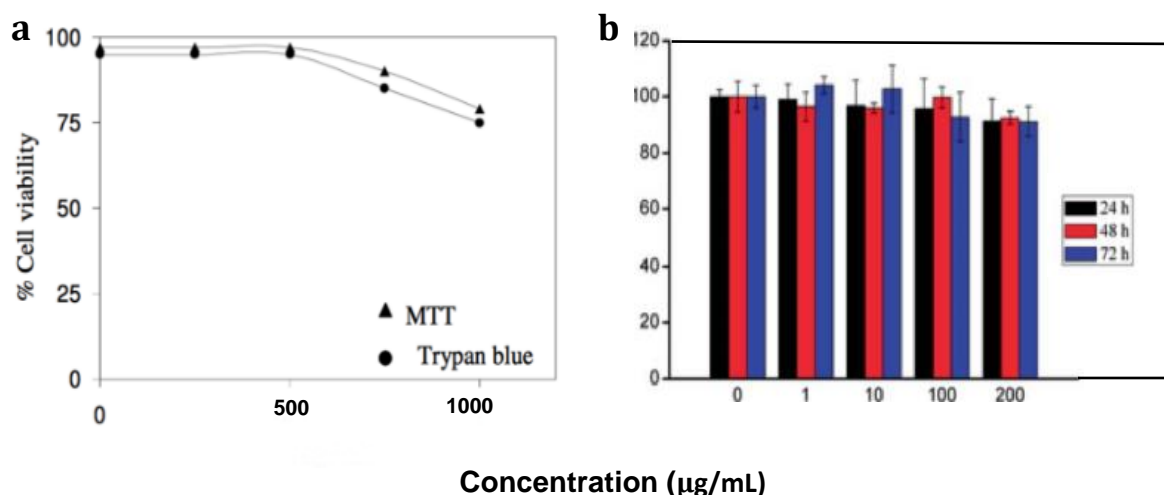
Figure 1-35 – Cell survival rate when exposed for 24h to solutions of C-dots synthesized from a) candle soot and b) electrochemically produced GQDs. Adapted from Ref. 82 and 86, respectively.

Yang et al.[87] concluded that after 4 weeks of exposure to PEG passivated C-dots (5 nm) (intravenously administrated), mice showed no health problems. Furthermore, when organs were collected, low accumulations of C-dots were found on liver and spleen, but displayed no abnormalities or necrosis. C-dots produced from hair fibres (7.5 nm)[61] were introduced into HeLa cells for fluorescence microscopy studies. The authors used concentrations of 200 g/mL and reported that at these concentrations the cells survival rate was ca. 85%.

More recently, Hua and coworkers[88] prepared C-dots (2.7 nm) from bacteria hydrothermal carbonization and reported that the obtained C-dots selectively stained dead cells (Figure 1-36 a), due to their high electronegativity (zeta potential of $\zeta = -42$ mV). Additionally, when compared to a commonly used marker cells – propidium iodide (PI), it produced considerably less effect on the cell viability, as seen in Figure 1-36 b. The authors suggested this to be the ideal method for cell live/dead differentiation.
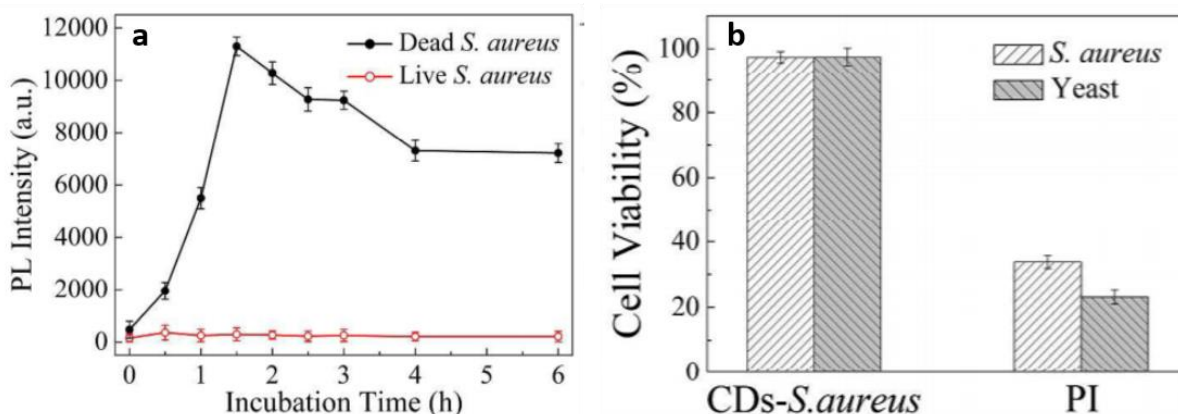
Figure 1-36 – a) Effect of the incubation time of a 200 µg/mL solution of bacteria-derived C-dots on dead (black) and live bacteria staining, and **b)** cell viability after incubation with C-dots and PI marker on bacteria and yeast. Adapted from Ref. 88.

1.3.5 Applications

1.3.5.1 Bioimaging

Quantum-dots and organic dyes are still the most used materials for bioimaging purposes mainly due to their high QY. Nevertheless, organic dyes still display photostability-related issues as well as not showing (or showing limited) emission in the NIR region, which is becoming of high interest for bioimaging applications. QDs, on the other hand, have showed great potential due to their size-tuneability fluorescence and two-photon/Upconversion emission. Even though other types of QDs have been developed, Cd-based QDs are still the most attractive[89] due to their optimum QYs and broad excitation bands. These however pose as highly toxic materials and their application is still under debate, particularly for *in vivo* studies.

C-dots, owing to their benign nature, simple preparation protocols and wide range of available materials, have emerged as natural alternatives for the above materials. Sun et al.[90] were one of the first groups to report the use of PPEI-EI surface passivated C-dots (~5 nm) produced by laser-ablation of a carbon target with two-photon excitation in the NIR region, for cancer cells targeting for *in vitro* studies. When excited in this region (λ_{exc} = 800 nm), the C-dots displayed luminescence in the visible region which allowed for the microscopy analysis of the cancer cells without background interference. The authors suggested that, due to the surface functionalization with

57

PPEI-EI, the C-dots were able to penetrate the cells and illuminate both the cell membranes and the cytoplasm (Figure 1-37), showing great labelling efficiency.
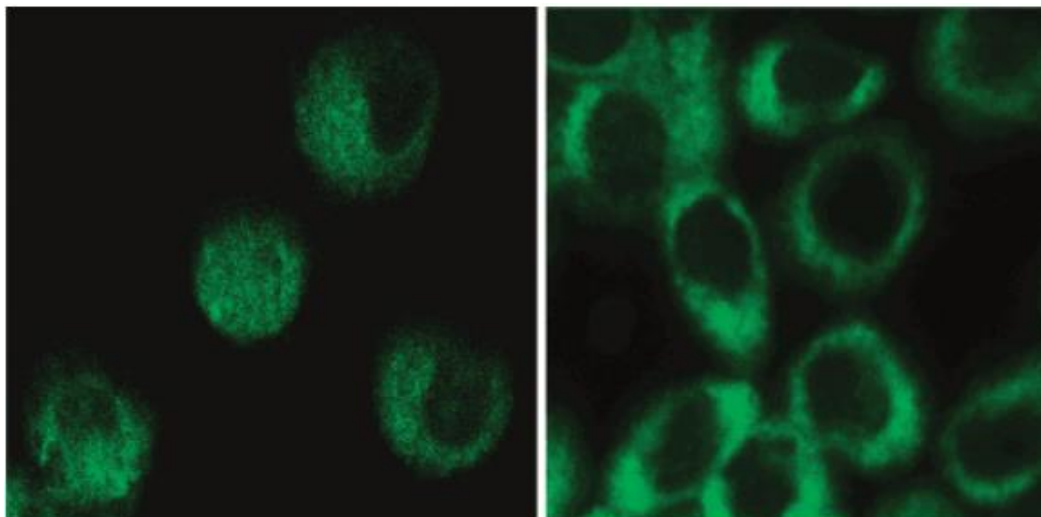
Figure 1-37 – Microscopy images of the two-photon luminescence of PPEI-EI surface-passivated C-dots obtained by laser ablation of a carbon target, showing illumination of both the cell membrane and cytoplasm. Adapted from Ref. 90.

Yang et al.[87] confirmed C-dots potential for *in vivo* studies (Figure 1-38). C-dots (~ 5nm) prepared by laser ablation encapsulated in a ZnS shell functionalized with PEG_{1500N}, were injected into mice through subcutaneous, intradermal and intravenous routes. ZnS-undoped C-dots were also tested. However, these showed significantly lower luminescence *in vivo* when compared to ZnS-doped C-dots, which is in line with reports for this type of C-dots behaviour in solution[91]. The authors evidenced that even though nanoparticles are known to accumulate in the liver, which may lead to hepatic failures, C-dots accumulated more significantly on kidneys (providing a secretion pathway), and only very low amounts of C-dots reached the liver. This was attributed to the presence of PEG and proved the biocompability of the as-prepared C-dots.
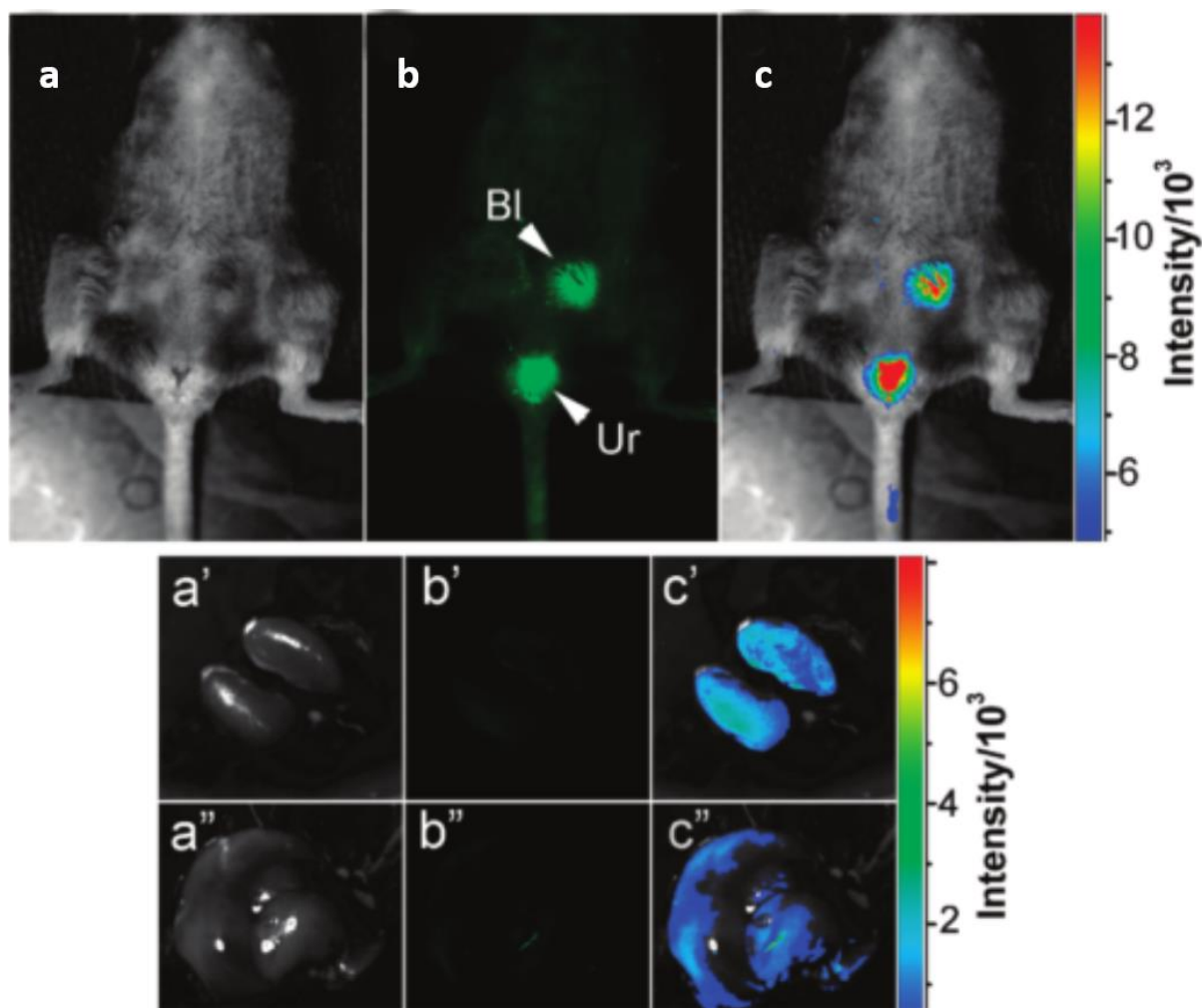
Figure 1-38 – C-dots prepared from laser ablation, intravenously injected in mice: a, a' and a") bright field images, b, b' and b") fluorescence images, and c, c' and c") colour coded images. a, b and c) show general distribution of C-dots in mice's body, a', b' and c') show the dissected kidneys images, and a", b" and c") show dissected liver images. Adapted from Ref. 87.

1.3.5.2 *Energy harvesting*

C-dots have been demonstrated as potential sensitizers in solar cells, mostly arising from their photon-to-electron conversion potential. Due to their broad absorption bands, they can absorb a higher range of the spectrum of sun radiation, and therefore, potentially, improve the power conversion efficiencies of solar cells.

Yan and coworkers[92] tested GQDs (13.5 nm, 168 π-conjugated carbon atoms) formed by all-organic synthesis, as solar cell sensitizers. They reported that the as-prepared GQDs displayed ε values considerably higher than those of commonly used for these applications (*e.g.* Ru complexes). Furthermore, these GQDs displayed a broad energy

absorption bands for (900 nm), which further supported the suitability of these materials for energy harvesting. GQDs were then deposited on a TiO_2 film and were tested as solar cell sensitizers, and it was noticed that the open-circuit current and fill factors were comparable to those typically obtained by the Ru-sensitized cells, proving the potential these materials hold. Nevertheless, a lower current density was reported, which was attributed to the low affinity between GQDs and TiO_2 layer, evidencing the further need for development in the field.

1.3.5.3 *Sensoring*

Another field they show promise in is as nano-sensors. Due to their large surface area and functionalization compatibility nature, these C-dots may be "tailored" specifically to target the molecule of interest. In this particular field, they have been successfully employed for the detection of different types of analytes like metal ions (Hg II [49], Fe III [93], Pb II [94], Cu II [95]), small molecules and other biomolecules of interest (melamine[96], glucose[97], dopamine[98] and ascorbic acid[99]).

In a typical procedure, Li et al.[100] suggested the use of C-dots (~9 nm) prepared from pyrolytic treatment of citric acid for the selective detection of 2,4,6-trinitrophenol (TNP). Even though TNP is extensively used in the chemical industry as an intermediate for the production of dyes, pesticides and pharmaceuticals[101], it is their use in the manufacture of explosives that is of particular concern. The authors demonstrated that these C-dots were selectively (and significantly) quenched in the presence of TNP (Figure 1-39 a). They argued that the mechanism behind the fluorescence quenching is based on the energy transfer between the PL emission of the C-dots and the absorption of the TNPs, since the latter displayed a broad absorption band that extended towards C-dots emission region (450 nm). The remarkable selectivity of this method was evidence when similar analogues (and other analytes) were concluded to not have any relevant effects on the C-dots fluorescence (Figure 1-39 b).
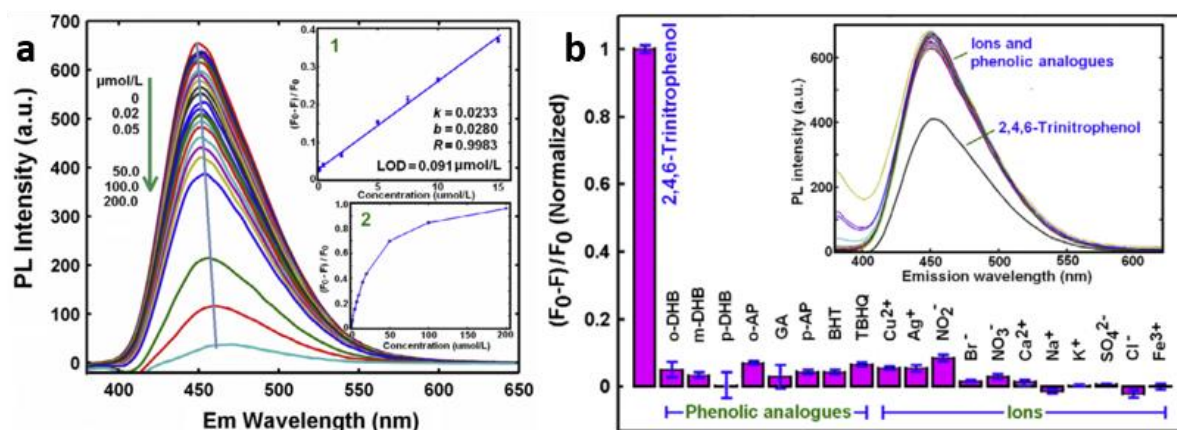
Figure 1-39 – a) Effect of increasing amounts of TNP in an aqueous solution of C-dots derived by citric acid pyrolysis (insets show the initial linearity of the quenching effects and consequent saturation at higher concentrations) and b) the selectivity of the as-prepared C-dots in the presence of other analytes. Adapted from Ref. 100.

1.4 Conclusion

It has been evidenced the importance of fluorescent materials on a variety of scientific fields. Organic dyes, due to their high quantum yields, well understood chemical composition and structure, remain at the centre of biomedical related applications such as bioimaging and drug control release. On the other hand, Quantum dots have recently raised some concerns over their cytoxicity, particularly Cadmium-based quantum dots, but they have found important uses, most significantly, in dye solar cells, light-emitting devices and nanosensors[12].

Since their emergence, C-dots have attracted significant research efforts. Owing to their ease of preparation and remarkable optical and electronical properties, it comes as no surprise they are considered nanomaterials with great potential. C-dots, with their low toxicity composition, high quantum yields and high photostability, are suggested to be of prime importance for bioimaging for both *in vitro* and *in vivo* studies.

C-dots with amorphous structure may be prepared following simple methods (hydrothermal treatment, microwave pyrolysis) using readily available carbon sources, such as soy milk, grass, citric acid, human hair fibres, among many others. Conversely, C-dots displaying graphitic structure, typically from the fractioning of

61

graphene-based materials (*e.g.* graphite and CNTs), display a tuneable band gap, according to the number of benzene rings present in their structure.

In terms of PL properties, C-dots typically display strong blue to green emission colours but there have also been reports which demonstrate the preparation of C-dots with longer wavelength emission such as yellow, orange and red. There are some similarities between QDs and C-dots PL properties, for instance on quantum confinement effects (QCE). However, it is not always the case that C-dots emission colours change according to their size as QDs do, and thus their PL properties cannot be as easily explained as QDs. Another difference, when comparing to the traditional QDs, is that C-dots present much wider peaks which is attributed to the more inhomogeneous composition of C-dots.

Additionally, surface/edges states of C-dots are also an important parameter to consider in C-dots fluorescence. With respect to GQDs, the predominant edge structure is the zigzag edge, facilitates the occurrence of emissive sites on their edges, due to the existence of carbene ions. On the other hand, amorphous C-dots usually display more possibilities in terms of surface chemistry, for instance, different heteroatoms may be added to their surface which may displace C-dots emission. Furthermore, different degrees of oxidation also produce shifts in fluorescence (oxidation produces red-shifts, and reduction produce blue-shifts).

An increasing number of reports have provided evidence that C-dots display Upconversion properties, introducing NIR analysis at considerable safer and simpler procedures when compared to their counterparts (QDs and upconverted rare-earth nanocrystals). These properties show great promise for bioimaging due to the possibility of reducing background interference. Since the human body is invisible to IR radiation, and these C-dots would emit at lower wavelengths (typically in the green region), it opens new possibilities in bio-labelling, controlled drug release, cell tissue recovery monitoring, etc. Their broad absorption bands also allow for a larger use of the range of sun's radiation spectrum and thus have been widely suggested as efficient materials for solar cells. Even though reports thus far have only been able to fall short of QDs and other dye-sensitized solar cells, theoretically, they are expected to afford solar cells with much higher energy conversion efficiencies.

1.5   References

1.   Resch-Genger, U., Grabolle, M., Cavaliere-Jaricot, S., Nitschke, R. & Nann, T. Quantum dots versus organic dyes as fluorescent labels. *Nat. Methods* **5,** 763–75 (2008).

2.   Zhang, J., Campbell, R. E., Ting, A. Y. & Tsien, R. Y. Creating new fluorescent probes for cell biology. *Nat. Rev. Mol. Cell Biol.* **3,** 906–18 (2002).

3.   Gu, Z. *et al.* Recent Advances in Design and Fabrication of Upconversion Nanoparticles and Their Safe Theranostic Applications. *Adv. Mater.* **25,** 3758–79 (2013).

4.   Massey, M., Wu, M., Conroy, E. M. & Algar, W. R. Mind your P's and Q's: The coming of age of semiconducting polymer dots and semiconductor quantum dots in biological applications. *Curr. Opin. Biotechnol.* **34,** 30–40 (2015).

5.   Valeur, B. & N. Berberan-Santos, M. Molecular Fluorescence - Principles and Applications. (John Wiley & Sons, Incorporated (Germany), 2013).

6.   Waggoner, A. Fluorescent labels for proteomics and genomics. *Curr. Opin. Chem. Biol.* **10,** 62–66 (2006).

7.   Chibisov, A. K. Triplet states of cyanine dyes and reactions of electron transfer with their participation. *J. Photochem.* **6,** 199–214 (1976).

8.   Sjoback, R., Nygren, J. & Kubista, M. Absorption and fluorescence properties of fluorescein. *Spectrochim. Acta Part A* **51,** L7–L21 (1995).

9.   Kubin, R. F. & Fletcher, A. N. Fluorescence quantum yields of some rhodamine dyes. *J. Lumin.* **27,** 455–62 (1982).

10.   Weber, G. & Teale, F. W. J. Determination of the absolute quantum yield of fluorescent solutions. *Trans. Faraday Soc.* **53,** 646–55 (1957).

11.   Alivisatos, A. P. Semiconductor Clusters, Quantum Nanocrystals, and Quantum Dots. *Science* **271,** 933–37 (1996).

12.   Burda, C., Chen, X., Narayanan, R. & El-Sayed, M. A. Chemistry and properties of nanocrystals of different shapes. *Chemical Reviews* **105,** 1025-102 (2005).

13. Shirasaki, Y., Supran, G. J., Bawendi, M. G. & Bulović, V. Emergence of colloidal quantum-dot light-emitting technologies. *Nat. Photonics* **7,** 13–23 (2012).

14. Alivisatos, A. P. Perspectives on the Physical Chemistry of Semiconductor Nanocrystals. *J. Phys. Chem.* **100,** 13226–39 (1996).

15. Anthony, S. ExtremeTech. (2012). Available at: https://www.extremetech.com/wp-content/uploads/2012/12/quantum_dots_c.jpg.

16. Sigma-Aldrich. Quantum Dots. Available at: http://www.sigmaaldrich.com/technical-documents/articles/materials-science/nanomaterials/quantum-dots.html#top.

17. Yáñez-Sedeño, P. *et al.* Biosensors in forensic analysis. A review. *Anal. Chim. Acta* **823,** 1–19 (2014).

18. Medintz, I. L., Uyeda, H. T., Goldman, E. R. & Mattoussi, H. Quantum dot bioconjugates for imaging, labelling and sensing. *Nat. Mater.* **4,** 435–46 (2005).

19. Cho, S. J. *et al.* Long-Term Exposure to CdTe Quantum Dots Causes Functional Impairments in Live Cells. *Langmuir* **23,** 1974–80 (2007).

20. Cruz-Acuña, M., Bailón-Ruiz, S., Marti-Figueroa, C. R., Cruz-Acuña, R. & Perales-Pérez, O. J. Synthesis, Characterization and Evaluation of the Cytotoxicity of Ni-Doped Zn (Se, S) Quantum Dots. *J. Nanomater.* **2015**, 1-8 (2015).

21. Dubertret, B., Skourides, P. & Norris, D. J. In Vivo Imaging of Quantum Dots Encapsulated in Phospholipid Micelles. *Science,* **28**, 1759-62, (2002).

22. Das, A. & Snee, P. T. Synthetic Developments of Nontoxic Quantum Dots. *ChemPhysChem* **17,** 598–617 (2016).

23. Peng, F. *et al.* Silicon nanomaterials platform for bioimaging, biosensing, and cancer therapy. *Acc. Chem. Res.* **47,** 612–23 (2014).

24. Park, J.-H. *et al.* Biodegradable luminescent porous silicon nanoparticles for in vivo applications. *Nat. Mater.* **8,** 331–36 (2009).

25. Mo, D., Hu, L., Zeng, G., Chen, G. & Wan, J. Cadmium-containing quantum dots: properties, applications, and toxicity. *Appl. Microbiol. Biotechnol.* (2017).

26.   Bacon, M., Bradley, S. J. & Nann, T. Graphene Quantum Dots. *Part. Part. Syst. Charact.* **31,** 415–28 (2014).

27.   Radovic, L. R. & Bockrath, B. On the chemical nature of graphene edges: Origin of stability and potential for magnetism in carbon materials. *J. Am. Chem. Soc.* **127,** 5917–27 (2005).

28.   Gusynin, V. P., Miransky, V. A., Sharapov, S. G., Shovkovy, I. A. & Wyenberg, C. M. Edge states on graphene ribbons in magnetic field: Interplay between Dirac and ferromagnetic-like gaps. *Phys. Rev. B - Condens. Matter Mater. Phys.* **79,** 1–13 (2009).

29.   Li, L. & Yan, X. Colloidal Graphene Quantum Dots. *J. Phys. Chem. Lett.* **1,** 2572–76 (2010).

30.   Kelarakis, A. Graphene quantum dots: In the crossroad of graphene, quantum dots and carbogenic nanoparticles. *Curr. Opin. Colloid Interface Sci.* **20,** 354–61 (2015).

31.   Hummers, W. S. & Offeman, R. E. Preparation of Graphitic Oxide. *J. Am. Chem. Soc.* **80,** 1339 (1958).

32.   Li, L. *et al.* Focusing on luminescent graphene quantum dots: current status and future perspectives. *Nanoscale* **5,** 4015–39 (2013).

33.   Shinde, D. B. & Pillai, V. K. Electrochemical preparation of luminescent graphene quantum dots from multiwalled carbon nanotubes. *Chem. - A Eur. J.* **18,** 12522–28 (2012).

34.   Dong, Y. *et al.* One-step and high yield simultaneous preparation of single- and multi-layer graphene quantum dots from CX-72 carbon black. *J. Mater. Chem.* **22,** 8764 (2012).

35.   Peng, J. *et al.* Graphene Quantum Dots Derived from Carbon Fibers. *Nano Lett.* **12,** 844–49 (2011).

36.   Pan, D., Zhang, J., Li, Z. & Wu, M. Hydrothermal route for cutting graphene sheets into blue-luminescent graphene quantum dots. *Adv. Mater.* **22,** 734–38 (2010).

37.   Zheng, L., Chi, Y., Dong, Y., Lin, J. & Wang, B. Electrochemiluminescence of water-soluble carbon nanocrystals released electrochemically from graphite. *J. Am. Chem. Soc.* **131,** 4564–65 (2009).

38.   Lu, J. *et al.* One-Pot Synthesis of Fluorescent Carbon Graphene by the Exfoliation of Graphite in Ionic Liquids. *ACS Nano* **3,** 2367–75 (2009).

39.   Ye, R. *et al.* Coal as an abundant source of graphene quantum dots. *Nat. Commun.* **4,** 1–7 (2013).

40.   Zhang, M. *et al.* Facile synthesis of water-soluble, highly fluorescent graphene quantum dots as a robust biological label for stem cells. *J. Mater. Chem.* **22,** 7461–67 (2012).

41.   Kosynkin, D. V. *et al.* Longitudinal unzipping of carbon nanotubes to form graphene nanoribbons. *Nature* **458,** 872–76 (2009).

42.   Pan, D. *et al.* Cutting sp2 clusters in graphene sheets into colloidal graphene quantum dots with strong green fluorescence. *J. Mater. Chem.* **22,** 3314 (2012).

43.   Shen, J., Zhu, Y., Chen, C., Yang, X. & Li, C. Facile preparation and upconversion luminescence of graphene quantum dots. *Chem. Commun.* **47,** 2580–82 (2011).

44.   Shen, J. *et al.* One-pot hydrothermal synthesis of graphene quantum dots surface-passivated by polyethylene glycol and their photoelectric conversion under near-infrared light. *New J. Chem.* **36,** 97–101 (2012).

45.   Lu, J., Yeo, P. S. E., Gan, C. K., Wu, P. & Loh, K. P. Transforming C60 molecules into graphene quantum dots. *Nat. Nanotechnol.* **6,** 247–52 (2011).

46.   Yan, X., Cui, X. & Li, L. S. Synthesis of large, stable colloidal graphene quantum dots with tunable size. *J. Am. Chem. Soc.* **132,** 5944–45 (2010).

47.   Liu, R., Wu, D., Feng, X. & Müllen, K. Bottom-up fabrication of photoluminescent graphene quantum dots with uniform morphology. *J. Am. Chem. Soc.* **133,** 15221–23 (2011).

48.   Chen, W., Hu, C., Yang, Y., Cui, J. & Liu, Y. Rapid synthesis of carbon dots by hydrothermal treatment of lignin. *Materials.* **9,** 1-8 (2016).

49.   Zhang, Y. L. W. *et al.* Water-soluble, nitrogen-doped fluorescent carbon dots for highly sensitive and selective detection of Hg [2+] in aqueous solution. *RSC Adv.* **5,** 40393–401 (2015).

50.   Sahu, S. *et al.* Simple one-step synthesis of highly luminescent carbon dots from orange juice: application as excellent bio-imaging agents. *Chem. Commun.* **48,** 8835–37 (2012).

51.   Jaiswal, A., Ghosh, S. S. & Chattopadhyay, A. One step synthesis of C-dots by microwave mediated caramelization of poly(ethylene glycol). *Chem. Commun.* **48,** 407–09 (2012).

52.   Zhu, H. *et al.* Microwave synthesis of fluorescent carbon nanoparticles with electrochemiluminescence properties. *Chem. Commun.* 5118–20 (2009).

53.   Chemat, F. & Poux, M. Microwave assisted pyrolysis of urea supported on graphite under solvent-free conditions. *Tetrahedron Lett.* **42,** 3693–95 (2001).

54.   Baker, S. N. & Baker, G. A. Luminescent Carbon Nanodots: Emergent Nanolights. *Angew. Chem. Int. Ed* **49,** 6726–44 (2010).

55.   Krysmann, M. J., Kelarakis, A. & Giannelis, E. P. Photoluminescent carbogenic nanoparticles directly derived from crude biomass. *Green Chem.* **14,** 3141–45 (2012).

56.   Liu, H., Ye, T. & Mao, C. Fluorescent carbon nanoparticles derived from candle soot. *Angew. Chem. Int. Ed. Engl.* **46,** 6473–75 (2007).

57.   Zhu, C., Zhai, J., Dong, S., Zhai, J. & Dong, S. Bifunctional fluorescent carbon nanodots: green synthesis via soy milk and application as metal-free electrocatalysts for oxygen reduction. *Chem. Commun.* **48,** 9367–69 (2012).

58.   Krysmann, M. J., Kelarakis, A., Dallas, P. & Giannelis, E. P. Formation mechanism of carbogenic nanoparticles with dual photoluminescence emission. *J. Am. Chem. Soc.* **134,** 747–50 (2012).

59.   Liu, R. *et al.* An aqueous route to multicolor photoluminescent carbon dots using silica spheres as carriers. *Angew. Chemie - Int. Ed.* **48,** 4598–601 (2009).

60.   Wang, W., Li, Y., Cheng, L., Cao, Z. & Liu, W. Water-soluble and phosphorus-containing carbon dots with strong green fluorescence for cell labeling. *J. Mater. Chem. B* **2,** 46–48 (2014).

61.   Sun, D. *et al.* Hair fiber as a precursor for synthesizing of sulfur- and nitrogen-co-doped carbon dots with tunable luminescence properties. *Carbon N. Y.* **64,** 424–34 (2013).

62.   Zhou, J. *et al.* Facile synthesis of halogenated carbon quantum dots as an important intermediate for surface modification. *RSC Adv.* **3,** 9625–28 (2013).

63.   Du, Q., Zhou, G., Zhou, J., Jia, X. & Zhou, H. Enhanced luminescence of novel $Y_2Zr_2O7:Dy^{3+}$ phosphors by Li^+ co-doping. *J. Alloys Compd.* **552,** 152–56 (2013).

64.   Wang, Y. *et al.* Thickness-dependent full-color emission tunability in a flexible carbon dot ionogel. *J. Phys. Chem. Lett.* **5,** 1412–20 (2014).

65.   Zhu, S. *et al.* The photoluminescence mechanism in carbon dots (graphene quantum dots, carbon nanodots, and polymer dots): current state and future perspective. *Nano Res.* **8,** 355–81 (2015).

66.   Chen, C.-F. *et al.* Controlling inelastic light scattering quantum pathways in graphene. *Nature* **471,** 617–20 (2011).

67.   Eda, G. *et al.* Blue photoluminescence from chemically derived graphene oxide. *Adv. Mater.* **22,** 505–09 (2010).

68.   Li, H. *et al.* Water-Soluble Fluorescent Carbon Quantum Dots and Photocatalyst Design. *Angew. Chemie - Int. Ed.* **49,** 4430–34 (2010).

69.   Chien, C.-T. *et al.* Tunable photoluminescence from graphene oxide. *Angew. Chem. Int. Ed. Engl.* **51,** 6662–66 (2012).

70.   Kelarakis, A. From highly graphitic to amorphous carbon dots: A critical review. *MRS Energy Sustain.* **1,** 1–15 (2014).

71.   Enoki, T., Fujii, S. & Takai, K. Zigzag and armchair edges in graphene. *Carbon N. Y.* **50,** 3141–45 (2012).

72.   Lin, L. & Zhang, S. Creating high yield water soluble luminescent graphene quantum dots via exfoliating and disintegrating carbon nanotubes and graphite flakes. *Chem. Commun.* **48,** 10177–79 (2012).

73.   Xu, X. *et al.* Electrophoretic analysis and purification of fluorescent single-walled carbon nanotube fragments. *J. Am. Chem. Soc.* **126,** 12736–37 (2004).

74.   Sun, Y., Zhou, B. & Lin, Y. Quantum-sized carbon dots for bright and colorful photoluminescence. *J. Am. Chem. Soc.* **128,** 7756–57 (2006).

75.   Bao, L. *et al.* Electrochemical tuning of luminescent carbon nanodots: From preparation to luminescence mechanism. *Adv. Mater.* **23,** 5801–06 (2011).

76.   Zheng, H. *et al.* Enhancing the luminescence of carbon dots with a reduction pathway. *Chem. Commun.* **47,** 10650 (2011).

77.   Das, S. K., Liu, Y., Yeom, S., Kim, D. Y. & Richards, C. I. Single-particle fluorescence intensity fluctuations of carbon nanodots. *Nano Lett.* **14,** 620–25 (2014).

78.   Tetsuka, H. *et al.* Optically tunable amino-functionalized graphene quantum dots. *Adv. Mater.* **24,** 5333–38 (2012).

79.   Kim, T. H., Ho, H. W., Brown, C. L., Cresswell, S. L. & Li, Q. Amine-rich carbon nanodots as a fluorescence probe for methamphetamine precursors. *Anal. Methods* **7,** 6869–76 (2015).

80.   Pan, L., Sun, S., Zhang, L., Jiang, K. & Lin, H. Near-infrared emissive carbon dots for two-photon fluorescence bioimaging. *Nanoscale* **8,** 17350–56 (2016).

81.   Zhao, W. W., Wang, J., Zhu, Y. C., Xu, J. J. & Chen, H. Y. Quantum Dots: Electrochemiluminescent and Photoelectrochemical Bioanalysis. *Anal. Chem.* **87,** 9520–31 (2015).

82.   Ray, S. C., Saha, A., Jana, N. R. & Sarkar, R. Fluorescent carbon nanoparticles: Synthesis, characterization, and bioimaging application. *J. Phys. Chem. C* **113,** 18546–51 (2009).

83.   Zhong, Y. *et al.* One-step synthesis of orange luminescent carbon dots for Ag^+ sensing and cell imaging. *J. Lumin.* **190,** 188–93 (2017).

84.   Wang, J. *et al.* Highly fluorescent carbon dots as selective and visual probes for sensing copper ions in living cells via an electron transfer process. *Biosens. Bioelectron.* **97,** 157–63 (2017).

85.   Vandarkuzhali, S. A. A. *et al.* Highly fluorescent carbon dots from Pseudo-stem of banana plant: Applications as nanosensor and bio-imaging agents. *Sensors Actuators B Chem.* **252,** 894–900 (2017).

86. Shang, W. *et al.* The uptake mechanism and biocompatibility of graphene quantum dots with human neural stem cells. *Nanoscale* **6,** 5799–806 (2014).

87. Yang, S. T. *et al.* Carbon dots for optical imaging in vivo. *J. Am. Chem. Soc.* **131,** 11308–09 (2009).

88. Hua, X.-W., Bao, Y.-W., Wang, H.-Y., Chen, Z. & Wu, F.-G. Bacteria-derived fluorescent carbon dots for microbial live/dead differentiation. *Nanoscale* **9,** 2150–61 (2017).

89. Chen, N. *et al.* The cytotoxicity of cadmium-based quantum dots. *Biomaterials* **33,** 1238–44 (2012).

90. Cao, L. *et al.* Carbon dots for multiphoton bioimaging. *J. Am. Chem. Soc.* **129,** 11318–19 (2007).

91. Sun, Y. *et al.* Doped Carbon Nanoparticles as a New Platform for Highly Photoluminescent Dots. *J. Phys. Chem. C* **112,** 18295–98 (2008).

92. Yan, X., Cui, X., Li, B. & Li, L. S. Large, solution-processable graphene quantum dots as light absorbers for photovoltaics. *Nano Lett.* **10,** 1869–73 (2010).

93. Vikneswaran, R., Ramesh, S. & Yahya, R. Green synthesized carbon nanodots as a fluorescent probe for selective and sensitive detection of iron(III) ions. *Mater. Lett.* **136,** 179–82 (2014).

94. Wee, S. S., Ng, Y. H., Ng, S. M. & Muk, S. Synthesis of fluorescent carbon dots via simple acid hydrolysis of bovine serum albumin and its potential as sensitive sensing probe for lead (II) ions. *Talanta* **116,** 71–76 (2013).

95. Lin, Y. *et al.* Tunable Fluorescent Silica-Coated Carbon Dots: A Synergistic Effect for Enhancing the Fluorescence Sensing of Extracellular Cu^{2+} in Rat Brain. *ACS Appl. Mater. Interfaces* **7,** 27262–70 (2015).

96. Dai, H. *et al.* A carbon dot based biosensor for melamine detection by fluorescence resonance energy transfer. *Sensors Actuators, B Chem.* **202,** 201–08 (2014).

97. Lu, Q. *et al.* Hydroxyl-rich C-dots synthesized by a one-pot method and their application in the preparation of noble metal nanoparticles. *Chem. Commun.* **51,** 7164–67 (2015).

98.   Li, Q., Xu, Z., Tang, W. & Wu, Y. Determination of Dopamine with a Modified Carbon Dot Electrode. *Anal. Lett.* **2719,** (2015).

99.   Yang, L. *et al.* A quadruplet electrochemical platform for ultrasensitive and simultaneous detection of ascorbic acid, dopamine, uric acid and acetaminophen based on a ferrocene derivative functional Au NPs/carbon dots nanocomposite and graphene. *Anal. Chim. Acta* **903,** 69–80 (2016).

100.   Li, Z., Wang, Y., Ni, Y. & Kokot, S. A sensor based on blue luminescent graphene quantum dots for analysis of a common explosive substance and an industrial intermediate, 2,4,6-trinitrophenol. *Spectrochim. Acta - Part A Mol. Biomol. Spectrosc.* **137,** 1213–21 (2015).

101.   Shen, J. *et al.* Biodegradation of 2,4,6-trinitrophenol by Rhodococcus sp. isolated from a picric acid-contaminated soil. *J. Hazard. Mater.* **163,** 1199–206 (2009).

102.   Bhunia, S. K., Saha, A., Maity, A. R., Ray, S. C. & Jana, N. R. Carbon Nanoparticle-based Fluorescent Bioimaging Probes. *Sci. Rep.* **3,** 1473 (2013).

103.   Du, Y. & Guo, S. Chemically doped fluorescent carbon and graphene quantum dots for bioimaging, sensor, catalytic and photoelectronic applications. *Nanoscale* **8,** 2532–43 (2016).

104.   Wen, X., Yu, P., Toh, Y.-R., Ma, X. & Tang, J. On the upconversion fluorescence in carbon nanodots and graphene quantum dots. *Chem. Commun.* **50,** 4703–06 (2014).

105.   Jiang, C. *et al.* Presence of photoluminescent carbon dots in Nescafe® original instant coffee: Applications to bioimaging. *Talanta* **127,** 68–74 (2014).

106.   Chandra, S. *et al.* Luminescent S-doped carbon dots: an emergent architecture for multimodal applications. *J. Mater. Chem. B* **1,** 2375 (2013).

107.   Vassilakopoulou, A., Georgakilas, V., Vainos, N. & Koutselas, I. Successful entrapment of carbon dots within flexible free-standing transparent mesoporous organic-inorganic silica hybrid films for photonic applications. *J. Phys. Chem. Solids* **103,** 190–96 (2017).

2 Experimental section

Name	Reagents	Treatment	Comments
aC-dots	Citric Acid, Ethanolamine	Pyrolysis	Hybrid powders consist of aC-dots physically mixed with different white powders (Laponite clay, Silica and Titania).
bC-dots	Grass, HNO_3,	Pyrolysis, Oxidation	Low fluorescence intensity in the powder form.
C-SiO$_2$	Silica (Ludox), C-18 silane, Ethylene diamine	Pyrolysis, Oxidation	Powders obtained were fluorescent without the need to further disperse in other matrices, and formed aggregate producing fractal motives.
In situ prepared C-dots on readily available polymers	PE and PEG as polymeric matrices; Ethanolamine as C-dots precursor.	Melt-mixing and Thermal treatment (lower temperatures used)	Polymers obtained were fluorescent in the solid state, and when dispersed (in the case of PEG)

2.1 C-dots nanopowders for fingerprint development purposes

2.1.1 C-dots derived from citric acid and ethanolamine pyrolysis (aC-dots)

The methodology used for C-dots synthesis has been previously reported in Ref. 1. Pyrolysis of citric acid (CA, purchased from Thermo Fisher Scientific) and ethanolamine (EA, ≥98% purchased from Sigma-Aldrich) on a 1:3 molar ratio, was performed at 180°C under reflux for 30 minutes, and for another 30 minutes at 230° without reflux to remove the water molecules formed in the previous step. Successive dialyses were performed, in order to remove impurities, through a SnakeSkin

membrane (3.5 kDa cut-off, purchased from Thermo Fisher Scientific) against distilled water. Both apparatus can be seen in Figure 2-1.
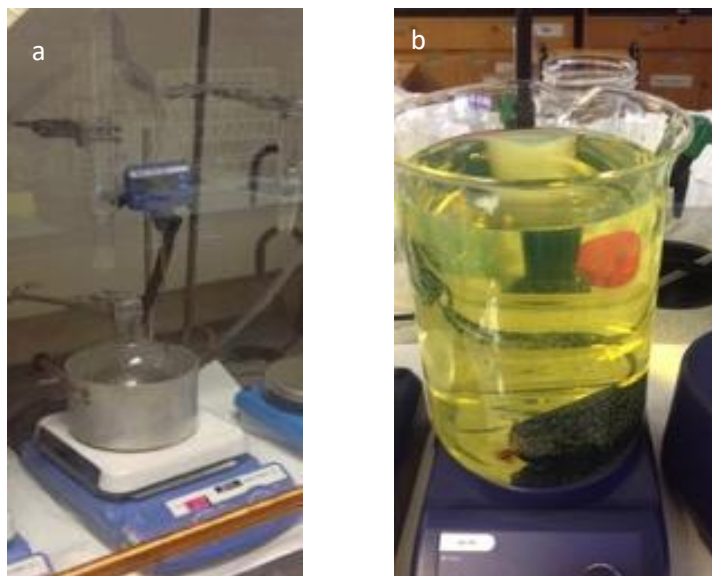
Figure 2-1 – a) Pyrolysis apparatus used for citric acid and ethanolamine pyrolysis (condenser is removed after 1h30), and b) aC-dots purification through dialysis on a snakeskin against water.

As C-dots are, in general, highly susceptible to self-quenching phenomena, solutions were diluted. This can prevent particle to particle interaction during sublimation, and then left for 3-4 days until samples were completely dried. The obtained solution was freeze dried to be used as fingerprint powder.

2.1.2 C-dots derived from crude biomass pyrolysis (bC-dots)

The methodology consists of thoroughly blending fresh grass and diluting it in a minimum quantity of water, and then keeping it in a furnace for 4h at 300°C [2]. The next step was to oxidize the material obtained after grass pyrolysis (Figure 2-2), to make it more hydrophilic and break down larger clusters. This is achieved by adding 3 M of HNO$_3$ (70%, purchased from Sigma Aldrich) and reflux it at 100°C, until a light brown product is obtained. The resultant material was then filtered through a filter paper (Whatman no. 41 porosity of 20 µm) on a Buchner funnel under vacuum, to remove the larger clusters. The obtained product was dialyzed in a SnakeSkin with a molecular

weight cut-off of 3.5 kDa, against deionized water to remove the excess of HNO_3. The final product was freeze-dried.

Figure 2-2 - Material obtained after grass pyrolysis.

2.1.3   Hybrid nano-powders

For fingerprint development purposes, silicon dioxide (SiO_2), titanium dioxide (TiO_2) or *Laponite (Lap)* clay were dispersed in an aC-dots solution (c-dots 1:150 weight ratio of white powders) and left in an ultrasonic bath for an hour to investigate if there were any interactions between the different components. Such a low ratio was used to understand the full depth of the potential of C-dots for solid fluorescence applications.

2.1.4   Characterization

2.1.4.1   _Fluorescence analysis_

Fluorescence analysis – a measure of the intensity in arbitrary units (a.u.) of the light emitted by an excited electron upon its relaxation to the ground state[3], was conducted on a Horiba Fluoromax® spectrofluorometer. It is known that C-dots display quenching effects at high concentrations and thus, intensity as a function of concentration was analysed for several concentrations at an excitation wavelength of 380 nm.

For the excitation-dependent emission, samples were analysed under excitation wavelengths between 290-500 nm, with 30 nm increments.

Solid-state fluorescence was also conducted on the hybrid powders. To this end, a sample holder was attached to the fluorometer. The sample holder was positioned at a 30º angle from the incident beam, to prevent the excitation signal from the machine

to be recorded and potentially damage the detector. Excitation wavelengths of 370 nm, 430 nm and 500 nm were used, and the emission was recorded on the range of 400-700 nm.

2.1.4.2 *Fingerprint methodology*

The researcher's index finger was rubbed on the forehead to get a mixture of both eccrine and sebaceous glands. This would generate a realistic fingerprint, as a mixture of components will be left behind in a real case scenario[4].

A series of fingermarks were deposited on microscope glass slides to assess the quality of the powders obtained (aC-dots:Lap; aC-dots:TiO$_2$; aC-dots:SiO$_2$), and were applied using a forensic squirrel-hair brush. Then, they were analysed under a *Zeiss® Axio Scope A1* fluorescent microscope. A commercial white fingerprint powder (WFP, purchased from Tetra Scene of Crime) was also used to reveal fingerprints as a control test. A metal spatula and a drink foil (Dr Pepper) were tested as alternative deposition surfaces.

Fingerprints were analysed in Automated Fingerprint Identification System (AFIS) software, to count the number of minutiae details that could be identified.

2.2 Carbogenically-coated silica nanoparticles for anti-counterfeit applications

2.2.1 *Synthetic procedure*

For the synthesis of the nanohybrid system, carbonised silica nanoparticles (C-SiO$_2$), 3 ml of colloidal silica nanoparticles (Ludox HS 30, purchased from Sigma-Aldrich) with an average diameter of 18 nm were reacted with 3g of Dimethyloctadecyl[3-(trimethoxysilyl)propyl]ammonium chloride (C-18 silane, purchased from Sigma-Aldrich), in acidic media - 1 ml of 1M HCl (37%, purchased from Sigma Aldrich) at 60 °C for 10 min. The dispersion was neutralized using a 0.1 M NaOH solution, was left for 24h at room temperature and dialyzed against deionized water using a SnakeSkin dialysis tubing membrane (3,5 kDa molecular weight cut-off, purchased from Thermo Fisher Scientific). TGA analysis (refer to section "Characterization" for more details on the parameters used) suggested that the surface-modified silica nanoparticles have

roughly 34 wt% organic content and helped determine the carbonization temperature. Thus, the nanoparticles were pyrolyzed in a furnace at 250°C for 3h and a dark powder was obtained. The powder was then subjected to surface oxidation, via treatment with 3M HNO_3 at 100°C, and further dialyzed against water. The C-SiO_2 were then treated with excess of ethylene diamine (Sigma-Aldrich) at 80°C for 1h followed by another purification step through dialysis.

2.2.2   Characterization

2.2.2.1   TGA characterization

Thermogravimetric analysis – the study of the mass changes occurring in a material due to controlled temperature changes[5], was performed using a Mettler Toledo TGA 1 STAR system, under nitrogen atmosphere and at a heating rate of 10°C/min, until a maximum temperature of 500°C was reached.

2.2.2.2   Elemental analysis

Elemental analysis for the elements C, H, N and S were conducted on a Flash 2000 CHNS-O Analyzer. The equipment was calibrated using a bypass - non-measurable sample with minor amounts of C-SiO_2 just to "clean" from possible contaminants; two standard runs - methionine was chosen as it had the likeliest similar elements percentage; and, two runs of the same standard as unknown sample – to check for the equipment's calibration efficiency. Finally, each sample was measured in duplicates and obtained percentages were averaged.

2.2.2.3   FTIR

Fourier Transform Infra-Red spectra – analysis of the vibrational modes of a material's functional groups[6], were recorded using a Nicolet IR2000 spectrophotometer. A total amount of 32 scans were run within a range of 3000-700 cm^{-1} and with a resolution of 8 cm^{-1}. The vibrational modes of functional groups of the as-prepared nanoparticles were investigated.

2.2.2.4 Photoluminescence spectra

Fluorescence analysis was conducted on a Horiba Fluoromax spectrofluorometer. For the excitation-dependent emission, samples were analysed under different excitation wavelengths, between 290-500 nm, with 30 nm increments and a slit of 2 nm.

2.2.2.5 TEM

Transmission Electron Microscopy photographs were obtained with a FEI T12 Spirit operated at 120 kV. A droplet of a dilute suspension (0.05mg/mL in water) was deposited on a carbon coated copper grid (Agar Scientific, USA) and air-dried.

2.2.2.6 SEM

Scanning Electron Microscopy photographs were taken of the microstructure of the nanotags generated on 6 mm Carbon Conductive SEM tabs (purchased from PELCO Tabs^{TM}), using a FEI Quanta 200 electron microscope.

2.2.2.7 Fluorescence imaging

The fluorescence microscopy images were obtained using a Zeiss Axio Scope A1 microscope equipped with band-pass filters. Three excitation wavelengths were used with 350, 395 and 590 nm.

2.2.2.8 Dynamic light scattering

Dynamic light scattering is the technique which analyses the random motion (Brownian motion) of particles in a solvent (usually water)[7].

The hydrodynamic diameter – the diameter of an equivalent hard sphere which diffuses at the same speed as the particle being measured, of C-SiO$_2$ of the nanoparticles were measured on well-filtered suspensions (Nylon membrane filters

with porosity 0.45 µm) using a Malvern Zetasizer Nano-ZS (Malvern Instruments, England) package which includes a 4 mW He–Ne laser operating at λ=633 nm.

2.2.2.9   *Fingerprint deposition and development*

Procedure followed as described in section 2.1.4.2.

2.2.2.10 *Nanotags development*

For the nanotags preparation, C-SiO$_2$ aqueous solutions of different pH values were left to air-dry in glass slides and in a polymeric substrate. For the investigation of the temperature effect on the nanotags, a marked pattern was subjected to 100°C for ~24h.

2.3   *In situ* preparation of C-dots in polymers matrices

For the polymer in-situ preparation of C-dots, 1 wt% of ethanolamine (≥98% purchased from Sigma-Aldrich) was added to two different polymers, polyethylene (MW 35k, purchased from Sigma-Aldrich) and polyethylene glycol (MW 1k, purchased from Sigma-Aldrich), and were heated up in two steps in a heating/stirring plate: initially at a temperature below the boiling point of the ethanolamine (b.p.$_{EA}$ 170°C) and above the melting point of the polymer (m.p.$_{PE}$ 90°C, m.p.$_{PEG}$ 37°C) for the amine to react, and at a temperature above the ethanolamine boiling point (at 180˚C), to remove all unreacted ethanolamine (each taking 30 minutes). The polymers were then left to recrystallize at room temperature, as shown in Figure 2-3. Control samples were also prepared - by processing the polymers the same way as before, but without adding the amine.

Figure 2-3 – Representative example of the as obtained polymers (EA-treated PEG).

2.3.1 Characterization

2.3.1.1 <u>Photoluminescence spectra</u>

Photoluminescence spectra of aqueous dispersion of C-dots under different excitation wavelengths were recorded at room temperature using a Horiba Jobin Yvon FluoroMax-4 spectrofluorometer.

For solid-state measurements, no extraction was made from the polymers.

2.3.1.2 <u>XRD</u>

X-ray diffraction – a technique used for the identification of a crystalline structure of a material[8], measurements were performed on a Bruker D2 Phaser coupled with a LYNXEYE 1-dimentional detector which suppresses the sample fluorescence. The diffractometer generates X-rays at 30kV/10mA, and uses a copper tube producing X-rays at λ=1.54Å.

2.3.1.3 <u>DSC</u>

Differential scanning calorimetry – a technique that measures the enthalpy changes involved in thermal transitions (*e.g.* melting and crystallization)[9], analysis was conducted on a TA *DSC Q2000*. Samples of, approximately, 15 mg were sealed inside

aluminium pans, and each run consisted of a heat/cool/heat temperature ramps, ranging from 0°C to 80°C and 160°C for PEG and PE, respectively.

2.4   References

1.   Krysmann, M. J., Kelarakis, A., Dallas, P. & Giannelis, E. P. Formation mechanism of carbogenic nanoparticles with dual photoluminescence emission. *J. Am. Chem. Soc.* **134,** 747–50 (2012).

2.   Krysmann, M. J., Kelarakis, A. & Giannelis, E. P. Photoluminescent carbogenic nanoparticles directly derived from crude biomass. *Green Chem.* **14,** 3141–45 (2012).

3.   Lakowicz, J. R. *Principles of Fluorescence Spectroscopy.* (Springer US, 2006).

4.   Girod, A., Ramotowski, R. & Weyermann, C. Composition of fingermark residue: a qualitative and quantitative review. *Forensic Sci. Int.* **223,** 10–24 (2012).

5.   Kaufmann, E. N. *Thermogravimetric Analysis* in *Characterization of Materials* (Hooboken, NJ: John Wiley and Sons, 2003).

6.   Kaufmann, E. N. *Fourier Transform Infrared (FTIR) Spectroscopy* in *Characterization of Materials* (Hooboken, NJ: John Wiley and Sons, 2003).

7.   Berne, B. J. *Dynamic Light Scattering: With Applications to Chemistry, Biology and Physics.* (Dover Publication Inc., 2003).

8.   Warden, B. E. *X-Ray Diffraction.* (Dover Publication Inc., 1969).

9.   Kaufmann, E. N. *Differential Scanning Calorimetry and Differential Thermal Analysis* in *Characterization of Materials* (Dover Publication Inc., 2003).

3   New types of hybrid nanopowders for fingerprint purposes

3.1   Introduction

From the available forensic physical evidence, fingerprints remain at the centre of individual identification. Even with DNA techniques experiencing greater advances in the last decades, fingerprints are still the only piece of evidence able to establish identity between identical twins.[1,2]

Fingerprint is the mark left behind by the friction of ridges, present in the fingers skin, on a given surface. There are several factors that influence the composition of the fingerprint (e.g. individual characteristics, nature of the surface and environmental conditions) but its major components are water and fatty substances [1–3]. The organic compounds are mainly originated on the epidermis, secretory glands in the dermis and with external contaminants. Subsequently, with the ageing of the fingerprint, water evaporates and the fingerprint becomes more hydrophobic.[3]

Occasionally, fingers may be contaminated with paint, ink or even blood, leaving a visible fingerprint. However, finger marks are frequently produced only by the natural secretions of the skin making it hard for crime scene investigators to detect or analyse them solely under natural light. This makes it essential to find the best procedures in order to develop and enhance these prints.

The identification of individuals by this physical evidence relies on an exclusive combination of different details (minutiae) comprised on the same fingerprint. The whole pattern is considered to have three levels of details:

- Level 1 – This is the largest level and can be identified macroscopically. It is the simplest way to distinguish between fingerprints, and thus be classified as: loops (subdivided into right or left depending on the delta position – level 2 detail), whorls and arches (classified as plain or tented). Figure 3-1 *a*, *b* and *c* show the different examples on this level of details;

- Level 2 – This level consists of every change that occurs on the ridges of fingerprints. It is thought to exist about 150 different details and their exclusive distribution over the global fingerprint is the reason behind their individuality.

Some examples of these details include deltas, lakes, ridge ends, bifurcations and dots, (Figure 3-1 d)

- Level 3 – Involves mainly sweat pores (Figure 3-1 e) and is usually disregarded from analysis as it is only detected by chemical procedures.
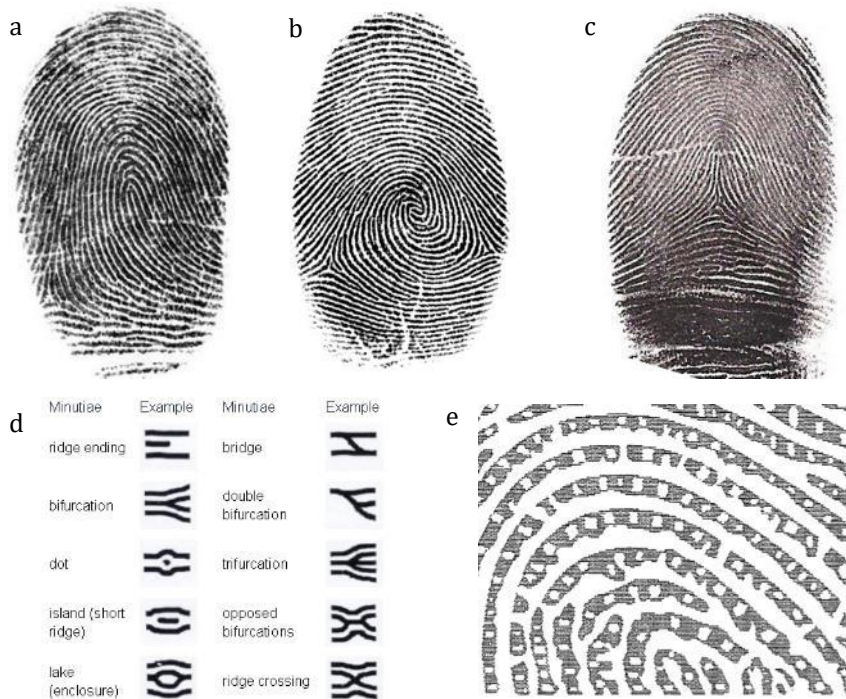
Figure 3-1 – Illustrative examples of: first level of classification of fingerprints – a) loop, b) whorl and c) arch, d) second level of details usually detected, and e) third level - sweat pores. Adapted from Ref. 4.

To reveal fingerprints, chemical or physical procedures can be used. Chemical reactions, like ninhydrin reagent or cyanoacrylate fuming, develop better shaped fingerprints, but typically demand time-consuming, toxic and expensive procedures[2]. Physical developers (mostly powders) on the other hand, provide experts with an effective, ready to use technique in crime scenes, and that is why they are more commonly employed.

Nanomaterials have great potential to be used as fingerprint powders. Their size not only facilitates better defined fingerprints, but also, given their optical properties, widens the range of surfaces fingerprints can be developed on. In addition, it gives them the potential to be used as more than just identification tools.

83

3.1.1 History of fingerprints' recovery

The use of fingerprints in crime resolution was first applied on the second half of the nineteenth century, and became well established in criminal investigations procedures [5]. The initial reported methods for latent fingerprint revelation were reagent-based. Silver nitrate (1877) and iodine vapours (1891) were the main solvents used, and had the advantage of being suitable for porous surfaces (like paper) and also non-porous surfaces[6]. Iodine vapours are still used by some labs in present forensic investigations.

The use of powders in the development of latent fingerprints only came later. This method relies on the physical affinity between finely divided material and the fatty components and the solution left by the skin ridges. The smaller the particles, the better the powder will adhere, producing a better resolved fingerprint, while at the same time, it is also important that the powder does not chemically interact with the surface [1,2].

Sir Edward Henry suggested the use of mercury-based powders[1]. The main problems about these were that mercury powders withheld several health hazards were withdrawn during the second half of the twentieth century.

Nowadays, there are a variety of powders that can be applied in different surfaces. The use of fingerprint powders has become such a routine procedure that the Home Office (UK), has developed a guideline for their application[7]. For smooth surfaces, aluminium flake and magnetic powders are recommended, as well as brass, black granular and magneta flake powders. Even though flake powders are more sensitive than granular powders, experts prefer to use nonmagnetic since they are easier to apply. On other surfaces, however, an efficient and generic procedure has not yet been found and there are not many powders that can be successfully employed. For dark surfaces white magnetic powders are suggested, and, contrariwise, for coloured surfaces black magnetic is recommended.

Since early stages, researchers understood that PL properties could be used to enhance contrast in fingerprint recovery. The use of cyanoacrylate ester fuming [8–10], ninhydrin-treated zinc chloride [11] and ninhydrin samples treated with NBD chloride (7-chloro-4-nitrobenzo-2-oxa-1,3-diazole) [12] were some of the first approaches with the aim to use luminescence to reveal fingerprint. Even though some of these methods

are still used, fluorogenic agents like NBD, have the problem of not being stable and sometimes producing background interfering luminescence [13].

Fluorescent physical treatments (fluorescent dusting powders) were also considered for fingerprint enhancement. The first attempts, in late 1980s, were powders mainly composed of transition metals. However, these materials were only applicable on smooth surfaces, and so presented limitations [13]. The next approaches tested were with lanthanide-based powders. These compounds presented great advantages, such as large stoke shifts, long luminescence lifetime and forming differently fluorescent products when different ligands are used[1]. Europium (Eu^{3+}) and Terbium (Tb^{3+}) are the most common ions used in fingerprint development, which emit red and green fluorescence, respectively, and absorb in ultraviolet region of the spectrum [11,14,15]. This large difference between absorption and emission bands makes it easier to eliminate background fluorescence interference [16].

Recently, new types of fluorescent nanopowders have been tested to enhance the rate of recoverable fingerprints in a crime scene, such as quantum dots (QDs)[16]. QDs are largely known for their fluorescent properties. Some of the benefits of this nanoparticles are that they have wide excitation spectra, are not as sensitive to photobleaching as other organic fluorophores, display improved selectivity and high fluorescent quantum yields [16–19]. A large number of works that have been published focus on the use of CdTe [19–21] and CdS [22,23] based QDs. All these research groups demonstrated that quantum dots are useful in fingerprint development, giving the marks strong contrast and good resolution. Nevertheless, there have been some concerns about the cytotoxic effects of these compounds, particularly the Cd-based quantum dots [17,23].

3.2   Carbon-dots based nanopowders

3.2.1   aC-dots

By systematically adjusting the pyrolysis conditions of carbon-rich precursors, nanoparticles with different properties are obtained. Following this procedure (Section 2.1), self-passivation of C-dots is achieved, as they are readily dispersible in water. At 180ºC, it has been concluded that an aC-dots precursor would be synthesized

showing high quantum yield (~50%). Further experiments characterized this fluorescent precursor (Figure 3-2 a) as displaying a maximum emission intensity at ~460 nm when excited at 375 nm. Higher temperatures would decompose these molecules and gradually form aC-dots. At 230ºC, aC-dots and the organic precursor reached equilibrium, hence the temperature chosen for the reaction – in order to have both fluorescent contributions. The temperature also affects the size of the obtained materials. TEM images (Figure 3-2 b and c) show that at 230°C NP's are 20 nm whereas at 300°C particles possess sizes of roughly 10nm, which is consistent with C-dots reports derived from pyrolytic routes[24].
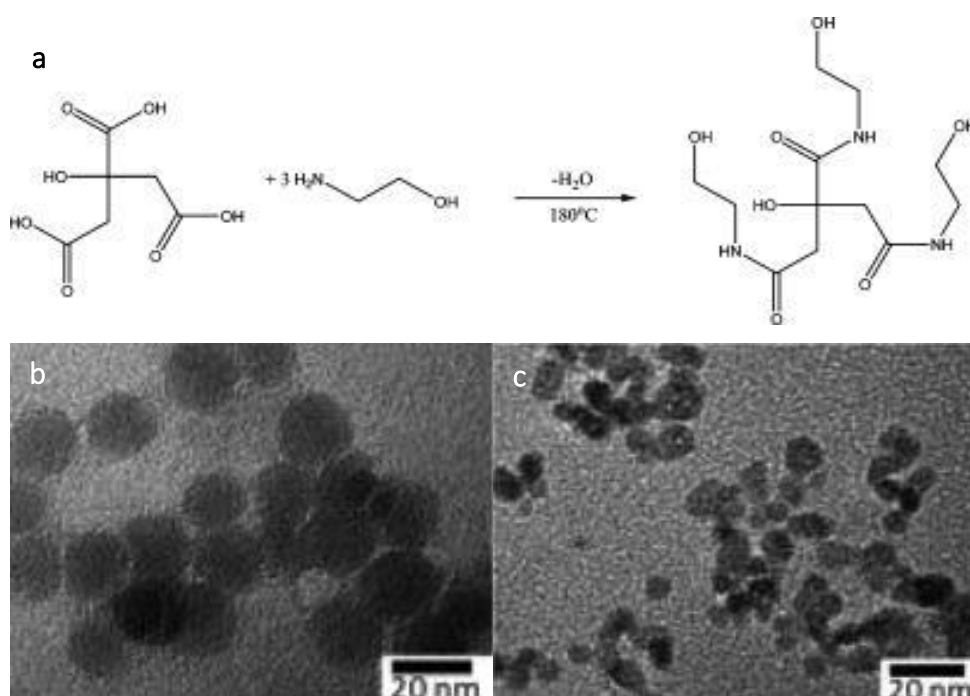
Figure 3-2– a) Proposed reaction for the formation of the fluorescent precursor at 180ºC, b) and c) TEM images of aC-dots produced by pyrolysis of CAEA at 230°C and 300°C, respectively. Adapted from Ref. 24.

If a too high concentration were to be used, variable results would be obtained as self-quenching phenomena occurs (particle-to-particle interactions), thus it was necessary to find that pre-saturation concentration. To that end, a series of concentrations were analysed on a spectrofluorometer at a fixed excitation wavelength of 380nm. Concentrations used were 2.5, 5, 10, 15, 25 and 50µg/mL, and results obtained can be seen in Figure 3-3 .
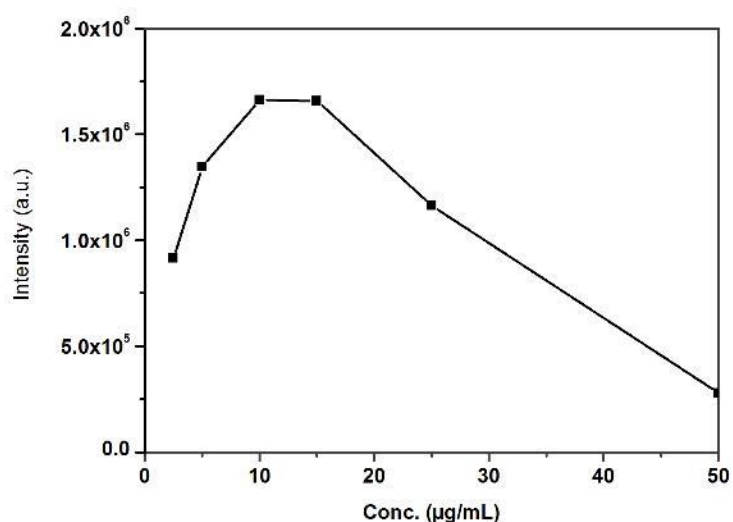
Figure 3-3 – Emission intensity at 465nm of different concentration of aC-dots solutions, under 380nm excitation.

Considering the results obtained in Figure 3-3, a 13 μg/mL sample of aC-dots was prepared and their UV absorbance and fluorescence properties were analysed. C-dots show a typical broad absorption in the UV region, with a tail which extends to the visible region, as can be seen in Figure 3-4. The peak at 250 nm is frequently ascribed to aromatic C-C bonds π- π* transitions and the broad peak at ~375 nm is attributed to C=O bonds *n*- π* transitions[25].

By analysing Figure 3-5, it is possible to distinguish two phenomena occurring: the contribution of the fluorophore producing a fixed wavelength emission at ~460nm (exc. wavelengths of 290 nm, 320 nm, 350 nm and 380 nm – black line on Figure 3-5), and an excitation-dependent emission at higher wavelengths.

87
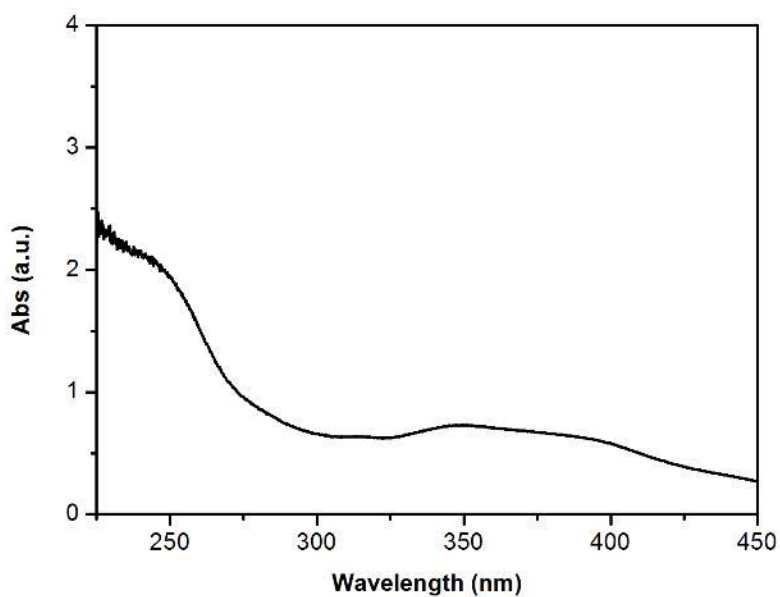
Figure 3-4 – UV-Vis absorption spectrum of aC-dots.
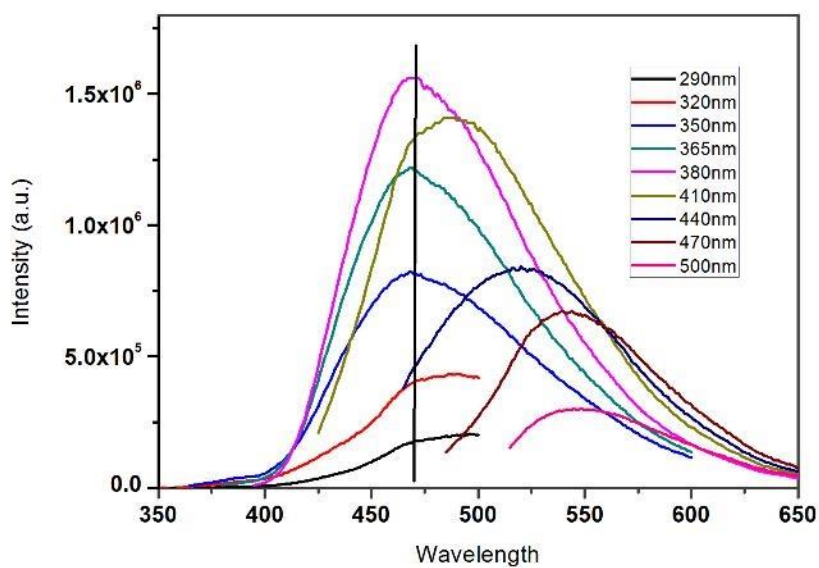
Figure 3-5 – PL emission spectra of aC-dots aqueous solution under different excitation wavelengths.

In Figure 3-6, it is possible to see the excitation-dependent emission phenomenon, as C-dots solutions fluorescence changes when interacting with different wavelength sources.

88
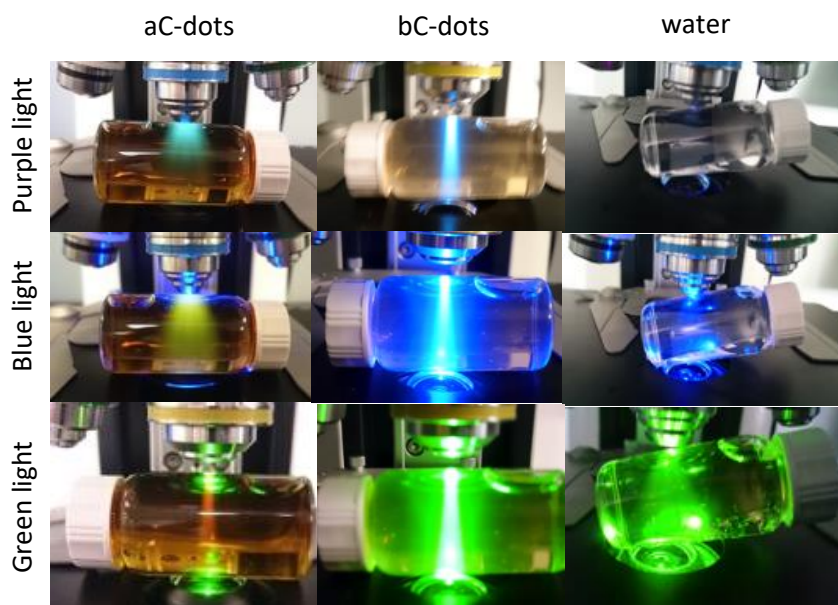
Figure 3-6 – Comparison between solutions of aC-dots, bC-dots, and water (from left to right) under different fluorescent lights: purple, cyan blue and green (from top to bottom).

Nanoparticles have a known tendency to form clusters in the micrometre scale, therefore C-dots powders didn't have any fluorescence under UV-light after freeze-drying the previously fluorescent solution (Figure 3-7).
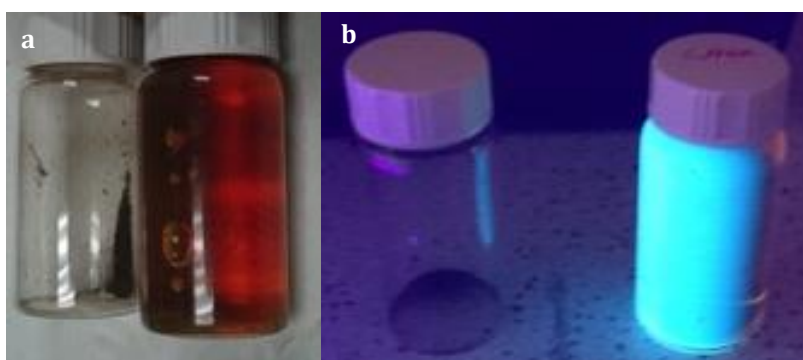
Figure 3-7 – aC-dots powder and aC-dots solution under a) white light, and under b) UV light.

3.2.2 bC-dots

Oxidation is an important step for the synthesis of bC-dots, as these procedures tend to generate rather larger particles with weak PL emission and limited water solubility. Refluxing under strong acid, tends to break these clusters and form polar groups[26], resulting in spherical particles of around 30 nm (Figure 3-8 a and b).
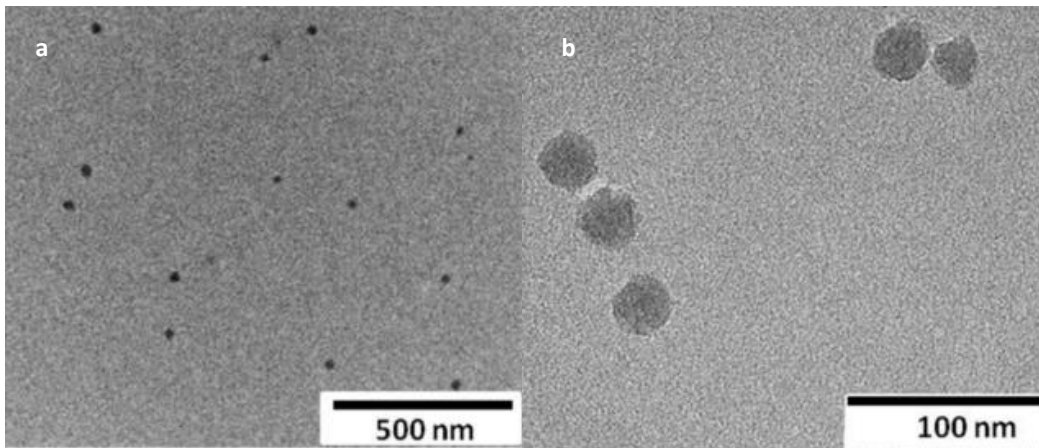
Figure 3-8 – TEM images of bC-dots with different magnifications. Adapted from Ref. 27.

By analysing the fluorescence spectra (Figure 3-9) the excitation-dependent emission is maintained, however, there is no longer the fixed high intensity emission peak characteristic to the fluorophore (λ_{max} = ~460 nm). This is known to influence these nanoparticles' overall fluorescence, and thus when investigated in a fluorescence microscope it was noticeable a decrease in the fluorescence intensity.
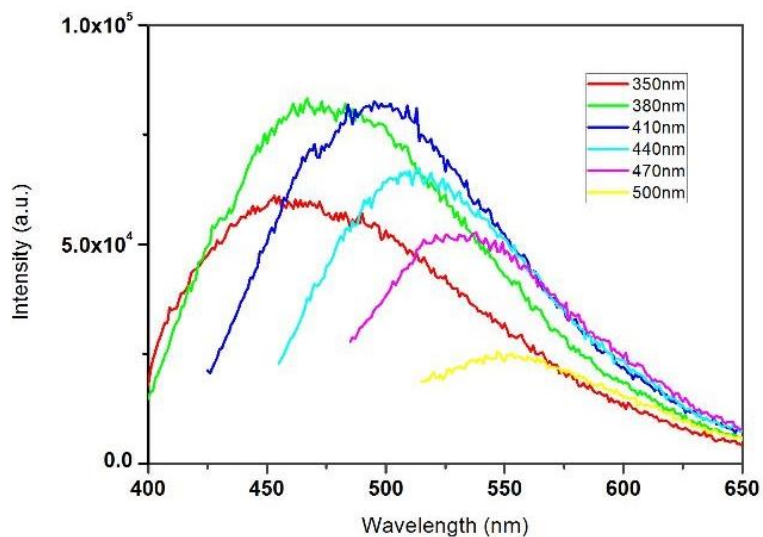
Figure 3-9 – Fluorescence spectra of bC-dots aqueous solution under different excitation wavelengths.

As fluorescence was considerable lower in bC-dots, due to the absence of fluorophore, they were not considered for fingerprint recovery experiments.

3.2.3 Hybrid powders

The fact that C-dots powder do not show optimal solid-state fluorescent properties has been already reported [28,29] and has been mainly attributed to particle-particle re-absorption effects. To overcome this, the possibility of diluting C-dots powders in different materials, and thus preserve their fluorescence properties, was assessed. At low weight percentages, C-dots quenching effects would be suppressed, as particle-to-particle interactions would be minimized.

The addition of the white powders, SiO_2 and Lap, had no significant influence on the aC-dots emission spectra (Figure 3-10 and Figure 3-11). TiO_2, on the other hand, is known to have optical properties (common ingredient in sunscreens to absorb UV radiation), so a difference in the emission spectra was expected, Figure 3-10 c, and Figure 3-11 (green line). UV-Vis spectra showed that the major optical properties were mainly from C-dots contribution, as no significant changes were observed before and after the addition of Laponite and SiO_2 (Figure 3-12 a and b, respectively). aC-dots/TiO_2, however, displayed a more intense peak at ~340nm (Figure 3-12 c), which is known to be a TiO_2 contribution[30].
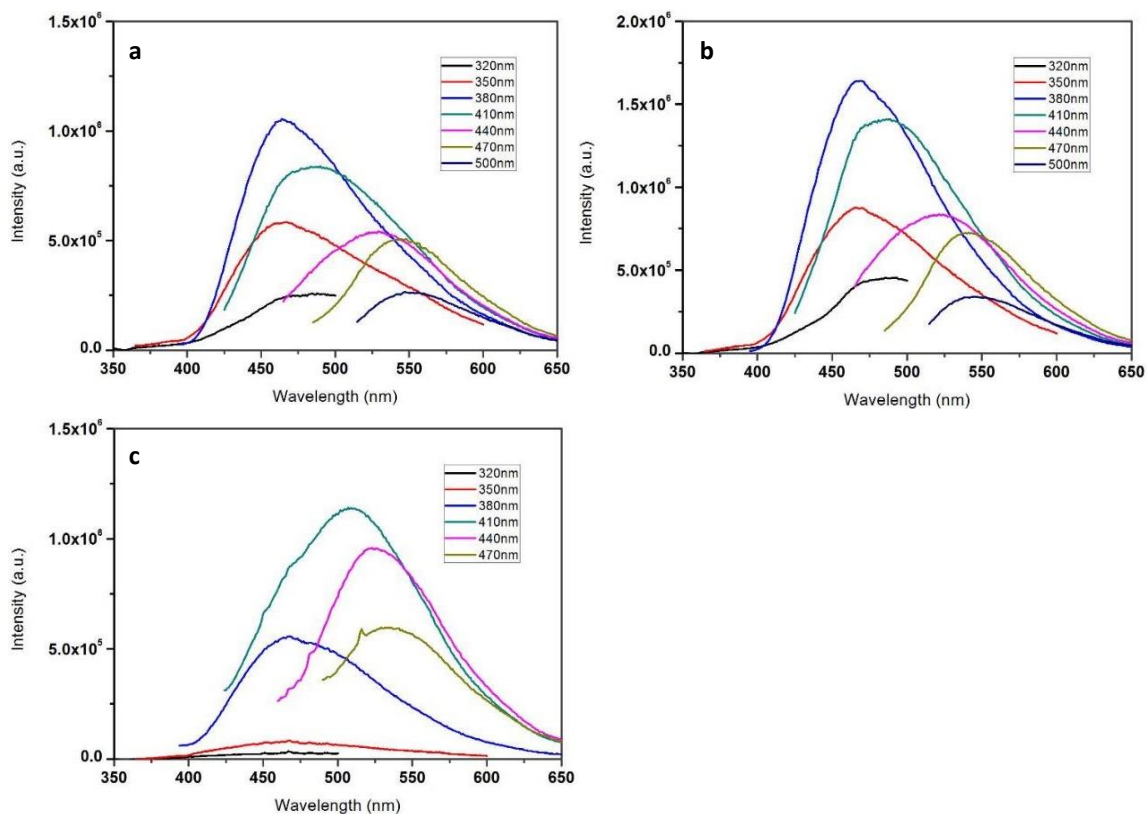
Figure 3-10 – aC-dots/SiO₂ (a), aC-dots/Lap (b) and aC-dots/TiO₂ (c) in a 1:150 weight ratio of C-dots in white powder fluorescence spectra under different excitation wavelengths.
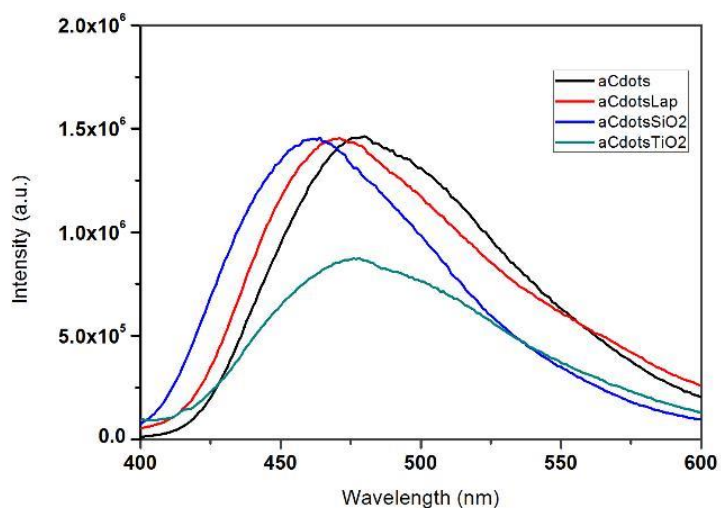
Figure 3-11 – Fluorescence spectra of aC-dots, aC-dots/SiO₂, aC-dots/TIO2 and aC-dots/Lap, showing no significant influence after the addition of other powders (apart from TiO2). Excitation wavelength used was 380nm.
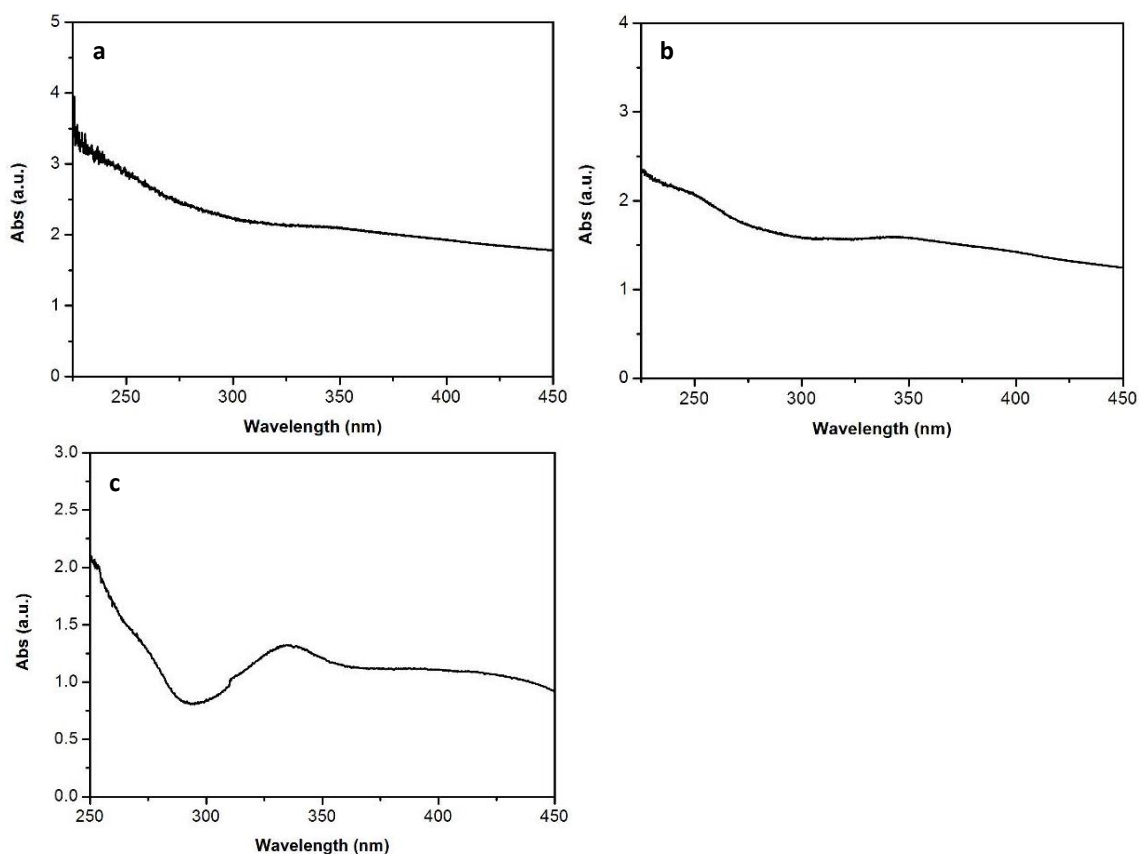
Figure 3-12 – UV-Vis absorption spectra of aC-dots/Lap (a), aC-dots/SiO$_2$ (b) and aC-dots/TiO$_2$ (c).

The hybrid powders obtained after freeze-drying (Figure 3-13) were investigated on a fluorescent microscope and showed excitation-dependent properties (Figure 3-14). Solid-state analysis (Figure 3-15) supported the fact that these powders were successfully imparted with fluorescence properties, even with minimal amounts of C-dots (1:150 weight ratio).

Figure 3-13 – Powders obtained after freeze-drying: a) aC-dots/SiO$_2$, b) aC-dots/TiO2 and c) aC-dots/Laponite.
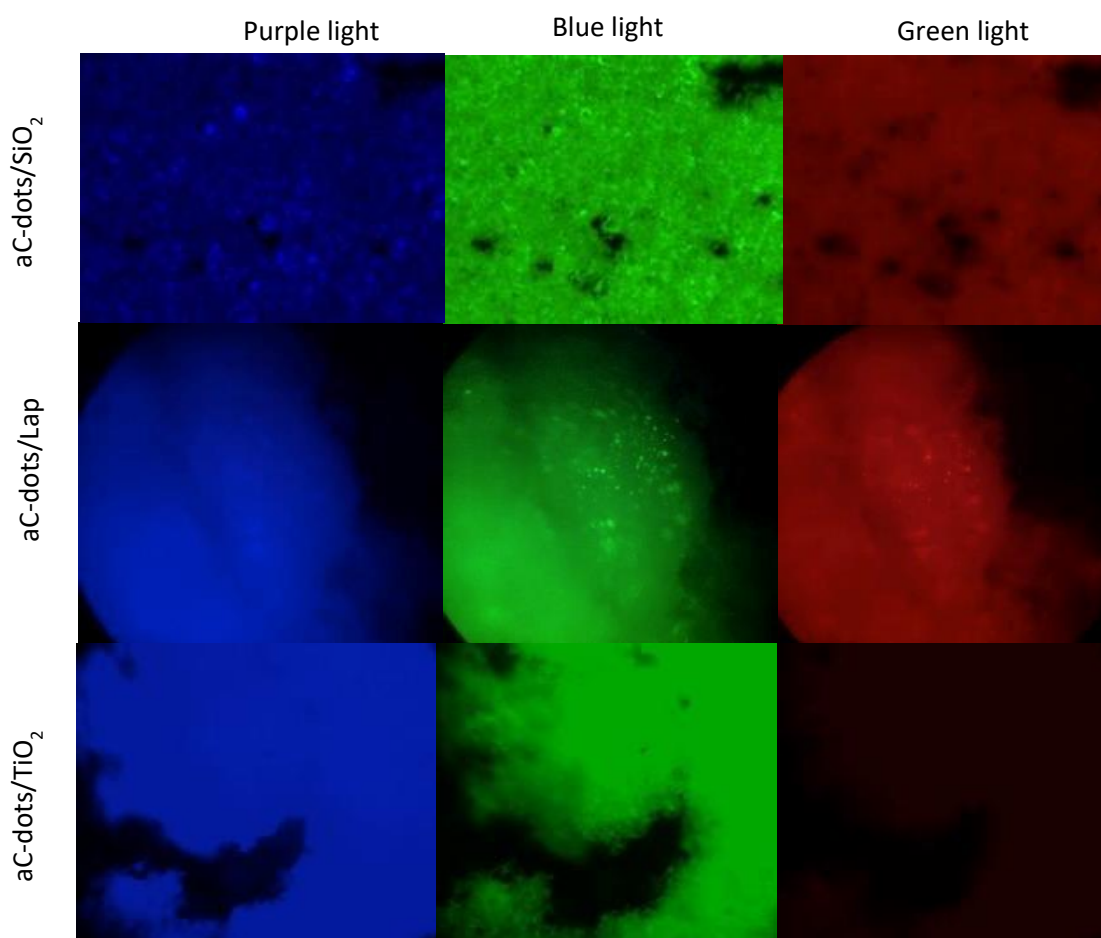
Figure 3-14 – aC-dots: -SiO₂, - Lap, - TiO2 investigated in a fluorescent microscope with different excitation sources.
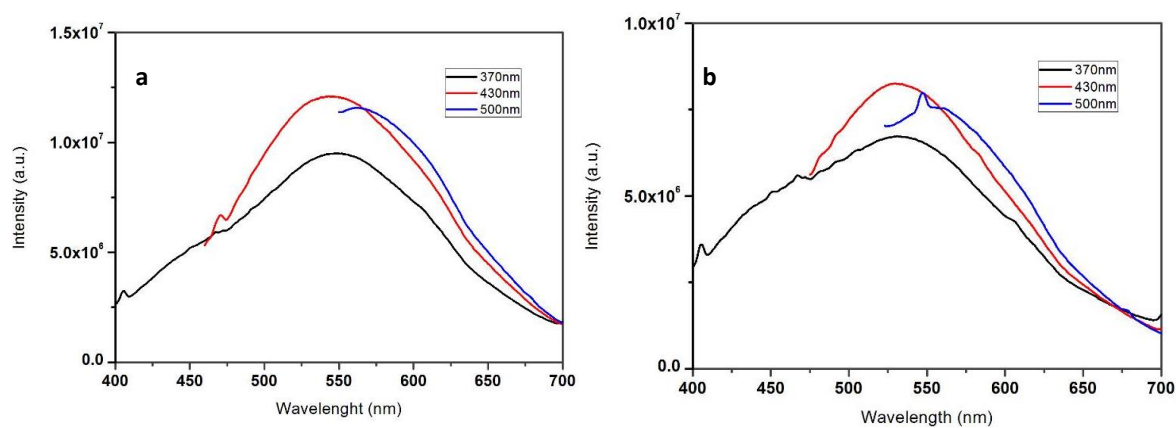
Figure 3-15 - Solid-state emission spectra of aC-dots/SiO₂ (a) and aC-dots/Lap (b) under different excitation wavelengths.

3.2.4 Fingerprints recovery

Fingerprints were successfully developed with good resolution for the powder formulations. The excitation-dependent properties of C-dots also rendered a multi-coloured fingerprint when excited with different wavelength lasers (Figure 3-16 and Figure 3-17).
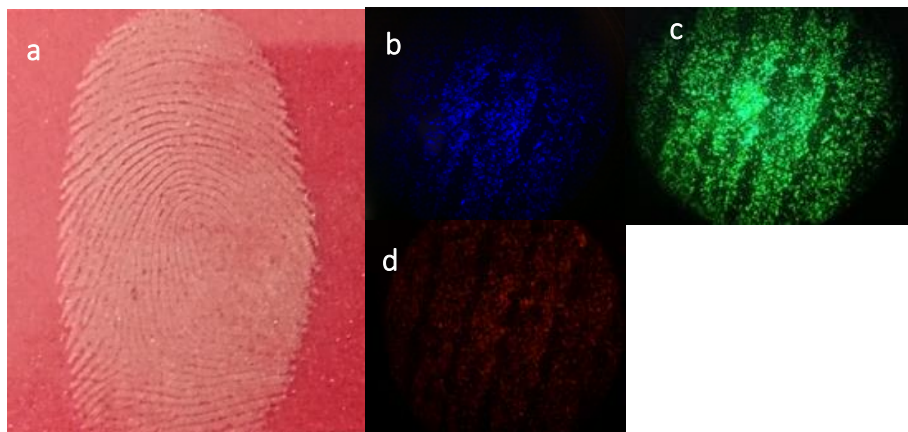
Figure 3-16 – a) Fingerprint on a glass slide developed with aC-dots/SiO$_2$, and b), c) and d) on a fluorescent microscope (100x magnification) under different excitation lights.
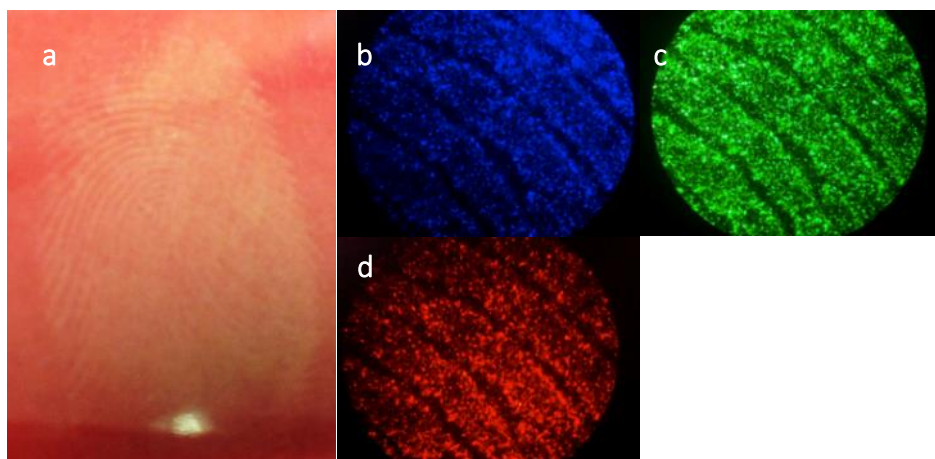
Figure 3-17 – a) Fingerprint on a glass slide developed with aC-dots/Lap, and b), c) and d) on a fluorescent microscope (100x magnification) under different excitation lights.

The main benefit from the above formulations is that this procedure would, theoretically, work with most powders, as long as they do not absorb radiation, like TiO$_2$. To further test this assumption, a mixture of a commercial white fingerprint powder (WFP) and aC-dots/Lap (~0.3% of C-dots) was used to recover fingerprints in a glass slide. It was proved that C-dots can be used as top-up materials with

conventional fingerprint powders, as the addition of low quantities was enough to "illuminate" the entire material (Figure 3-18).
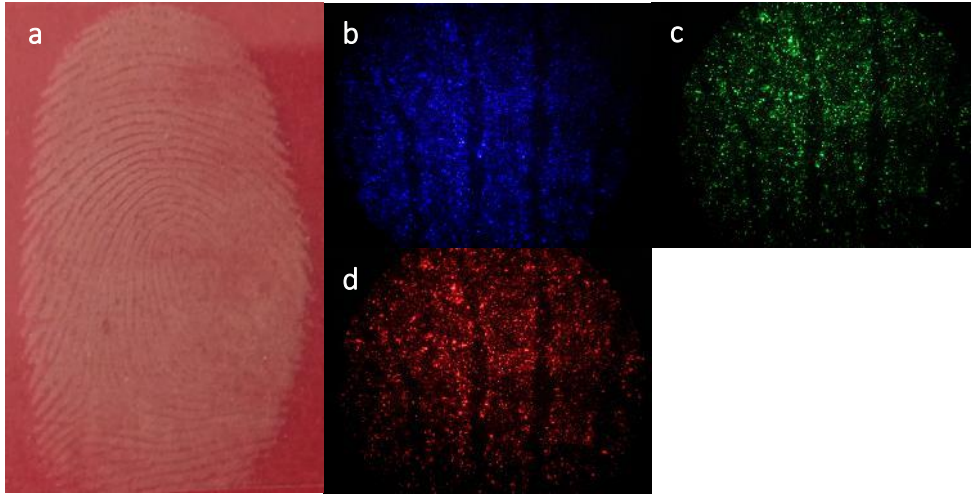
Figure 3-18 – a) Fingerprint on a glass slide developed with aC-dots/Lap and WFP, and b), c) and d) on a fluorescent microscope (100x magnification) under different excitation lights.

The number of level 2 details identified (details index in Table 1) was used as the parameter to assess the quality of the developed powders. AFIS results showed that both aC-dots/SiO$_2$ and aC-dots/Lap were able to successfully reveal fingerprints as the details recovered were on the same level of the commercial WFP (Table 1).

Table 1 – Fingerprints developed with the different powders formulations and respective AFIS results with details count (glass surface was used).

Fingerprint developed	Powder composition	Details Index
	White fingerprint powder (commercial)	65
	aC-dots/Lap	66
	aC-dots/SiO$_2$	71
	aC-dots/SiO$_2$ + WFP	59
	Laponite (no c-dots)	45
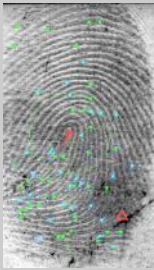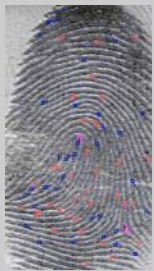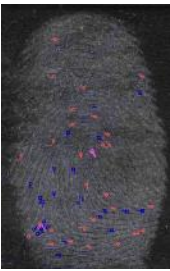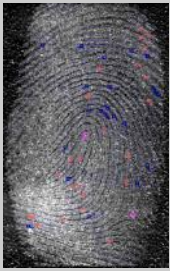
To test the versatility of the prepared hybrid powders, fingerprints were deposited on different surfaces. In Figure 3-19 is depicted a fingerprint that was successfully revealed on a metal surface. Fluorescent magnified pictures show a clearly defined bifurcation, one of the many minutiae that can help to identify an individual in forensic investigations.
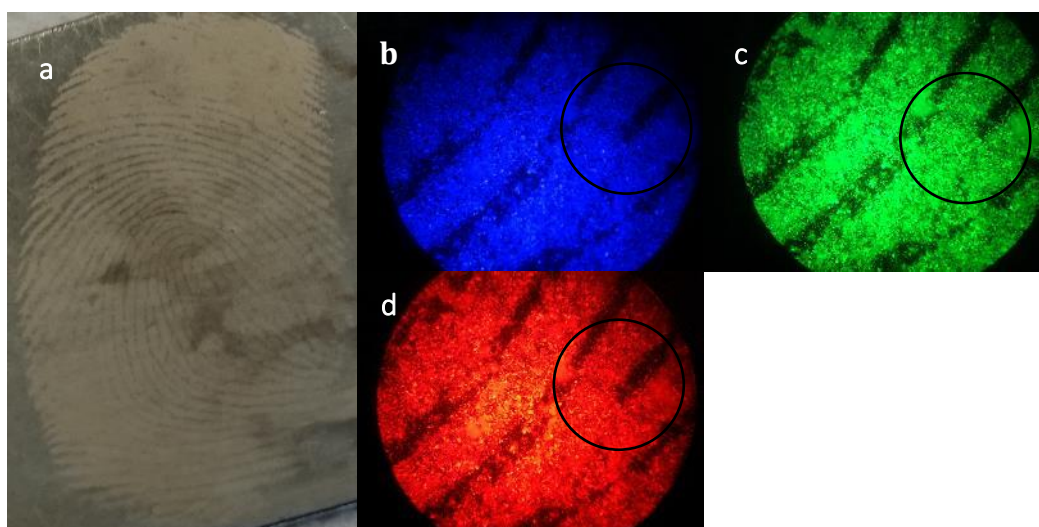
Figure 3-19 – a) Fingerprint deposited on a metal surface developed with aC-dots/Laponite, and b), c) and d) under different excitation wavelengths.

Another surface tested was a soft drink foil (Dr Pepper bottle foil). The bottle used was selected as it had a multi-coloured pattern and showed a strongly coloured background. With the as-prepared hybrid powders, under white and green light it is not possible to discern the ridges from the background (Figure 3-20 b and e, respectively), whereas with UV and blue light well resolved features can be seen (Figure 3-20 c and d). In addition, a fingerprint on the same surface was revealed with white fingerprint powder and it wasn't possible to distinguish it from the background when exposed to white or fluorescent lights (Figure 3-21).
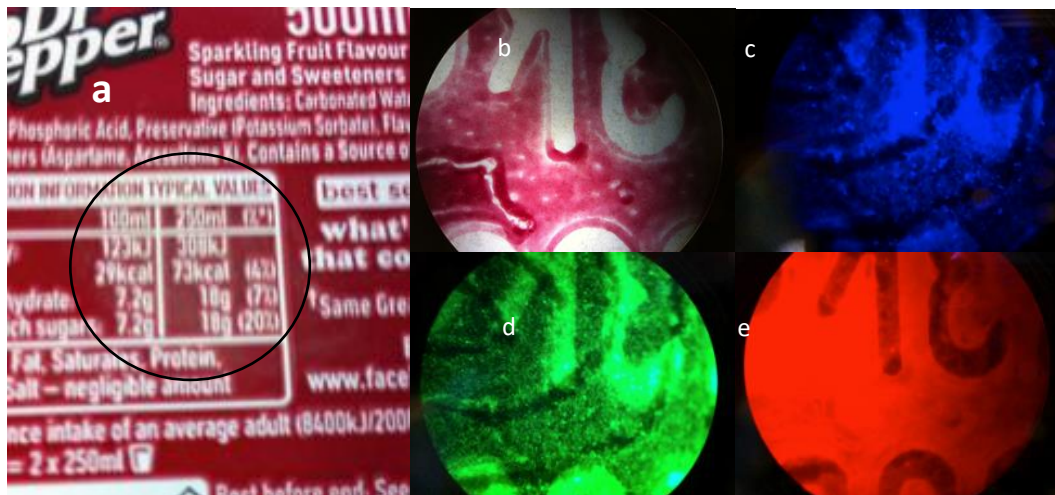
Figure 3-20 – a) Fingerprint deposited on a bottle drink foil developed with aC-dots/SiO₂, magnified 100x under white light (b), and b), c) and d) different fluorescent lights.
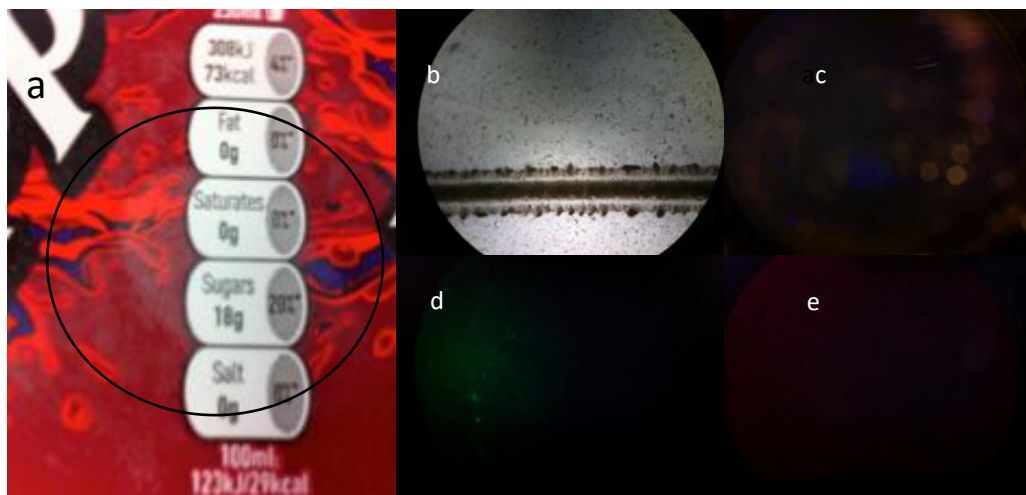
Figure 3-21 – a) Fingerprint deposited on a bottle drink foil developed with white fingerprint commercial powder, b) magnified 100x under white light, and b), c) and d) different fluorescent lights.

3.3 C-SiO₂

The main advantage of these powders is that they don't need any further treatment or dispersion as the incorporation of C-dots on the Silica nanoparticles' surface allowed for the prevention of particle-to-particle interactions and, consequent, fluorescence quenching. After freeze-drying, these powders were tested as fingerprint physical developers in different surfaces like a standard computer mouse, rough plastic surface and metal surface (Figure 3-22 b, c and d, respectively) and showed good contrast and resolution for forensic investigation standards. Furthermore, a direct assessment

obtained from a split mark comparison between a latent mark developed with C-SiO$_2$ and with an Instant White Fingerprint Powder (commercial) (Figure 3-22 a) revealed that the former affords clearer and more resolved fingerprints which is further supported by AFIS analysis. Figure 3-23 shows a minutia count of 73 for the C-SiO$_2$ which was even higher than that of a commonly used fingerprint powder (same as used in previous chapter, WFP).
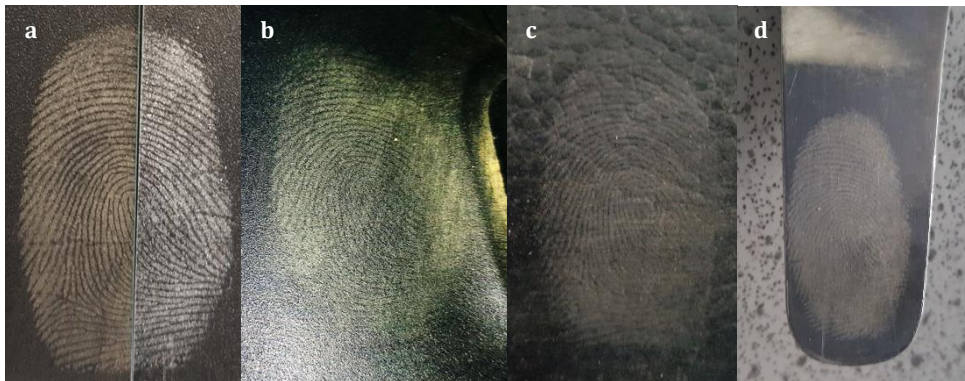
Figure 3-22 – a) Split fingerprint on glass slides developed with C-SiO$_2$ (left) and White fingerprint powder (right), and fingerprints developed on a variety of surfaces: b) computer mouse (under UV light), c) deposited on a rough plastic surface (white light) and d) deposited on a metal surface (white light).
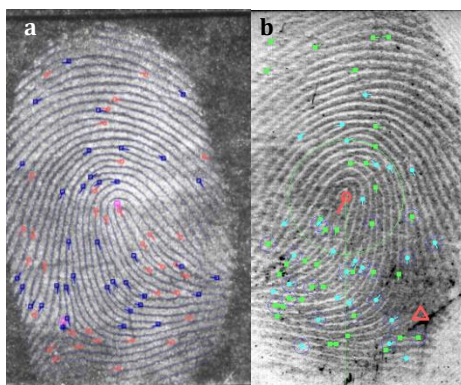
Figure 3-23 - AFIS analysis of a fingerprint developed with a) C-SiO$_2$ nanoparticles and b) commercial WFP showing 73 and 65 minutiae, respectively.

These nano-powders have also been noted to preserve the colour tuneable properties of C-dots which may be important for strongly coloured or multi-patterned surfaces. In Figure 3-24 a series of microscopic pictures were *photoshoped* together in order to

give a better idea of how these powders behave when excited under different wavelength lasers. A diverse range of minutiae may be identified from those microscopic images (*e.g.* bifurcations, ridge ending, pores…) which further demonstrates the enhanced resolution of these nanopowders.

Due to their large Stokes-shifts and colour tuneability, these powders may prove to be an important tool on suppressing any problems that would arise from colourful, shiny or even fluorescent backgrounds. Figure 3-25 is a demonstration of this property, as a green fluorescent background was chosen as the substrate and when exposed to a green light (445 nm) a lower resolution fingerprint was obtained but incidentally under UV light a considerably better resolved fingerprint was revealed.
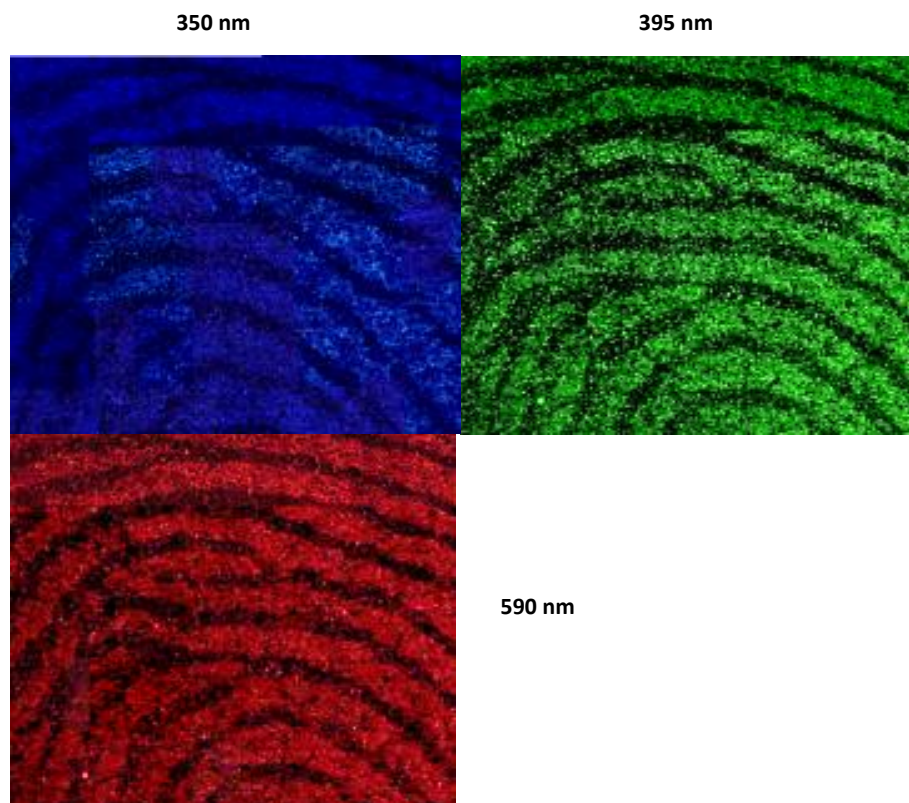
Figure 3-24 – Fluorescent microscopy images of a fingerprint developed with the C-SiO$_2$ nanopowders.

Laser	365 nm	410 nm	445 nm	475 nm	520 nm
Filter	400 nm	455 nm	45 5nm	495 nm	530 nm
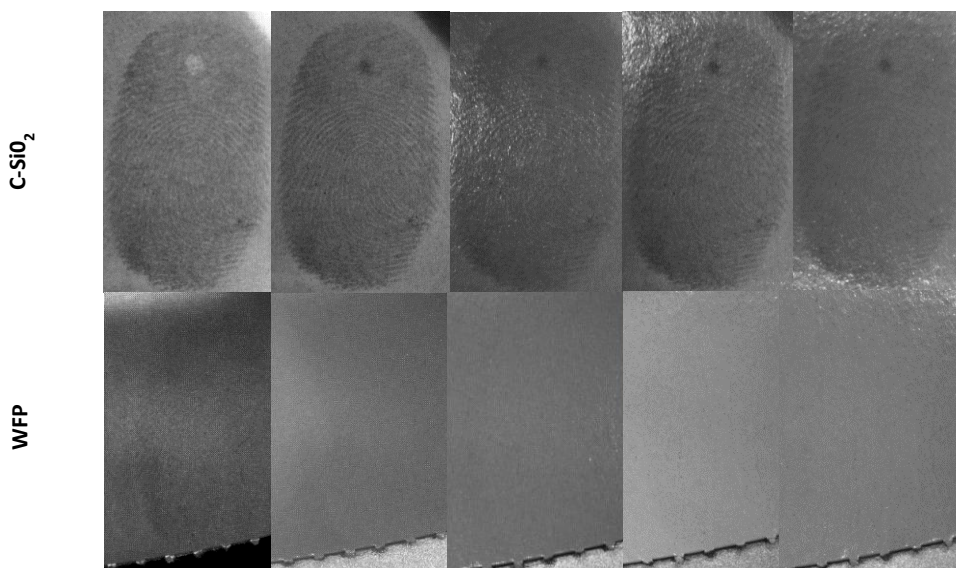
Figure 3-25 – Comparison between the C-SiO$_2$ (upper images) and a commercial instant white fingerprint powder on a glass slide investigated on a crime lite imager.

3.4 Conclusion

In summary, it has been demonstrated for the first time the use of C-dots to recover latent fingerprints. Environmentally benign, low toxicity and cheap synthetic routes were used to prepare C-dots from carbon rich precursors (Citric acid and crude biomass). The presence of amines (ethanolamine and urea) during pyrolysis proved to be essential for having nanoparticles with higher quantum yields, when compared to grass derived C-dots. However, as C-dots tend to display quenching effects when in solid-state, they were dispersed into other nanopowders (SiO$_2$, TiO$_2$ and Laponite clay), in a 1:150 ratio. This would keep C-dots as PL cores and provide with the necessary flowabilty to be used as fingerprint developers.

In terms of the C-SiO$_2$ nanopowders, these showed similar results when compared to the other here suggested formulations, with the added advantage that no further dilution in white powders is required, since the silica nanoparticles prevent the quenching effects arising from C-dots' particle-to-particle interactions.

Fingerprints were recovered on surfaces with different characteristics, namely glass slides, metal surfaces, soda bottle foil, plastic and rough surfaces, showing the versatile nature of these nanohybrids. Not only did they work as standard fingerprint powders (AFIS results were similar to a commercial fingerprint powder), but their PL properties also showed great potential. Even with minor amounts of carbogenic nanoparticles, the hybrid powders rendered colour-tuneable fingerprints, which is of great contrast importance, particularly in the case of multi-coloured or strongly coloured surfaces. As a result, C-dots allow forensic investigators to carry only one powder to a crime scene, and once applied they can take any colour it's needed for better distinction from the background, whereas with other powders if the most suitable one is not applied first, the fingerprint is already compromised.

3.5 References

1. Sodhi, G. S. S. & Kaur, J. Powder method for detecting latent fingerprints: A review. Forensic Sci. Int. 120, 172–76 (2001).

2. Wilshire, B. Advances in fingerprint detection. Endeavour 9327, 12–15 (1996).

3. Girod, A., Ramotowski, R. & Weyermann, C. Composition of fingermark residue: a qualitative and quantitative review. Forensic Sci. Int. 223, 10–24 (2012).

4. Godsey, M. The wrongful convictions blog (Access date: 10/03/16).

5. Thomas, G. et al. The physics of fingerprints and their detection. J. Phys. E. 11, 722–31 (1978).

6. Knowles, A. M. Aspects of physicochemical methods for the detection of latent fingerprints. J. physics. E, Sci. instruments 11, 713–21 (1978).

7. Bandey, H. Fingerprint powders guidelines. Home Off. Sci. Dev. Branch 09/07, 1–4 (2007).

8. Menzel, E. R., Burt, J. A., Sinor, T., Tubach-Ley, W. B. & Jordan, K. J. Laser Detection of Latent Fingerprints: Treatment with Glue Containing Cyanoacrylate Ester. J. Forensic Sci. 28, 307–17 (1983).

9. Karlinszky, L. & Harkai, G. Detection of Latent Fingerprints: Application of Cyanoacrylate for the inside of Cars. Forensic Sci. Int. 46, 29–30 (1990).

10. Kobus, H. J., Warrener, R. N. & Stoilovic, M. Two simple staining procedures which improve the contrast and ridge detail of fingerprints developed with 'Super Glue'(cyanoacrylate ester). Forensic Sci. Int. 23, 233–40 (1983).

11. Herod, D. W. & Menzel, E. R. Laser detection of latent fingerprints: ninhydrin followed by zinc chloride. J. Forensic Sci. 27, 513–18 (1982).

12. Salares, V. R., Eves, C. R. & Carey, P. R. On the detection of fingerprints by laser excited luminescence. Forensic Sci. Int. 14, 229–37 (1979).

13. Lee, H. C. & Gaensslen, R. E. Advances in Fingerprint Technology. (CRC Press, 2001).

14. Parnell, A. J. Lanthanide Luminescence and its Applications in Forensic Science. 1994, (The University of Waikato, 2011).

15. Saif, M. Synthesis of down conversion, high luminescent nano-phosphor materials based on new developed Ln3+:Y2Zr2O7/SiO2 for latent fingerprint application. J. Lumin. 135, 187–95 (2013).

16. Menzel, E. R. Recent advances in photoluminescence detection of fingerprints. Sci. World J. 1, 498–509 (2001).

17. Gao, F. et al. Application of core–shell-structured CdTe@SiO2 quantum dots synthesized via a facile solution method for improving latent fingerprint detection. J. Nanoparticle Res. 14, 1-11 (2012).

18. Becue, A., Moret, S., Champod, C. & Margot, P. Use of quantum dots in aqueous solution to detect blood fingermarks on non-porous surfaces. Forensic Sci. Int. 191, 36–41 (2009).

19. Yu, X. et al. Application of mercaptosuccinic acid capped CdTe quantum dots for latent fingermark development. Forensic Sci. Int. 231, 125–30 (2013).

20. Cai, K., Yang, R., Wang, Y., Yu, X. & Liu, J. Super fast detection of latent fingerprints with water soluble CdTe quantum dots. Forensic Sci. Int. 226, 240–43 (2013).

21. Liu, J., Shi, Z., Yu, Y., Yang, R. & Zuo, S. Water-soluble multicolored fluorescent CdTe quantum dots: Synthesis and application for fingerprint developing. J. Colloid Interface Sci. 342, 278–82 (2010).

22. Algarra, M. et al. CdS nanocomposites assembled in porous phosphate heterostructures for fingerprint detection. Opt. Mater. (Amst). 33, 893–98 (2011).

23. Dilag, J., Kobus, H. & Ellis, A. V. CdS/polymer nanocomposites synthesized via surface initiated RAFT polymerization for the fluorescent detection of latent fingermarks. Trends Anal. Chem. 228, 105–14 (2013).

24. Krysmann, M. J., Kelarakis, A., Dallas, P. & Giannelis, E. P. Formation mechanism of carbogenic nanoparticles with dual photoluminescence emission. J. Am. Chem. Soc. 134, 747–50 (2012).

25.   Zhu, S. et al. The photoluminescence mechanism in carbon dots (graphene quantum dots, carbon nanodots, and polymer dots): current state and future perspective. Nano Res. 8, 355–81 (2015).

26.   Kelarakis, A. From highly graphitic to amorphous carbon dots: A critical review. MRS Energy Sustain. 1, 1–15 (2014).

27.   Krysmann, M. J., Kelarakis, A. & Giannelis, E. P. Photoluminescent carbogenic nanoparticles directly derived from crude biomass. Green Chem. 14, 3141–45 (2012).

28.   Qu, S., Wang, X., Lu, Q., Liu, X. & Wang, L. A biocompatible fluorescent ink based on water-soluble luminescent carbon nanodots. Angew. Chem. Int. Ed. Engl. 51, 12215–18 (2012).

29.   Zhu, S. et al. Highly photoluminescent carbon dots for multicolor patterning, sensors, and bioimaging. Angew. Chemie - Int. Ed. 52, 3953–57 (2013).

30.   Yang, G., Jiang, Z., Shi, H., Xiao, T. & Yan, Z. Preparation of highly visible-light active N-doped TiO2 photocatalyst. J. Mater. Chem. 20, 5301–09 (2010).

4 Carbogenically-coated silica nanoparticles and their anti-counterfeit applications

4.1 Introduction

4.1.1 Anti-counterfeit research background

Counterfeiting, the act of making an exact or partial imitation of something valuable with the intent to deceive or defraud, is a crime that affects all the different fields of industry and, inevitably, has a severe effect in the global economy[1,2]. According to the Worlds Customs Organization around 6% of global goods are potentially counterfeit[1]. This criminal act can have an impact in research sectors, impeding the progress of society, but also in art and pharmaceutical industry[2]. The latter can be of particular concern considering that it's not always the case of a complete replication of drugs, but also changing their chemistry and/or diluting it which can lead to serious health problems. In a study conducted recently, it was estimated that about 15% of drugs currently sold in the world are counterfeit and that in developing countries figures may be as high as 50% of total drugs sold. [2–4]

The current most reliable strategies for the detection of counterfeited drugs follow a combination of two methods: colourimetric essays and analytical techniques, such as high-pressure liquid chromatography (HPLC), mass spectrometry (MS), nuclear magnetic resonance (NMR), etc. Colourimetric tests, are also known as screening tests due to their fast and qualitative nature. They tend to be cheap, portable and easy to apply and read. However, they are usually only able to inform on whether, or not, a specific moiety or compound is present, which firstly: may lead to numerous false negatives/positives; and secondly: does not provide information regarding the quantity of active ingredient, which is one of the most common types of tampering in counterfeited drugs. It comes as no surprise then, that samples being investigated, need to be further analysed on more powerful and informative techniques. Analytical techniques tend to leave little margin for error and have extremely low limits of detection, but their operation requires far more proficient personnel, tend to have higher costs of running and maintenance, and ultimately are rendered unviable for routine tests, which drastically decrease the number of assessed products.[5,6]

It is then essential the design of new, time-efficient methodologies that are able to certify the authenticity of original products, without prohibitive costs and by using toxic-free materials. Several research groups have tried to provide the means to solve these issues, with some of the most significant examples being computer-based hologram graphics[7,8], which is based on the recognition of computer generated graphics, Laser Surface Authentication[9], which analyses the pattern of naturally-occurring imperfections of papers through laser speckle in order to give an authentication means without having to make any further modification to the surface; and radio frequency identification (RFID)[10], the use of radio frequency waves for the automatic identification of objects. However, these are frequently not robust enough or far too expensive, and thus research efforts have focused on presenting more reliable approaches to this problem.

As with many other fields, nanomaterials allowed for a new dimension of tools. On one study, conducted by Demirok et al.[11], a nanowire-based barcode was created using a ternary alloy composed of Ni, In and Zn. The superimposing character of the nanowires created a multi-layered pattern which increased the level of complexity of the system. The decoding of this system is performed using a multi-readout approach, which consists of X-ray fluorescence analysis, square-wave voltammetry and vibrating sample magnetometry, as shown in Figure 4-1, thus allowing for a very specific fingerprinting of the images created. The main problem with this method was the high complexity and costs involved with these techniques.
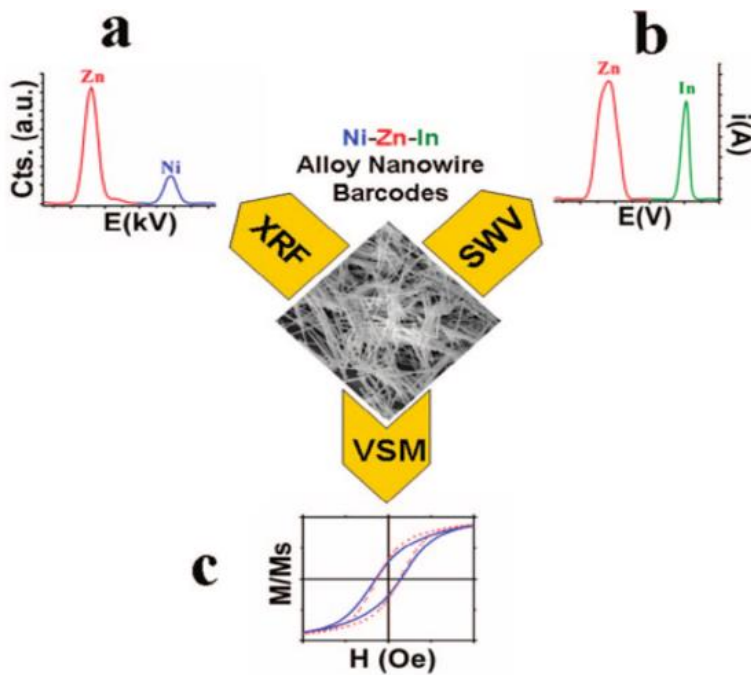
Figure 4-1 – Illustration of the multi-readout method for the unique identification of the ternary alloys nanowires. Reprinted from Ref. 11.

Quantum-dots have also been suggested as alternatives due to their high quantum yields and stable fluorescence. Lu et al.[12] suggested the use of polyethyleneimine branched quantum dots to create rewritable fluorescent patterns that could be used as memory chips for security purposes. The authors demonstrated that these systems could be used for anti-counterfeit purposes and that in the dark they maintained about 60% of their original fluorescence after 30 days of being prepared. Additionally, by tuning the size of the quantum dots, they created a two coloured (red and green) binary code that could be used as chips for securely encoded messages (Figure 4-2 a). Nevertheless, these nanoparticles show high susceptibility to photo-oxidation which lead to the fluorescent being reduced to zero after only 5 days under room light, as demonstrated in Figure 4-2 b. Alternatively, Sun and co-workers[13] developed printable oils containing ZnO quantum dots with lanthanum enhanced fluorescence. The incorporation of La allowed for an impressive improvement in the quantum yield (from 30% to 78%) and displayed a versatile range of application methods, such as dip-pen writing, screen-printing, gravure/letter-press printing, etc.
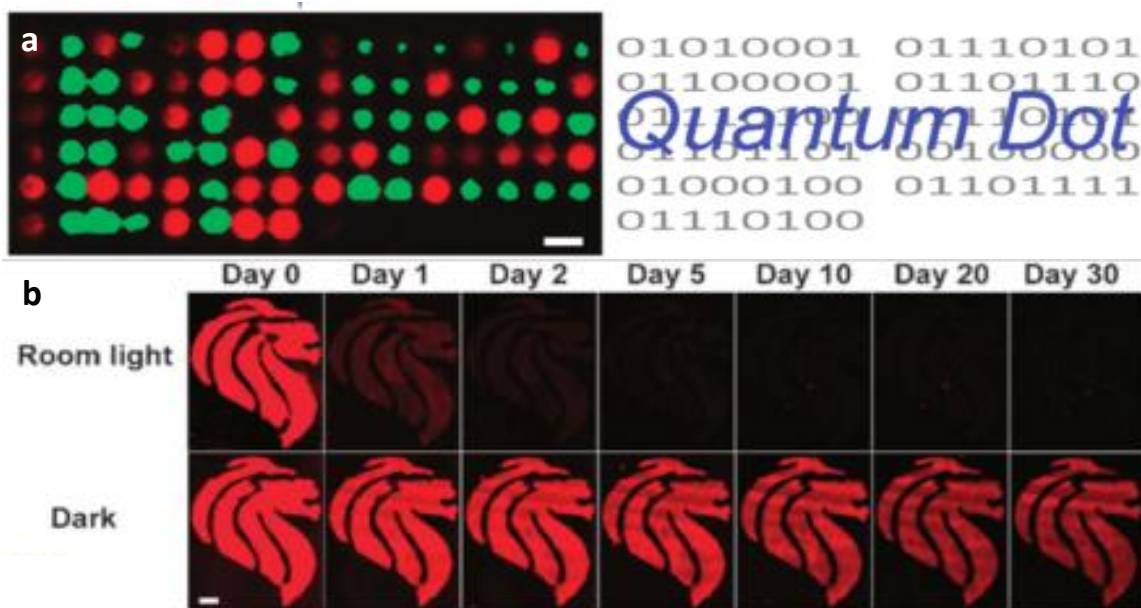
Figure 4-2 – a) Binary code encrypted message using quantum dots and b) comparison of behaviour of these nanoparticles over time under room light and in a dark room. Adapted from Ref. 12.

More recently, trends in the field have focused particularly on exploring the upconversion properties of rare-earth nanocrystals. These nanomaterials have the peculiarity of behaving against the Stokes Shift rule[13] (and hence the name Anti-Stokes shift), meaning they emit radiation at shorter wavelengths than they absorb. More specifically, these nanocrystals have the ability to absorb radiation in the IR region and emit in the visible region of the spectrum. Meruga et al.[14] demonstrated how this can be particularly useful for anti-counterfeit applications. By using Yb^{3+}/Er^{3+} and Yb^{3+}/Tm^{3+} doped β-$NaYF_4$ nanoparticles-based gels, they were able to develop a printable ink to then create invisible quick response (QR) codes. When exposed to IR radiation the QR code would be revealed in a green colour (visible radiation), as seen in Figure 4-3 a and b, which then could be recognized by a mobile device application. Furthermore, they were able to conceal letters of a different colour inside the QR code (Figure 4-3 c), by using the second combination of rare-earth elements which showed longer transitions and therefore higher energy of radiation (blue-coloured emission).
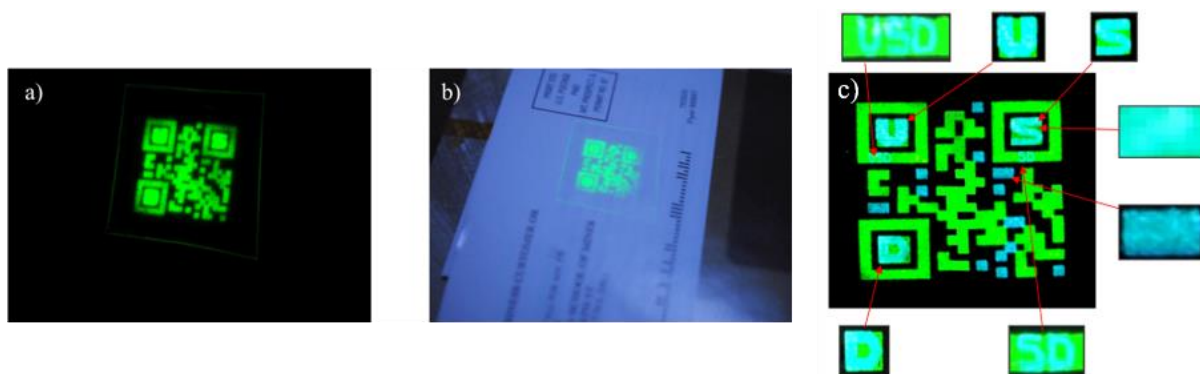
Figure 4-3 – a) Upconverted QR code in a transparent tape, b) the same tape in a piece of paper and c) shows the higher degree of complexity that can be achieved by using different types of nanoparticles within the same code. Adapted from Ref. 14.

4.1.2 C-dots as potential anti-counterfeit tools

With C-dots benign nature and cheap and easy preparation, they pose as natural alternatives to the above described methods, and thus their potential as anti-counterfeit tools will be assessed in this chapter. However, considering the inherent problems of the self-quenching C-dots, the strategy employed was to dilute them in other nanoparticles. Since silica/C-dots optical interactions were already investigated in a physical mixture (Chapter 3), and no considerable effect was noticed on their optical properties, silica was chosen as the other one of the components. The fact that silica nanoparticles display optical transparency suggests potential as a great platform to be combined with the distinguished C-dots fluorescence properties.

Even though silica nanoparticles may not be the most versatile tool *per se*, their composition allows for a rather tuneable environment which opened the way for them to become one of most important minerals currently in use in the nanomaterials field. This in practice meant they found the most widespread range of applications in science, most significantly in photovoltaic cells[15–19], surface coatings[20–25], nano-sensoring[26–31], controlled drug delivery[32–36] and bioimaging[37–41].

4.1.3 C-dots/Silica nanohybrids

Silica can be conjugated with different types of nanoparticles with the aim to preserve or even enhance its intrinsic fluorescent properties. C-dots, by displaying optimum

optical properties, a non-toxic character and a wide array of surface functionalities, emerged as the natural replacement for all the other types of nanoparticles.

Due to C-dots' low toxicity, they have found use in biological applications[34]. Several studies took advantage of the self-assemble properties of precursors like 3-Aminopropyl)triethoxysilane (APTES) to integrate the highly fluorescent C-dots into a Silica nanoparticles' cores, thus creating Core-Shell nano-hybrid systems. In one of these works[42], the synthesis of these nanoparticles allowed for the sensitive and selective detection of Cu^{2+} ions in rats' brain. The sensing mechanism for the detection of Cu^{2+} ions in rats' brain is depicted in Figure 4-4. The interactions between the metal ions and the N and O atoms on C-dots surface, as well as the negatively charged Silica nanoparticles surface, would induce a quenching on the C-dots fluorescence which could be visually noticed. This system allowed for *in vivo* analysis of these ions without the risk for chronic toxicity that usually arises from the use of quantum dots, one of the best current alternatives available. Burns et al.[43], on the other hand, suggested the use of these nanohybrids for near-infrared (NIR) detection of tumours. Since the human body is "transparent" to radiation from this region of the spectrum[43], it is considered optimum for bioimaging without background interference. This research group also found that functionalizing the nanoparticles with neutral organic coating facilitated their urinary excretion. Figure 4-5 shows the C-dots/Silica nanoparticles bioaccumulation in rats' kidneys, and that these nanoparticles have low lifetimes in the rats' organism, as 60-70% of the nanoparticles are excreted after 48h depending on the nanoparticles size. Their bioimaging potential is substantial, which can be mainly attributed to their biostability, biocompatibility and high quantum yields.
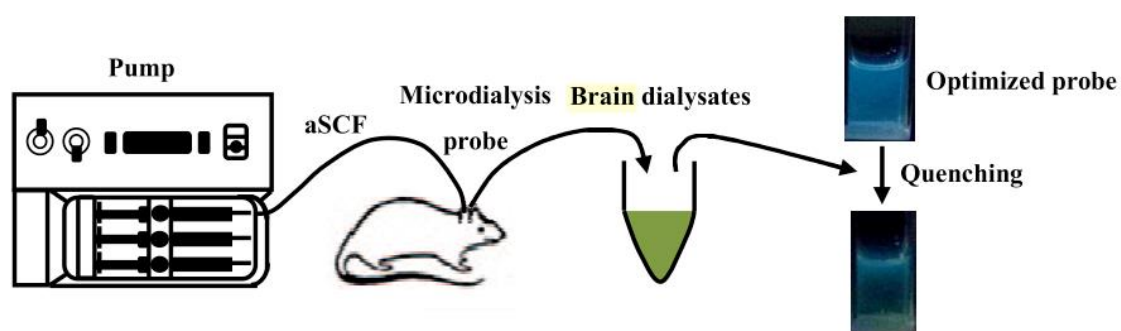
Figure 4-4 – Schematics for the sensing of Cu2+ in rats' brain using silica/C-dots nanohybrids. Adapted from Ref. 42.
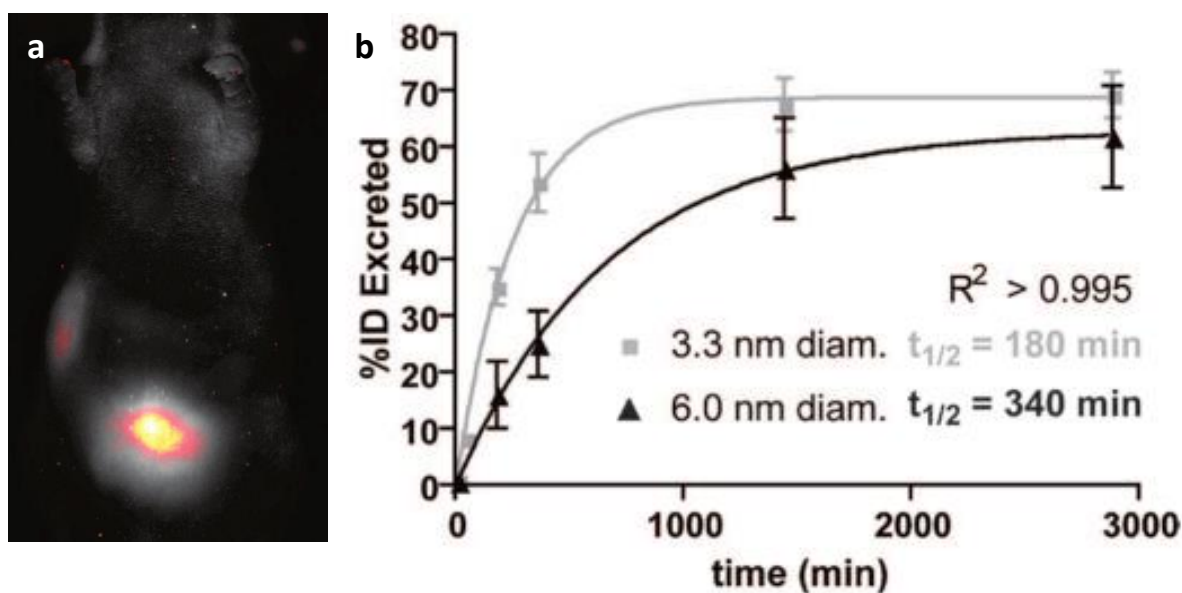
Figure 4-5 – a) In vivo imaging of the silica/C-dots nanoparticles, showing that these accumulate mostly in the kidneys, and b) the excretion times of the 3.3 nm and 6 nm nanoparticles. Adapted from Ref. 43.

Chromium (VI) is one of the most carcinogenic, teratogenic, mutagenic and therefore it is of high interest to be able to target these metal ions[44]. Liu and his research group[44] demonstrated the use of carbon dot-silica nanohybrids to eliminate Cr (VI), a common effluent pollutant from industrial discharges. The C-dots/Silica nano-hybrid were prepared by co-hydrolysis and condensation of amine-silane functionalized carbon dots and then conjugation with Tetraethyl orthosilicate (TEOS). The integration of C-dots in the mesoporous structure of Silica allowed for an increase in the fluorescence lifetime, as well as an increase in the visible light absorption, which in turn lead to an entrapment of the Cr (VI) ions and their photo-reduction to the far less toxic species Cr (III) (Figure 4-6).
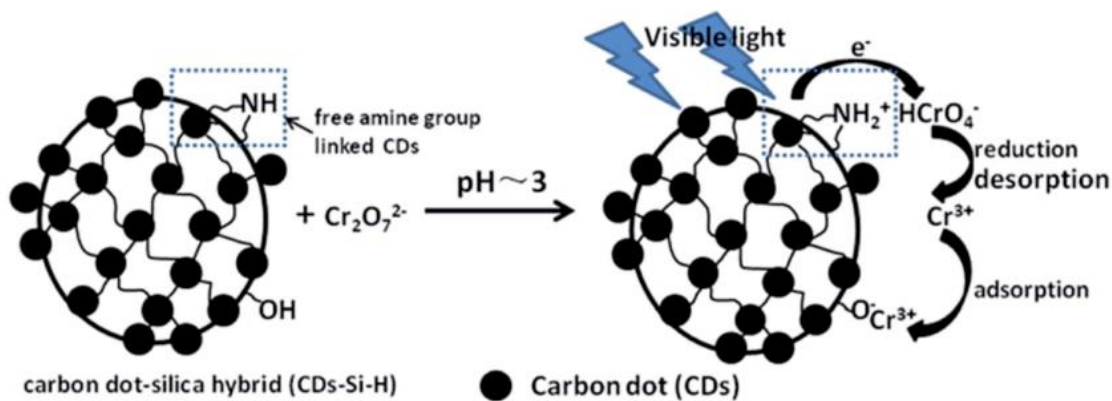
Figure 4-6 – Schematic depiction of the fluorescence sensing mechanism for the detection and reduction of the Cr (VI) species. Adapted from Ref 44.

4.2 Carbogenically coated silica nanoparticles

The synthetic procedure relied on the treatment of the silica nanoparticles with a C-18 silane and then this systems pyrolysis to create C-dots on the silica's surface.
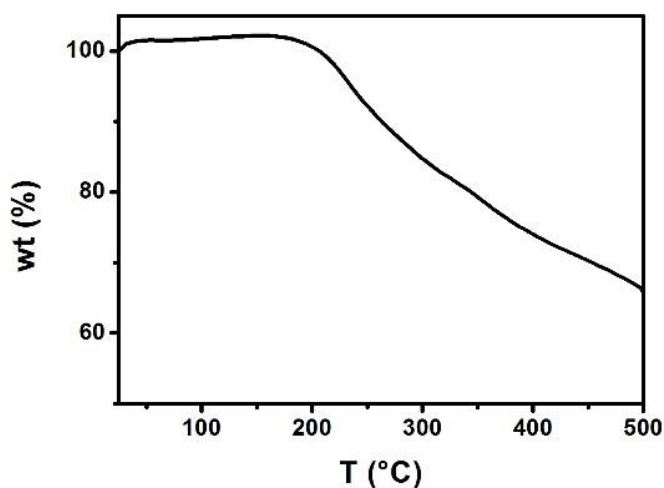
Figure 4-7 – TGA thermograph of the surface treated silica nanoparticles before carbonization.

Thermogravimetric analysis (TGA) prior to the carbonization step proves the presence of high organic content (34%) on the surface of the functionalized silica nanoparticles (Figure 4-7). This demonstrates that the surface of the nanoparticles was successfully and heavily coated with silane polymer and the existence of active sites for the

114

carbonization into C-dots. Elemental analysis thus received of the synthesized C-SiO$_2$ (post-carbonization) shows a high percentage of C, H and N on the C-SiO$_2$ surface (26, 4 and 5% respectively) and, as expected, no S was present.

The FTIR spectra (Figure 4-8) of the silica nanoparticles and carbonized silica nanoparticles show strong peaks at 1070 cm^{-1} corresponding to Si-O-Si anti-symmetric stretching vibrations ($\mathbf{\upsilon_{as}}$), whereas the peak at 790 cm^{-1} relates to Si-O symmetric stretching vibrations ($\mathbf{\upsilon_s}$). Furthermore, the carbonized silica nanoparticles show a broad peak at 1380 cm^{-1}, which correspond to the vibrational stretch of C-H groups, at 1550 cm^{-1} and 1658 cm^{-1}, attributed to the anti-symmetric and symmetric stretching vibrations of N-C=O, respectively, and finally two peaks at 2850 cm^{-1} and 2920 cm^{-1}, which are assigned to the symmetric and anti-symmetric stretching vibration of sp^2 C-H. These results confirm that the nanoparticle's surface is highly populated with several functional groups[45,46].
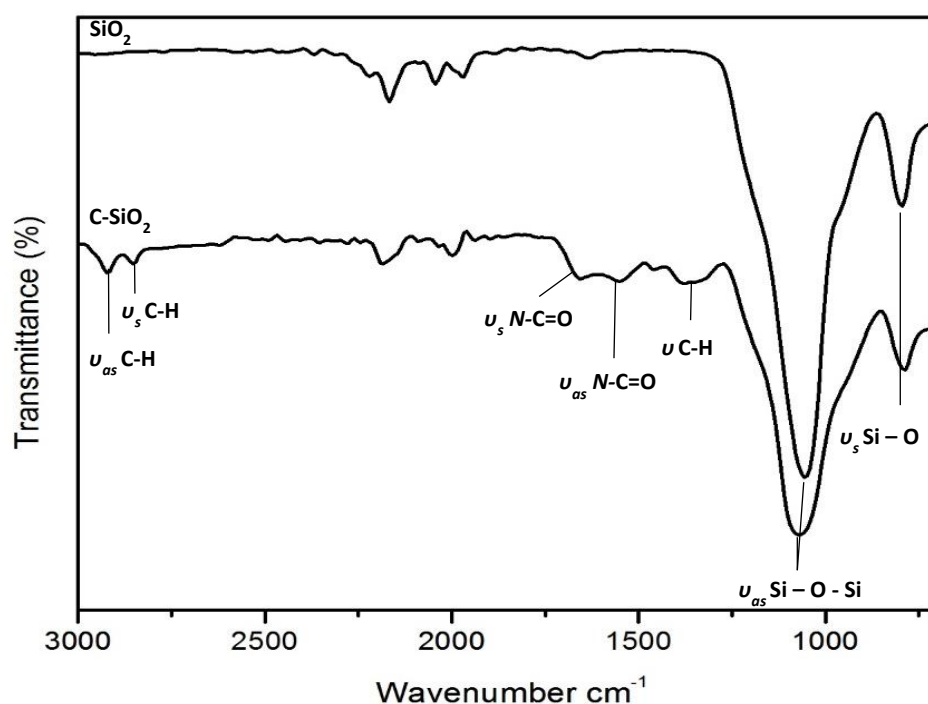
Figure 4-8 – FTIR spectra of the colloidal SiO$_2$ and C-SiO$_2$ (υ_s and υ_{as} stand for symmetric and anti-symmetric stretching vibrations, respectively).

Transmission electron microscopy (TEM) and atomic force microscopy (AFM) show an average size of 22±2 nm (Figure 4-9). Moreover, the measurement of the hydrodynamic radius of the as-prepared nanoparticles demonstrated that they form stable colloidal solutions within the ranges of pH 10.2 (initial pH) to pH 9 which is consistent with the existence of surface functionalities produced from the oxidation/amine treatment. When acidified, however, agglomerates started forming, Figure 4-10, and some particles precipitated.
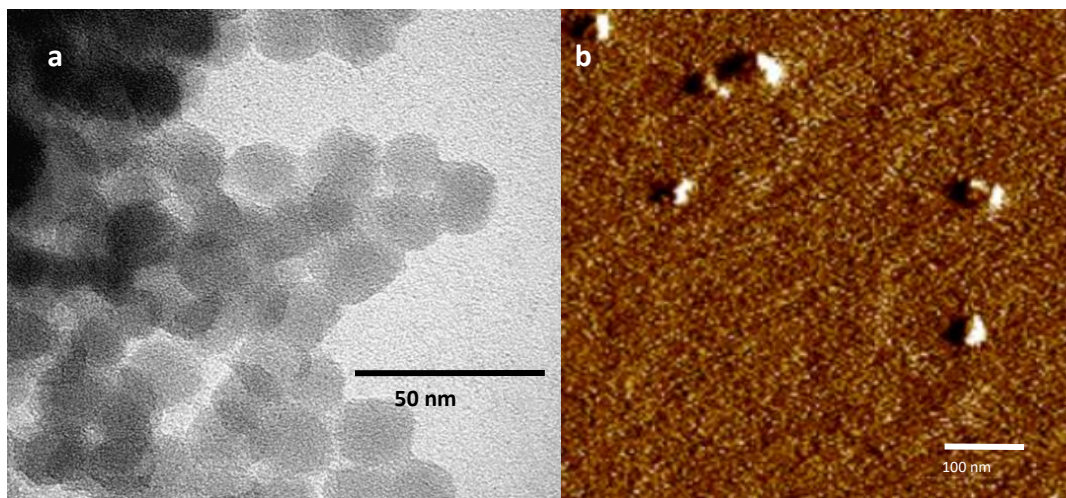
Figure 4-9 – a) TEM image and b) AFM images of C-SiO$_2$ nanoparticles, showing an average size of 22 ±2 nm.
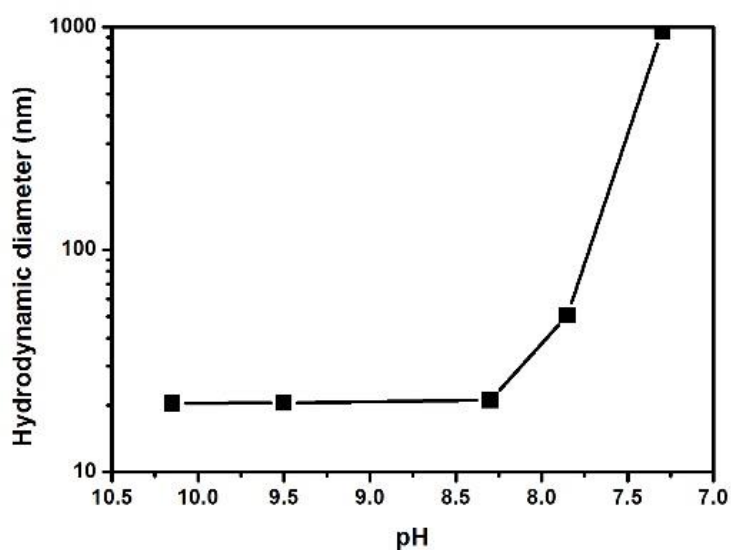
Figure 4-10 – Hydrodynamic diameter of 0.1wt% C-SiO$_2$ in water as a function of pH.

The production of C-dots was proved by fluorescence analysis. The C-SiO$_2$ nanoparticles showed the C-dots' characteristic excitation-dependent emission (Figure 4-11) with a broad wavelength region of emission. Even though it does not exist yet one widely accepted fluorescence mechanism, most authors agree that it arises from surface defects and the conjugated π-domains [47,48] (refer to chapter 1 for more detailed PL analysis of C-dots).
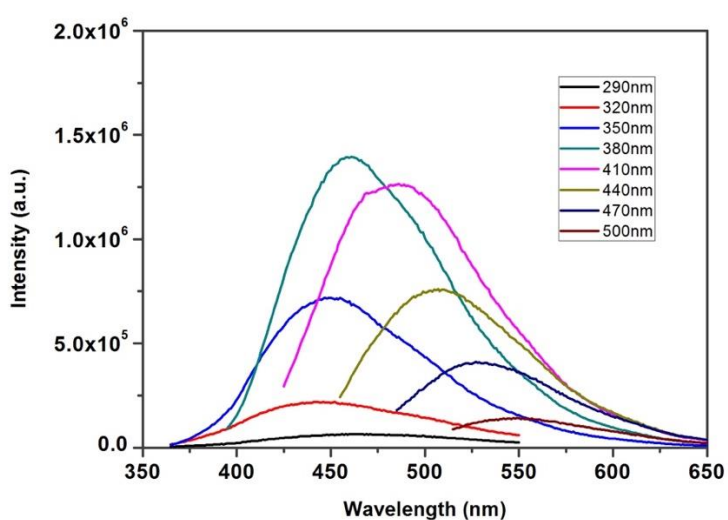
Figure 4-11 – Fluorescence spectra of C-SiO$_2$ aqueous solution under different excitation wavelengths.

For the nanotags preparation for anti-counterfeit purposes, C-SiO$_2$ solutions were acidified to different pH and were left to evaporate at room temperature. These nanoparticles produced motives with uniquely shaped patterns, resembling fractal structures, which ca be used as anti-counterfeit tools. These motives were analysed in a fluorescence microscope and were found to show the same excitation-dependent fluorescence behaviour as the C-SiO$_2$ aqueous suspensions. Not only do these motives conformation change consistently with every deposition (Figure 4-12) but also have their structured modified when subjected to different conditions (*e.g.* pH, concentration, substrate of deposition, etc) as depicted in Figure 4-13, Figure 4-14 and Figure 4-15. Therefore, adding to these properties, the fact that they display ease of preparation, relatively cheap and non-toxic nature, and since they are virtually impossible to replicate, it makes them potential assets as anti-counterfeits tools. In order to assess their resistance, C-SiO$_2$ nanotags were submitted to high temperatures (100°C for several hours) and no considerable effects were noticed in the motives (Figure 4-16), and so it's possible to conclude that they are temperature-resistant materials. This resistance is most likely related to the fact that these nanomaterials do not possess organic or polymeric molecules in their structure. SEM images (Figure 4-17) revealed the advanced structural complexity of the motives formed by these nano-hybrids.

Figure 4-12 - Fluorescence microscopy images (under three excitation wavelengths) of air-dried aqueous dispersions of C-SiO$_2$ at pH 7.
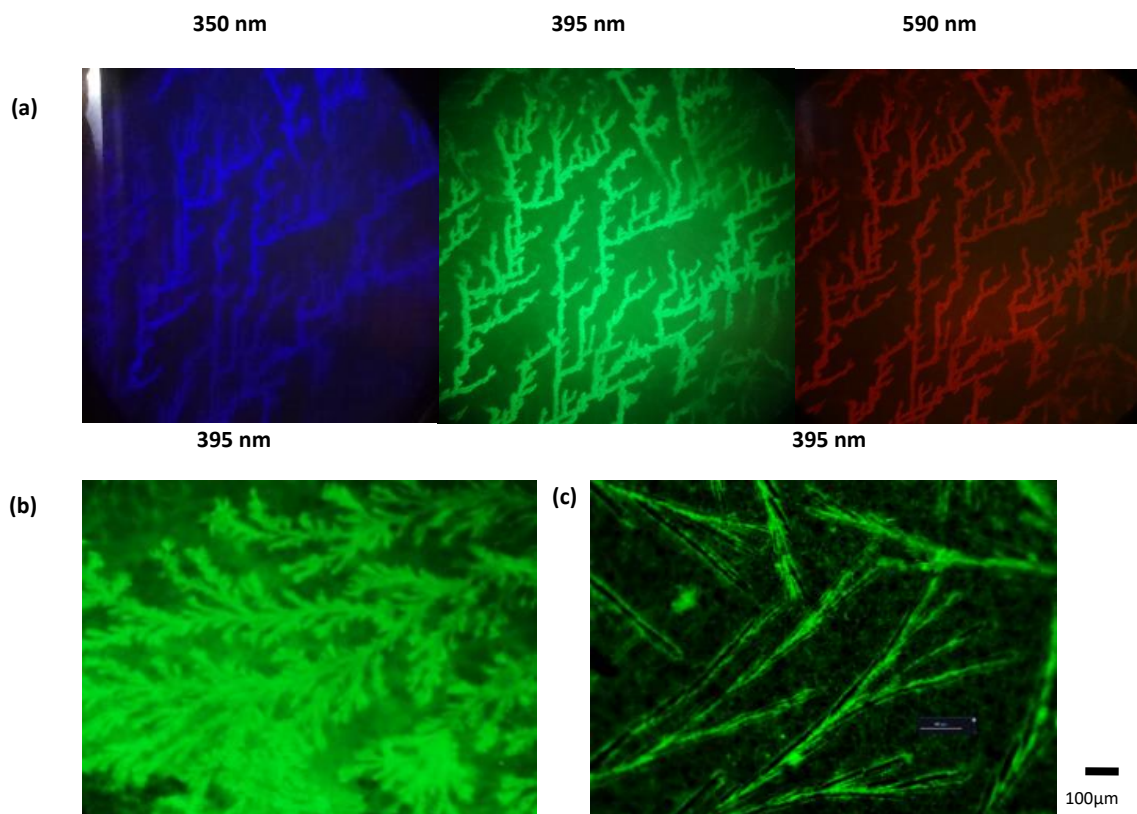
Figure 4-13 – Fluorescent microscopy images of the nanotags: a) deposited in glass and illuminated under different excitation wavelengths, b) deposited in glass from a more concentrated suspension and c) deposited on a polymeric surface.
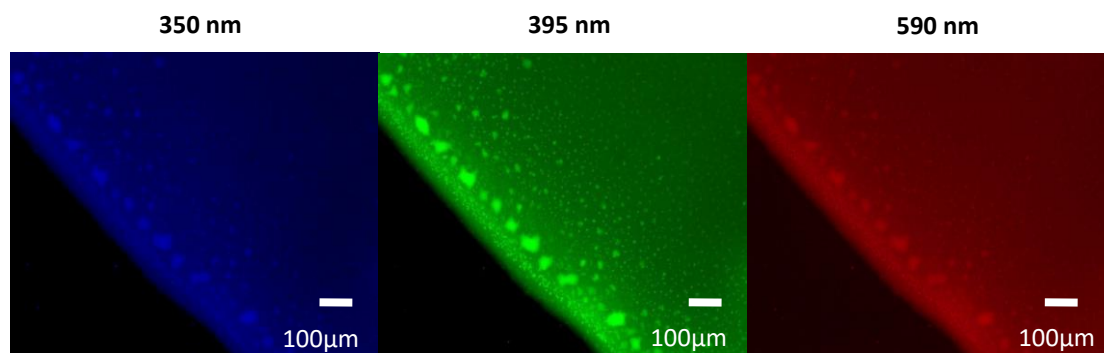
Figure 4-14 – Fluorescence microscopy images (under three excitation wavelengths) of air-dried aqueous dispersions of C-SiO$_2$ with pH 10, indicating the absence of structured PL motives, in strong contrast to the behaviour observed when in solution of pH 7.
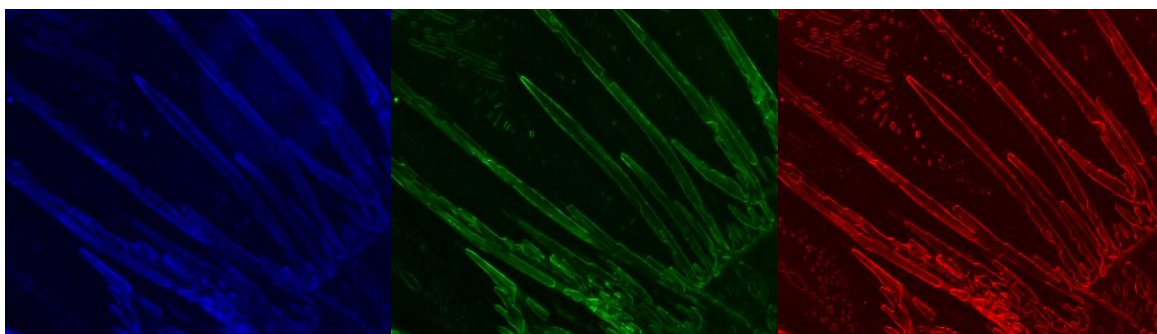
Figure 4-15 - Fluorescence microscopy images (under three excitation wavelengths) of air-dried aqueous dispersions of C-SiO$_2$ at pH 2.

350 nm	395 nm	590 nm
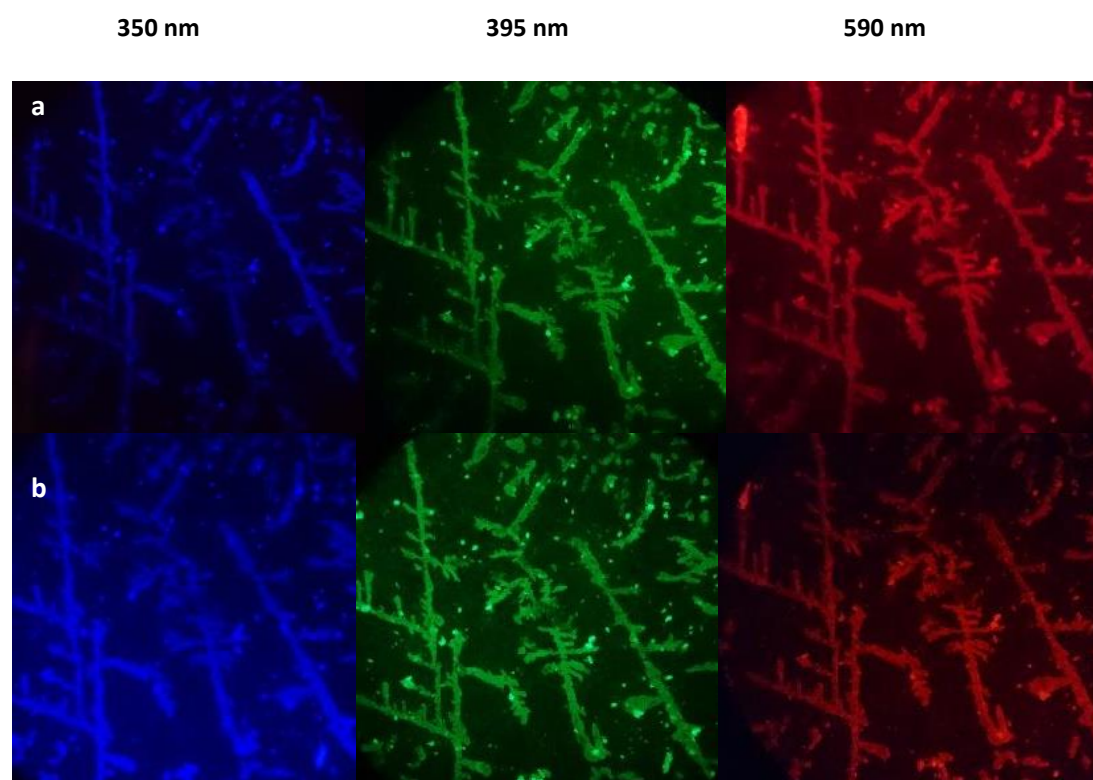
Figure 4-16 – Fluorescence microscopy images (under three different excitation wavelengths) of self-assembled motives of C-SiO$_2$ generated on a glass surface a) before and b) after being heated to 100°C for several hours.
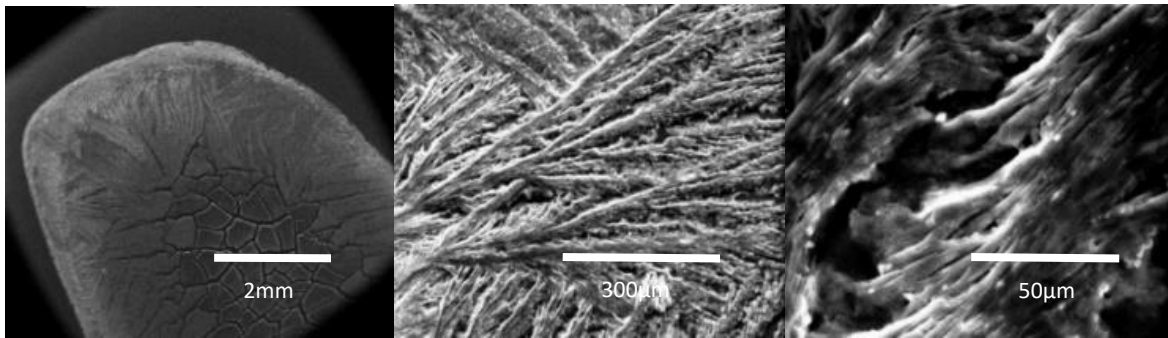
Figure 4-17 – SEM images of the motives formed at pH 7 under different magnifications.

4.3 Conclusion

It has been demonstrated the use of carbogenically coated Silica nanoparticles for the production of nanotags for anti-counterfeit purposes. These materials show the unique excitation-dependence fluorescence of C-dots, along with the stability of silica cores.

The silica nanoparticles susceptibility to pH changes allowed for the development of the excitation-dependent nanotags. By reducing the pH, the C-SiO$_2$ aqueous suspensions produce fractal structures, which after evaporation leave behind non-replicable, multi-coloured, temperature-resistant motives that can be used for anti-counterfeit purposes. In combination with a relatively simple software it could be used similarly to QR code readers, making it an extremely portable solution. In addition, these nano-hybrids pose as cheaper, non-toxic and more complex alternatives to the recently emerging suggested methods like dye-doped nanomaterials or upconverting nanocrystals.

4.4 References

1. Kim, J. *et al.* Anti-counterfeit nanoscale fingerprints based on randomly distributed nanowires. *Nanotechnology* **25,** 1–7 (2014).

2. Lancet, T. Fighting fake drugs: The role of WHO and pharma. *Lancet* **377,** (2011).

3. Fadlallah, R., El-Jardali, F., Annan, F., Azzam, H. & Akl, E. A. Strategies and Systems-Level Interventions to Combat or Prevent Drug Counterfeiting: A Systematic Review of Evidence Beyond Effectiveness. *Pharmaceut. Med.* **30,** 263–76 (2016).

4. Cockburn, R., Newton, P. N., Agyarko, E. K., Akunyili, D. & White, N. J. The global threat of counterfeit drugs: Why industry and governments must communicate the dangers. *PLoS Med.* **2,** 302–08 (2005).

5. Martino, R., Malet-Martino, M., Gilard, V. & Balayssac, S. Counterfeit drugs: Analytical techniques for their identification. *Anal. Bioanal. Chem.* **398,** 77–92 (2010).

6. Bansal, D., Malla, S., Gudala, K. & Tiwari, P. Anti-counterfeit technologies: A pharmaceutical industry perspective. *Sci. Pharm.* **81,** 1–13 (2013).

7. Wachulak, P. W. *et al.* Sub 400 nm spatial resolution extreme ultraviolet holography with a table top laser. *Opt. Express* **14,** 9636–42 (2006).

8. Martinez, C. *et al.* Complementary computer generated holography for aesthetic watermarking. *Opt. Express* **20,** 5547–56 (2012).

9. Buchanan, J. D. R. *et al.* Forgery: 'fingerprinting' documents and packaging. *Nature* **436,** 475 (2005).

10. Roberts, C. M. Radio frequency identification (RFID). *Comput. Secur.* **25,** 18–26 (2006).

11. Demirok, U. K., Burdick, J. & Wang, J. Orthogonal Multi-Readout Identification of Alloy Nanowire Barcodes. J. Am. Chem. Soc., **131,** 22–23 (2009).

12. Lu, Z., Liu, Y., Hu, W., Lou, X. W. D. & Li, C. M. Rewritable multicolor fluorescent patterns for multistate memory devices with high data storage capacity. *Chem. Commun.* **47,** 9609–11 (2011).

13. Sun, L. W. *et al.* Lanthanum-doped ZnO quantum dots with greatly enhanced fluorescent quantum yield. *J. Mater. Chem.* **22,** 8221–27 (2012).

14. Meruga, J. M. *et al.* Security printing of covert quick response codes using upconverting nanoparticle inks. *Nanotechnology* **23,** 1–9 (2012).

15. Chebotareva, A. B., Untila, G. G. & Kost, T. N. Heavily phosphorus-doped silicon nanoparticles as intermediate layer in solar cell based on IFO/p-Si heterojunction. *Sol. Energy* **122,** 650–57 (2015).

16. Yun, J. *et al.* Light trapping in bendable organic solar cells using silica nanoparticle arrays. *Energy Environ. Sci.* **8,** 932–40 (2015).

17. Wang, P., Zakeeruddin, S. M., Comte, P., Exnar, I. & Grätzel, M. Gelation of ionic liquid-based electrolytes with silica nanoparticles for quasi-solid-state dye-sensitized solar cells. *J. Am. Chem. Soc.* **125,** 1166–67 (2003).

18. Darbandi, M., Thomann, R. & Nann, T. Single Quantum Dots in Silica Spheres by Microemulsion Synthesis. *Chem. Mater.* **17,** 5720–25 (2005).

19. Matheu, P., Lim, S. H., Derkacs, D., McPheeters, C. & Yu, E. T. Metal and dielectric nanoparticle scattering for improved optical absorption in photovoltaic devices. *Appl. Phys. Lett.* **93,** 1–4 (2008).

20. Cebeci, F. Ç., Wu, Z., Zhai, L., Cohen, R. E. & Rubner, M. F. Nanoporosity-driven superhydrophilicity: A means to create multifunctional antifogging coatings. *Langmuir* **22,** 2856–62 (2006).

21. Du, Y., Luna, L. E., Tan, W. S., Rubner, M. F. & Cohen, R. E. Hollow silica nanoparticles in UV-visible antireflection coatings for poly(methyl methacrylate) substrates. *ACS Nano* **4,** 4308–16 (2010).

22. Prevo, B. G., Hon, E. W. & Velev, O. D. Assembly and characterization of colloid-based antireflective coatings on multicrystalline silicon solar cells. *J. Mater. Chem.* **17,** 791–99 (2007).

23. Hoshikawa, Y. *et al.* Mesoporous silica nanoparticles with remarkable stability and dispersibility for antireflective coatings. *Chem. Mater.* **22,** 12–14 (2010).

24. Wu, Z. *et al.* Deformable antireflection coatings from polymer and nanoparticle multilayers. *Adv. Mater.* **18,** 2699–702 (2006).

25. Chau, J. L. H., Hsieh, C. C., Lin, Y. M. & Li, A. K. Preparation of transparent silica-PMMA nanocomposite hard coatings. *Prog. Org. Coatings* **62,** 436–39 (2008).

26. Wu, Y., Xue, P., Kang, Y. & Hui, K. M. Highly Specific and Ultrasensitive Graphene-Enhanced Electrochemical Detection of Low-Abundance Tumor Cells Using Silica Nanoparticles Coated with Antibody-Conjugated Quantum Dots. *Anal. Chem.* **85,** 3166–73 (2013).

27. Singh, G. & Rani, S. A proficient magnetic nano-platform with covalently assembled methyl red indicator for the dual recognition of pH and Hg2+. *Sensors Actuators B Chem.* **244,** 861–75 (2017).

28. Kim, Y., Lee, K. M. & Chang, J. Y. Highly luminescent tetra(biphenyl-4-yl)ethene-grafted molecularly imprinted mesoporous silica nanoparticles for fluorescent sensing of diethylstilbestrol. *Sensors Actuators B Chem.* **242,** 1296–304 (2016).

29. Ramachandran, K., Raj kumar, T., Babu, K. J. & Gnana kumar, G. Ni-Co bimetal nanowires filled multiwalled carbon nanotubes for the highly sensitive and selective non-enzymatic glucose sensor applications. *Sci. Rep.* **6,** 1–12 (2016).

30. Ye, H. *et al.* Methyl Parathion Degrading Enzyme-based Nano-hybrid Biosensor for Enhanced Methyl Parathion Recognition. *Electroanalysis* **28,** 1591–96 (2016).

31. Kadimisetty, K. *et al.* 3D-printed supercapacitor-powered electrochemiluminescent protein immunoarray. *Biosens. Bioelectron.* **77,** 188–93 (2016).

32. Sun, Y. Y. L. *et al.* Nanoassembles constructed from mesoporous silica nanoparticles and surface-coated multilayer polyelectrolytes for controlled drug

delivery. *Microporous Mesoporous Mater.* **185,** 245–53 (2014).

33. Vivero-Escoto, J. L., Slowing II, Trewyn, B. G. & Lin, V. S. Mesoporous silica nanoparticles for intracellular controlled drug delivery. *Small* **6,** 1952–67 (2010).

34. Jiao, J. *et al.* Fluorescent carbon dot modified mesoporous silica nanocarriers for redox-responsive controlled drug delivery and bioimaging. *J. Colloid Interface Sci.* **483,** 343–52 (2016).

35. Singh, R. K., Patel, K. D., Mahapatra, C., Kang, M. S. & Kim, H. W. C-Dot Generated Bioactive Organosilica Nanospheres in Theranostics: Multicolor Luminescent and Photothermal Properties Combined with Drug Delivery Capacity. *ACS Appl. Mater. Interfaces* **8,** 24433–44 (2016).

36. Li, Q. L. *et al.* pH and Glutathione Dual-Responsive Dynamic Cross-Linked Supramolecular Network on Mesoporous Silica Nanoparticles for Controlled Anticancer Drug Release. *ACS Appl. Mater. Interfaces* **7,** 28656–64 (2015).

37. Liu, Q., Yang, T., Feng, W. & Li, F. Blue-emissive upconversion nanoparticles for low-power-excited bioimaging in vivo. *J. Am. Chem. Soc.* **134,** 5390–97 (2012).

38. Nakamura, M., Shono, M. & Ishimura, K. Synthesis, characterization, and biological applications of multifluorescent silica nanoparticles. *Anal. Chem.* **79,** 6507–14 (2007).

39. Velusamy, M. *et al.* A new series of quadrupolar type two-photon absorption chromophores bearing 11, 12-dibutoxydibenzo[a,c]-phenazine bridged amines; their applications in two-photon fluorescence imaging and two-photon photodynamic therapy. *Adv. Funct. Mater.* **19,** 2388–97 (2009).

40. LeCroy, G. E. *et al.* Functionalized carbon nanoparticles: Syntheses and applications in optical bioimaging and energy conversion. *Coord. Chem. Rev.* **320–321,** 66–81 (2016).

41. Zhang, T. *et al.* Facilely prepared carbon dots and rare earth ion doped hybrid composites for ratio-metric pH sensing and white-light emission. *RSC Adv.* **6,** 61468–72 (2016).

42. Lin, Y. *et al.* Tunable Fluorescent Silica-Coated Carbon Dots: A Synergistic Effect for Enhancing the Fluorescence Sensing of Extracellular Cu^{2+} in Rat Brain. *ACS Appl. Mater. Interfaces* **7,** 27262–70 (2015).

43. Burns, A. a *et al.* Fluorescent Silica Nanoparticles with Efficient Urinary Excretion for Nanomedicine. *Nano Lett.* **9,** 442–48 (2009).

44. Liu, Y. *et al.* The effective removal of Cr(vi) ions by carbon dot-silica hybrids driven by visible light. *RSC Adv.* **6,** 68530–37 (2016).

45. Cui, X. *et al.* A fluorescent biosensor based on carbon dots-labeled oligodeoxyribonucleotide and graphene oxide for mercury (II) detection. *Biosens. Bioelectron.* **63,** 506–12 (2015).

46. Stobinski, L. *et al.* Multiwall carbon nanotubes purification and oxidation by nitric acid studied by the FTIR and electron spectroscopy methods. *J. Alloys Compd.* **501,** 77–84 (2010).

47. Kelarakis, A. Graphene quantum dots: In the crossroad of graphene, quantum dots and carbogenic nanoparticles. *Curr. Opin. Colloid Interface Sci.* **20,** 354–61 (2015).

48. Gan, Z., Xu, H. & Hao, Y. Mechanism for excitation-dependent photoluminescence from graphene quantum dots and other graphene oxide derivates: Consensus, debates and challenges. *Nanoscale* **8,** 7794–807 (2016).

5 *In Situ* preparation of C-dots in polymers matrix

5.1 Introduction

Fluorescent materials have gained a central importance in several fields of science and have thus been subjected to extensive research in the past few decades. Due to their varied chemical and mechanical properties, polymers are ideal materials to impart with fluorescence. So far, fluorescent polymers have been demonstrated as potential tools for optoelectronics, chemical sensing and bioimaging applications[1]. Polymer-based fluorescent materials display unique advantages when compared to other materials (particularly, to the most commonly employed alternatives – small organic fluorophores), such as photo- and structural-stability, electronic communication/amplification through the polymer backbone, greater binding efficiency and recognition selectivity, and ultimately, they are easier to turn into devices (*e.g.* sensing films).[1,2] Within this section, a greater focus will be given to fluorescent conjugated polymers and nanocomposites, due to the similarities with the systems presented in this chapter (fluorescent nanocomposites).

5.1.1 Conjugated polymers

Within the class of fluorescent polymers, one of particular interest are the conjugated polymers. These are materials that benefit from having alternating sp^2 and sp carbons along it's backbone, creating valence bands (filled with electrons) and conducting bands (electron-free), resulting on semiconducting materials[3]. They have found use in numerous scientific fields, namely sensing, bioimaging and electronic and light-emitting devices[2,4]. Some of the most common examples of conjugated polymers can be seen in Figure 5-1.
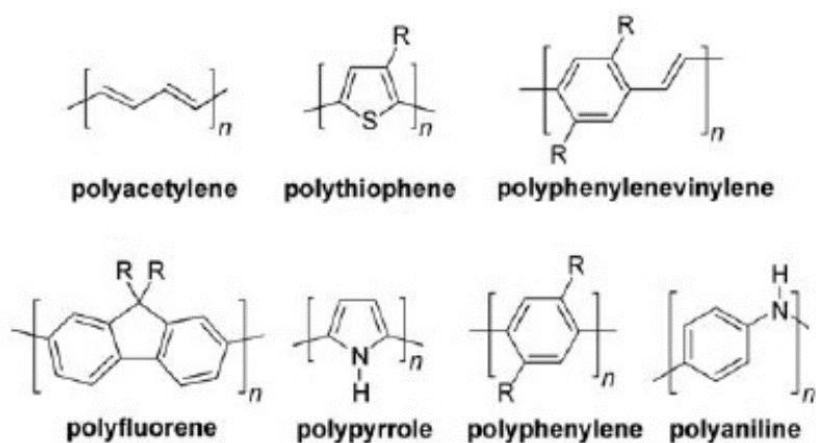
Figure 5-1 – Representation of some of the most common conjugated polymers. Adapted from Ref. 5.

Kim et al.[6] described how the inherently conductive properties of poly(p-phenylene ethynylene), or PPE, could be used for the sensitive and specific detection of K^+ ions. The authors explored the well-known sandwich complex induced by these metal cations. They reported that the resulting crosslinking between the PPE units, with the K^+ ions as the contact points between layers (Figure 5-2 a), produced a red-shift (from 434 to 459nm) in the UV absorbance, consistent with the π-stacking aggregates of PPE, as well as a general quenching in the fluorescence intensity and a red-shift in the I_{max} at high concentration (Figure 5-2 b). Moreover, the authors demonstrated that these effects were specific to K^+ ions, as both Na^+ and Li^+ ions produced no significant quenching to the polymers fluorescence.
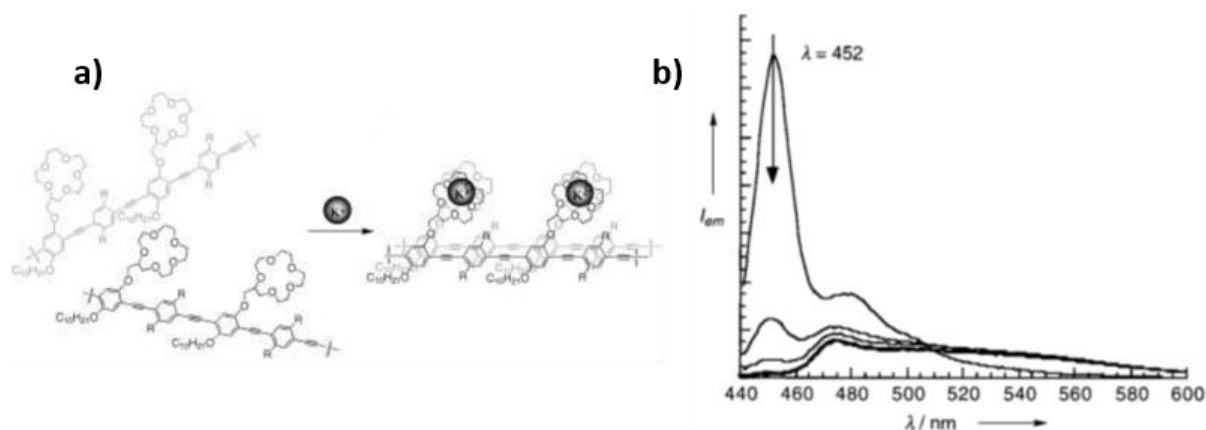
Figure 5-2 – a) Schematic representation of the "sandwich" stacking of PPE chains with K+ ions as crosslinking agents, and b) emission spectra of this system, when in presence of increasing concentration of K+. Adapted from Ref. 6.

Miyata et al.[7] suggested the use of a π-conjugated organoboron polymer for the detection of fluoride ions. This work is of particular interest since sensors tend to target metal cations and, in this case, anions (F-) are targeted. These ions are usually associated with chemical and nuclear weapons' manufacture, and thus their detection is of relevance for national security agencies. The mechanism of detection relied on the fluorine atoms coordinating the boron atoms on the polymer backbone and the resulting change in the hybridization of the boron from sp^2 to sp^3, resulting on a quenching in the polymer's fluorescence.

Moreover, fluorophores may be added to conjugated polymers to enhance their optical properties, either to its backbone, by alternating highly electronic conducting monomers (*e.g.* benzene, acetylene and PPV) with fluorophore derivative ligands, such as coumarin, terpyridine or quinoline [8–10]; or to their side chains by functionalizing polymers with similar fluorophore derivatives[11–13]. In both cases, these systems present clear advantages since the fluorescent dyes are covalently bonded to the polymers, making them resistant to hostile environments, like for bioimaging purposes where they might be decomposed otherwise[1].

Interestingly, Kim et al.[14] reported a fluoride sensor based on the amplifying fluorescence response of a conjugated polymer. The authors described that by using PPE with a coumarin derivative attached to the sidechains, the system would become highly sensitive to the fluoride ions, since a fluoride-induced lactonization of the derivative would originate the coumarin fluorophore. The mechanism behind F-

129

detection, Figure 5-3, can be explained with the presence of a conduction band (sidechains - coumarin derivative) and a valence band (backbone – PPE). When a photon is absorbed by the valence band, it creates an exciton which migrates along the backbone, until it absorbs an excited electron back, which, if it is originated from a fluorine-modified sidechain (coumarin), it will emit an enhanced fluorescence response, due to the fluorophore being more fluorescent than its derivative.
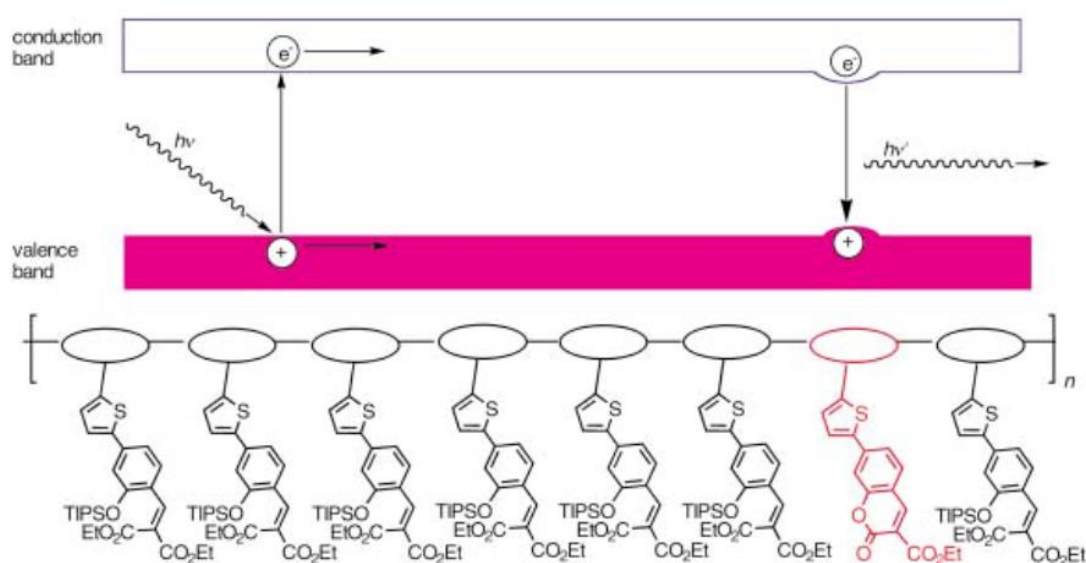
Figure 5-3 – Schematic illustration of the underlying mechanism for the sensitive detection of fluoride ions using the conjugated polymer system based on PPE-coumarin derivative. Adapted from Ref. 14.

Nonetheless, it is also the case that these materials display low solubility in water, and even though this might be overcome by the attachment of different functional groups, this will add even more steps to already an extensive and complex procedure.

5.1.2 Nanocomposites

Another approach frequently pursued is the combination of polymers with nanoparticles to create nanocomposite systems. They display an organic phase (polymers) and an inorganic phase (silica, Au or Ag nanoparticles, etc.), and are able to maintain the advantages of both systems. Due to the broad use of nanocomposites definition found in the literature, all systems containing an inorganic and organic phase

will be considered as composites. Silica mesoporous materials are the most commonly used as inorganic phase, as they display large surface areas, well-defined porosity, ease of preparation and recyclability[1]. Nanoparticles are generally known to have good electron conductivity and, due to their large surface area/volume ratio, they can be tuned with signal units to perform with high selectivity and sensitivity, an important feature in the sensing field[15].

One of the most common purposes of the nanocomposites is the development of more stable nanoparticles dispersions. To this end, several polymers have been grafted into nanoparticles' surface, in order to induce higher affinity between the surface and the solvent or polymers' matrices[16]. Hong and co-authors[17] demonstrated that bare ZnO nanoparticles precipitated completely after 4h, whereas polystyrene (PS)-grafted ZnO afforded more stable solutions in acetone. Other examples include TiO_2-g-poly(methyl methacrylate, MMA) in tetrahydrofuran (THF)[18], Al_2O_3-g-polystyrene/polyacrylamide (PS/PAAM) in THF and acetone[19], respectively, Fe_2O_4- and TiO_2-g-PS in several organic solvents[20].

Another application studied for nanocomposite materials is the enhancement of the mechanical properties of polymers. Hashimoto et al.[21] investigated the effect of adding silanated TiO_2 to high density polyethylene (HDPE) and how this would be useful for bone repair applications. It was found that this nanocomposite material had its Young's modulus and bending yield strength increased from 65 MPa to 10 GPa and from 49MPa to 7.5GPa, respectively, showing a dramatic increase in the mechanical properties. Mechanistically, it was concluded that the silane functional groups were the bridging agents between TiO_2 nanoparticles and the HDPE polymer, as demonstrated in Figure 5-4.
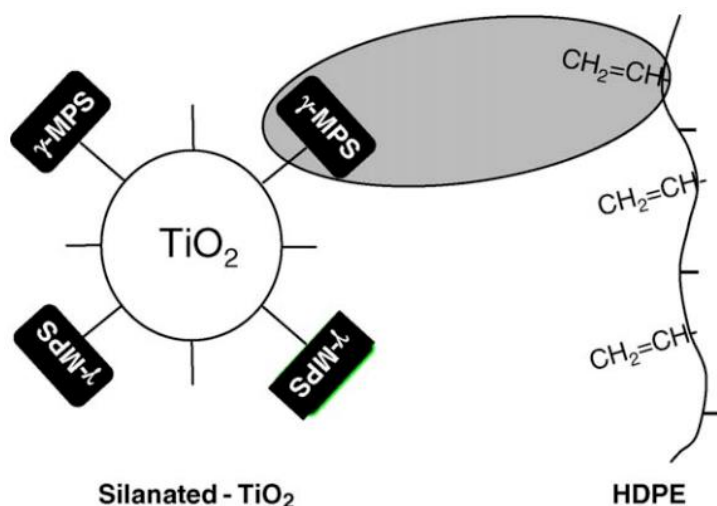
Figure 5-4 – Suggested adhesion mechanism for the silane-functionalized TiO2 and HDPE. Adapted from Ref. 21.

5.1.2.1 *Fluorescent nanocomposites*

Owing to their size, nanoparticles may display unique optical properties, and are generally more robust than their counterparts, organic dyes. However, they have a known tendency to form aggregates and thus require further stabilization[16]. One way to achieve this is functionalize them with polymeric materials, in nanocomposite systems.

Waldron et al.[22] suggested the use of PbSe QDs impregnated in an epoxy polymer matrix (Angstrom Bond AB9093). The authors reported a significant QY decrease (from 55% to 26%) when compared to the same type of QDs in organic solvents, such as toluene and hexane, which they attributed to the oxidation of QDs and the loss of protective ligands during incorporation in the polymer matrix. Nonetheless, when compared to similar QDs dispersed in different polymers matrices (*e.g.* PMMA), they showed an improvement in quantum yield of ~ 10%, which the authors claim to be highest recorded QY for QDs-based solid devices. These systems are particularly advantageous for luminescent solar concentrators owing to their wide absorption bands and structural stability.

Sarkar et al.[23] developed a "turn-on" Zn(II)-sensor based on a mesoporous silica nanocomposite. The mesoporous silica is functionalized with 3-aminopropyltriethoxysilane (3-APTES) and covalently grafted with 4-methyl-2,6-

132

diformyl phenol, a chromophore. This nanocomposite had the peculiarity of displaying enhanced fluorescence intensity upon the titration with Zn (II) ions (Figure 5-5 a), whilst when other cations were present no relevant effect in the fluorescence was noted (Figure 5-5 b).

Chen et al.[24] investigated the effect of gold nanoparticles on a Rhodamine-derivative dye PL properties. This research group prepared a nanocomposite system based on a gold core, coated with a PVP film and a dye-incorporated silica shell (Figure 5-6 a, b and c) was used. The incorporation of the Au cores proved to have a significant increase on the system's fluorescence intensity (Figure 5-6 d), by a factor of 9.6. The authors suggested that these nanocomposite systems are of great importance to understand the mechanisms of metal enhanced fluorescence.
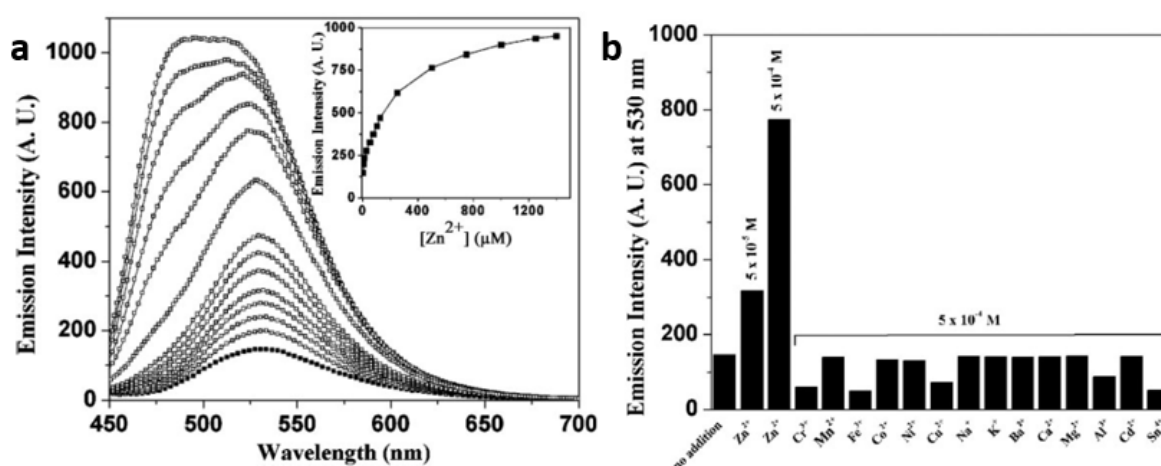
Figure 5-5 – a) Emission spectra of the mesoporous silica/silane/chromophore nanocomposite system, showing an increase in the fluorescence intensity upon titration with Zn (II) (inset shows fluorescence intensity as a function of Zn^{2+} ions concentration) and b) the effect of different metal cations in this system's fluorescence intensity. Adapted from Ref. 23.
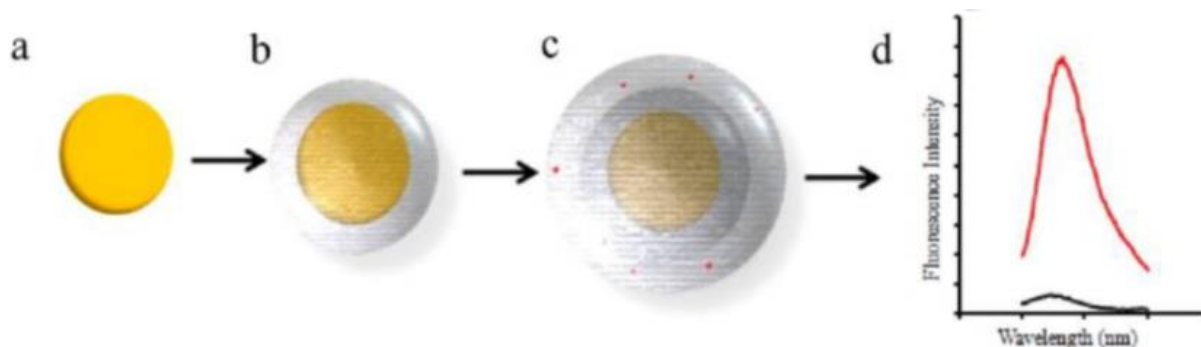
Figure 5-6 – Schematic representation of the several layers of the nanocomposite with a) Au core, b) addition of a PVP layer, c) coating with a Silica Shell doped with a Rhodamine-derivative dye, and d) comparison of the fluorescence intensity in the absence (black line) and presence (red line) of the Au core. Adapted from Ref. 24.

5.1.3   C-dots and polymers

Carbon-dots (or C-dots) have emerged in the past decade as the potential alternatives for nearly all the other fluorescent materials. They pose as non-toxic nanoparticles, with high quantum yields, and even unique fluorescent effects such as excitation-dependent emission[26]. Moreover, it has been demonstrated that they may be prepared strictly following environmentally benign methods and chemicals[27,28].

Coincidently, the use of polymers and C-dots have converged and risen as a trend in the materials science field[29]. Polymers may be used as a carbon-source for the preparation of C-dots, as surface passivators and doping agents, or as an integral part of nanocomposite systems[29]. In the following subsections, a brief literature review of such methods will be reviewed.

5.1.3.1   *Polymers as carbon-rich precursors*

Owing to their high percentage of carbon content, polymers have found an important role as carbon-rich sources for C-dots preparation. Their macromolecular structures usually are broken down and crosslinked into forming C-dots[30]. Both synthetic and natural polymers may be used for this end.

Konwar et al. [31] reported that when a chitosan hydrogel is heated up in a microwave, C-dots with narrow and sharp PL peaks are obtained. Additionally, lignin, a natural polymer with high percentage of –OH groups, can also be used for C-dots preparation,

as Chen et al.[32] demonstrated. In this work, by using a strong oxidizing agent (H_2O_2), OH• radical groups are formed that can then break down the carbon-carbon bonds of the polymer to form C-dots. This method rendered C-dots with a size distribution of 2-10 nm (Figure 5-7 a) and graphitic structure (lattice spacing of 0.21 nm), and proved useful for bioimaging purposes (Figure 5-7 b).
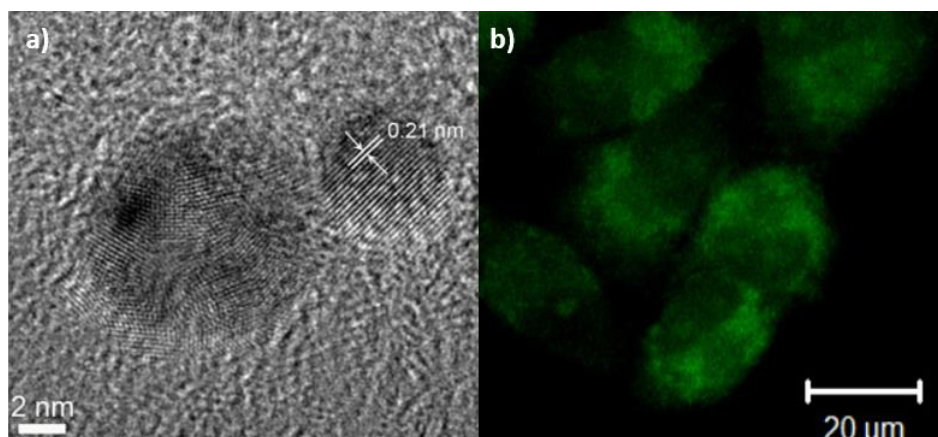
Figure 5-7 – a) TEM images of the C-dots obtained by hydrothermal treatment of lignin, and b) their application for labelling of HeLa cells. Adapted from Ref. 32.

Synthetic polymers, on the other hand, allow for more versatile approaches in C-dots preparation. As a good example of this, Liu et al.[33] used silica nanoparticles functionalized with a triblock co-polymer F127 as carriers for further polymerization of resols on their surface and then formation of C-dots through pyrolysis. The silica carriers here have a dual effect on the process, as they act as anchors and substrate for the polymerization and prevent the C-dots nanoparticles from aggregating. Some other synthetic polymers used include polyethylene glycol[34], PMA-EDY[35], and several 1-4-addition polymers[36].

5.1.3.2 _Polymers as passivating agents_

C-dots are known to have defect sites on their surface susceptible to their environment, which, may result on quenching their optical properties and limit their range of applications. One way to prevent this is to attach functional groups to C-dots' surface, and thus render more stable nanoparticles. The generation of carboxyl, carbonyl and hydroxyl groups is an efficient strategy to block quenching, but it is when this is coupled with doping atoms, like N, S, Si and P, that the highest quantum yields

are achieved[37]. Wang and coworkers[38] reported the simultaneous passivation and N-doping of C-dots with a amine-terminated PEG (Figure 5-8). This method afforded C-dots with quantum yield of 60%, and was one of the first reports to rival with the Cd-based quantum dots QYs.
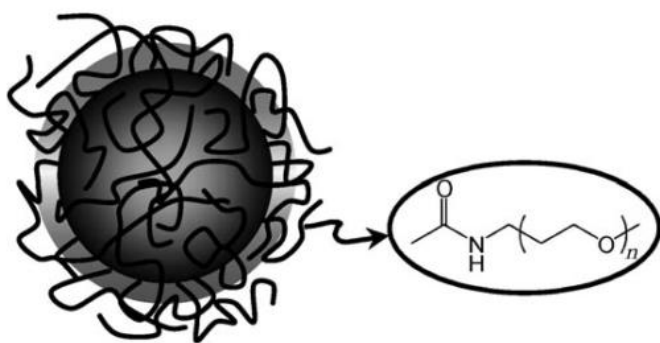
Figure 5-8 – Schematic illustration of the amine-terminated PEG surface passivated C-dots. Adapted from Ref. 38.

5.1.3.3 *C-dots/Polymer nanocomposites*

Due to their toxic-free nature, C-dots pose as the natural choice for nanocomposite systems. Most authors have focused on dispersing already synthesized C-dots in the polymers' matrix, or on adding C-dots to the polymerization process. Even if it is a fairly simple approach, it has been shown to have the potential to be of use in the fields of bioimaging and controlled drug release monitoring purposes[39], but also as a nano-sensor platform for the detection of a wide range of analytes of interest, such as heavy metals[40], mycotoxins[41] or environmental pollutants[42]. For instance, Gogoi et al.[40] described a method where they prepared a solid sensing platform based on C-dots incorporated in an agarose gel, for the detection of heavy metals, such as Cr^{6+}, Cu^{2+}, Fe^{3+}, Pb^{2+} and Mn^{2+}. The detection mechanism relied on the fact that the presence heavy metals affected the UV-Vis reflectance of the gels. Additionally, it was found that the gels also acted as filter membranes for the same heavy metals, and when C-dots were present in the system, the absorbing properties were greatly enhanced, after only 24h of being submerged in the contaminated solutions (Figure 5-9).
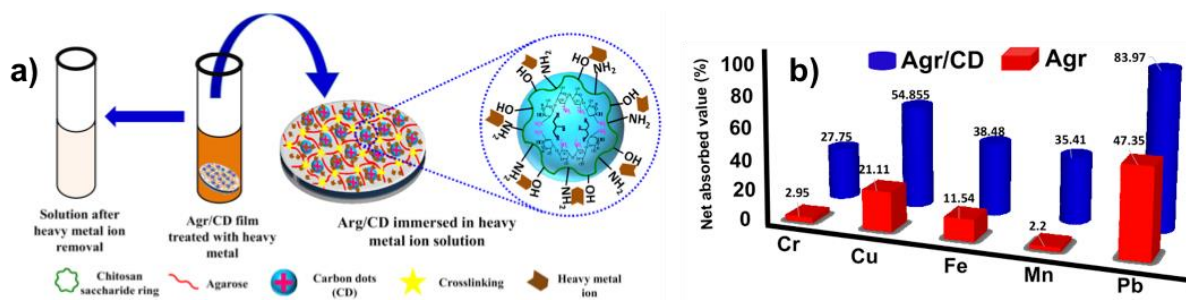
Figure 5-9 – a) The suggested mechanism for the detection of heavy metals, and b) comparison between the filtering capabilities of the Agarose gel, and agarose gel/C-dots nanocomposite system for heavy metals. Reprinted from Ref. 40.

Furthermore, Bhunia et al.[43] suggested the simultaneous preparation of C-dots and PDMS polymerization to create fluorescent films. The authors described that by using different C-dots precursors they were able to prepare films which emitted different colours within the visible range when excited under UV radiation, as depicted in Figure 5-10. This method shows clear advantages when compared to simply melt mixing the C-dots in the polymers, as it prevents the particle to particle interactions. Nonetheless it involves more complex procedures and the use of toxic solvents, such as THF, and the polymerization process may be affected by the presence of different functional groups in the surroundings.
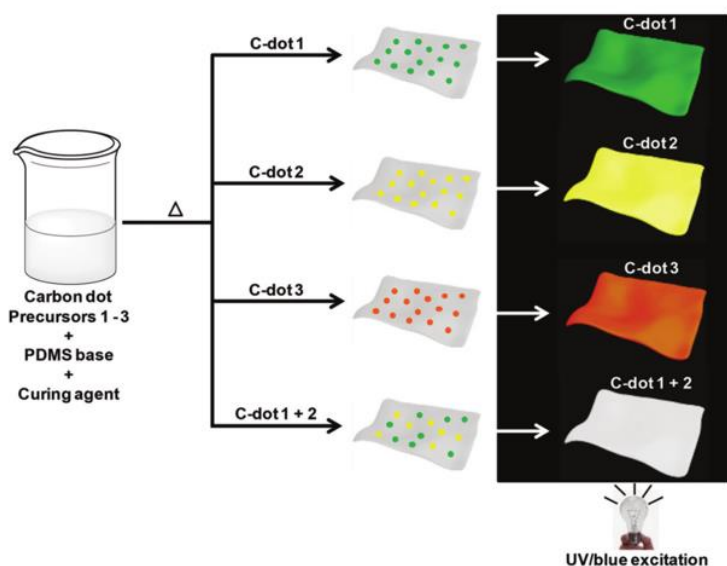
Figure 5-10 – Schematic representation of the preparation of the C-dot films, and the resulting fluorescent colours under UV radiation when different precursors are used. Adapted from Ref. 43.

5.2 *In situ* preparation of C-dots in polymers matrix

For the *in situ* preparation of C-dots in polymer matrices, minor amounts of ethanolamine (EA) were added to PE and PEG - in a weight ratio of 1 wt% (10 mg of EA/ 1 g of polymer) through melt-mixing. Polymers processed similarly, but without ethanolamine, were also prepared. For a complete protocol description please refer to section 2.3.

When investigated under a UV light, the EA-treated PE fluorescence became evident when compared with PE and similarly processed PE (without the amine), as demonstrated in Figure 5-11 a, b and c. EA-treated PEG also showed fluorescence when exposed to UV radiation (Figure 5-12 a), and when excited with different lasers was able to produce images with different colours (Figure 5-12 b, c and d).

The polymers were then analysed on a spectrofluorometer. When excited with different wavelength radiation, the EA-treated PE and PEG polymers showed an excitation-dependent behaviour (Figure 5-13 a and b), usually attributed to C-dots[26,30]. Furthermore, it was noticed that the fluorescence arose specifically from the EA treatment, as similarly processed polymers which were not treated with the amine (Figure 5-13 a and b, left plots) showed virtually no fluorescence intensity.
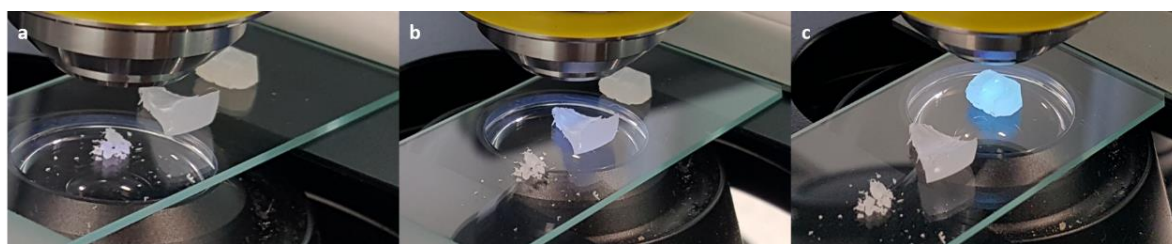
Figure 5-11 – Images of a) PE, b) processed PE (no EA treatment) and c) PEEA when exposed to an UV light.
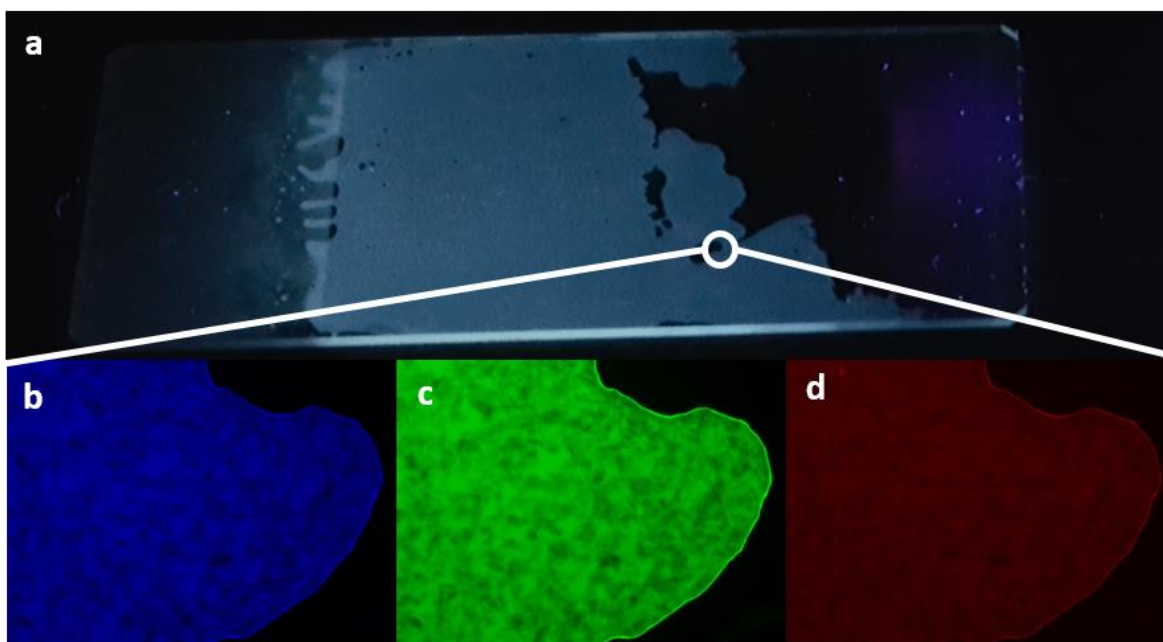
Figure 5-12 –Staining of a glass slide with EA-treated PEG a) under UV light and b), c) and d) investigated on a fluorescence microscopy under different excitation wavelengths.
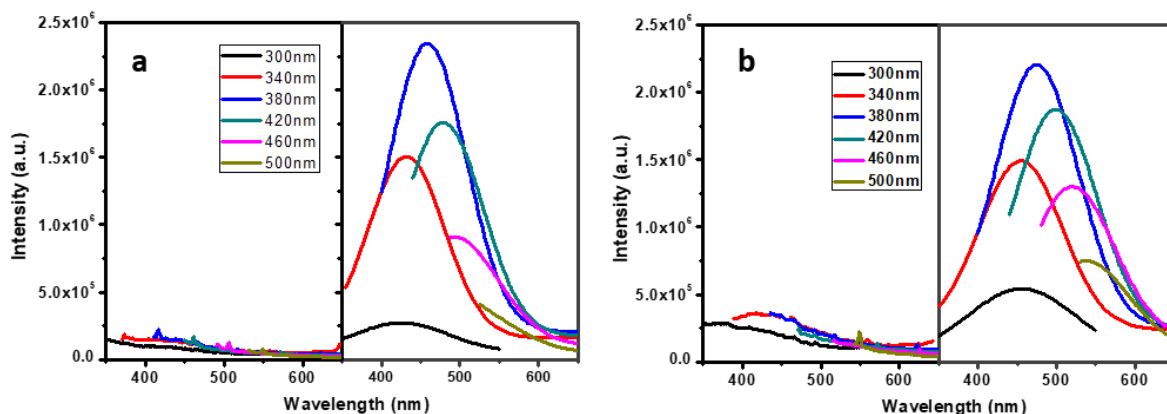
Figure 5-13 – Solid-state fluorescence spectra of a) EA-treated PE and b) EA-treated PEG, when excited with different wavelengths lasers (fluorescence spectra of the similarly processed polymers but without the EA treatment are shown on the left side of each plot).

Figure 5-14 illustrates the strategies followed to isolate the fluorescent material from the polymer. For PE, and considering its high-water insolubility, 1 g of the EA-treated PE was left vigorously stirring overnight, to try to remove the particles closer to the

surface of the polymer, and then was filtered out to remove the polymer. For PEG, given that this polymer is soluble in water and it has low molecular weight (MW = 1000 g/mol), 1 g of the EA-treated PEG was dissolved in water, and then PEG was dialyzed using a snakeskin membrane with a molecular weight cut-off of 3.5kDa. It was noticed that the fluorescent material stayed inside the membrane, which excludes the possibility of it arising from the presence of low molecular weight fluorophores.

Figure 5-15 shows a comparison between the different PEG-related samples. PEG (black line) has several characteristic peaks at 3482 cm^{-1}, 2883 cm^{-1}, 1464 cm^{-1}, 1107 cm^{-1} and 528 cm^{-1}, which are usually ascribed to O-H stretching, C-H bending, C-O stretching and O-H out-of-plane bending, respectively [44–46]. The EA-treated PEG (blue line) showed the same peaks, which may be due to the very low percentage of EA added (1%). The isolated C-dots (red line) also show very similar FTIR spectrum and this suggests a highly PEGylated surface.

The extracted C-dots from the PE matrix (Figure 5-16) show a FTIR spectrum which resembles more those of traditional C-dots, with peaks at 3324 cm^{-1}, 1642 cm^{-1}, 1399 cm^{-1} and 1056 cm^{-1}, typically ascribed to O-H stretching, C-H stretching, N-C=O symmetrical and anti-symmetrical stretching, C-H bending and C-O stretching, respectively [47–49]. Conversely, PE FTIR shows only C-H bond stretching (at 2915 and 2848 cm^{-1}, for symmetrical and anti-symmetrical, respectively), bending (1466 cm^{-1}) and rocking deformation (719 cm^{-1}).
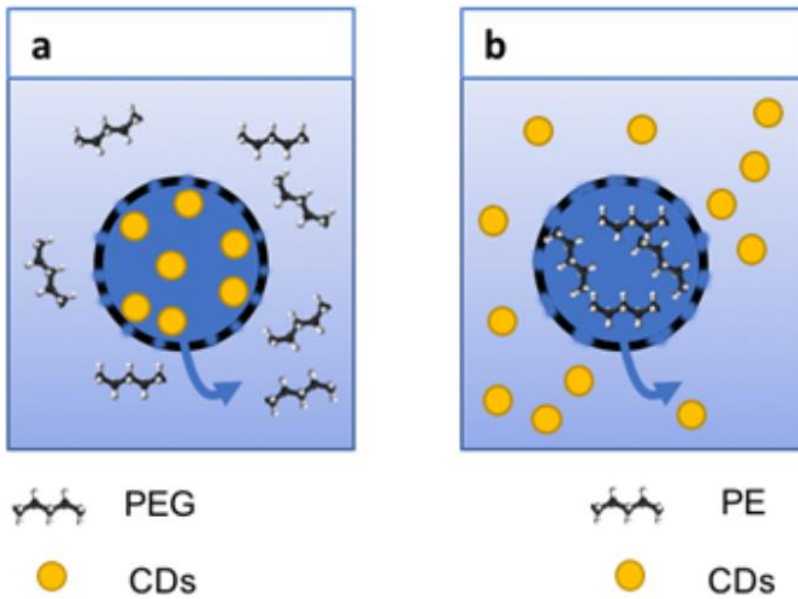
Figure 5-14 – Schematic illustration of the strategies employed to isolate the fluorescence particles from within the polymers' matrix. For PEG, a Snakeskin dialysis membrane with a molecular weight cut-off larger than that of the polymer's and smaller than the C-dots was used, in order to remove the polymer and keep the nanoparticles inside the membrane. Since PE is not soluble in water, the nanocomposites were thoroughly washed with distilled water to disperse nanoparticles closer to the surface of the polymers, and the latter were then removed by filtration.
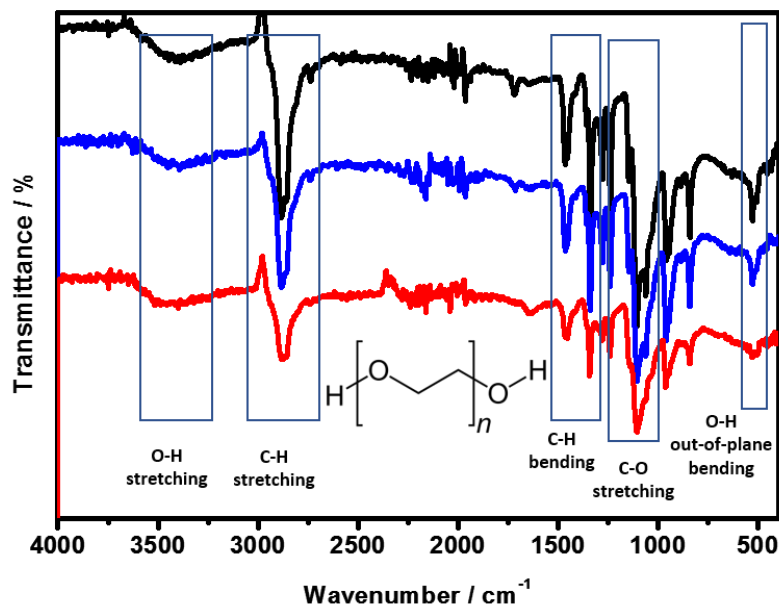
Figure 5-15 – FTIR spectra of PEG 1000 (black), EA-treated PEG (blue) and C-dots isolated from the polymer matrix (red).

141
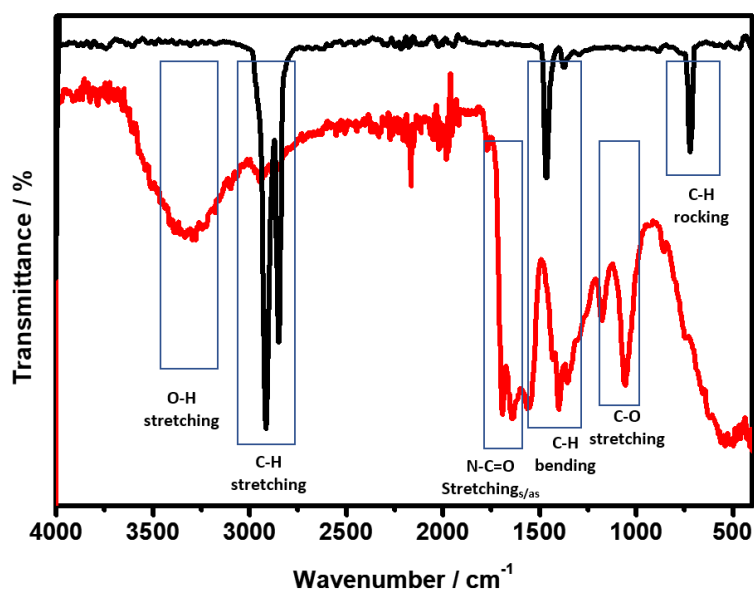
Figure 5-16 – FTIR spectrum of PE (black) and C-dots extracted from PE polymer (red).

The solutions fluorescence was analysed on a spectrofluorometer, without any further purification, and emission was recorded when samples were irradiated with different wavelength excitation lasers. For both polymers, the solutions fluorescence spectra showed excitation-dependent emission (Figure 5-17 a and b), similarly to the solid state. The fact that these fluorescent particles display high solubility and stability in water and excitation-dependent emission strongly suggests that these nanoparticles are in fact C-dots, and hence demonstrates that these nanoparticles may be prepared *in situ* without the need for any extra solvents.
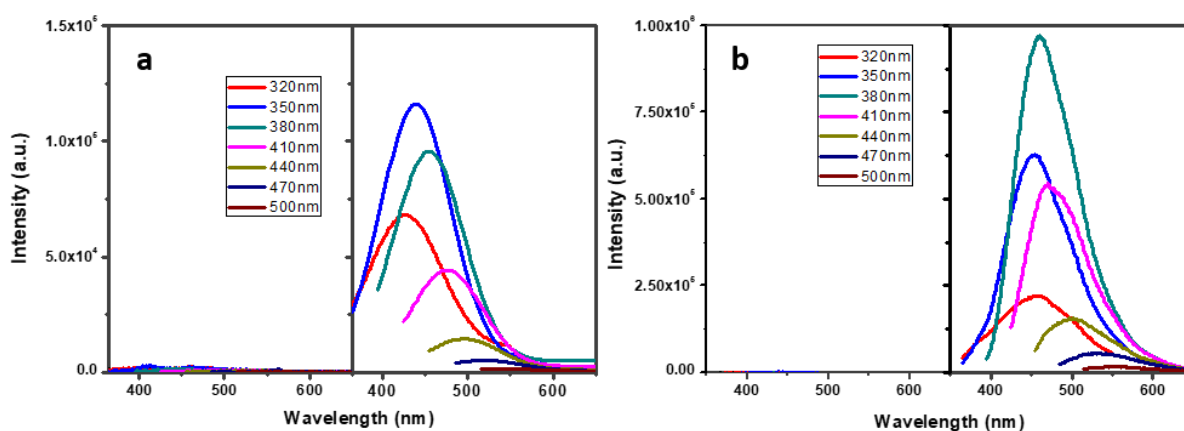
Figure 5-17 – Liquid-state fluorescence spectra of PE (a) and PEG-isolated C-dots, and comparison with processed polymers without the amine treatment, (right and left plots, respectively).

X-ray Diffraction (XRD) and Differential Scanning Calorimetry (DSC) of the as-prepared nanocomposites were analysed to investigate on how the C-dots may affect these polymers' crystallinity. In Figure 5-18 is shown the diffraction pattern of processed and C-dots/PE nanocomposites. It is clear that the orthorhombic structure of polyethylene is maintained after EA treatment, as it displays the characteristic peaks at 2Θ = 21° and 24°, which corresponds to the [100] and [200] Bragg reflections [50,51], with interplanar spacing of d = 1.7 and 1.5 nm, respectively. Being a semi-crystalline polymer, the hump at lower angles of the diffraction pattern can be attributed to scattering from the amorphous portion of polyethylene structure[52], which is calculated to be 60% for both the processed and C-dots-PE . Polyethylene glycol shows a single peak at 2Θ = 19.4°, which corresponds to an interplanar spacing of d = 1.8 nm, and shows an amorphous structure possibly due to its low mw (Figure 5-19).
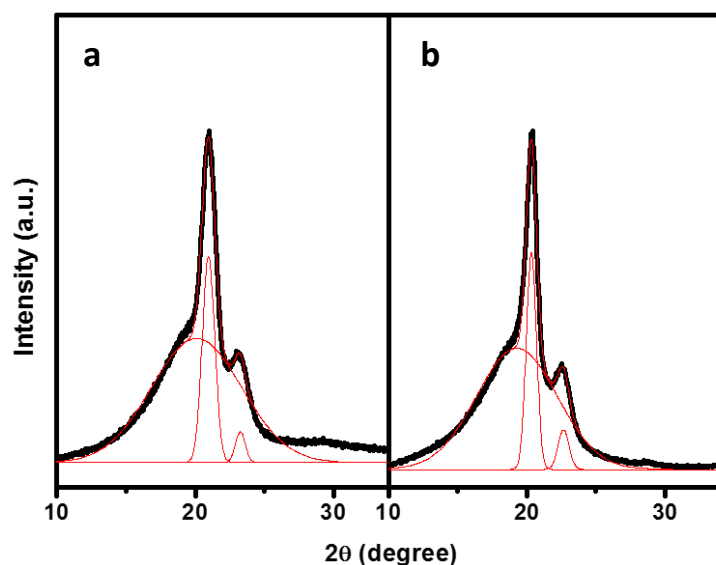
Figure 5-18 – X-ray diffraction patterns of processed PE polymers a) without EA-treatment and b) with EA treatment.
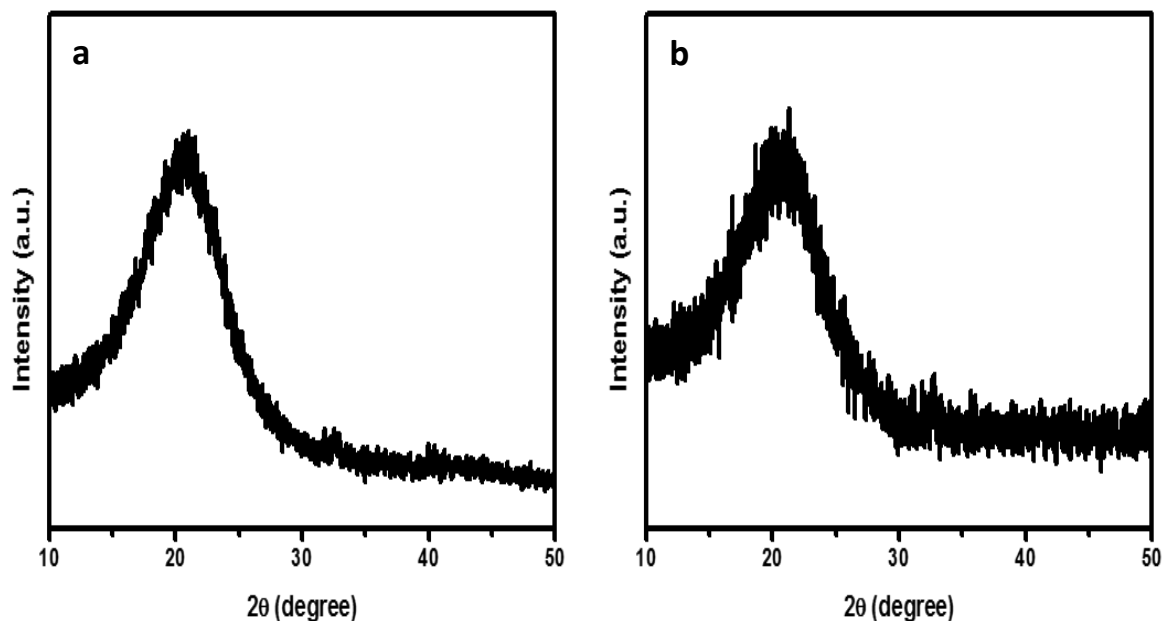
Figure 5-19 - X-ray diffraction patterns of processed PEG polymers without and after the EA treatment.

Each polymer was then exposed to temperatures above their annealing point to erase their thermal history. From the second heating curves from DSC data , it is possible to conclude that neither the processing at high temperatures (Figure 5-20 a and c), nor the EA treatment (Figure 5-20 b and d), produced any significant effects on the polymers' crystallization behaviour, since in both cases the melting point decreased less than 1°C, and the enthalpy change was less than 2 and 1 J/g for PE and PEG respectively. These values are in agreement with previous reports for similar polymers[53,54].
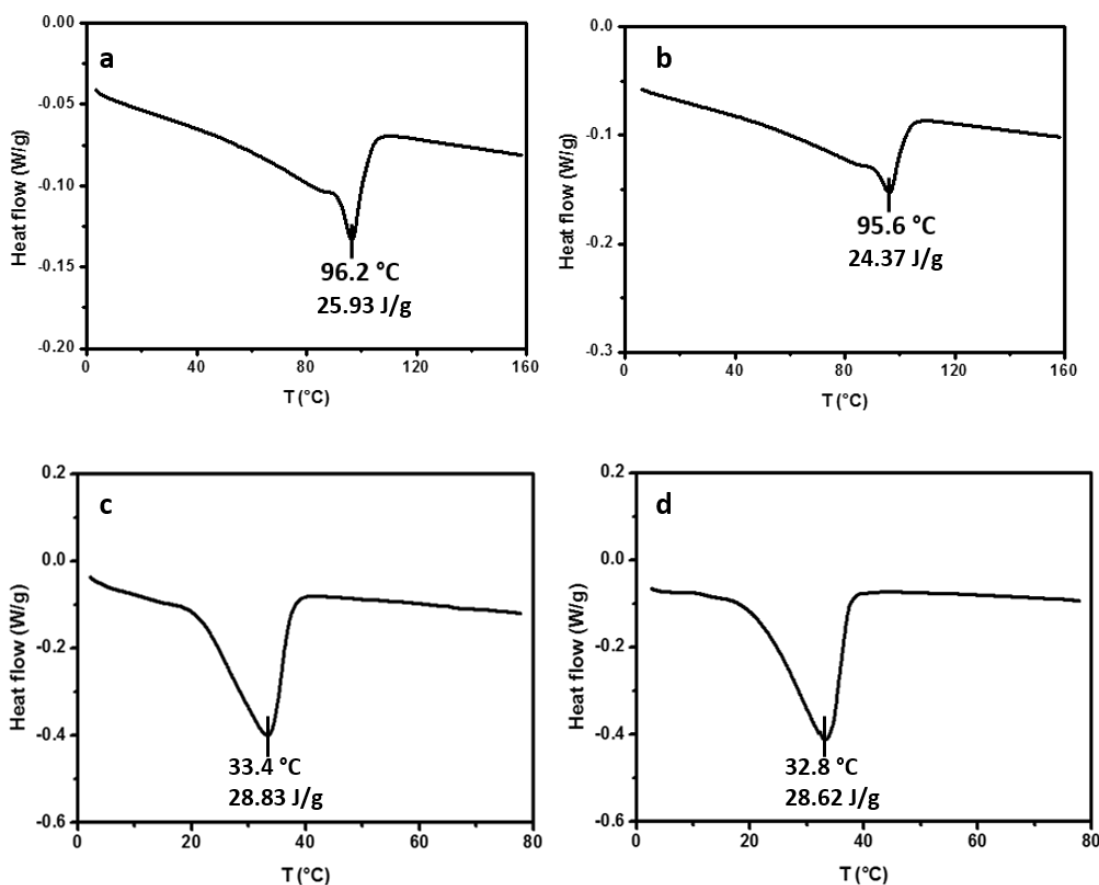
Figure 5-20 – Second heating curves for a) and b) PE and c) and d) PEG, and comparison between polymers after being processed (a and c) and after being EA-treated (b and d).

The main reason behind the choice of these two polymers relate to their different nature (molecular weight and water solubility) and frequent applications. PE, for example, is one the of most common plastics in use today. To prevent its persistence in the environment, it can be recycled by means of extrusion at high temperatures[55,56]. Several materials may be added to the recycling polymers during extrusion, designated as downstream feeding, which may include liquid feed. Even though this might be better suited for twin screw extruders, if the liquid is mixed with fractions of the polymer before extrusion, it might also be possible for single screw extruders[57]. Hence, in principle, the method reported here would be compatible with the recycling process for this type of polymers. Moreover, it was noticed that by adding increasing amounts of the carbon-rich precursor to PE, the solid-state fluorescence was greatly enhanced until a plateau was reached at around 5 wt%, as demonstrated in Figure 5-21.
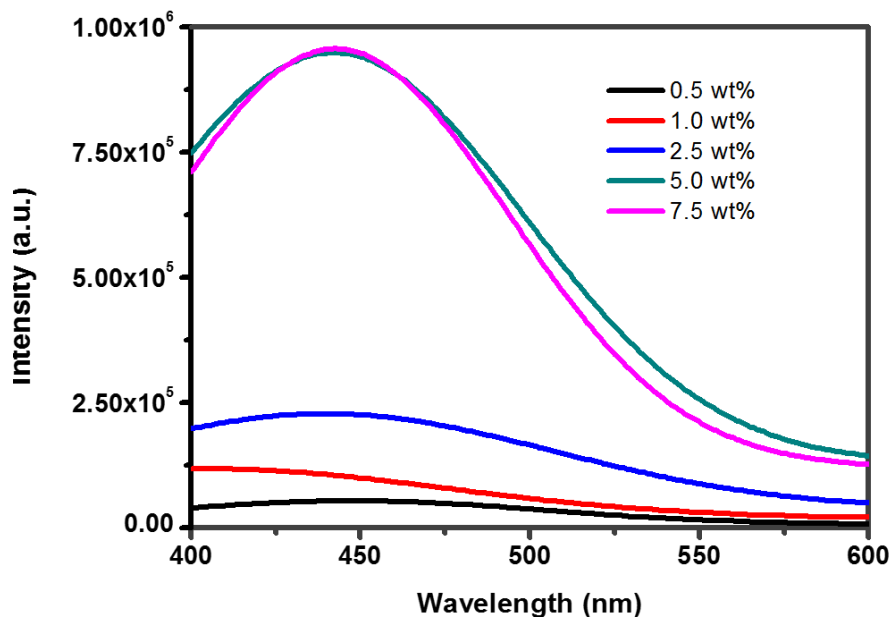
Figure 5-21 – Solid state fluorescence spectra of C-dots extracted from PE matrix with increasing initial weight percentage of EA.

Even, though, PEG has not had such impact in consumer products, it is considered an important polymer from a biomedical research point of view. For instance, reports have suggested the use of PEG for controlled drug release[58] and monitoring, to which fluorophores may be added. This allows for a better understanding of the whole drug release process. However, these fluorophores are usually susceptible to decomposing in hostile environments, and usually involve using to other nanoparticles and their associated hazardous risks. We suggest that C-dots may be incorporated in the PEG matrix without affecting its water solubility. Since most applications take advantage of this water solubility, the effect of EA's initial concentration in the liquid state fluorescence was further investigated. Figure 5-22 shows that, similarly to PE, an increase in the intensity occurs with increasing weight percentage of EA up to a point where a plateau is reached around 5 wt%.
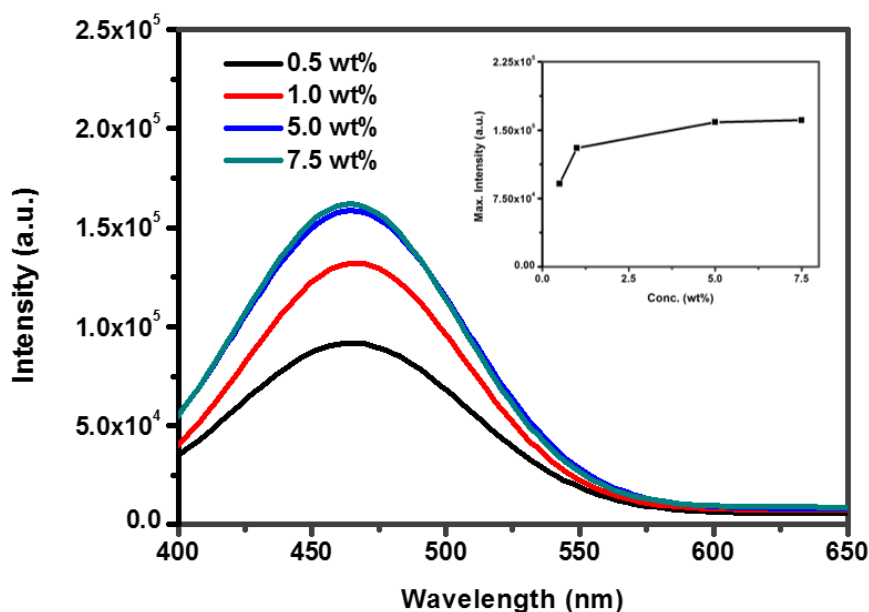
Figure 5-22 – Liquid state fluorescence spectra of C-dots isolated from PEG matrix with increasing initial weight percentage of EA.

5.3 Conclusion

In conclusion, we report a simple, cost-effective, versatile and non-toxic strategy for the in-situ preparation of C-dots in different polymers. This method imparted polyethylene and polyethylene glycol with these nanoparticles multi-coloured emission both in the liquid and solid states. By using ethanolamine as the C-dots precursor, through a melt mixing process, solvents are avoided altogether. The results here presented suggest that this protocol may be suitable as an "add-on" during recycling of polymers as the only conditions required (mixing and high temperatures) are already part of the extrusion procedure. EA, as a liquid may also be added to the extruder, which would facilitate the recycled polymers to find new types of applications. Furthermore, increasing amounts of precursor also afforded enhanced fluorescence in the polymers (up to a 5 wt% of EA, where a plateau is reached). For polymers soluble in water, it is suggested that their optical properties would allow for better monitoring of controlled drug release and for bioimaging applications.

Due to the different nature of the polymers tested – molecular weight of PE = 35kDa, against 1kDa of PEG, and PEG being highly soluble in water and PE not being soluble at all; the results here presented suggest that this method may be used for the *in-situ* preparation of C-dots on a wider range of polymers.

5.4 References

1   Kim, H. N., Guo, Z., Zhu, W., Yoon, J. & Tian, H. Recent progress on polymer-based fluorescent and colorimetric chemosensors. *Chem. Soc. Rev.* **40,** 79–93 (2011).

2.   Wu, C. & Chiu, D. T. Highly fluorescent semiconducting polymer dots for biology and medicine. *Angew. Chemie - Int. Ed.* **52,** 3086–109 (2013).

3.   Alvarez, A., Costa-Fernández, J. M., Pereiro, R., Sanz-Medel, A. & Salinas-Castillo, A. Fluorescent conjugated polymers for chemical and biochemical sensing. *TrAC - Trends Anal. Chem.* **30,** 1513–25 (2011).

4.   Thomas, S. W., Joly, G. D. & Swager, T. M. Chemical sensors based on amplifying fluorescent conjugated polymers. *Chem. Rev.* **107,** 1339–86 (2007).

5.   Rasmussen, S. C. Designing Organic Semiconducting Materials: The Promise of Flexible Electronics. 1–6 (2011). Available at: http://www.azom.com/article.aspx?ArticleID=5591.

6.   Kim, J., McQuade, D. T., McHugh, S. K. & Swager, T. M. Ion-specific aggregation in conjugated polymers: Highly sensitive and selective fluorescent ion chemosensors. *Angew. Chemie - Int. Ed.* **39,** 3868–72 (2000).

7.   Miyata, M. & Chujo, Y. π-Conjugated Organoboron Polymer as an Anion Sensor. *Polym. J.* **34,** 967–69 (2002).

8.   Kimura, M., Horai, T., Hanabusa, K. & Shirai, H. Fluorescence chemosensor for metal ions using conjugated polymers. *Adv. Mater.* **10,** 459–62 (1998).

9.   Bangcuyo, C. G. *et al.* Quinoline-Containing, Conjugated Poly(aryleneethynylene)s: Novel Metal and H^{+}-Responsive Materials. Macromolecules **35,** 1563–68 (2002).

10. Wang, B. Y., Liu, X. Y., Hu, Y. L. & Su, Z. X. Synthesis and photophysical behavior of a water-soluble coumarin-bearing polymer for proton and Ni^{2+} ion sensing. *Polym. Int.* **58,** 703–09 (2009).

11. Grabchev, I., Sali, S., Betcheva, R. & Gregoriou, V. New green fluorescent polymer sensors for metal cations and protons. *Eur. Polym. J.* **43,** 4297–305 (2007).

12. Liu, Y., Meng, L., Lu, X., Zhang, L. & He, Y. Thermo and pH sensitive fluorescent polymer sensor for metal cations in aqueous solution. *Polym. Adv. Technol.* **19,** 137–43 (2008).

13. Li, N. *et al.* A polymeric chemosensor for Fe^{3+} based on fluorescence quenching of polymer with quinoline derivative in the side chain. *Mater. Chem. Phys.* **114,** 339–43 (2009).

14. Kim, T. H. & Swager, T. M. A Fluorescent Self-Amplifying Wavelength-Responsive Sensory Polymer for Fluoride Ions. *Angew. Chemie - Int. Ed.* **42,** 4803–06 (2003).

15. Rajesh, Ahuja, T. & Kumar, D. Recent progress in the development of nano-structured conducting polymers/nanocomposites for sensor applications. *Sensors Actuators, B Chem.* **136,** 275–86 (2009).

16. Kango, S. *et al.* Surface modification of inorganic nanoparticles for development of organic-inorganic nanocomposites - A review. *Prog. Polym. Sci.* **38,** 1232–61 (2013).

17. Hong, R. Y. *et al.* Synthesis, surface modification and photocatalytic property of ZnO nanoparticles. *Powder Technol.* **189,** 426–32 (2009).

18. Shirai, Y., Kawatsura, K. & Tsubokawa, N. Graft polymerization of vinyl monomers from initiating groups introduced onto polymethylsiloxane-coated titanium dioxide modified with alcoholic hydroxyl groups. *Prog. Org. Coatings* **36,** 217–24 (1999).

19. Rong, M. Z., Ji, Q. L., Zhang, M. Q. & Friedrich, K. Graft polymerization of vinyl monomers onto nanosized alumina particles. *Eur. Polym. J.* **38,** 1573–82 (2002).

20. Kobayashi, M., Matsuno, R., Otsuka, H. & Takahara, A. Precise surface structure control of inorganic solid and metal oxide nanoparticles through surface-initiated radical polymerization. *Sci. Technol. Adv. Mater.* **7,** 617–28 (2006).

21. Hashimoto, M., Takadama, H., Mizuno, M. & Kokubo, T. Enhancement of mechanical strength of TiO2/high-density polyethylene composites for bone repair with silane-coupling treatment. *Mater. Res. Bull.* **41,** 515–24 (2006).

22. Waldron, D. L., Preske, A., Zawodny, J. M., Krauss, T. D. & Gupta, M. C. Lead selenide quantum dot polymer nanocomposites. *Nanotechnology* **26,** 1–6 (2015).

23. Sarkar, K. *et al.* Selective zinc(II)-ion fluorescence sensing by a functionalized mesoporous material covalently grafted with a fluorescent chromophore and consequent biological applications. *Adv. Funct. Mater.* **19,** 223–34 (2009).

24. Chen, J., Jin, Y., Fahruddin, N. & Zhao, J. X. Development of gold nanoparticle-enhanced fluorescent nanocomposites. *Langmuir* **29,** 1584–91 (2013).

25. Zhang, J., Xu, S. & Kumacheva, E. Photogeneration of fluorescent silver nanoclusters in polymer microgels. *Adv. Mater.* **17,** 2336–40 (2005).

26. Kelarakis, A. From highly graphitic to amorphous carbon dots: A critical review. *MRS Energy Sustain.* **1,** 1–15 (2014).

27. Krysmann, M. J., Kelarakis, A. & Giannelis, E. P. Photoluminescent carbogenic nanoparticles directly derived from crude biomass. *Green Chem.* **14,** 3141–45 (2012).

28. Zhu, C., Zhai, J., Dong, S., Zhai, J. & Dong, S. Bifunctional fluorescent carbon nanodots: green synthesis via soy milk and application as metal-free electrocatalysts for oxygen reduction. *Chem. Commun. (Camb).* **48,** 9367–69 (2012).

29. Zhou, Y., Sharma, S., Peng, Z. & Leblanc, R. Polymers in Carbon Dots: A Review. *Polymers (Basel).* **9,** 1–20 (2017).

30. Baker, S. N. & Baker, G. A. Luminescent Carbon Nanodots : Emergent Nanolights. *Angew. Chem . Int. Ed* **49,** 6726–44 (2010).

31. Chowdhury, D., Gogoi, N. & Majumdar, G. Fluorescent carbon dots obtained from chitosan gel. *RSC Adv.* **2,** 12156–59 (2012).

32. Chen, W., Hu, C., Yang, Y., Cui, J. & Liu, Y. Rapid synthesis of carbon dots by hydrothermal treatment of lignin. *Materials (Basel).* **9,** 1–8 (2016).

33. Liu, R. *et al.* An aqueous route to multicolor photoluminescent carbon dots using silica spheres as carriers. *Angew. Chemie - Int. Ed.* **48,** 4598–601 (2009).

34. Li, H. *et al.* Carbon dots from PEG for highly sensitive detection of levodopa. *J. Mater. Chem. B* **3,** 2378–87 (2015).

35. Zhu, B. *et al.* Preparation of carbon nanodots from single chain polymeric nanoparticles and theoretical investigation of the photoluminescence mechanism. *J. Mater. Chem. C* **1,** 580–86 (2013).

36. Jiang, Z. *et al.* Photoluminescent carbon dots from 1,4-addition polymers. *Chemistry* **20,** 10926–31 (2014).

37. Zhou, Y., Sharma, S., Peng, Z. & Leblanc, R. Polymers in Carbon Dots: A Review. *Polymers (Basel).* **9,** 1–20 (2017).

38. Wang, X. *et al.* Bandgap-like strong fluorescence in functionalized carbon nanoparticles. *Angew. Chemie - Int. Ed.* **49,** 5310–14 (2010).

39. Sachdev, A., Matai, I. & Gopinath, P. Carbon dots incorporated polymeric hydrogels as multifunctional platform for imaging and induction of apoptosis in lung cancer cells. *Colloids Surfaces B Biointerfaces* **141,** 242–52 (2016).

40. Gogoi, N., Barooah, M., Majumdar, G. & Chowdhury, D. Carbon dots rooted agarose hydrogel hybrid platform for optical detection and separation of heavy metal ions. *ACS Appl. Mater. Interfaces* **7,** 3058–67 (2015).

41. Xu, L., Fang, G., Pan, M., Wang, X. & Wang, S. One-pot synthesis of carbon dots-embedded molecularly imprinted polymer for specific recognition of sterigmatocystin in grains. *Biosens. Bioelectron.* **77,** 950–56 (2016).

42. Hao, T. *et al.* An eco-friendly molecularly imprinted fluorescence composite material based on carbon dots for fluorescent detection of 4-nitrophenol. *Microchim. Acta* **183,** 2197–203 (2016).

43. Bhunia, S. K., Nandi, S., Shikler, R. & Jelinek, R. Tuneable light-emitting carbon-dot/polymer flexible films prepared through one-pot synthesis. *Nanoscale* **8,** 3400–06 (2016).

44. Snavely, D. L. & Dubsky, J. Near-IR spectra of polyethylene, polyethylene glycol, and polyvinylethyl ether. *J. Polym. Sci. Part A Polym. Chem.* **34,** 2575–

79 (1996).

45.   Bhattarai, N., Ramay, H. R., Gunn, J., Matsen, F. A. & Zhang, M. PEG-grafted chitosan as an injectable thermosensitive hydrogel for sustained protein release. *J. Control. Release* **103,** 609–24 (2005).

46.   Shameli, K. *et al.* Synthesis and characterization of polyethylene glycol mediated silver nanoparticles by the green method. *Int. J. Mol. Sci.* **13,** 6639–50 (2012).

47.   Stobinski, L. *et al.* Multiwall carbon nanotubes purification and oxidation by nitric acid studied by the FTIR and electron spectroscopy methods. *J. Alloys Compd.* **501,** 77–84 (2010).

48.   Cui, X. *et al.* A fluorescent biosensor based on carbon dots-labeled oligodeoxyribonucleotide and graphene oxide for mercury (II) detection. *Biosens. Bioelectron.* **63,** 506–12 (2015).

49.   Fan, Z., Li, S., Yuan, F. & Fan, L. Fluorescent graphene quantum dots for biosensing and bioimaging. *RSC Adv.* **5,** 19773–89 (2015).

50.   Aggarwal, Sundar L; Sweeting, O. J., Aggarwal, S. L. & Sweeting, O. J. Polyethylene : preparation, structure, and properties. *Chem. Rev.* **57,** 665–742 (1957).

51.   Wei, P. & Bai, S. Fabrication of a high-density polyethylene/graphene composite with high exfoliation and high mechanical performance via solid-state shear milling. *RSC Adv.* **5,** 93697–705 (2015).

52.   Kakudo, M. & Ullman, R. Polyethylene crystallinity from x-ray studies. *J. Polym. Sci.* **45,** 91–104 (1960).

53.   Atkinson, C. M. L. & Richardson, M. J. Thermodynamic properties of ideally crystalline polyethylene. *Trans. Faraday Soc.* **65,** 1764–73 (1968).

54.   Morris, K. R., Knipp, G. T. & Serajuddin, A. T. M. Structural Properties of Polyethylene Glycol-Polysorbate 80 Mixture, a Solid Dispersion Vehicle. *J. Pharm. Sci.* **81,** 1185–88 (1992).

55.   Hamad, K., Kaseem, M. & Deri, F. Recycling of waste from polymer materials: An overview of the recent works. *Polym. Degrad. Stab.* **98,** 2801–12 (2013).

56.   Jin, H., Gonzalez-Gutierrez, J., Oblak, P., Zupancic, B. & Emri, I. The effect of extensive mechanical recycling on the properties of low density polyethylene. *Polym. Degrad. Stab.* **97,** 2262–72 (2012).

57.   Giles, H. F., Wagner, J. R. & Mount, E. M. *Extrusion:The Definitive Processing Guide and Handbook.* (2005).

58.   Otsuka, H., Nagasaki, Y. & Kataoka, K. PEGylated nanoparticles for biological and pharmaceutical applications. *Adv. Drug Deliv. Rev.* **64,** 246–55 (2012).

6 Summary and Outlook

In this thesis, it has been suggested novel applications for C-dots. They pose as toxic-free alternatives to other types of nanomaterials, such as QDs. Their PL properties are clearly one of their greatest assets and, so far, no other materials have been found to behave similarly.

For instance, in the field of fingerprint recovery, there is still a lack for a single method (or type of powder) that can be applied to different crime scene scenarios. Forensic experts are then required to carry several fingerprint powder pots into crime scenes. Furthermore, should a fingerprint be developed with the "wrong" powder, or not sufficient contrast be achieved, that would result in a piece of evidence being lost. By using C-dots based nanopowders, not only they maintain the necessary flowability for well resolved fingerprints (as proved by AFIS results), fingerprint experts would be able to tune the powder colours in order to achieve best contrast, just by adjusting the excitation wavelength of the laser source. Additionally, it has been shown that C-dots may be diluted in other non-UV absorptive powders, which suggests that they could be used as additives to fingerprint powders already in use in forensic practices. Future work could involve the preparation of C-dots with different types of functional groups on their surface. For instance, by testing other types of white fingerprint powders, currently used in forensic investigations, may help improve the resolution obtained with the C-dots hybrid nanopowders. Furthermore, the attachment of hydrophobic functional groups could provide even better resolved fingerprints due to adhesion to the fatty acids on the fingerprints

Another forensic application explored here was the use of C-dots-based materials as anti-counterfeit tools. Counterfeit is one of the crimes with greatest economic impact in current society. Most methods suggested require complex, costly and often-times toxic reagents and make their final application as anti-counterfeit tools unviable. Carbogenically coated silica (C-SiO$_2$) have been demonstrated to produce toxic-free, cost-efficient and highly complex patterns which are here suggested to be efficient tools for anti-counterfeit purposes. Since the patterns are easily prepared they may be deposited in different surfaces, which could prove to be convenient for authentication

in a wide variety of products. Moreover, they showed no effects when exposed to high temperatures, and the patterns were maintained intact. The excitation-dependent emission of C-dots was also verified which afforded these nanotags another level of complexity. Next steps would involve a more interdisciplinary approach, as the development of software recognition systems would render this a more reliable approach. Due to the visual characteristics of the nanotags, we believe that they could be informatically "translated" to a binary code system, which would afford their reading and recognition easier, faster and potentially portable. Moreover, if fluorophores were to be added to the Silica/C-dots core-shell suspensions, it may provide another level of complexity at a specific wavelength (fluorophore $\lambda_{emission}$), as it could make these pattern even more difficult to replicate.

The *in situ* preparation of C-dots proved to be a versatile approach to induce PL in different polymer matrices. Current methods to do this require the use of costly materials, like conjugated polymers or extensive procedures. Here we suggested the use of ethanolamine as the carbon-rich precursor, and the *in situ* preparation of C-dots by melt mixing in polymers matrices. PE, as one of the most used polymers for common household plastics, has a significant impact in the environment, and thus its recycling is of high importance. In principle, the results here described suggest that this methodology would be compatible with this polymers recycling. Ethanolamine could be added to the extrusion process in very low ratios (1 wt%) and fluorescent polymers could be obtained at reduced costs, which would afford them new applications. On the other hand, PEG is considered an important polymer for biomedical research and is frequently used as surface passivator for nanoparticles and other fluorescent materials to afford them more biocompatible. This simplet approach has been demonstrated to achieve both with reduced costs and toxicity: to form the fluorescent pegylated nanoparticles. We suggest here that this method could be potentially employed to induce fluorescence to other matrices (not only polymers but, for instance, clays as well), so future work would involve the use of different materials to test the full potential of this procedure.

7 Attachments

7.1 Papers published during PhD period

Carbon dot based nanopowders and their application for fingerprint recovery†

D. Fernandes,[a] M. J. Krysmann[b] and A. Kelarakis*[a]

The incorporation of a minor amount of carbogenic nanoparticles into powder compositions imparts remarkable colour-tuneability, without compromising the flowability. In a proof-of-concept demonstration we report the use of these hybrid nanopowders for the visual enhancement of latent fingerprints where they effectively resolve issues arising from poor contrast against multi-coloured or patterned backgrounds.

Carbogenic nanoparticles (otherwise known as C-dots) represent a rapidly emerging class of high performance photoluminescent (PL) nanoemitters showing great potential for multicolour printing, bioimaging, selective sensors and catalysis.[1–6] Unlike conventional polyaromatic dyes and heavy metal based quantum dots, C-dots are biocompatible and non-toxic to humans and the environment.[7] In addition, C-dots can be synthesized following cost-efficient and, to a certain extent, green protocols. With respect to the starting materials and the synthetic route, the structure of C-dots, their graphitization degree and their elemental content (in carbon, oxygen and heteroatoms) vary significantly, giving rise to an expanding gallery of photoactive materials.[8] To that end, graphitic C-dots are facilely produced by oxidation or electro-oxidation of carbon nanotubes or graphite, while amorphous C-dots are conveniently derived *via* thermal or hydrothermal treatments of carbon rich precursors such as polymers,[9] carbohydrates,[10] grass,[11] hair fibers,[12] fruit juice[13] and soy milk.[14] Likewise, C-dots based nanocomposites are formed, for example, a nanomaterial that exhibits supreme magnetic and fluorescence properties is derived by thermal treatment of carbon precursors in the presence of iron oxide.[15]

A large body of the literature lays emphasis on the exceptional photoluminescence properties of aqueous dispersions of C-dots. Systematic studies indicate that surface passivation of C-dots (for example *via* amine[16] or sodium borohydrate[17] treatment) not only enhances the colloidal stability, but also improves the fluorescence intensity. Despite intensive efforts, the origin of their intriguing photophysical behaviour is still not well understood and contributions stemming from either the carbogenic core[18] or the surface functionalities[19] have been identified. It has been demonstrated that isolated sp^2 centres placed in a sp^3 network show inherent photoluminescence characteristics and those defects structurally resemble the carbon atoms placed on the surface of C-dots.[20]

By comparison, much less information is available regarding the solid-state physics and the photoluminescence performance of anhydrous C-dots. In this study we report for the first time the preparation of hybrid nanopowders containing low concentration levels of C-dots (typically below 1 wt%) homogenously dispersed within the major phase (silica, titania, laponite, white fingerprint powder). Those materials combine the distinct advantages arising from the supreme flowability of the major powder component and the unique photoluminescence of C-dots.

In particular, we demonstrate the use of the nanopowders for the recovery of latent fingerprints, *e.g.* poorly visible impressions unintentionally deposited at crime scenes. Fingerprint dusting visually enhances those marks so that they can be photographed and processed for identification purposes. Forensic analysis compares the recovered fingerprints with those available in national and international databases populated by a large set of exemplar fingerprints recorded *via* digital imaging or ink fingerprinting.

It is interesting to note that water-based formulations based on C-dots have been shown to be highly effective for ink fingerprinting.[21–23] This process refers to the intentional recording of fingerprints by pressing the ink covered fingertips against a suitable substrate.

Our work, however, centres on dusting (using a brush) chance impressions found at crime scenes, as opposed to previous reports

[a] *Centre for Materials Science, School of Forensic and Investigative Sciences, University of Central Lancashire, Preston PR1 2HE, UK. E-mail: akelarakis@uclan.ac.uk, antonios.kelarakis@gmail.com*

[b] *School of Pharmacy and Biosciences, University of Central Lancashire, Preston PR1 2HE, UK*

† Electronic supplementary information (ESI) available: Detailed experimental section, TEM images of C-dots, photoluminescence spectra of aqueous dispersions and fluorescence images of fingerprints in various surfaces. See DOI: 10.1039/c5cc00468c

156
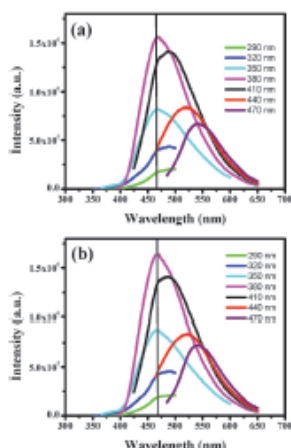
Fig. 1 Photoluminescence spectra (under different excitation wavelengths) of aqueous dispersions containing (a) 13 µg ml⁻¹ C-dots and (b) 13 µg ml⁻¹ C-dots in the presence of (150 times higher concentration) silica nanoparticles.

Fig. 2 Fluorescence microscopy images of 0.7 wt% C-dot–silica nanopowder obtained under (a) UV violet, (b) blue and (c) green excitation wavelength.

that focus on creating exemplar ink fingerprints. In other words, we demonstrate for the first time the use of C-dots based powders for latent fingerprint enhancement. Significantly, this report expands the application spectrum of C-dots beyond the liquid phase dispersions and polymer composites, by introducing a novel class of non-toxic, yet colour tuneable and highly fluorescent hybrid nanopowders.

We have previously reported that controlled thermal annealing of a mixture of citric acid and ethanolamine leads to a series of photoactive materials with dual photoluminescence emission.[24] In the early stages of pyrolysis intermolecular condensation generates amide rich functionalities that are progressively consumed to generate carbogenic nanocores. As a result, the C-dots prepared at 230 °C have an average diameter of 19 ± 2 nm (ESI,† Fig. S1) and show an excitation wavelength independent emissive contribution stemming from amide groups (note the vertical line in Fig. 1a for the excitation wavelengths 350 and 380 nm) and an excitation wavelength dependent emissive mode characteristic of their carbogenic nature (note the peaks in Fig. 1a corresponding to excitation wavelengths 410, 440, 470 nm). Self-passivation is an important feature of this type of materials, given that surface polar groups formed *in situ* during pyrolysis enhance both the colloidal stability and the photoluminescence properties of the aqueous dispersions.

Fig. 1 compares the fluorescence spectra of an aqueous dispersion containing 13 µg ml⁻¹ C-dots in the presence of a large excess of silica nanoparticles (Fig. 1b) with the silica-free dispersion (Fig. 1a). It is clear that photoluminescence is not significantly quenched by the silica nanoparticles and both emissive modes are active. This effect points to the lack of specific particle–particle interactions that could alter the charge distribution on the surface of C-dots. (The fluorescence spectra of C-dots–fingerprint powder and C-dots–laponite aqueous dispersions are shown in the ESI,† Fig. S2a and b, respectively.)
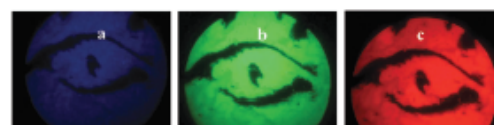
The C-dots–SiO₂–water system was freeze-dried, yielding a fine nanopowder having 0.7 wt% carbogenic content. Fig. 2 suggests that the hybrid nanopowder adopts different colours when exposed to different types of incident radiation. For reference, we note that the preparation of fine powder purely from C-dots is rather challenging due to the strong tendency of carbogenic nanoparticles to aggregate. It has been reported that solid powder of C-dots is not photoactive possibly due to extensive clustering and self-quenching effects.[25]

The remarkable photophysical behaviour of the hybrid nanopowders shows great potential for a versatile range of technologically important applications. In a proof-of-concept demonstration, we explore here the use of the hybrid nanopowders for latent fingerprint detection. It suffices to say that fingerprint analysis remains the cornerstone of forensic investigation, which has provided reliable evidence for more than a century. Recent approaches in fingerprint development capitalise on the ability of nanoparticles not only to visually enhance fingerprints, but also to detect certain analytes within them.[26–28] Many types of fingerprint powders[29] have been suggested throughout the years including aluminium flakes, magnetic powders, luminescent powders and, more recently, formulations containing gold nanoparticles, or semiconductor quantum dots (which are generally considered to be toxic[30]). However, there is a persisting need for the development of an environmentally benign, low cost and universal fingerprint powder suitable for being used in the crime scene that will ideally provide a strong contrast against a variety of radically different backgrounds.

Owing to their minor C-dot content, the hybrid nanopowders retain the supreme flowability of the silica nanoparticles and can be easily applied with a brush to a fresh fingerprint deposited on a glass microscope slide. As seen in Fig. 3, the hybrid nanopowder reveal high quality images that show well-resolved ridge patterns that meet the requirements for individual identification for forensic purposes.

Significantly, the developed fingerprints exhibit colour-tuneability in response to the wavelength of the incident beam. In Fig. 3 it can be clearly seen that the fingerprints appear to be blue, green or red when they are excited in the violet, blue and green wavelength regions, respectively. Likewise, color-tuneable patterns were obtained using 0.7 wt% C-dots–laponite for fingerprints deposited on glass and metal surfaces (ESI,† Fig. S3 and S4, respectively). In contrast, no signal is detected in the absence of C-dots in an otherwise identical experiment (ESI,† Fig. S5).

This remarkable optical behaviour offers significant advantages to forensic investigation by circumventing issues related to strong background interference arising from textured or
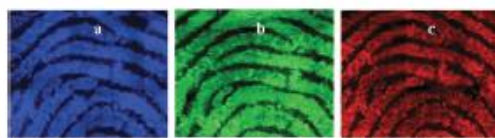
Fig. 3 Fluorescence microscopy images of fingermarks developed with hybrid nanopowder (0.7 wt% C-dot–silica) on a glass slide under (a) violet, (b) blue and (c) green excitation wavelength. A number of fluorescence images (captured at 100× magnification) have been merged via the Photoshop software to create the larger images displayed.

Fig. 5 AFIS analysis for fresh fingerprints developed using (a) a commercial white fingerprint powder and (b) a C-dot based hybrid nanopowder.

multi-coloured surfaces. To that end, a fingerprint deposited in a soft drink bottle foil (Fig. 4a) shows a poor contrast under bright field illumination (Fig. 4b), while only weak ridge patterns are detected under green light (Fig. 4e). At the same time, well resolved features are discerned under violet and blue radiation (Fig. 4c and d, respectively).

In other words, the hybrid nanopowders presented here can facilitate optimal visualization for fingerprints found in radically different substrates. In that sense, the forensic investigator can be released from the need to carry and use a number of different powders to accommodate a variety of backgrounds at the crime scene. Recall that C-dots are non-toxic[7,31] and thus can be readily used in the crime scene, following standard forensic procedures.

Automated Fingerprint Identification System (AFIS) analysis is the standard method of evaluating the quality of the fingerprint images. AFIS analysis for a fresh fingerprint developed by a commercial white fingerprint powder reveals 65 minutiae as shown in Fig. 5a. Under identical conditions the C-dot based hybrid nanopowder yields an improved image quality displaying 71 minutiae (Fig. 5b).

To further test the generality of the effects described above we prepared hybrid nanopowders by using a different type of C-dots that are derived via pyrolysis of biomass. The corresponding hybrid powders (based on titania or laponite) show similar effects, albeit their PL intensity is substantially weaker (ESI,† Fig. S6 and S7, respectively).

In conclusion, we have described the synthesis of hybrid nanopowders containing minor amounts of C-dots that exhibit colour-tuneability without any adverse effects on the flowability of the diluent. While this behavior shows great potential in a variety of applications, we have focused on their use in fingerprint enhancement. We demonstrate here that the non-toxic hybrid nanopowders can be readily applied for fingerprint development, affording improved image quality and optimal contrast against colored backgrounds.

Notes and references

1 S. Baker and G. Baker, Angew. Chem., Int. Ed., 2010, 49, 6726.
2 J. Silva and H. Gonçalves, Trends Anal. Chem., 2011, 30, 1327.
3 H. Li, Z. Kang, Y. Liu and S.-T. Lee, J. Mater. Chem., 2012, 22, 24230.
4 J. Shen, Y. Zhu, X. Yang and C. Li, Chem. Commun., 2012, 48, 3686.
5 L. Li, G. Wu, G. Yang, J. Peng, J. Zhao and J.-J. Zhu, Nanoscale, 2013, 5, 4015.
6 K. Hola, Y. Zhang, Y. Wang, E. Giannelis, R. Zboril and A. Rogach, Nano Today, 2014, 9, 590.
7 Q.-L. Zhao, Z.-L. Zhang, B.-H. Huang, J. Peng, M. Zhang and D.-W. Pang, Chem. Commun., 2008, 5116.
8 A. Kelarakis, MRS Energy & Sustainability, 2014, 1, E2.
9 W. Kong, R. Liu, H. Li, J. Liu, H. Huang, Y. Liu and Z. Kang, J. Mater. Chem. B, 2014, 2, 5077.
10 H. Peng and J. Travas-Sejdic, Chem. Mater., 2009, 21, 5563.
11 M. Krysmann, A. Kelarakis and E. Giannelis, Green Chem., 2012, 14, 3141.
12 D. Sun, R. Ban, P.-H. Zhang, G.-H. Wu, J.-R. Zhang and J.-J. Zhu, Carbon, 2013, 64, 424.
13 S. Sahu, B. Behera, T. Maiti and S. Mohapatra, Chem. Commun., 2012, 48, 8835.
14 C. Zhu, J. Zhai and S. Dong, Chem. Commun., 2012, 48, 9367.
15 S. Srivastava, R. Awasthi, D. Tripathi, M. K. Rai, V. Agarwal, V. Agrawal, N. S. Gajbhiye and R. K. Gupta, Small, 2012, 8, 1099.
16 Y.-P. Sun, B. Zhou, Y. Lin, W. Wang, K. Fernando, P. Pathak, M. Meziani, B. Harruff, X. Wang, H. Wang, P. Luo, H. Yang, M. Kose, B. Chen, L. Veca and S.-Y. Xie, J. Am. Chem. Soc., 2006, 128, 7756.
17 H. Zheng, Q. Wang, Y. Long, H. Zhang, X. Huang and R. Zhu, Chem. Commun., 2011, 47, 10650.
18 H. Li, X. He, Z. Kang, H. Huang, Y. Liu, J. Liu, S. Lian, C. Tsang, X. Yang and S.-T. Lee, Angew. Chem., Int. Ed., 2010, 49, 4430.
19 C. Chien, S. Li, W. Lai, Y. Yeh, H. Chen, I. Chen, L. Chen, K. Chen, T. Nemoto, S. Isoda, M. Chen, T. Fujita, G. Eda, H. Yamaguchi, M. Chhowalla and C. Chen, Angew. Chem., Int. Ed., 2012, 51, 6662.
20 L. Cao, M. J. Meziani, S. Sahu and Y. P. Sun, Acc. Chem. Res., 2013, 46, 171.
21 S. Qu, X. Wang, Q. Li, X. Liu and L. Wang, Angew. Chem., Int. Ed., 2012, 51, 12215.
22 C.-I. Wang, W.-C. Wu, A. P. Periasamy and H.-T. Chang, Green Chem., 2014, 16, 2509–2514.
23 M. Xu, G. He, Z. Li, F. He, F. Gao, Y. Su, L. Zhang, Z. Yang and Y. Zhang, Nanoscale, 2014, 6, 10307.

Fig. 4 (a) Fingermarks in a soft drink bottle foil developed with 0.7 wt% C-dot–silica hybrid nanopowder, (b) their bright field image and (c–e) their fluorescence microscopy images under violet, blue and green excitation wavelength, respectively.

158

24 M. Krysmann, A. Kelarakis, P. Dallas and E. Giannelis, *J. Am. Chem. Soc.*, 2012, **134**, 747.
25 S. Zhu, Q. Meng, L. Wang, J. Zhang, Y. Song, H. Jin, K. Zhang, H. Sun, H. Wang and B. Yang, *Angew. Chem., Int. Ed.*, 2013, **52**, 3953.
26 P. Hazarika and D. Russell, *Angew. Chem., Int. Ed.*, 2012, **51**, 3524.
27 X. Spindler, O. Hofstetter, A. McDonagh, C. Roux and C. Lennard, *Chem. Commun.*, 2011, **47**, 5602.
28 K. Li, W. Qin, F. Li, X. Zhao, B. Jiang, K. Wang, S. Deng, C. Fan and D. Li, *Angew. Chem.*, 2013, **125**, 11756.
29 G. Sodhi and J. Kaur, *Forensic Sci. Int.*, 2001, **120**, 172.
30 N. Chen, Y. He, Y. Su, X. Li, Q. Huang, H. Wang, X. Zhang, R. Tai and C. Fan, *Biomaterials*, 2012, **33**, 1238.
31 L. Shen, L. Zhang, M. Chen, X. Chen and J. Wang, *Carbon*, 2013, **55**, 343.

159

ChemComm

Carbogenically coated silica nanoparticles and their forensic applications†

D. Fernandes,[a] M. J. Krysmann[b] and A. Kelarakis*[a]

Carbogenically coated silica nanoparticles (C-SiO₂) exhibit color-tunability and carry great promise for two important forensic applications. First, the C-SiO₂ nanopowders are ideal for fingerprint development, yielding strong contrast against multicoloured and patterned backgrounds. Second, spontaneous nanoparticle aggregation leads to non-duplicable, inexpensive nanotags that can support sustainable technologies to combat counterfeiting.

The remarkable photophysical properties of carbogenic nanoparticles (otherwise known as C-dots) are systematically explored in a variety of applications including printing inks, photocatalysis, biologically labelling, bioimaging and chemical sensing.[1–5] Their non-toxic and biocompatible nature[6,7] endows distinct advantages over conventional polyaromatic dyes and heavy metal-based quantum dots.

Large-scale and cost-effective synthesis of C-dots is realised via pyrolytic decomposition of virtually any type of carbon-rich precursors including plants tissue,[8] natural saccharides,[9,10] animal products[11] and synthetic polymers.[12,13] Alternatively, C-dots with varying graphitization degree are derived through disintegration,[14] hydrothermal treatment[15] and electrooxidation[16] of carbon nanotubes, carbon nanofibers and graphite. In principle, quantum yield can be improved via surface passivation,[17] heteroatom doping[18] and the in situ formation of organic chromophores.[19,20]

In this report we focus on the exploitation of the advanced photophysical properties of carbogenically coated silica nanoparticles (C-SiO₂) in two distinct forensic applications. First, we demonstrate that the colour-tuneable C-SiO₂ can be used as high performance nanopowders for latent fingerprint enhancement.

Second, spontaneous aggregation of the C-SiO₂ during solvent evaporation generates non-duplicable photoluminescent motives that are ideal nanotags to mark and authenticate products. As reviewed recently a number of studies report the use of SiO₂ based nanomaterials for fingerprint enhancement.[21] Notable contributions focus on the use of surface modified SiO₂ nanoparticles to gain insights into the mechanisms responsible for fingermark detection[22] and the use of fluorescent dye-doped SiO₂ nanoparticles to improve the image homogeneity and reduce donor inter-variability.[23]

To synthesize C-SiO₂, colloidal silica was treated with dimethyloctadecyl[3-(trimethoxysilyl)propyl]ammonium chloride to give a product with 34 wt% organic content as determined by TGA (ESI,† Fig. S1). Subsequently, the product was pyrolysed at 250 °C before being subjected to surface oxidation via HNO₃, amine functionalization and excessive dialysis against water. Elemental analysis of C-SiO₂ thus received suggests the presence of 26% C, along with minor amounts of H and N (4 and 5%, respectively). The FTIR spectrum (ESI,† Fig. S2) shows peaks attributed[24,25] to the vibrational stretching of C–H (1380 cm⁻¹), the anti-symmetric and symmetric stretching vibrations of N–C=O (1550 cm⁻¹ and 1658 cm⁻¹, respectively) and symmetric (2850 cm⁻¹) and anti-symmetric (2920 cm⁻¹) stretching vibration of sp² C–H.

The TEM image of C-SiO₂ (Fig. 1) indicates the presence of spherical nanoparticles with average diameter 22 ± 2 nm. The nanoparticles are easily dispersed in water forming stable colloidal dispersions with pH = 10.2, consistent with the presence of surface functionalities generated through the acid/amine treatment. Fig. 2 suggests that the aqueous dispersions exhibit excitation wavelength dependent photoluminescent emission, in a manner similar to that observed for other carbon-based nano-emitters such as C-dots and graphene dots. The emission mechanism is not thoroughly understood, however contributions stemming from surface defects and the conjugated π-domains have been identified.[26,27]

The freeze-dried fine powder shows excellent flowability and can be easily applied to a variety of non-porous surfaces (ESI,† Fig. S3). The nanopowder adheres strongly to the fingerprints

[a] Centre for Materials Science, School of Physical Sciences and Computing, University of Central Lancashire, Preston PR1 2HE, UK. E-mail: akelarakis@uclan.ac.uk; Tel: +44(0) 1772 4172

[b] School of Pharmacy and Biosciences, University of Central Lancashire, Preston PR1 2HE, UK
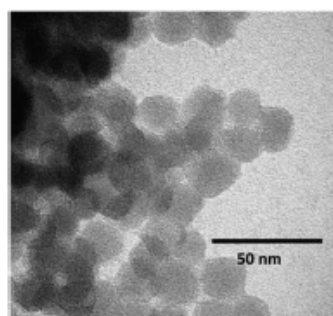
Fig. 1 TEM image of the C-SiO$_2$ nanoparticles.
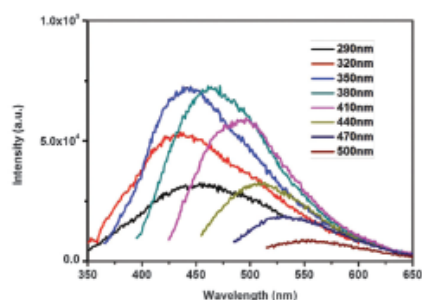
Fig. 2 Photoluminescence spectra of C-SiO$_2$ aqueous solutions under different excitation wavelengths.

Fig. 3 (a) Fluorescent microscopy images of a fingerprint developed with the C-SiO$_2$ nanopowder. (b) Comparison between the C-SiO$_2$ and a commercial fingerprint powder on a fluorescent background investigated on a crime lite imager (445 nm laser with a 455 nm filter).

revealing well-resolved patterns that meet the standard for individual identification (ESI,† Fig. S3 and S4). Automated Fingerprint Identification System (AFIS) analysis of a fingerprint developed by C-SiO$_2$ reveals 73 minutiae (details of a fingerprint such as ridge ending, ridge bifurcation, etc) compared to 65 minutiae for an identical fingerprint developed by a standard white fingerprint powder (WFP) (ESI,† Fig. S5).

Significantly, as shown in Fig. 3a the nanopowders exhibit colour-tunability and emit within the blue, green and red region when they are irradiated by violet, blue and green light, respectively. The supreme photophysical properties of C-SiO$_2$ can open new horizons in forensic investigation by bypassing problems related to strong background interference from overlapping letters or fluorescent, multi-coloured and textured substrates. To demonstrate this behaviour, a set of fingerprints deposited on a highly fluorescent cardboard were developed under identical conditions using the C-SiO$_2$ nanopowder and a commercial WFP, respectively. High quality images are collected for the C-SiO$_2$ enhanced fingerprints (left image in Fig. 3b) under a 445 nm wavelength laser on a crime-lite imager. In contrast, the fingerprints developed using the standard WFP suffer from strong background interference leading to poor image quality (right image in Fig. 3b). A full set of images under the different wavelengths available on the crime lite imager can be seen in ESI,† Fig. S6. Moreover,

a fingerprint developed with C-SiO$_2$ compares favourably with that developed by a commercial fluorescent powder, in the sense that the latter shows strong contrast only under certain illumination wavelengths (ESI,† Fig. S7).

Fingerprint matching remains by far the most reliable biometric method used by law enforcement for individual identification, but its accuracy critically depends on the quality of the recovered impressions. To that end, a large number of fingerprint powders have been developed to maximize contrast against a variety of radically different substrates. In that sense, the use of a single, yet colour-tunable C-SiO$_2$ nanopowder offers significant advantages in terms of dusting speed and image quality.

We have recently introduced a close related class of nanopowders comprising minor amounts of C-dots that also exhibit colour-tunability with respect to the incident radiation and, thus, are suitable for fingerprint enhancement.[28] Another study describes the use of aqueous dispersions of C-dot/poly(dimethylacrylamide) nanocomposites for fingerprint detection.[29] Notably, nanopowders with high C-dot content are not photoactive, presumably due to extensive self-quenching effects.[30] A recent study suggests that blue, green and tan silicon–carbon dots/silica nanocomposite powders show adjustable optical properties as a function of their composition and structure.[31] Here we demonstrate colour-tuneable nanopowders containing a single type of nanoparticles and are, thus, distinctly different from the nanocomposite and hybrid materials reported previously. The main advantage of C-SiO$_2$ nanoparticles compared to C-dots refers to their much larger carbogenic surface that holds great promise for selective and sensitive sensing of forensically important compounds found in fingerprints. We note that this report is a proof-of-concept investigation corresponding to phase 1 pilot studies as described by the International Fingerprint Research Group.[32]

When the pH of the aqueous suspension of C-SiO$_2$ drops below 8.5, the colloidal stability is compromised as evident by the evolution of large aggregates (ESI,† Fig. S8). During water evaporation from an acidified dispersion, the C-SiO$_2$ were seen to undergo spontaneous and random self-assembly, giving rise

161

ChemComm
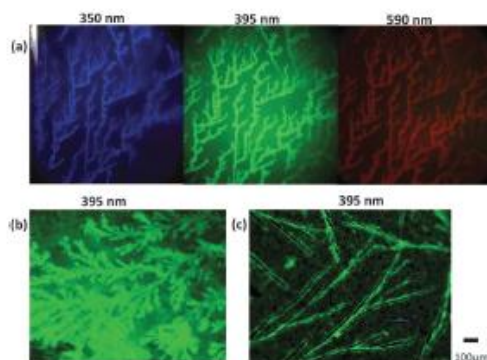
Fig. 4 Fluorescent microscopy images of the nanotags; (a) deposited in glass and illuminated under different excitation wavelengths, (b) deposited in glass from a more concentrated suspension, (c) deposited on a polymeric surface.

to motives that are highly fluorescent under laser radiation as shown in Fig. 4a. For comparison, we display two more images; one derived from a more concentrated dispersion (Fig. 4b) and one formed on a polymeric surface (Fig. 4c). (In contrast, no patterns are formed from dispersions with pH = 10, as shown in ESI,† Fig. S9).

The SEM images displayed in Fig. 5 reveal a high level of structural complexity confirming that the motives are nearly impossible to duplicate and can serve as nanotags for object authentication. The nanotags adhere strongly to a variety of substrates (polymers, metals, glass) and remain unaltered even after prolonged exposure to high temperature (ESI,† Fig. S10). We attribute this remarkable structural stability and durability to their organic-free and polymeric-free composition.

Suffice to say that counterfeit accounts for a 5–7% world trade, causing a severe financial drain to the global economy. This crime deprives taxable income from *bona fide* business, discourages investment for innovation and inhibits social progress. Counterfeit drugs not only fail to cure, but they can cause severe health issues. Recent trends to address this problem rely on the use of upconverting nanocrystals[33] and dye-doped nanoparticles[34] in integrated safety features and security graphics; however, those sophisticated compounds are often toxic and prohibitively expensive. In contrast, C-SiO$_2$ based nanotags are cost-effective and non-toxic for humans and the environment. Moreover, by virtue of their colour-tuneable nature, C-SiO$_2$ based nanotags impart enhanced security features, compared to commonly used dyes that display only one fixed colour.

In conclusion, we introduce a new class of colour-tuneable nanomaterials (C-SiO$_2$) and we demonstrate their great potential in two distinct forensic applications. As fingerprint powders they circumvent problems stemming from poor image quality against multicoloured substrates. As nanoparticles that undergo spontaneous and random aggregation, they generate non-repeatable motives with a high level of structural complexity that can be used to mark and authenticate products. Those inexpensive and non-toxic nanotags are viable alternatives to current solutions with prohibitively high cost and they can support sustainable technologies to combat counterfeiting.

References

1 S. N. Baker and G. A. Baker, *Angew. Chem., Int. Ed.*, 2010, **49**, 6726–6744.
2 K. Hola, Y. Zhang, Y. Wang, E. P. Giannelis, R. Zboril and A. L. Rogach, *Nano Today*, 2014, **9**, 590–603.
3 A. Kelarakis, *MRS Energy Sustainability*, 2014, **1**, 1–15.
4 Y. Wang and A. Hu, *J. Mater. Chem. C*, 2014, **2**, 6921–6939.
5 S. Y. Lim, W. Shen and Z. Gao, *Chem. Soc. Rev.*, 2014, **44**, 362–381.
6 H. Tao, K. Yang, Z. Ma, J. Wan, Y. Zhang, Z. Kang and Z. Liu, *Small*, 2012, **8**, 281–290.
7 J. Wei, J. Shen, X. Zhang, S. Guo, J. Pan, X. Hou, H. Zhang, L. Wang and B. Feng, *RSC Adv.*, 2013, **3**, 13119–13122.
8 M. J. Krysmann, A. Kelarakis and E. P. Giannelis, *Green Chem.*, 2012, **14**, 3141–3145.
9 H. Peng and J. Travas-Sejdic, *Chem. Mater.*, 2009, **21**, 5563–5565.
10 L. Zhou, B. He and J. Huang, *Chem. Commun.*, 2013, **49**, 8078–8080.
11 J. Wang, C. F. Wang and S. Chen, *Angew. Chem., Int. Ed.*, 2012, **51**, 9297–9301.
12 J. Gu, W. Wang, Q. Zhang, Z. Meng, X. Jia and K. Xi, *RSC Adv.*, 2013, **3**, 15589–15591.
13 A. Jaiswal, S. S. Ghosh and A. Chattopadhyay, *Chem. Commun.*, 2012, **48**, 407–409.
14 L. Lin and S. Zhang, *Chem. Commun.*, 2012, **48**, 10177–10179.
15 D. Pan, J. Zhang, Z. Li and M. Wu, *Adv. Mater.*, 2010, **22**, 734–738.
16 J. Zhou, C. Booker, R. Li, X. Zhou, T. K. Sham, X. Sun and Z. Ding, *J. Am. Chem. Soc.*, 2007, **129**, 744–745.
17 H. Zheng, Q. Wang, Y. Long, H. Zhang, X. Huang and R. Zhu, *Chem. Commun.*, 2011, **47**, 10650–10652.
18 Y. Dong, H. Pang, H. Bin Yang, C. Guo, J. Shao, Y. Chi, C. M. Li and T. Yu, *Angew. Chem., Int. Ed.*, 2013, **125**, 7954–7958.
19 M. J. Krysmann, A. Kelarakis, P. Dallas and E. P. Giannelis, *J. Am. Chem. Soc.*, 2012, **134**, 747–750.
20 S. Zhu, X. Zhao, Y. Song, S. Lu and B. Yang, *Nano Today*, 2016, **11**, 128–132.
21 A. Leśniewski, *Synth. Met.*, 2016, DOI: 10.1016/j.synthmet.2016.03.032.
22 S. Moret, A. Bécue and C. Champod, *Nanotechnology*, 2014, **25**, 1–10.
23 S. Moret, A. Bécue and C. Champod, *Forensic Sci. Int.*, 2016, **259**, 10–18.
24 X. Cui, L. Zhu, J. Wu, Y. Hou, P. Wang, Z. Wang and M. Yang, *Biosens. Bioelectron.*, 2015, **63**, 506–512.
25 L. Stobinski, B. Lesiak, L. Kover, J. Toth, S. Biniak, G. Trykowski and J. Judek, *J. Alloys Compd.*, 2010, **501**, 77–84.
26 A. Kelarakis, *Curr. Opin. Colloid Interface Sci.*, 2015, **20**, 354–361.
27 Z. Gan, H. Xu and Y. Hao, *Nanoscale*, 2016, **8**, 7794–7807.
28 D. Fernandes, M. J. Krysmann and A. Kelarakis, *Chem. Commun.*, 2015, **51**, 4902–4905.
29 J. Dilag, H. Kobus, Y. Yu, C. T. Gibson and A. V. Ellis, *Polym. Int.*, 2015, **64**, 884–891.
30 S. Zhu, Q. Meng, L. Wang, J. Zhang, Y. Song, H. Jin, K. Zhang, H. Sun, H. Wang and B. Yang, *Angew. Chem., Int. Ed.*, 2013, **52**, 3953–3957.
31 C. Shih, P. Chen, G. Lin, C. Wang and H. Chang, *ACS Nano*, 2015, **9**, 312–319.
32 International Fingerprint Research Group (IFRG), *J. Forensic Identif.*, 2014, **64**, 174–200.
33 N. M. Sangeetha, P. Moutet, D. Lagarde, G. Sallen, B. Urbaszek, X. Marie, G. Viau and L. Ressier, *Nanoscale*, 2013, **5**, 9587–9592.
34 J. Kim, J. M. Yun, J. Jung, H. Song, J.-B. Kim and H. Ihee, *Nanotechnology*, 2014, **25**, 155303.

Fig. 5 SEM images of the formed patterns under different magnifications.

162

CrossMark

ORIGINAL PAPER

Synthesis and electrochemical characterization of nitrogen-doped and nitrogen–phosphorus-doped multi-walled carbon nanotubes

Shereen Haj Othman[1] · Uwe Ritter[1] · Eoin K. McCarthy[2] · Diogo Fernandes[3] ·
Antonios Kelarakis[3] · Nikos G. Tsierkezos[1]

Abstract Nitrogen-doped and nitrogen–phosphorus-doped
multi-walled carbon nanotubes (N-MWCNTs and N–P-
MWCNTs, respectively) were fabricated by chemical vapor
deposition and characterized using scanning electron micros-
copy and transmission electron microscopy in combination
with energy dispersive X-ray spectroscopy and Raman spec-
troscopy. The electrochemical response of N-MWCNTs and
N–P-MWCNTs towards ferrocyanide/ferricyanide was initial-
ly studied. The findings exhibit weakening of electrochemical
response and sensitivity of nanotubes with phosphorus dop-
ing, and thus, within the composite films tested, those consist
exclusively of N-MWCNTs exhibit the greatest electrocatalyt-
ic activity. N–P-MWCNT film was further applied for indi-
vidual electrochemical analysis of ascorbic acid (AA), uric
acid (UA), and dopamine (DA), and lower limits of detections
of 11.6, 7.8, and 1.9 μM were estimated, respectively. The
findings demonstrate that AA does not interfere with UA,
but considerable interference of AA in analysis of DA was
observed. Thus, the simultaneous analysis of AA, UA, and
DA on N–P-MWCNTs appears to be restricted.

✉ Nikos G. Tsierkezos
nikos.tsierkezos@tu-ilmenau.de

[1] Department of Chemistry, Institute of Chemistry and Biotechnology,
Ilmenau University of Technology, Weimarer Straße 25,
98693 Ilmenau, Germany

[2] Advanced Microscopy Laboratory, CRANN, Trinity College Dublin,
Dublin 2, Ireland

[3] Centre for Materials Science, School of Physical Sciences and
Computing, University of Central Lancashire,
Preston, Lancashire PR1 2HE, UK

Introduction

Due to their excellent electrical, chemical, and mechanical
properties, the multi-walled carbon nanotubes (MWCNTs)
are quite promising and attractive nanomaterials for applica-
tions in electrochemical analysis [1–7]. With this respect,
MWCNTs were extensively used for fabrication of electrodes
in electrochemical sensing since they enhance the electron
transfer rate, the current response, the sensitivity, and the de-
tection capability of sensing systems [8, 9]. According to lit-
erature reports, composite films consisted of MWCNTs were
successfully used with great electrochemical performance for
electrochemical analysis of numerous redox systems of great
interest [10–12].

The introduction of elements into the structure of carbon
nanotubes changes their electronic structure and consequently
affects their electronic and chemical properties [13]. It is re-
markable that the doped sites within carbon nanotubes signif-
icantly modify their chemical reactivity extending, thus, the
spectrum of their possible applications, especially in the field
of electrochemical sensing.

Nitrogen can be easily incorporated into the structure of
carbon nanotubes by substitution. According to literature re-
ports, nitrogen can be incorporated within carbon nanotubes
in pyridine-, pyrrole-, and/or azepine-like fashion [14–16].
Nitrogen acts as an electron donor in carbon nanotubes caus-
ing a shift in Fermi level to the conduction bands and making
all nitrogen-doped carbon nanotubes metallic, regardless of
their geometry. In addition, phosphorus can be also effectively
incorporated into carbon nanotubes either as single substitu-
tional dopant or as co-dopant along with nitrogen [17–19].

Springer

Theoretical studies exhibited that both phosphorus and phosphorus–nitrogen defects in carbon nanotubes are characterized by the presence of highly localized state close to Fermi level, something that is quite promising for their application in electrochemical sensing [20]. With this respect, the production of sensors based on nitrogen–phosphorus-doped carbon nanotubes will be of great interest in electrochemical analysis.

The aim of research work is the fabrication of combined nitrogen–phosphorus-doped multi-walled carbon nanotubes (further denoted as N–P-MWCNTs) and their application in electrochemical analysis. Specifically, N–P-MWCNTs were synthesized onto silicon/silicon oxide substrate by means of chemical vapor deposition (CVD) with simultaneous decomposition of triphenylphosphine (TPP) that acts as carbon- and phosphorus-source material and acetonitrile (ACN) that acts as carbon- and nitrogen-source material in the presence of ferrocene (FeCp$_2$), which serves as catalyst. The concentration of TPP was varied in the range of 0–1.0% wt. while those of ACN and FeCp$_2$ were kept constant. In addition, nitrogen-doped carbon nanotubes (further denoted as N-MWCNTs) were fabricated with decomposition of ACN in presence of FeCp$_2$. The N–P-MWCNT films were characterized by means of scanning electron microscopy (SEM) and transmission electron microscopy (TEM) in combination with energy dispersive X-ray spectroscopy (EDX) as well as by Raman spectroscopy. Furthermore, the electrochemical response of N-MWCNT and N–P-MWCNT films towards ferrocyanide/ferricyanide, $[Fe(CN)_6]^{3-/4-}$, was studied by means of cyclic voltammetry (CV) and electrochemical impedance spectroscopy (EIS) in aqueous KCl solution (1.0 M). In addition, the N–P-MWCNT film was further applied for the electrochemical analysis of ascorbic acid (AA), uric acid (UA), and dopamine (DA) in phosphate buffer solution (pH 7.0).

Experimental

Chemicals and solutions

Triphenylphosphine (>99.0%), acetonitrile (>99.9%), ferrocene (>98.0%), potassium hexacyanoferrate(III) (>99.0%), potassium hexacyanoferrate(II) trihydrate (>98.5%), potassium chloride (>99.0%), and dopamine (>99.0%) were purchased from Sigma-Aldrich, while L(+)-ascorbic acid (>99.7%) and uric acid (>98.0%) were purchased from Merck and Fluka, respectively.

For electrochemistry measurements, 1.0 mM K$_3$Fe(CN)$_6$/K$_4$Fe(CN)$_6$ solution was prepared by dissolving the appropriate amounts of K$_3$Fe(CN)$_6$ and K$_4$Fe(CN)$_6$ in 1.0 M KCl. High-quality distilled water with specific conductivity of about 0.1 μS cm^{-1} was used for preparation of solutions. The solutions in concentration range of 0.099–0.990 mM were prepared directly in electrochemical cell with

progressive addition of proper volume of 1.0 mM K$_3$Fe(CN)$_6$/K$_4$Fe(CN)$_6$ solution in 1.0 M KCl.

The solutions of AA, DA, and UA of desired concentrations in ranges of 0.250–0.668 mM (AA), 0.017–0.196 mM (DA), and 0.032–0.211 mM (UA) were prepared directly in electrochemical cell with addition of proper volumes of stock solutions of biomolecules into phosphate buffer solution (pH 7.0). The concentration range of AA was higher since the composite films exhibit weaker electrochemical response towards AA compared to other studied biomolecules (DA and UA). The measurements were performed at the room temperature.

Fabrication of N–P-MWCNT and N-MWCNT films

N–P-MWCNTs were grown directly onto silicon/silicon oxide substrate by means of CVD with decomposition of ACN (carbon- and nitrogen-source material) and TPP (carbon- and phosphorus-source material) in the presence of FeCp$_2$ (catalyst). The mass percent of TPP in ACN/TPP/FeCp$_2$ ternary mixture was varied in order to find the optimum experimental conditions for production of high quality and purity N–P-MWCNTs. Specifically, the mass percent of TPP in ACN/TPP/FeCp$_2$ ternary mixture was varied in the range of 0–1.0% wt., while the mass percent of FeCp$_2$ was fixed to 2.0% wt. (Table S1, Electronic Supplementary Material). For the growth process, the ACN/TPP/FeCp$_2$ ternary mixture was introduced to furnace at the temperature of 850 °C through a syringe with flow rate of 10 mL h^{-1} (the growing time was fixed at about 18 min). In all cases, the pyrolysis experiments were carried out by spraying 3 mL of ACN/TPP/FeCp$_2$ ternary mixture. N-MWCNTs were also produced by means of CVD with decay of ACN in presence of FeCp$_2$ (Table S1, Electronic Supplementary Material). The scheme of CVD apparatus and experimental details concerning the pyrolysis process were already reported in previous published articles [21, 22].

In order to construct the working electrode for the electrochemistry measurements, the N-MWCNT- and N–P-MWCNT-based films were initially connected to platinum wire by using silver conducting coating, and once the silver coating was dried, the silver conducting part of composite films was fully covered with varnish protective coating [23].

Apparatus and experiments

The electrochemical impedance spectra were recorded on working station Zahner (IM6/6EX, Germany) in the frequency range of 0.1 Hz–100 kHz. The obtained data were analyzed by means of Thales software (version 4.15). As working electrode, either N-MWCNT or N–P-MWCNT composite films were applied, while as auxiliary and reference electrodes, a platinum plate and Ag/AgCl (saturated KCl), respectively,

were used. The measurements were performed at the room temperature. Prior electrochemistry measurements, the solutions were deoxygenated by purging with high-purity nitrogen. More details regarding the electrochemistry measurements were already reported in previous published articles [24–26].

The morphology and elemental composition of N-MWCNT and N–P-MWCNT composite films were examined by transmission electron microscope (FEI Titan S/TEM 80-300 kV) and scanning electron microscope (Zeiss ULTRA Plus SEM) equipped with an energy dispersive X-ray spectrometer [27].

Raman spectra were recorded using a microscope-fitted Horiba Jobin Yvon HR800 Raman spectrometer that was calibrated using a Si substrate. The spectra were collected within the range of 1000–2000 cm^{-1} (scanning intervals of 1.66 cm^{-1}) with a slit and hole of 300 and 200 cm^{-1}, respectively. An air cooled CLDS point mode diode 532 nm laser was used, and the radiation was limited to 10% to avoid damage of the carbon nanotubes samples. The spectra were averaged by 10 accumulations of 2 s each (using LabSpec 6 software).

Results and discussion

Scanning electron and transmission electron microscopic analysis

The SEM and TEM techniques were used to investigate the surface of N-MWCNT and N–P-MWCNT composite films as well as to observe directly the morphology of synthesized carbon nanotubes. Representative SEM and TEM images taken for selected sample, namely for N–P-MWCNT composite film fabricated with decomposition of 0.5% TPP, are shown in Fig. 1. The SEM and TEM images taken for the other samples were omitted since they show similar characteristics with those obtained for this particular N–P-MWCNT film. Furthermore, SEM and TEM images of N-MWCNTs are published in our previous articles [28, 29].

The low-magnification SEM images show that the surface of N–P-MWCNT film is quite homogeneous, and the high-magnification SEM micrographs exhibit that the packing organization and thus the arrangement of aligned carbon nanotubes on oxidized silicon substrate are enhanced. This observation is probably attributed to the bamboo-shaped configuration of carbon nanotubes that contain nitrogen incorporated into their structure [30].

TEM images confirm that the carbon nanotubes are bamboo-shaped demonstrating that the addition of TPP, and thus, the phosphorus doping of carbon nanotubes does not affect significantly their shape that tends to be similar with that of pure N-MWCNTs. TEM/EDX analysis of N–P-

MWCNTs confirms that the carbon nanotubes incorporate phosphorus (Fig. S1, Electronic Supplementary Material).

Electrochemical response of N–P-MWCNT composite films towards $[Fe(CN)_6]^{3-/4-}$

In order to investigate the effect of nitrogen and phosphorus doping on electrocatalytic activity of carbon nanotubes, the electrochemical response of N-MWCNT and N–P-MWCNT composite films towards $[Fe(CN)_6]^{3-/4-}$ in aqueous 1.0 M KCl solution was tested in the concentration range of 0.099–0.990 mM. As an example, representative CV curves recorded for various concentrations of $[Fe(CN)_6]^{3-/4-}$ on N-MWCNTs and two different N–P-MWCNT composite films at the scan rate of 0.02 V s^{-1} are presented in Fig. 2. Furthermore, the variation of oxidation peak current density with the concentration of $[Fe(CN)_6]^{3-/4-}$ is shown in Fig. S2 (Electronic Supplementary Material). The estimated electrochemical parameters of $[Fe(CN)_6]^{3-/4-}$ on N-MWCNTs and various N–P-MWCNT composite films are reported in Table 1.

As it can be seen in CV curves shown in Fig. 2, the redox system $[Fe(CN)_6]^{3-/4-}$ exhibits a pair of quite reversible redox peaks on N-MWCNT and N–P-MWCNT films. The oxidation–reduction peak current ratio is equal to unity and independent of applied scan rate indicating that there are no parallel chemical reactions coupled to electrochemical process. Similarly, the oxidative and reductive peak currents are constant for numerous cycles, indicating that there are no chemical reactions coupled to electron transfer process and confirming that the redox system is stable in time frame of experiment and that the charge transfer process occurring on N-MWCNT and N–P-MWCNT films is quite reversible.

The half-wave potential estimated for $[Fe(CN)_6]^{3-/4-}$ redox system on N-MWCNTs and N–P-MWCNTs appears to be similar within experimental error ($E_{1/2} \approx 0.280$ V vs. Ag/AgCl), something that is quite expectable for reversible redox systems. Furthermore, the anodic peak current was found to vary linearly with the square root of scan rate in the range of 0.02–0.14 V s^{-1}, demonstrating that $[Fe(CN)_6]^{3-/4-}$ is diffusion controlled on N-MWCNT and N–P-MWCNT films.

It is quite interesting that a diminishing of film's current response takes place with the increase of concentration of decomposed TPP during synthesis process. For instance, the current response of N-MWCNTs towards $[Fe(CN)_6]^{3-/4-}$ appears to be around 51, 90, and 133% greater compared to those measured under the same experimental conditions on N–P-MWCNT-1 (0.2% wt. TPP), N–P-MWCNT-3 (0.6% wt. TPP), and N–P-MWCNT-5 (1.0% wt. TPP), respectively. Consequently, it is obvious that the phosphorus doping of carbon nanotubes affects negatively their electrocatalytic activity and diminishes significantly their electrochemical response towards studied system. This finding is in absolute agreement with our previous published results that the
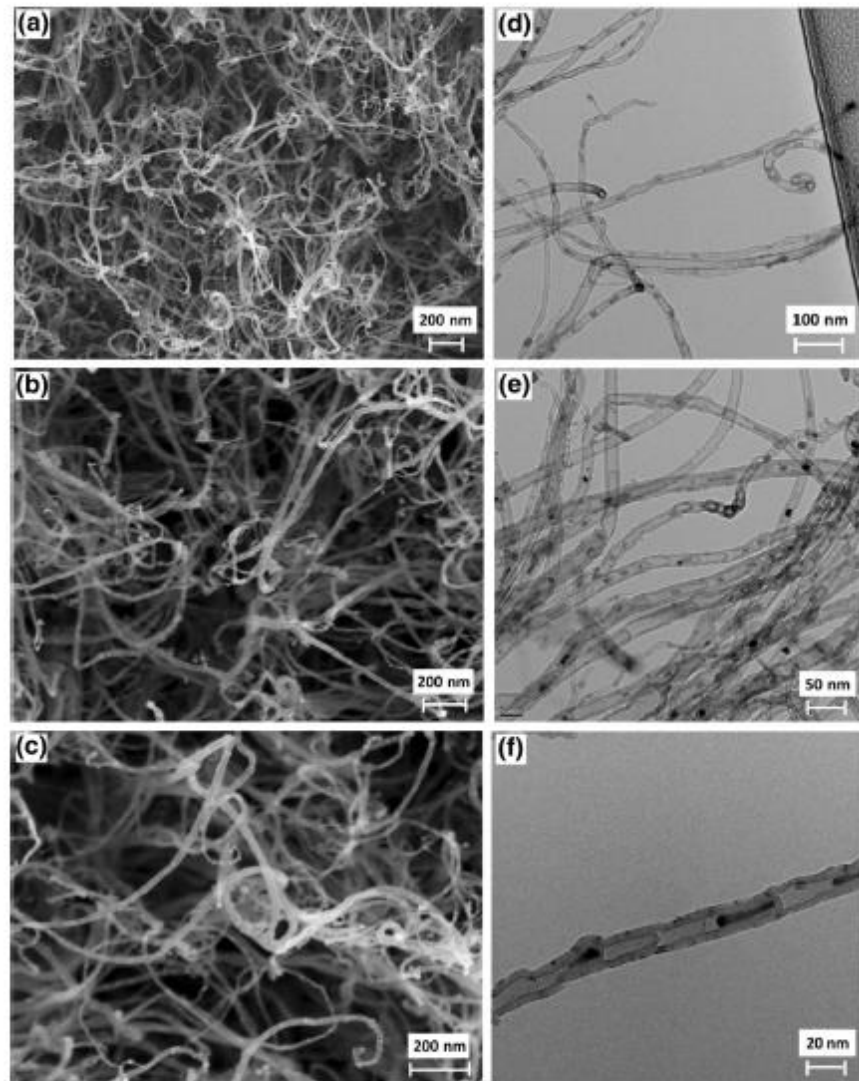
electrochemical response of N-MWCNTs appears to be greater compared to that of P-MWCNTs [33].

The anodic and cathodic peak potential separation (ΔE_p) estimated for $[Fe(CN)_6]^{3-/4-}$ on N-MWCNT and various N–P-MWCNT films lies in the range from 0.059 to 0.097 V (at the scan rate of 0.02 V s^{-1}), demonstrating kinetic differences within the various fabricated composite films (Table 1). Namely, the smallest ΔE_p value of $[Fe(CN)_6]^{3-/4-}$ was obtained on N-MWCNTs ($\Delta E_p \approx 0.059$ V), while the greatest ΔE_p value was measured onto N–P-MWCNTs fabricated with decomposition of 1.0% wt. TPP ($\Delta E_p \approx 0.097$ V). It is astonishing that the ΔE_p value increases progressively with the increase of % wt. of the decomposed TPP used for synthesis of N–P-MWCNTs (Fig. S3, Electronic Supplementary Material). This

finding demonstrates that the kinetic of the investigated system decreases with the increasing of decomposed TPP used for the synthesis process. Consequently, the heterogeneous electron transfer rate constants (k_s) determined for $[Fe(CN)_6]^{3-/4-}$ on N-MWCNTs and various N–P-MWCNT composite films by means of electrochemical absolute rate relation [34], which appears to be in the range from 2×10^{-3} to 4.3×10^{-2} cm s^{-1} (Table 1), decrease with the increase of concentration of decomposed TPP. Namely, the findings demonstrate that the progressive phosphorus doping of carbon nanotubes results to diminishing of kinetic of electrochemical process occurring onto carbon nanotubes (Fig. 3a).

For the estimation of lower limit of detection and sensitivity of N-MWCNTs and various N–P-MWCNT composite

Fig. 2 CVs recorded for various concentrations of $[Fe(CN)_6]^{3-/4-}$ (1.0 M KCl) on N-MWCNTs (**a**), N–P–MWCNT-3 (**b**), and N–P–MWCNT-5 (**c**) at 0.02 V s^{-1}. The CVs (from inner to outer) correspond to the following concentrations: $c_1 = 0.196$ mM, $c_2 = 0.415$ mM, $c_3 = 0.595$ mM, $c_4 = 0.797$ mM, and $c_5 = 0.990$ mM. **d** EIS spectra recorded for $[Fe(CN)_6]^{3-/4-}$ (1.0 M KCl) on N-MWCNTs (*filled square*), N–P–MWCNT-3 (*filled circle*), and N–P–MWCNT-5 (*filled triangle*)
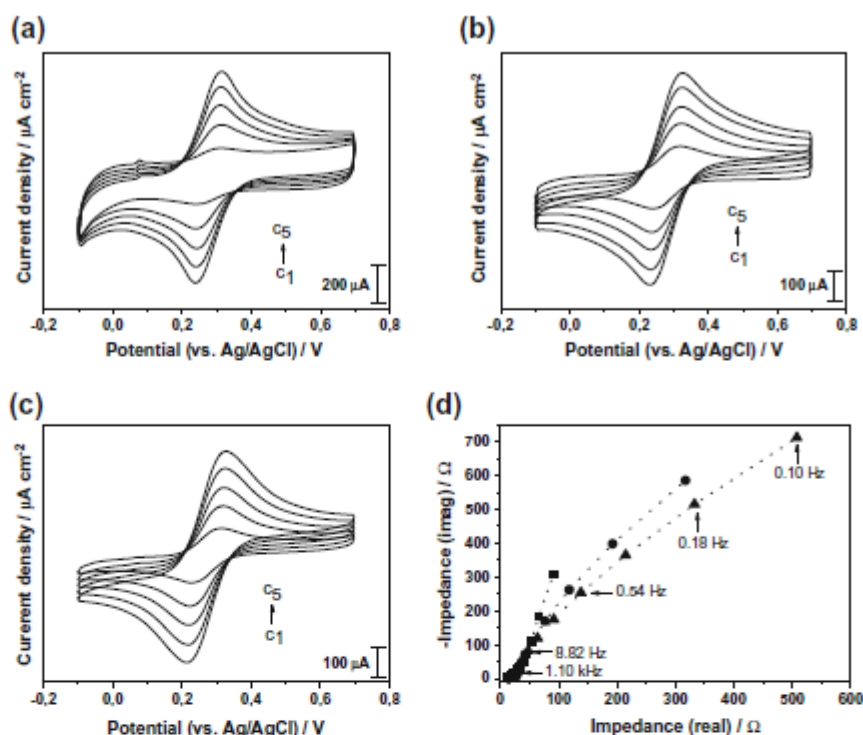
films towards $[Fe(CN)_6]^{3-/4-}$, the variation of oxidation peak current with the concentration of redox system in concentration range of 0.099–0.990 mol L^{-1} was examined. The electrochemical response of N-MWCNT and N–P-MWCNT films towards $[Fe(CN)_6]^{3-/4-}$ plotted as oxidation peak current density vs. concentration of electroactive compound appears to be linear in investigated concentration range (Fig. S2, Electronic Supplementary Material). From the standard deviation of electrochemical response and the slope of linear oxidation current-concentration plots, the detection limit of N-MWCNT and N–

P-MWCNT composite films towards $[Fe(CN)_6]^{3-/4-}$ was estimated. The obtained limits of detection of composite films towards $[Fe(CN)_6]^{3-/4-}$ are reported along with their sensitivities in Table 1. The variation of sensitivity and lower limit of detection with the % wt. of decomposed TPP used for synthesis of nanotubes is presented graphically in Fig. 3b, c, respectively. The results reveal that the N-MWCNTs possess the lowest detection limit, and thus, the highest sensitivity within composite films was tested. Namely, the findings demonstrate that the lower limit of detection tends to increase, and thus, the

Table 1 Electrochemical parameters determined for $[Fe(CN)_6]^{3-/4-}$ (1.0 M KCl) on novel N-MWCNT and N–P-MWCNT composite films at the scan rate of 0.02 V s^{-1}

Composite film	$E_{1/2}$ (V)	ΔE_p (V)	$10^3 k_s$ (cm s^{-1})[c]	R_{ct} (Ω)	LOD (μM)	S/A·(M^{-1} cm^{-2})
N-MWCNTs[a]	0.277	0.059	43	4.7	0.341	0.464
N–P-MWCNT-1[b]	0.280	0.062	32	8.4	0.392	0.403
N–P-MWCNT-2[b]	0.278	0.064	27	14.5	0.454	0.350
N–P-MWCNT-3[b]	0.280	0.071	14	16.6	0.505	0.314
N–P-MWCNT-4[b]	0.280	0.072	13	16.8	0.522	0.304
N–P-MWCNT-5[b]	0.278	0.097	2	19.5	0.532	0.297

[a] Data taken from our previously published article [31]

[b] Data from present work

[c] k_s values determined from electrochemical absolute rate relation: $\psi = (D_o/D_R)^{\alpha/2} k_s (n\pi F v D_o/RT)^{-1/2}$, where ψ is kinetic parameter; α the charge transfer coefficient ($\alpha \approx 0.5$); D_o and D_R the diffusion coefficients of oxidized and reduced species, respectively ($D_o \approx D_R$); and n the number of electrons involved in redox reaction ($n = 1$) [32]

167

Fig. 3 Variation of charge transfer rate (**a**), sensitivity (**b**), lower limit of detection (**c**), and charge transfer resistance (**d**) of $[Fe(CN)_6]^{3-/4-}$ (1.0 M KCl) with the % wt. of decomposed TPP used for fabrication of N–P-MWCNT composite films
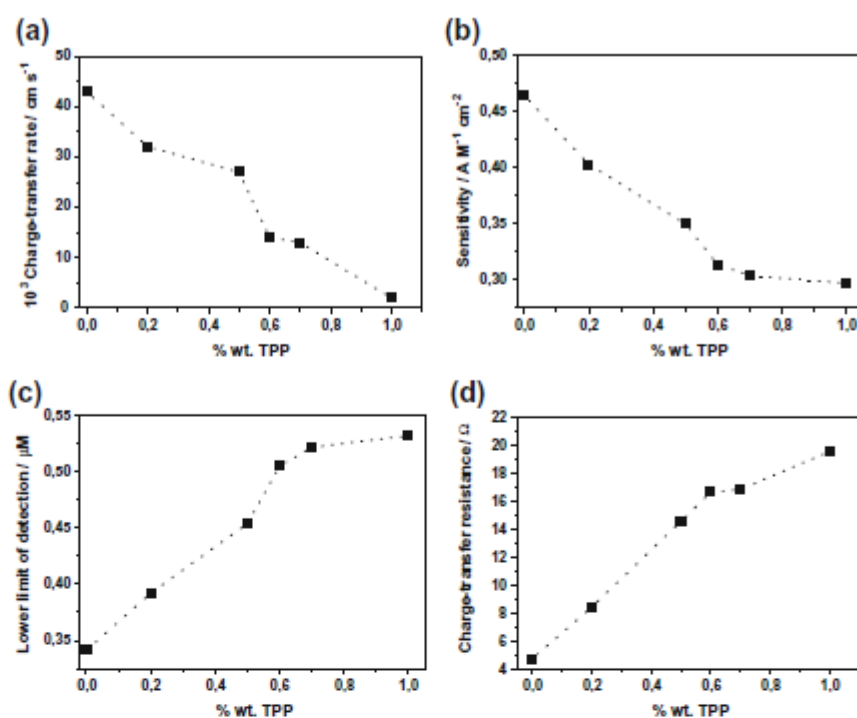
sensitivity tends to decrease with increasing the concentration of decomposed TPP used for the fabrication of N–P-MWCNT films. It is interesting that the sensitivity of N-MWCNTs appears to be about 13, 32, and 36% greater compared to those of N–P-MWCNT-1, N–P-MWCNT-3, and N–P-MWCNT-5 composite films, respectively.

The electrochemical behavior of $[Fe(CN)_6]^{3-/4-}$ redox system on N-MWCNTs and various N–P-MWCNT films was further investigated by means of electrochemical impedance spectroscopy technique. Representative EIS spectra recorded for $[Fe(CN)_6]^{3-/4-}$ (1.0 mol L^{-1} KCl) on N-MWCNTs and two different N–P-MWCNT composite films (N–P-MWCNT-3 and N–P-MWCNT-5) are shown in Fig. 2d. The presentation of EIS spectra of the other N–P-MWCNT films was skipped since only some minor differences can be observed among the EIS spectra, and consequently, the spectra are overlapped.

The EIS spectra were simulated by means of modified Nyquist circuit for estimating the charge transfer resistance, which is a parameter that controls the electron transfer kinetics of redox system at electrode interface and represents the barrier for electron transfer (the hindering behavior of interface properties of electrode) [35]. Specifically, to describe the impedance behavior of N-MWCNTs and various N–P-MWCNT films, an equivalent circuit involving a capacitor element C_b, due to the additional impedance caused by the electrical connection of film, must be considered. Thus, the modified

Nyquist circuit used for the simulation of impedance data can be represented as follows: $(R_s + C_b + (C_{dl}/(R_{ct} + Z_w))$, where R_s is the solution resistance, C_{dl} the double-layer capacitance (constant phase element was used instead of pure capacitor), R_{ct} the charge transfer resistance, and Z_w the Warburg diffusion impedance (Fig. S4, Electronic Supplementary Material). The obtained simulation error was in all cases less than ~3%. The estimated R_{ct} values for $[Fe(CN)_6]^{3-/4-}$ on N-MWCNTs and various N–P-MWCNT composite films are included in Table 1. Furthermore, the R_{ct} values are presented graphically vs. the % wt. of decomposed TPP used for synthesis of N–P-MWCNTs in Fig. 3d.

The findings demonstrate that the doping of carbon nanotubes with phosphorus leads to greater charge transfer resistance and thus to higher barrier for electron transfer, resulting therefore to slower kinetics of redox process occurring on these particular films (it is well known that the heterogeneous charge transfer rate varies inversely with charge transfer resistance) [36]. It is amazing that on the film consisting of N-MWCNTs, the R_{ct} value appears to be up to ~300% smaller compared to that obtained on N–P-MWCNT films. Namely, upon increasing of % wt. of decomposed TPP using the fabrication of N–P-MWCNTs from 0.2 to 1.0%, the charge transfer resistance increases from 78 up to 315%, resulting thus to harsh diminishing of kinetic of electrochemical process. It is interesting that the charge transfer resistance of fabricated

films, which increases with the following order: N-MWCNTs < N–P-MWCNT-1 < N–P-MWCNT-2 < N–P-MWCNT-3 < N–P-MWCNT-4 < N–P-MWCNT-5 (Fig. 3d), follows the falling with the same order of the kinetic parameter k_s estimated from the ΔE_p values (Fig. 3a). Furthermore, it is remarkable that with the same order, the limit of detection increases (Fig. 3c) and thus the sensitivity of composite films towards $[Fe(CN)_6]^{3-/4-}$ decreases (Fig. 3b). It can be, consequently, concluded that the increase of concentration of decomposed TPP and consequently the phosphorus-doping of nanotubes results to greater barrier and, thus, to lower kinetic of the electron transfer affecting significantly the sensitivity and detection capability of fabricated composite films. These results clearly demonstrate the greater electrocatalytic activity of films consisting exclusively of N-MWCNTs.

Raman spectroscopy studies were carried out for undoped multi-walled carbon nanotubes (MWCNTs), phosphorus-doped multi-walled carbon nanotubes (P-MWCNTs), N–P-MWCNTs, and N-MWCNTs. The Raman spectra of carbon nanotubes consist of two main bands, namely the so-called D-band (1336–1343 cm^{-1}) and the G-band (1567–1573 cm^{-1}), and their frequency is slightly affected by doping of nanotubes (Fig. S5, Electronic Supplementary Material). It is well known that the G-band corresponds to the high-frequency E_{2g} first-order mode and can be attributed to opposing movement of two-neighboring carbon atoms in graphene sheet [37], while the D-band results from defects in curved graphene sheets, as well as from ends and finite size crystalline domains of carbon nanotubes [38]. The ratio of relative intensities of G- and D-bands (I_G/I_D) is a measure of degree of structural order. For carbon nanotubes with different surface modifications, the change in intensity ratio (I_G/I_D) can be attributed to the change in surface functionalities or local defects resulting from bond breakage between C–C bonds in nanotubes [39]. In this work, the N-MWCNT films were found to exhibit smaller value of intensity ratio (I_G/I_D) compared to N–P-MWCNT film, indicating greater degree of structural defects in N-MWCNTs. Namely, it was found that the (I_G/I_D) ratio progressively decreases and consequently the degree of defects increases, with the following order: undoped-MWCNTs > P-MWCNTs > N–P-MWCNTs > N-MWCNTs (Table S2, Electronic Supplementary Material). It is thus obvious that the enhanced electrochemical response of N-MWCNTs is attributed to the greater degree of defects that these particular nanotubes possess.

The lifetime of fabricated N-MWCNT and N–P-MWCNT films was investigated. With this respect, the electrochemical response of composite films towards $[Fe(CN)_6]^{3-/4-}$ was studied continuously for a period of 7 days. The findings indicate that the electrochemical current response of composite films decreases at about ~2 and ~6% after 3 and 7 days, respectively. These finding show the great stability of fabricated carbon nanotube-based composite films.

Application of N–P-MWCNTs in electrochemical sensing of AA, DA, and UA

The response of selected N–P-MWCNT film (namely the N–P-MWCNTs fabricated upon decomposition of 1% wt. TPP) towards oxidation of molecules with biological interest, such as DA and UA, was tested in phosphate buffer solution at pH 7.0. The influence of AA as interfering material was additionally studied since AA can interfere in high concentrations with the electrochemical analysis of DA and UA. Representative CVs recorded for various concentrations of AA, DA, and UA (phosphate buffer solution, pH 7.0) are shown in Fig. 4. The detection limits of N–P-MWCNTs towards oxidation of studied biomolecules are reported along with literature values for comparison reasons in Table S3 (Electronic Supplementary Material).

CVs recorded for various concentrations of AA (phosphate buffer solution, pH 7.0) on N–P-MWCNTs are shown in Fig. 4a. As it can be seen in these CVs, the irreversible oxidation of AA onto N–P-MWCNTs occurs at the potential of about 0.228 V (vs. Ag/AgCl). It is well known that AA can be electrochemically oxidized to dehydro-L-ascorbic acid [41]. The findings demonstrate that the ability of N–P-MWCNTs to diminish the oxidation overpotential of AA is significantly lesser compared to that of N-MWCNTs. Specifically, the oxidation overpotential of AA onto N-MWCNTs, which lies in negative potential region (−0.014 V vs. Ag/AgCl), seems to be about 240 mV less anodic (positive) compared to that measured onto N–P-MWCNTs. These findings clearly demonstrate that the tendency of carbon nanotubes doped with nitrogen to lower the overpotential of AA is greater compared to that of carbon nanotubes doped with phosphorus. It was also observed that the response of N–P-MWCNTs towards oxidation of AA is somehow restricted. Namely, it was verified that for the same concentration of biomolecules the peak current response (peak current density) of N–P-MWCNTs towards oxidation of AA appears to be significantly lesser (between 30 and 40% lesser) compared to the current response towards oxidation of DA and UA. Thus, it is not surprising that the lower limit of detection of N–P-MWCNTs towards oxidation of AA estimated in the concentration range of 0.250–0.668 mM at about 11.6 μμ appears to be significantly poorer compared to those estimated for DA and UA (Table S3, Electronic Supplementary Material).

In CVs shown in Fig. 4b, it can be seen that the quasi-reversible oxidation peak of DA onto N–P-MWCNTs occurs at about 0.222 V (vs. Ag/AgCl), which lies very close to oxidation peak of AA measured on this particular composite film (0.228 V vs. Ag/AgCl). As was already suggested, the oxidation of DA can be characterized as two-electron transfer process that leads to formation of dopamine-o-quinone [42]. These findings demonstrate that quite significant interference

of AA in electrochemical analysis of DA (and the inverse interference of DA in analysis of AA) is expected. In order to estimate the lower limit of detection of N–P-MWCNTs towards oxidation of DA, various concentrations of DA were measured in the range of 0.017–0.196 mM. The detection limit of N–P-MWCNTs towards oxidation of DA was estimated to be 1.9 μM. It can be seen that the limit of detection of N–P-MWCNTs towards DA appears to be about 80% lower of that obtained for same composite film towards AA (Table S3, Electronic Supplementary Material).

The CVs recorded for UA reveals that the irreversible oxidation peak of UA onto N–P-MWCNTs appears at about +0.360 V (vs. Ag/AgCl) (Fig. 4c) that lies at about 132 and 138 mV more anodic (positive) potential compared to oxidation peaks of AA and DA, respectively. In previous published studies, it was suggested that the oxidation peak can be attributed to primary two electron oxidation of UA to uric acid diimine [43]. It is remarkable that the oxidation peak separation between AA–UA and DA–UA couples is nearly the same (about 135 mV), and thus, it is quite obvious that the simultaneous electrochemical analysis of AA–UA (in absence of DA) and DA–UA (in nonexistence of AA) can be carried out in a single measurement. In order to estimate the lower limit of detection of N–P-MWCNTs towards oxidation of UA, CVs for various concentrations of UA in the range of 0.032–0.211 mM were recorded (Fig. 4c). The detection limit of

7.8 μM estimated for N–P-MWCNTs towards oxidation of UA demonstrates that the detection ability of N–P-MWCNTs towards oxidation of UA appears to be about 310% poorer of that obtained for DA and about 32% greater of that measured for AA (Table S3, Electronic Supplementary Material). It is, however, very interesting that the obtained limits of detection of N–P-MWCNT composite film towards AA, DA, and UA appear to be about 30% poorer compared to those obtained for N-MWCNTs towards oxidation of same biomolecules (Fig. 4d) [40]. These findings support once more the conclusion that N-MWCNT film has better response in electrochemical sensing than N–P-MWCNTs. In addition, the modification of N-MWCNTs with gold nanoparticles enhances even more (about 90%) the sensitivity of the composite film towards oxidation of AA, DA, and UA [40]. This result show the important influence of metal nanoparticles on improvement of electrocatalytic properties of carbon nanotubes. However, according to the comparison shown in Table S3 (Electronic Supplementary Material), it is obvious that the N–P-MWCNT composite films appear to be enough sensitive to be used in individual electrochemical sensing of studied biomolecules.

The restricted tendency of N–P-MWCNT composite film to diminish the oxidation overpotential of AA results to significant interference of AA in simultaneous voltammetric analysis of AA and DA. Consequently, in CVs recorded for
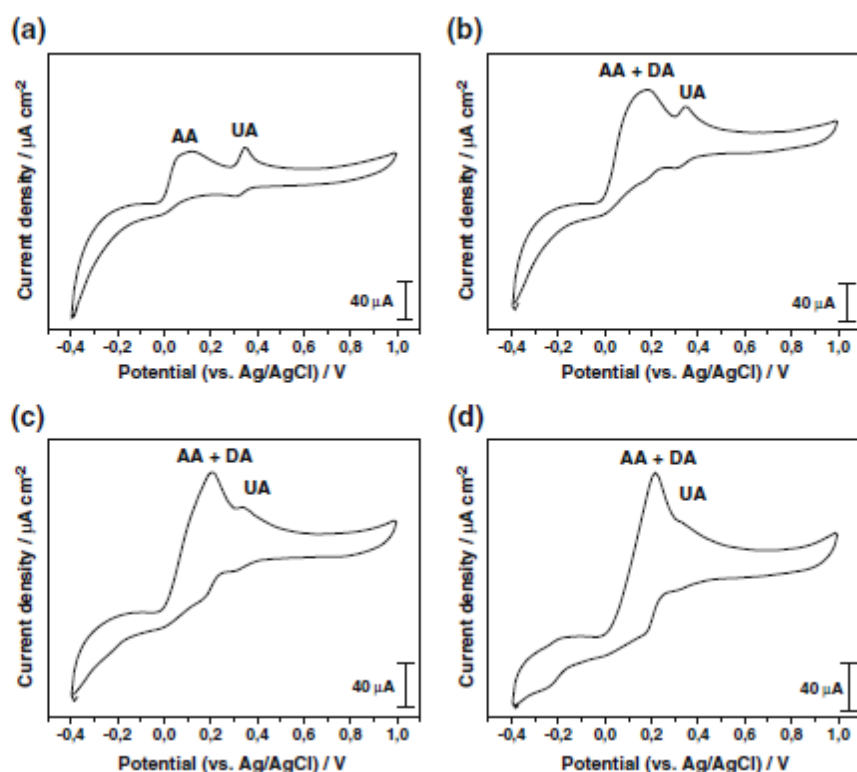
AA/DA/UA ternary mixtures, the redox waves of AA and DA overlap each other hindering, thus, their simultaneous electrochemical analysis (Fig. 5b–d). The findings exhibit that the AA oxidation wave interferes with DA, and likewise, the oxidation wave of DA hinders the oxidation wave of AA. Nevertheless, the AA/UA and DA/UA binary systems can be successfully simultaneously analyzed in single experiment on N–P-MWCNT film since their electrochemical waves do not overlap each other. For instance, in CVs recorded for AA/ UA (1:1) binary system, well-separated oxidation waves were recognized with peak potential separations of ~200 mV that permit their simultaneous analysis in a single measurement. It is interesting that well-separated redox waves can be still observed in AA/UA binary systems even if the concentration of AA is five times higher compared to that UA (Fig. 5a). Similar results were obtained for the DA/UA binary system (data not shown).

decomposition of ACN in presence of catalyst. The N–P-MWCNTs were characterized using SEM and TEM in combination with EDX as well as by means of Raman spectroscopy. Electrochemical studies reveal that N–P-MWCNT film is quite suitable for individual analysis of AA, DA, and UA with limits of detection at 11.6, 1.9, and 7.8 μM, respectively. The interference of AA in simultaneous analysis of UA and DA was investigated. The findings demonstrate that AA does not interfere with UA, but nevertheless, considerable interference of AA in electrochemical analysis of DA (and the inverse interference of DA in analysis of AA) was recognized. N–P-MWCNT composite film appears to be evidently electrochemically less sensitive compared to N-MWCNT film.

Conclusions

The fabrication of N–P-MWCNTs on Si/SiO$_2$ substrate was carried out with simultaneous decomposition of TPP and ACN in the presence of catalyst by means of spray pyrolysis. For comparison reasons, N-MWCNTs were fabricated with

References

1. Milowska K, Birowska M, Majewski JA (2012) Mechanical and electrical properties of carbon nanotubes and graphene layers functionalized with amines. Diam Relat Mater 23:167–171

2. Matzui L, Ovsienko IV, Len TA, Yu P, Scharff P (2005) Transport properties of composites with carbon nanotube-based composites. Fullerenes Nanotubes Carbon Nanostruct 13:259–265

3. Mykhailenko O, Matsui D, Yu P, Le Normand F, Eklund P, Scharff P (2007) Monte Carlo simulation of intercalated carbon nanotubes. J Mol Model 13:283–287

4. Ovsienko IV, Len TA, Matzui LY, Prylutskyy YI, Ritter U, Scharff P, Le Normand F, Eklund P (2007) Resistance of a nanocarbon material containing nanotubes. Mol Cryst Liq Cryst 468:289–297

5. Lazarenko A, Vovchenko L, Matsui D, Yu P, Matzuy L, Ritter U, Scharff P (2008) Electrical and thermal conductivity of polymer-nanocarbon composites. Mol Cryst Liq Cryst 497:397–407

6. Grechnev GE, Desnenko VA, Fedorchenko AV, Panfilov AS, Kolesnichenko YA, Matzui LY, Grybova MI (2010) Structure and magnetic properties of multi-walled carbon nanotubes modified with iron. Low Temp Phys 36:1086–1090

7. Ritter U, Scharff P, Grechnev GE, Desnenko VA, Fedorchenko AV, Panfilov AS, Prylutskyy YI, Kolesnichenko YA (2011) Structure and magnetic properties of multi-walled carbon nanotubes modified with cobalt. Carbon 49:4443–4448

8. Luo H, Shi Z, Li N, Gu Z, Zhang Q (2001) Investigation of the electrochemical and electrocatalytic behavior of single-wall carbon nanotube film on a glassy carbon electrode. Anal Chem 73:915–920

9. Musameh M, Wang J, Merkoci A, Lin YH (2002) Low-potential stable NADH detection at carbon-nanotube-modified glassy carbon electrodes. Electrochem Commun 4:743–746

10. Jacobs CB, Peairs MJ, Venton BJ (2010) Review: carbon nanotube based electrochemical sensors for biomolecules. Anal Chim Acta 662:105–127

11. Xie X, Gan T, Sun D, Wu K (2008) Application of multi-walled carbon nanotubes/nafion composite film in electrochemical determination of Pb^{2+}. Fullerenes Nanotubes Carbon Nanostruct 16:103–113

12. Brahman PK, Dar RA, Tiwari S, Pitre KS (2012) Electrochemical behavior of gatifloxacin at multi-walled carbon nanotube paste electrode and its interaction with DNA. Rev Anal Chem 31:83–92

13. Debnarayan J, Chia-Liang S, Li-Chyong C, Kuei-Hsien C (2013) Effect of chemical doping of boron and nitrogen on the electronic, optical, and electrochemical properties of carbon nanotubes. Prog Mater Sci 58:565–635

14. Liu H, Zhang Y, Li R, Sun X, Abou-Rachid H (2012) Thermal and chemical durability of nitrogen-doped carbon nanotubes. J Nanopart Res 14:1016–1023

15. Boncel S, Pattinson SW, Geiser V, Shaffer MSP, Koziol KKK (2014) En route to controlled catalytic CVD synthesis of densely packed and vertically aligned nitrogen-doped carbon nanotube arrays. Beilstein J Nanotechnol 5:219–233

16. Li XF, Lian KY, Liu L, Wu Y, Qiu Q, Jiang J, Deng M, Luo Y (2016) Unraveling the formation mechanism of graphitic nitrogen-doping in thermally treated graphene with ammonia. Sci Rep 6:23495 (10 pages)

17. Maciel IO, Campos-Delgado J, Cruz-Silva E, Pimenta MA, Sumpter BG, Meunier V, Lopez-Urias F, Munoz-Sandoval E, Terrones H, Terrones M, Jorio A (2009) Synthesis, electronic structure, and Raman scattering of phosphorus-doped single-wall carbon nanotubes. Nano Lett 9:2267–2272

18. Cruz-Silva E, Cullen DA, Gu L, Romo-Herrera JM, Munoz-Sandoval E, Lopez-Urias F, Sumpter BG, Meunier V, Charlier JC, Smith DJ, Terrones H, Terrones M (2008) Heterodoped nanotubes: theory, synthesis, and characterization of phosphorus-nitrogen doped multiwalled carbon nanotubes. ACS Nano 2:441–448

19. Wang SY, Ren Y, Cheng CW, Chen JK, Tzou DY (2013) Micromachining of copper by femtosecond laser pulses. Appl Surf Sci 273:302–308

20. Cruz-Silva E, Lopez-Urias F, Munoz-Sandoval E, Sumpter BG, Terrones H, Charlier JC, Meunier V, Terrones M (2009) Electronic transport and mechanical properties of phosphorus- and phosphorus-nitrogen-doped carbon nanotubes. ACS Nano 3:1913–1921

21. Tsierkezos NG, Ritter R (2010) Synthesis and electrochemistry of multi-walled carbon nanotube films directly attached on silica substrate. J Solid State Electrochem 14:1101–1107

22. Tsierkezos NG, Ritter R (2012a) Oxidation of dopamine on multi-walled carbon nanotubes. J Solid State Electrochem 16:2217–2226

23. Tsierkezos NG, Wetzold N, Ritter U (2013a) Electrochemical responses of carbon nanotubes-based films printed on polymer substances. Ionics 19:335–341

24. Tsierkezos NG, Wetzold N, Ritter U, Hübler AC (2013b) Analysis of dopamine on printed polymer thin film consisting of multi-walled carbon nanotubes. Monatsh Chem 144:581–588

25. Tsierkezos NG, Ritter U (2012b) Simultaneous detection of ascorbic acid and uric acid at MWCNT modified electrodes. J Nanosci Lett 2:25–39

26. Tsierkezos NG, Wetzold N, Hübler AC, Ritter U, Szroeder P (2013c) Multi-walled carbon nanotubes printed onto polycarbonate substrate for electrochemical sensing. Sens Lett 11:1465–1471

27. Tsierkezos NG, Ritter U (2011) Application of electrochemical impedance spectroscopy for characterisation of the reduction of benzophenone in acetonitrile solutions. Phys Chem Liq 49:729–742

28. Tsierkezos NG, Ritter U, Knauer A, Szroeder P (2014a) Electrocatalytic activity of nitrogen-doped carbon nanotubes decorated with gold nanoparticles. Electrocatalysis 5:87–95

29. Tsierkezos NG, Knauer A, Ritter U (2014b) Thermodynamic investigation of ferrocyanide/ferricyanide redox system on nitrogen-doped multi-walled carbon nanotubes decorated with gold nanoparticles. Thermochim Acta 576:1–8

30. Katayama T, Araki H, Yoshino K (2002) Multi-walled carbon nanotubes with bamboo-like structure and effects of heat treatment. J Appl Phys 91:6675–6678

31. Tsierkezos NG, Haj Othman S, Ritter U, Hafermann L, Knauer A, Köhler JM (2014c) Nitrogen-doped multi-walled carbon nanotubes modified with platinum, palladium, rhodium and silver nanoparticles in electrochemical sensing. J Nanopart Res 16:2660–2672

32. Brett CMA, Brett AMO (1998) Electroanalysis. Oxford University Press Inc., New York

33. Tsierkezos NG, Ritter U, Nugraha Thaha Y, Downing C, Szroeder P, Scharff P (2016a) Multi-walled carbon nanotubes doped with boron as an electrode material for electrochemical studies on dopamine, uric acid, and ascorbic acid. Microchim Acta 183:35–47

34. Nicholson RS (1965) Theory and application of cyclic voltammetry for measurement of electrode reaction kinetics. Anal Chem 37:1351–1355

35. Esplandiu MJ, Pacios M, Bellido E, Del Valle M (2007) Carbon nanotubes and electrochemistry. Z Phys Chem 221:1161–1173

36. Tsierkezos NG, Szroeder P, Ritter U (2011) Multi-walled carbon nanotubes as electrode materials for electrochemical studies of organometallic compounds in organic solvent media. Monatsh Chem 142:233–242

37. Nemanish RJ, Solin SA (1979) First- and second-order Raman scattering from finite-size crystals of graphite. Phys Rev B 20:392–401

38. Choi S, Park KH, Lee S, Koh KH (2002) Raman spectra of nano-structured carbon films synthesized using ammonia-containing feed gas. J Appl Phys 92:4007–4011

39. Tian ZQ, Jiang SP, Liang YM, Shen PK (2005) Synthesis and characterization of platinum catalysts on multi-walled carbon nanotubes by intermittent microwave irradiation for fuel cell applications. J Phys Chem B 110:5343–5350

40. Tsierkezos N, Haj Othman S, Ritter U, Hafermann L, Knauer A, Köhler JM, Downing C, McCarthy EK (2016b) Electrochemical

analysis of ascorbic acid, dopamine, and uric acid on nobel metal modified nitrogen-doped carbon nanotubes. Sensor Actuat B Chem 231:218–229

41. Climent MA, Rodes A, Valls MJ, Peres JM, Fellu JM, Aldaz A (1994) Voltammetric and subtractively normalized interfacial FTIR study of the adsorption and oxidation of L(+)-ascorbic acid on Pt electrodes in acid medium: effect of Bi adatoms. J Chem Soc Faraday Trans 90:609–615

42. Razmi H, Agazadeh M, Habibi B (2003) Electrocatalytic oxidation of dopamine at aluminum electrode modified with nickel pentacyanonitrosylferrate films, synthesized by electroless procedure. J Electroanal Chem 547:25–33

43. Owens JL, Marsh HA, Dryhurst G (1978) Electrochemical oxidation of uric acid and xanthine: an investigation by cyclic voltammetry, double potential step chronoamperometry and thin-layer spectroelectrochemistry. J Electroanal Chem 91:231–247
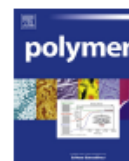
Novel hydrogels containing Nafion and poly(ethylene oxide) based block copolymers

CrossMark

D. Fernandes [a], W. Kluska [a], J. Stanislawska [a], B. Board [a], M.J. Krysmann [b], A. Kelarakis [a, *]

[a] Centre for Materials Science, School of Physical Sciences and Computing, University of Central Lancashire, Preston, PR1 2HE, UK
[b] School of Pharmacy and Biosciences, University of Central Lancashire, Preston, PR1 2HE, UK

ABSTRACT

We present a novel family of biocompatible hydrogels containing Nafion and poly(ethylene oxide) based block copolymers. In aqueous environment, thermodynamically stable ionomer-copolymer complexes are formed, as evident by light scattering and quartz crystal microbalance experiments. Moreover, incorporation of Nafion dramatically modifies the phase behaviour and the rheological properties of copolymer hydrogels. The hybrid systems not only undergo sharp and thermally reversible sol-gel transitions below the body temperature, thus retaining their injectable nature, but they also generate mechanically robust hydrogels. Moreover, ibuprofen was continuously released over a period of 26 days for the Nafion/Pluronic hydrogel, compared to only 3 days for the Nafion-free system. The hybrid gels are promising candidates for 3D-bioprinting and controlled drug release applications.

© 2017 Published by Elsevier Ltd.

1. Introduction

Hydrogels are water swollen networks of chemically or physically crosslinked macromolecular chains having a highly porous structure that exhibit complex viscoelastic characteristics [1–3]. The physical properties of those soft systems can be largely tuned with respect to the chemical composition of the polymeric components and their crosslinking density. Stimuli-responsive hydrogels can sense and adapt to changes in their surroundings such as temperature, pH, ionic strength, pressure, light, electric field and the presence of certain chemical trigers [4,5].

Particular emphasis is given to the development of injectable systems [6,7] that gel *in situ* under physiological conditions facilitating the controlled and sustained release of the entrapped drugs. Because they can be applied in nonsurgical treatments (tissue engineering, drug delivery, wound repair, dermal filling, etc.), they offer obvious advantages in terms of therapy cost and duration as well as patient comfort and recovery. Injectable hydrogels are derived by natural polymers (such as hyaluronic acid [8], cellulose [9], proteins and peptides [10], chitosan [11]) or synthetic macromolecules (composed of acrylates methacrylates, vinyl ethers, cyclic esters, amino acids, acrylamides, etc.) [12].

The dynamic presence of poly(ethylene oxide) (PEO) based copolymers in the field of injectable hydrogels can be traced back to their interesting self-assembly properties that allow sharp sol-gel thermoreversible transitions below body temperature [13,14]. This class of nanostructured gels exhibit minimal cytotoxicity and improved pharmacokinetics [15], but they typically suffer from weak mechanical properties and rapid drug release. Well-explored approaches to overcome those challenges rely on the development of photocrosslinked [16], stereocomplexed [17] and multicomponent [18] systems.

In this report we demonstrate that introduction of Nafion to hydrogels containing PEO based copolymers improves their drug release profile and enhances their mechanical strength, without compromising their injectable character. Nafion is primarily known as the proton exchange membrane in fuel cells [19,20]. Early studies have demonstrated its biocompatible nature [21,22], but it has only recently attracted significant attention for biomedical applications such as implant coatings [23], biosensors [24,25] and biocompatible capsules [26]. Its amphiphilic structure consists of a remarkably robust Teflon-like backbone decorated with highly polar pendant groups. Due to this macromolecular design, Nafion interacts strongly with non-ionic block copolymers [27,28] giving rise to thermodynamically stable supramolecular assemblies.

* Corresponding author.
E-mail address: akelarakis@uclan.ac.uk (A. Kelarakis).

2. Experimental section

2.1. Materials

Two Nafion dispersions (in water and low aliphatic alcohols, respectively) were obtained by Ion Power. Pluronic P123 was obtained by Sigma Aldrich and is referred here as $E_{19}P_{69}E_{19}$. The notations are as follows: E stands for an oxyethylene unit OCH_2CH_2, P for oxypropylene $OCH_2CH(CH_3)$, while the subscripts denote number-average block of repeat units. The copolymer $B_{20}E_{510}$, where B stands for an oxybutylene unit $OCH_2CH(C_2H_5)$, was synthesized by sequential anionic polymerization of 1,2-butylene oxide followed by ethylene oxide, using potassium activated 2-butanol as initiator [29].

2.2. Methods

2.2.1. Dynamic light scattering (DLS)

DLS measurements at $T = 25\ ^\circ C$ were conducted using a Malvern Zetasizer Nano-ZS (Malvern Instruments, England) system equipped with a He-Ne laser beam with $\lambda = 633$ nm. Prior to the measurements the samples were filtered through Nylon membrane filters with a pore size of 0.2 μm directly to the measuring cuvettes.

2.2.2. Quartz crystal microbalance with dissipation monitoring (QCM-D)

QCM-D experiments were conducted at $T = 25\ ^\circ C$ using a Q-sense E1 unit. SiO_2 modified crystals with fundamental resonance frequency close to 5 MHz were coated with Nafion. To that end, a drop of ethanol containing 0.5 wt% Nafion was deposited in each crystal that was subsequently left for at least 48 h at room temperature to ensure complete evaporation of the solvent. The thus prepared Nafion-coated crystals were mounted to a flow cell (flow rate = 0.2 ml/min) and their interaction with water and copolymer solutions were monitored. When a layer of material with mass Δm is deposited on the crystal surface, its resonant frequency is reduced by Δf according to Sauerbrey relation [30].

$$\Delta m = -(C/N)\Delta f \tag{1}$$

where N denotes the overtone number and C the integrated crystal sensitivity. The dissipation factor D is defined as

$$D = E_d/(2\pi E_s) \tag{2}$$

where E_d is the energy dissipated during one period of oscillation and E_s is the energy stored in the system [31]. For simplicity, only the third overtones (N = 3) are described in this report.

2.2.3. Rheology

The viscoelastic properties of the hydrogels were studied using a stress controlled AR-G2 rheometer (TA). All measurements were performed within the linear viscoelastic region (strain 2%), using a parallel plate cell with 50 mm diameter. Frequency sweep data were collected at selected temperatures, while temperature ramps were performed at $\omega = 1$ rad/sec with a heating rate of 1 °C/min. Extra care was taken to minimize evaporation by using a solvent trap to maintain a water saturated environment.

2.2.4. Small angle X-ray scattering (SAXS)

SAXS experiments were performed on beamline I22, Diamond Light Source Synchrotron Radiation Source, U.K. The wavelength of synchrotron radiation was 1 Å and the sample-to-detector distance was 6 m. Samples were mounted between mica windows in a liquid cell equipped with water-bath temperature control. Two dimensional SAXS patterns were collected using a Pilatus P3-2M area detector. All patterns were corrected for the incident beam fluctuations as well as air and instrument scattering, before being converted into 1D profiles using the Dawn software.

2.2.5. Drug release profiles

A gel containing 32.5 wt% $E_{19}P_{69}E_{19}$ and 0.5 wt% ibuprofen (Sigma- Aldrich) was transferred into a Snakeskin dialysis membrane (with molecular weight cut-off 3.5 kDa) and was subsequently immersed in phosphate buffer saline solution (pH 7.4) at a constant temperature of 37 °C. Samples of the buffer solution were withdrawn at predetermined times and the ibuprofen content was determined on a basis of a calibration curve using a Shimadzu UV3600 UV-Vis, at 265 nm. An, otherwise identical, experiment was conducted for the gel containing 32.5 wt% $E_{19}P_{69}E_{19}$ and 10 wt% Nafion.

3. Results and discussion

Intensity fraction distributions of apparent hydrodynamic radius (r_h) of 0.5 wt % $B_{20}E_{510}$ aqueous solutions (circles in Fig. 1) indicate the presence of highly swollen micelles with $r_h = 31$ nm, in agreement with previous studies [29]. Judging by its B block length [14], the critical micelle concentration (cmc) of $B_{20}E_{510}$ is expected to fall below 10^{-4} wt%, consistent with the absence of a unimer peak. Addition of 0.5 wt% Nafion results in particles with $r_h = 80$ nm (squares in Fig. 1), an effect that suggests extensive Nafion-copolymer binding. For reference, a 0.5 wt % aqueous dispersion of Nafion shows a wide size distribution below 20 nm (data not shown here) and unbound Nafion particles might count for the minor peak observed in Fig. 1.

Previous reports [27,28] provide clear evidence that Nafion forms supramolecular assemblies with $E_{18}B_{10}$, $E_{19}P_{69}E_{19}$ and $M_{18}E_{20}$ (M_{18} stands for $C_{18}H_{37}$) in water. For example, the critical micelle temperature (cmt) of $E_{19}P_{69}E_{19}$ solutions was found to systematically increase in the presence of Nafion, indicating strong copolymer adsorption to the ionomer backbone [27]. The complexation has been attributed to hydrophobic interactions and extensive hydrogen bonding between Nafion's protons and the ether oxygen of EO [32]. It is interesting to note the architectural similarity between the copolymer's hydrophilic building block -OCH_2CH_2- and Nafion's side chain -OCF_2CF_2-.

Each one of the QCM-D sensorgrams in Fig. 2 describes an initial equilibrium of a Nafion coated crystal against air in order to determine the fundamental resonance frequency, followed by a subsequent equilibrium against flowing water to determine the

Fig. 1. Time course of frequency (filled symbols) and dissipation factor (open symbols) of a Nafion-coated crystal resonator in QCM-D experiments at 25 °C. "W" and "S" denote the injection of water and the copolymer solutions containing 0.5 wt% E19P69E19 (a) and 0.5 wt% B20E510 (b), respectively.
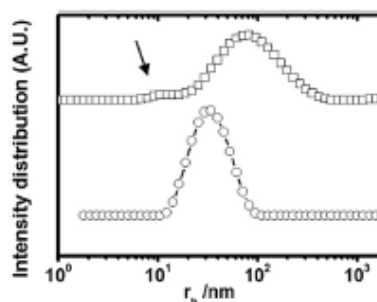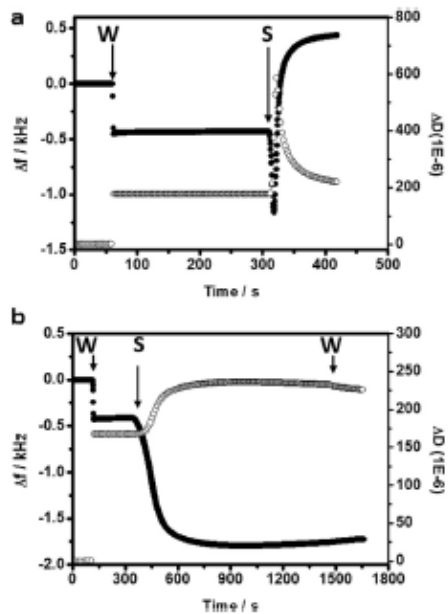
175

Fig. 2. Time course of frequency (filled symbols) and dissipation factor (open symbols) of a Nafion-coated crystal resonator in QCM-D experiments at 25 °C. "W" and "S" denote the injection of water and the copolymer solutions containing 0.5 wt% $E_{19}P_{69}E_{19}$ (a) and 0.5 wt% $B_{20}E_{510}$ (b), respectively.

baseline of the hydrated membrane. The pronounced drop in f that follows the hydration of the crystals reveals the ample water uptake of the Nafion's ionic domains that does not, however, result in the dissolution of the membrane.

Introduction of 0.5 wt% $E_{19}P_{69}E_{19}$ solution (Fig. 2a) to the hydrated Nafion membrane initially causes a dramatic decrease in f due to extensive copolymer adsorption, an effect that reduces the rigidity of the membrane as revealed by the accompanying increase in D. When the amount of the attached polymer exceeds a critical threshold, a rapid increase in f is observed due to the dissolution of the Nafion membrane. The detergency efficiency of $E_{19}P_{69}E_{19}$ against Nafion ultrathin membranes has been described in detail previously [27,28], and the underlying mechanism holds true for $E_{18}B_{10}$ and $M_{18}E_{20}$.

Introduction of $B_{20}E_{510}$ solution (Fig. 2b) also gives rise to a significant decrease in f and an accompanying increase in D, indicating rapid and extensive Nafion-copolymer binding. By virtue of their super-swollen nature ($r_h = 31$ nm), the adsorbed copolymer chains impose significant steric constrains so that the rather limited amount of copolymer attached is incapable in solubilising Nafion. It has been estimated that each E-unit in the corona of $B_{20}E_{510}$ micelles is associated with 96 water molecules [33], out of which only 6 water molecules are present in the hydration layer [34] and the remaining is essentially bulk water. Nevertheless, QCM-D sensorgram suggest that $B_{20}E_{510}$ chains are firmly adsorbed to Nafion's surface and are not detached upon prolonged water rinsing. In contrast, in an otherwise identical experiment, it was found that a significant portion of the attached PEO on the Nafion membrane can be removed under water flow [27]. The difference between the two systems, highlight the role of hydrophobic-hydrophobic interactions between the substrate and the adsorbed $B_{20}E_{510}$ chains that are not present in the case of PEO (that lacks hydrophobic groups).

The sol-gel phase diagram of concentrated aqueous dispersions of PEO based block copolymers is governed by the exothermic dissolution of ethylene glycol that favours micellization and, thereby, micellar packing at intermediate temperatures, but also accounts for pronounced corona dehydration and collapse of the close packing at elevated temperatures. As shown in Fig. 3, upon heating the 32.5 wt% $E_{19}P_{69}E_{19}$ aqueous dispersion exhibits a sharp sol-gel transition at 19 °C (G' exceeds 1 kPa and $G' > G''$) and the structure collapses at 42 °C into a soft gel phase (G' falls much below 1 kPa, but remains higher than G''). Soft gels are described as defected closely packed systems, where interacting micellar aggregates give rise to a moderate viscoelastic response (e.g. stronger than sol, but weaker than a hard gel) [35].

Addition of 5 wt% and 10 wt% Nafion modifies the phase diagram, given that the hybrid systems remain within the sol phase at temperatures up to 45 and 34 °C (G' exceeds 1 kPa and $G' > G''$), respectively and the gels formed are stable up to the highest temperature tested (60 °C). The inset shown in Fig. 3 demonstrates a tube inversion test and shows the immobile nature of a 32.5 wt% $E_{19}P_{69}E_{19}/10$ wt% Nafion gel at 40 °C. Significantly, the sol-gel transitions observed for the hybrid systems are thermoreversible and they remain unaltered upon repetitive heat-cool-heat cycles. In other words, while Pluronic hydrogels tend to exhibit a sol-gel-sol transition upon heating, addition of Nafion leads to a monotonous enhancement of viscoelasticity as a function of temperature. For reference, we note that a 13.9 wt% aqueous dispersion of the thermo and pH responsive linear triblock copolymer, poly(-methoxydi(ethylene glycol) methacrylate-co-methacrylic acid)-b-PEO-b poly(methoxydi(ethylene glycol) methacrylate-co-methacrylic acid) at pH = 4 undergoes sol-gel transition at 36.1 °C and maintains a plateau G' value close to 3 kPa at least up to 65 °C [36].

The SAXS patterns shown in Fig. 4 indicate a body centered cubic (bcc) packing for 32.5 wt% $E_{19}P_{69}E_{19}$ at 20 °C with reflections at $q/q^* = 1:\sqrt{2}:\sqrt{3}$, where q stands for the scattering vector and q^* for the first order reflection [37]. The bcc structure is somewhat maintained in the presence of 1 wt% Nafion, although the hybrid is a weaker gel. Addition of 5 wt% Nafion has a profound impact, leading to a fluid system with broad scattering peaks ($q/q^* = 1:\sqrt{3}:\sqrt{7}$) that are roughly consistent with hexagonal packing of cylinders [38]. Moreover, in the presence of 10 wt% Nafion the
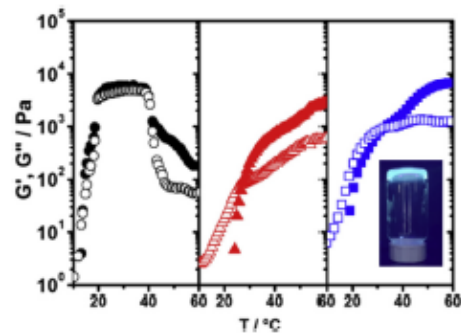
Fig. 3. Temperature sweeps ($\omega = 1$ rad/s, strain amplitude = 2%) for aqueous gels containing 32.5 wt% $E_{19}P_{69}E_{19}$ in the absence (black circle) and the presence of 5 wt% Nafion (red triangles) and 10 wt% Nafion (blue squares). Solid symbols denote stroage modules (G') and open symbol denote loss modules (G''). The insert shows a photo of the gel containing 32.5 wt% $E_{19}P_{69}E_{19}/10$ wt% Nafion at 40 °C) (a fluroscence dye has been added to facilitate imaging under UV radiation). (For interpretation of the references to colour in this figure legend, the reader is referred to the web version of this article.)
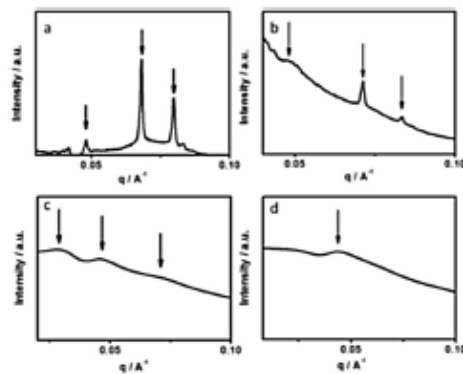
Fig. 4. SAXS patterns of aqueous gels of 32.5 wt% $E_{19}P_{69}E_{19}$ in the absence of Nafion (a) and in the presence of 1 wt% Nafion (b), 5 wt% Nafion (c) and 10 wt% Nafion (d).

fluid system does not possess any long range correlation. The dramatic effects induced by Nafion to the phase behaviour of the gels are in line with the extensive adsorption of $E_{19}P_{69}E_{19}$ to Nafion backbone, an effect that reduces the effective volume fraction of the dispersed particles, ultimately removing the close packing constrains. We note that SAXS profiles at 45 °C and 65 °C indicated the absence of an ordered structure for all hydrogels in the absence and in the presence of 5 and 10 wt% Nafion.

Fig. 5 shows the release profiles of ibuprofen from 32.5 wt% $E_{19}P_{69}E_{19}$ in the absence (black circles) and presence (blue squares) of 10 wt% Nafion against phosphate buffer (pH = 7.4) solution at 37 °C. A rather rapid release is observed from the copolymer gel given that 65 and 91 wt% of the drug was released within the first 24 and 72 h, respectively. For reference we note, that aceclofenac and paclitaxel are fully released within 24 h from a Pluronic micellar solution [39] and a Pluronic hydrogel [40], respectively. However, the diffusion of ibuprofen from the hybrid hydrogel is much slower given that 21, 55 and 93 wt% of the drug is released after 24, 240 and 624 h, respectively. Taking into account that the two systems have similar rheological properties at 37 °C (Fig. 3), the improved release profile seen for the hybrid system can be attributed to a lower level of porosity/higher tortuosity or stronger matrix-drug interactions in the presence of Nafion. Further work is underway to elucidate the diffusion mechanism in this complex system. In a control experiment we investigated the drug release profile from an acidified 32.5 wt% Pluronic gel (pH = 3, in accordance to that measured for the Nafion/Pluronic gel), but the effect of pH adjustment was found to be minimal.
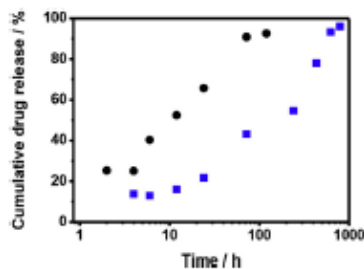
Fig. 5. Release profiles of ibuprofen from 32.5 wt% $E_{19}P_{69}E_{19}$ in the absence (black circles) and presence (blue squares) of 10 wt% Nafion against phosphate buffer solution (pH = 7.4) at 37 °C. (For interpretation of the references to colour in this figure legend, the reader is referred to the web version of this article.)

Frequency sweeps shown in Fig. 6a suggest that the 5 wt% aqueous solution of $B_{20}E_{510}$ forms a gel from 20 to 45 °C and the G' show a maximum value of 800 Pa (ω = 1 rad/s) at 30 °C. Low G' values in, otherwise immobile, gels close to their critical gel concentration, have been reported previously for copolymers with long E blocks [29]. As seen in Fig. 6b, introduction of 10 wt% Nafion allows the formation of mechanically robust hydrogels with G' higher than 9 kPa and 23 kPa (ω = 1 rad/s) at T = 40 °C and 45 °C. At 40 °C and 45 °C, G' and G'' are only weakly dependent on frequency, indicating solid-like rheological response.

Fig. 7 compares the temperature dependence of G' for 5 wt% $B_{20}E_{510}$ (open circles) and 5 wt% $B_{20}E_{510}$/10 wt% Nafion (full squares) (the data points at ω = 1 rad/s were read off from frequency sweeps and were combined in a single curve). It can be seen that within the temperature range 20–30 °C, the hybrid gel shows one order of magnitude lower G' compared to its Nafion-free counterpart, an obvious advantage for injectable applications. At temperature above 30 °C the hybrid undergoes an abrupt (albeit thermally reversible) sol-gel transition that results in the formation of a mechanically robust hydrogel. (Due to the pronounced differences in their viscoelastic properties at 37 °C between the two systems shown in Fig. 7, we did not conduct drug release studies). Despite this abrupt phase transformation upon heating, SAXS patterns shown in Fig. 8 indicate that the structure of the system lacks long range order at 15 °C as expected for a fluid, but this observation remains unaltered at 45 °C, even though the hydrogel behaves rheologically as a solid-like material. With respect to the 5 wt% $B_{20}E_{510}$, we note that the bcc structure of this type of super-swollen gels close to their critical gel concentration has been confirmed so far only by SANS measurements [41], while our SAXS data did not show any refractive peaks.
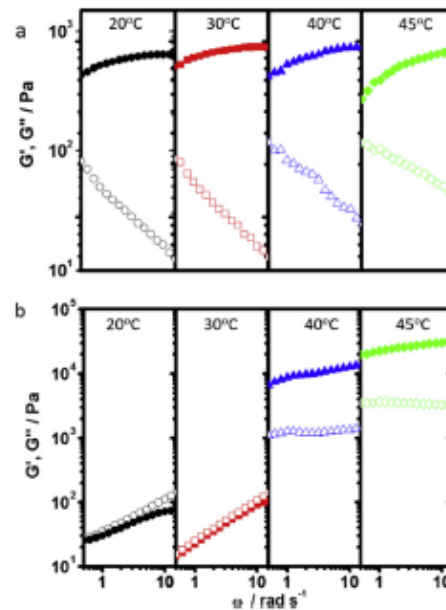
Fig. 6. Frequency dependence (strain amplitude ~ 2%) of storage modulus (G', solid symbols) and loss modulus (G'', open symbols) at various temperatures (black circles for 20 °C, red squares for 30 °C, blue triangles for 40 °C, green diamonds for 45 °C) for aqueous gels containing 5 wt% $B_{20}E_{510}$ in the absence (a) and in the presence of 10 wt% Nafion (b). (For interpretation of the references to colour in this figure legend, the reader is referred to the web version of this article.)

**Fig. 7.** Temperature dependence of storage modulus G' ($\omega = 1$ rad/s, strain amplitude = 2%) for aqueous gels containing 5 wt% $B_{20}E_{510}$ in the absence (open circles) and in the presence of 10 wt% Nafion (solid squares). The data were read off from frequency sweeps measurements.
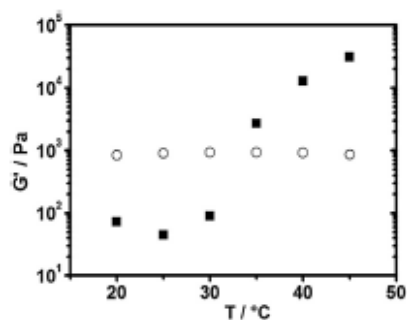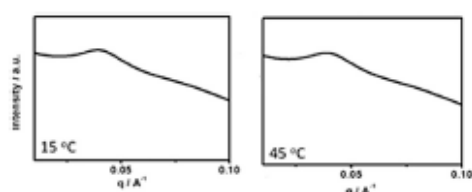

Fig. 8. SAXS patterns of an aqueous gel containing 5 wt% $B_{20}E_{510}$ in the presence of 10 wt% Nafion at the temperatures indicated.

4. Conclusions

In water, Nafion and PEO based copolymers undergo synergistic mixing as evident by light scattering and QCM-D experiments. At higher concentrations the supramolecular assemblies exhibit an abrupt sol-gel transition below body temperature, generating thermoreversibe hydrogels. The 5 wt% $B_{20}E_{510}$/10 wt% Nafion hybrid hydrogel at body temperature exhibits significantly improved mechanical strength compared to its Nafion-free counterpart. Moreover, the hybrid $E_{19}P_{69}E_{19}$/Nafion gel exhibits dramatically improved drug release profile *in vitro* over a prolonged period of time. Those biocompatible systems offer exciting opportunities for the development of a new generation of super-tough nanogels and bioinks.

Acknowledgements

References

[1] A.S. Hoffman, Stimuli-responsive polymers: biomedical applications and challenges for clinical translation, Adv. Drug Deliv. Rev. 65 (2013) 10–16, http://dx.doi.org/10.1016/j.addr.2012.11.004.
[2] T.R. Hoare, D.S. Kohane, Hydrogels in drug delivery: progress and challenges, Polym. Guildf. 49 (2008) 1993–2007, http://dx.doi.org/10.1016/j.polymer.2008.01.027.
[3] J. Kopecek, Hydrogel biomaterials: a smart future? Biomaterials 28 (2007) 5185–5192, http://dx.doi.org/10.1016/j.biomaterials.2007.07.044.
[4] M.C. Koetting, J.T. Peters, S.D. Steichen, N.A. Peppas, Stimulus-responsive hydrogels: theory, modern advances, and applications, Mat. Sci. Eng. R. Rep. 93 (2015) 1–49, http://dx.doi.org/10.1016/j.mser.2015.04.001.
[5] C. Tsitsilianis, Responsive Reversible Hydrogels from associative "smart" macromolecules, Soft Matter 6 (2010) 2372–2388, http://dx.doi.org/10.1039/b923947b.
[6] K.H. Bae, L.-S. Wang, M. Kurisawa, Injectable biodegradable hydrogels: progress and challenges, J. Mat. Chem. B 1 (2013) 5371–5388, http://dx.doi.org/10.1039/c3tb20940g.
[7] L. Yu, J. Ding, Injectable hydrogels as unique biomedical materials, Chem. Soc. Rev. 37 (2008) 1473–1481, http://dx.doi.org/10.1039/b713009k.
[8] X. Xu, A.K. Jha, D.A. Harrington, M.C. Farach-Carson, X. Jia, Hyaluronic acid-based hydrogels: from a natural polysaccharide to complex networks, Soft Matter 8 (2012) 3280–3294, http://dx.doi.org/10.1039/C2SM06463D.
[9] C. Vinatier, O. Gauthier, A. Fatimi, C. Merceron, M. Masson, A. Moreau, F. Moreau, B. Fellah, P. Weiss, J. Guicheux, An injectable cellulose-based hydrogel for the transfer of autologous nasal chondrocytes in articular cartilage defects, Biotechnol. Bioeng. 102 (2009) 1259–1267, http://dx.doi.org/10.1002/bit.22137.
[10] A.M. Jonker, D.W.P.M. Löwik, J.C.M. Van Hest, Peptide- and protein-based hydrogels, Chem. Mater 24 (2012) 759–773, http://dx.doi.org/10.1021/cm202640w.
[11] H. Tan, C.M. Ramirez, N. Miljkovic, H. Li, J.P. Rubin, K.G. Marra, Thermosensitive injectable hyaluronic acid hydrogel for adipose tissue engineering, Biomaterials 30 (2009) 6844–6853, http://dx.doi.org/10.1016/j.biomaterials.2009.08.058.
[12] A.P. Constantinou, T.K. Georgiou, Tuning the gelation of thermoresponsive gels, Eur. Polym. J. 78 (2016) 366–375, http://dx.doi.org/10.1016/j.eurpolymj.2016.02.014.
[13] P. Alexandridis, J.F. Holzwarth, T.A. Hatton, Micellization of poly(ethylene oxide)-Poly(propylene oxide)-Poly(ethylene oxide) triblock copolymers in aqueous solutions: thermodynamics of copolymer association, Macromolecules 27 (1994) 2414–2425, http://dx.doi.org/10.1021/ma00087a009.
[14] C. Booth, D. Attwood, Effects of block architecture and composition on the association properties of poly(oxyalkylene) copolymers in aqueous solution, Macromol. Rapid Commun. 21 (2000) 501–527, http://dx.doi.org/10.1002/1521-3927(20000601)21:9<501::AID-MARC501>3.0.CO;2-R.
[15] L. Yu, J. Ding, Injectable hydrogels as unique biomedical materials, Chem. Soc. Rev. 37 (2008) 1473–1481, http://dx.doi.org/10.1039/b713009k.
[16] N.E. Fedorovich, I. Swennen, J. Girones, L. Moroni, C.A. Van Blitterswijk, E. Schacht, J. Alblas, W.J.A. Dhert, Evaluation of photocrosslinked lutrol hydrogel for tissue printing applications, Biomacromolecules 10 (2009) 1689–1696, http://dx.doi.org/10.1021/bm801463q.
[17] H.J. Chung, Y. Lee, T.G. Park, Thermo-sensitive and biodegradable hydrogels based on stereocomplexed Pluronic multi-block copolymers for controlled protein delivery, J. Control. Release 127 (2008) 22–30, http://dx.doi.org/10.1016/j.jconrel.2007.12.008.
[18] Y. Lee, H.J. Chung, S. Yeo, C.-H. Ahn, H. Lee, P.B. Messersmith, T.G. Park, Thermo-sensitive, injectable, and tissue adhesive sol–gel transition hyaluronic acid – pluronic composite hydrogels prepared from bio-inspired catechol-thiol reaction, Soft Matter 6 (2010) 977, http://dx.doi.org/10.1039/b919944f.
[19] K.A. Mauritz, R.B. Moore, State of understanding of nafion, Chem. Rev. 104 (2004) 4535–4585, http://dx.doi.org/10.1021/cr0207123.
[20] A. Kelarakis, R.H. Alonso, H. Lian, E. Burgaz, L. Estevez, E.P. Giannelis, Nanohybrid nafion membranes for fuel cells, ACS Symp. Ser 1034 (2010), http://dx.doi.org/10.1021/bk-2010-1034.ch012.
[21] R.F.B. Turner, D.J. Harrison, R.V. Rajotte, Preliminary in vivo biocompatibility studies on perfluorosulphonic acid polymer membranes for biosensor applications, Biomaterials 12 (1991) 361–368, http://dx.doi.org/10.1016/0142-9612(91)90003-S.
[22] R.F.B. Turner, C.S. Sherwood, Biocompatibility of perfluorosulfonic acid polymer membranes for biosensor applications, Diagn. Biosens. Polym. 17 (1994) 211–221, http://dx.doi.org/10.1021/bk-1994-0556.ch017.
[23] P. Hashemi, P.L. Walsh, T.S. Guillot, J. Gras-Najjar, P. Takmakov, F.T. Crews, R.M. Wightman, Chronically implanted, nafion-coated Ag/AgCl reference electrodes for neurochemical applications, ACS Chem. Neurosci. 2 (2011) 658–666, http://dx.doi.org/10.1021/cn2000684.
[24] D. Chen, C. Wang, W. Chen, Y. Chen, J.X.J. Zhang, PVDF-Nafion nanomembranes coated microneedles for in vivo transcutaneous implantable glucose sensing, Biosens. Bioelectron. 74 (2015) 1047–1052, http://dx.doi.org/10.1016/j.bios.2015.07.036.
[25] R.F. Vreeland, C.W. Atcherley, W.S. Russell, J.Y. Xie, D. Lu, N.D. Laude, F. Porreca, M.L. Heien, Biocompatible PEDOT: nafion composite electrode coatings for selective detection of neurotransmitters in vivo, Anal. Chem. 87 (2015) 2600–2607, http://dx.doi.org/10.1021/ac502165f.
[26] Z. Dai, H. Mohwald, Highly stable and biocompatible nafion-based capsules with controlled permeability for low-molecular-weight species, Chem. Eur. J. 20 (2002) 4751–4755, http://dx.doi.org/10.1002/1521-3765(20021018)8:20.
[27] A. Kelarakis, E.P. Giannelis, Nafion as cosurfactant: solubilization of nafion in water in the presence of pluronics, Langmuir 27 (2011) 554–560, http://dx.doi.org/10.1021/la103318u.
[28] A. Kelarakis, M.J. Krysmann, Trivial and non-trivial supramolecular assemblies based on nafion, Colloids Interface Sci. Commun. 1 (2014) 31–34, http://dx.doi.org/10.1016/j.colcom.2014.06.005.
[29] A. Kelarakis, V. Havredaki, K. Viras, W. Mingvanish, F. Heatley, C. Booth,

S.M. Mai, Aqueous solutions and gels of diblock copolymers of 1,2-butylene oxide and ethylene oxide studied by light scattering and rheology, J. Phys. Chem. B 105 (2001) 7384–7393, http://dx.doi.org/10.1021/jp003364m.

[30] G. Sauerbrey, Verwendung von Schwingquarzen zur Wagungdünner Schichten und zur Mikrowagung, Z. Fur Phys. 155 (1959) 206–222, http://dx.doi.org/10.1007/BF01337937.

[31] M. Rodahl, F. Höök, A. Krozer, P. Brzezinski, B. Kasemo, Quartz crystal microbalance setup for frequency and Q - factor measurements in gaseous and liquid environments 66 (1995) 3924–3930, http://dx.doi.org/10.1063/1.1145396.

[32] J. Hu, V. Baglio, V. Tricoli, A.S. Arico, V. Antonucci, PEO-PPO-PEO triblock copolymer/Nafion blend as membrane material for intermediate temperature DMFCs, J. Appl. Electrochem 38 (2008) 543–550, http://dx.doi.org/10.1007/s10800-007-9471-5.

[33] A. Kelarakis, J.J. Crassous, M. Ballauff, Z. Yang, C. Booth, Micellar spheres in high frequency oscillatory field, Langmuir 22 (2006) 6814–6817, http://dx.doi.org/10.1021/la0607860.

[34] N. Goutev, Z.S. Nickolov, G. Georgiev, H. Matsuura, Hydration of a short chain poly(oxyethylene) (C1E2C1) studied by analysis of the O-H Raman band, J. Chem. Soc. Faraday Trans. 93 (1997) 3167–3171, http://dx.doi.org/10.1039/A702629C.

[35] A. Kelarakis, V. Havredaki, C. Booth, Aqueous gels of diblock oxyethylene-oxypropylene copolymers, Macromol. Chem. Phys. 204 (2003) 15–21.

[36] T.G. O'Lenick, X. Jiang, B. Zhao, Thermosensitive aqueous gels with tunable sol - gel transition temperatures from thermo- and pH-responsive hydrophilic ABA triblock copolymer, Langmuir 26 (2010) 8787–8796, http://dx.doi.org/10.1021/la9045308.

[37] A. Kelarakis, V. Castelletto, C. Chaibundit, J. Fundin, V. Havredaki, I.W. Hamley, C. Booth, Rheology and structures of aqueous gels of triblock(oxyethylene/oxybutylene/oxyethylene) copolymers with lengthy oxyethylene blocks, Langmuir 17 (2001) 4232–4239, http://dx.doi.org/10.1021/la0101806.

[38] R. Chang, Y. Huang, G. Shan, Y. Bao, X. Yun, T. Dong, P. Pan, Alternating poly(lactic acid)/poly(ethylene-co-butylene) supramolecular multiblock copolymers with tunable shape memory and self-healing properties, Polym. Chem. 6 (2015) 5899–5910, http://dx.doi.org/10.1039/C5PY00742A.

[39] S.S. Kulthe, N.N. Inamdar, Y.M. Choudhari, S.M. Shirolikar, L.C. Borde, V.K. Mourya, Mixed micelle formation with hydrophobic and hydrophilic Pluronic block copolymers: implications for controlled and targeted drug delivery, Colloids Surf. B Biointerfaces 88 (2011) 691–696, http://dx.doi.org/10.1016/j.colsurfb.2011.08.002.

[40] G.M. Zentner, R. Rathi, C. Shih, J.C. Mcrea, M. Morgan, S. Weitman, Biodegradable block copolymers for delivery of proteins and water-insoluble drugs, J. Control. Release 72 (2001) 203–215, http://dx.doi.org/10.1016/S0168-3659(01)00276-0.

[41] V. Castelletto, I.W. Hamley, J.S. Pedersen, Small-angle neutron scattering study of the structure of superswollen micelles formed by a highly asymmetric poly(oxybutylene)-poly(oxyethylene) diblock copolymer in aqueous solution, Langmuir 20 (2004) 2992–2994, http://dx.doi.org/10.1021/la036.

179

7.2 Patent

Method of fingerprinting with using carbogenic nanoparticles
WO 2016042337 A1

ABSTRACT

The present invention relates to a powder composition, in particular a fingerprint powder composition for the visualisation of latent fingerprints. Such fingerprint powder compositions comprise carbogenic nanoparticles which, when mixed with a suitable diluent (including any existing or future fingerprint powders), exhibits excitation- dependent emission properties which enable the fingerprint powder compositions and imagable fingerprint impression patterns formed therefrom to be imaged in a variety of different colours by simply varying the wavelength(s) of any excitation radiation. As certain backgrounds can render visualisation of fingerprint impression patterns very difficult, having the flexibility to judiciously tune the foreground colour of the fingerprint impression patterns is a significant advantage since it permits instantaneous improvements in visualisation without needing to resort to using a different fingerprint powder. The invention also relates *inter alia* to corresponding methods and specialised apparatus for fingerprinting.

Publication number	WO2016042337 A1
Publication type	Application
Application number	PCT/GB2015/052698
Publication date	Mar 24, 2016
Filing date	Sep 18, 2015
Priority date ⓘ	Sep 19, 2014
Also published as	US20170281053
Inventors	Antonios KELARAKIS, Marta J. KRYSMANN, Diogo FERNANDES
Applicant	University Of Central Lancashire
Export Citation	BiBTeX, EndNote, RefMan

Patent Citations (4), Classifications (6), Legal Events (3)

External Links: Patentscope, Espacenet